



Numerical modeling of dry and lubricated sliding contact of (visco)elastic bodies

by
Tibor J. Goda

Budapest University of Technology and Economics
Department of Machine and Product Design

A thesis submitted in intended fulfilment of the requirements for the title of

Doctor of Science (D.Sc.)

at the
Hungarian Academy of Sciences

Budapest, 2016.

This thesis is dedicated to my family for their help, encouragement and patience during my research activity and the preparation process of the thesis as well as for the calm background without which this thesis would not have come into being.

Contents

Statement of originality and declaration of authorship	6
1. Introduction	7
2. Outline of the thesis.....	9
3. Topics addressed in the thesis	10
3.1. Practical importance of the topics.....	10
3.2. Related industrial R&D projects of the author	11
4. Dry and lubricated sliding friction of rubbers and rubber-like (viscoelastic) materials	12
4.1. Separable rubber friction contributions	12
4.1.1. Dry friction	13
4.1.2. Lubricated friction	13
4.1.3. Viscoelastic component of rubber friction	15
4.1.4. Adhesion component of rubber friction	15
4.2. Viscoelastic friction predictions	16
4.3. Finite element modeling of viscoelastic friction.....	18
4.3.1. Two-dimensional single asperity contact model for the simulation of asperity-asperity interaction: Qualitative analysis	19
4.3.2. Two-dimensional single asperity contact model for the simulation of hard, ideally smooth asperity sliding on smooth rubber plane.....	22
4.3.3. Two-dimensional single asperity contact models for the simulation of hard, rough asperity sliding on smooth rubber plane	23
4.3.4. Two-dimensional FE model for the simulation of hard sinusoidal one-scale surface sliding on smooth rubber plane.....	25
4.3.5. Two-dimensional FE model for the simulation of hard, multi-scale sinusoidal surface sliding on smooth rubber plane	27
4.3.6. Three-dimensional FE model for the simulation of hard, apparently smooth surface sliding on smooth rubber plane.....	30
4.3.7. Three-dimensional FE modeling of viscoelastic friction at macro-scale ...	32
4.4. Experimental investigation of apparently smooth, hard surface generated viscoelastic friction on the basis of literature results	36
4.4.1. Unlubricated frictional behavior of nitrile butadiene rubber (NBR).....	37
4.4.2. Frictional behavior of nitrile butadiene rubber (NBR) under oil lubricated condition.....	39
4.4.3. Critical discussion of the most important literature results	47
4.4.4. Conclusions	51
4.5. Numerical modeling of mixed friction of sliding rubber components using stochastic modeling approach	51

4.5.1. State of the art.....	51
4.5.2. Separation of nominally flat rough surfaces in contact: Greenwood-Williamson's contact theory vs. Persson's contact theory	52
4.5.3. Salant et al.'s stochastic mixed friction model and its implementation	59
4.5.4. Verification problem: Ideal smooth flat surface in contact with combined sinusoidal/flat surface.....	65
4.5.5. Verification problem: Ideal smooth flat surface in contact with parabolic surface	67
4.5.6. Verification problem: Ideal smooth flat surface in contact with sinusoidal surface	68
4.5.7. Windscreen wiper application	71
4.5.8. Sealing application: O-ring.....	76
5. Numerical modeling of wall (macro-scale) friction in hoppers/silos using simple law of friction at the particle- (micro-) scale: Discrete modeling approach.....	82
5.1. Fundamentals of DEM.....	82
5.2. Application of the discrete modeling approach in numerical tribology	83
5.3. Implementation of the discrete element method in 3D.....	84
5.4. Application of the computer code developed by the author of the thesis for wall friction prediction.....	90
5.4.1. Literature results	90
5.4.2. Discrete element simulations for nonaxisymmetric hoppers/silos filled with viscoelastic granular material.....	92
5.4.3. Results for hopper.....	94
5.4.4. Results for silo with a hopper bottom.....	97
5.4.5. Results for flat-bottomed silo	100
5.4.6. Discussion of the flow behavior	103
6. Summary	104
7. New scientific results	106
References	108
Összefoglalás.....	115
Acknowledgements	117
Appendix A	118
A.1. Modeling of time independent, nonlinear (perfectly) elastic response of rubbers and rubberlike materials.....	118
A.2. Finite element modeling of small strain linear viscoelastic behavior of rubbers and rubberlike materials.....	118
A.3. Finite element modeling of large strain (finite) linear viscoelastic behavior of rubbers and rubber-like materials	123

A.4. Parameter identification based on the time (frequency)-temperature correspondence principle	124
A.5. Extension of the material model over the viscoplastic material behavior	128
Appendix B	130
B.1. Surface roughness spectral density	130
Appendix C	134
C.1. Modeling of viscoelastic material behavior of EPDM 75 IRHD	134

Statement of originality and declaration of authorship

As author of the thesis entitled „*Numerical modeling of dry and lubricated sliding contact of (visco)elastic bodies*” I confirm that this thesis is original and is submitted to the Hungarian Academy of Sciences for the title of Doctor of Science. In all the cases when the research work presented has been done myself jointly with others I have made clear what was done by others and what I have contributed myself. According to this I confirm that my contribution to the research presented here is as follows.

The thesis focuses on the numerical modeling of friction with particular regard to FE modeling of (a) viscoelastic component of rubber friction, (b) mixed friction of rubber components, and (c) discrete element simulation of wall friction in three-dimensional nonaxisymmetric hoppers/silos. The research being concerned with the FE prediction of viscoelastic friction (see Chapter 4.3) has been performed in the frame of project KRISTAL (Knowledge-based radical innovation surfacing for tribology and advanced lubrication) funded under the 6th Framework Program of the European Union (Project reference: 515837, www.cordis.europa.eu/project/rcn/75754_en.html) and in collaboration with PhD students, namely László Pálfi, Nándor Békési and Enikő Soós. My role in the project was, at the beginning, of twofold. On the one hand I contributed to the research as researcher, whilst on the other hand I supervised the research work. In the last one and half year of the project, these tasks were supplemented with the leadership of the project. In respect of FE prediction of viscoelastic friction I contributed to the research through elaboration of theoretical models, calibration of viscoelastic material models and evaluation/interpretation of simulation results. My research in the field of viscoelastic friction prediction has also been supported by the János Bolyai Scholarship of the Hungarian Academy of Sciences. My latest research (see Chapter 4.4) is directed to the critical discussion of experimental results obtained by others for apparently smooth, hard surface generated viscoelastic friction. The computational algorithm for the discrete Fourier transformation of surface height profiles (surface topography) of rough surfaces obtained from series of finite line scans (see Appendix B) was developed and implemented myself.

The research connecting to mixed friction simulation of rubber components and presented in Chapter 4.5 is my individual work excepting the influence coefficient matrices and the FE models for O-rings and wiper blades. The latter have been constructed by my former PhD student Gábor Bódai within the frame of our research project supported by the “Development of quality-oriented and harmonized R+D+I strategy and functional model at BME” project (New Hungary Development Plan, Project ID: TÁMOP-4.2.1/B-09/1/KMR-2010-0002). The development, the implementation and the application of the one-dimensional, steady-state mixed friction computational algorithm have been supported by the János Bolyai Scholarship of the Hungarian Academy of Sciences and the EU-6 project KRISTAL.

Third part of the research work summarized here, namely the discrete element modeling of wall friction in hoppers/silos (see Chapter 5) is entirely my individual work. The three-dimensional, generally applicable discrete element computational algorithm needed for the simulations has been developed and implemented myself in the frame of the project “Numerische Simulation technischer Partikelsysteme auf Hochleistungsrechnern” of German Research Fund (DFG).

As a last point I confirm that where I have quoted from the work of others, the source is given. Additionally it is also confirmed that the new scientific results formulated in this thesis are original and my own results.

1. Introduction

In 1699, Amontons found experimentally that the kinetic friction force arising between dry, apparently (macroscopically) smooth metal surfaces is approximately linearly proportional to the applied normal force under a wide range of conditions. It is the case when e.g. both the friction force and applied load are linearly proportional to real area of contact. In other words, his friction tests showed that the ratio of friction force to normal force is constant and is independent of the nominal or apparent contact area, normal force, sliding velocity and roughness. This implies that the nominal frictional shear stress is approximately linearly proportional to the nominal contact pressure defined as the ratio of applied normal load and the nominal (apparent) contact area. Traditionally, the constant ratio of friction (tangential) force and applied normal force is termed coefficient of friction. In connection with Amontons's empirical law of dry friction, however, it must be noted that it can be considered as a very simple approximation of the real friction phenomenon only. In 1780, Coulomb revised Amontons's law and pointed out experimentally that the ratio of friction force and normal force, in reality, depends on the normal force, sliding velocity, nominal contact area, roughness, etc. Coulomb's friction tests made it clear that apparently smooth metal-metal contact pairs, as a good approximation, obey Amontons's law of friction while wood-metal and wood-wood contact pairs disobey this law. The ratio of dry friction force to normal force for sliding rubbers, and rubber-like (viscoelastic) materials is usually also not constant. In this thesis, the ratio of friction (tangential) force and applied normal force acting on sliding rubber components is termed apparent coefficient of friction. Nowadays, it is widely accepted that the ratio of rubber friction force and normal force depends on the sliding velocity, nominal contact area, normal force, temperature and so on. Another important characteristic of rubber friction is that the friction force is caused by concurrently acting rubber friction mechanisms which differ from the friction producing mechanisms of contacting metal surfaces. Although Amontons's law of friction, due to its simplicity, is extensively used in engineering practice this very short review on the history of science of friction shows clearly that the traditional macroscopic approach where a constant coefficient of friction is assigned to the sliding pair cannot be applied for rubber and rubber-like materials. In order to develop reliable rubber friction laws it is essential to understand the causes and consequences of phenomena influencing friction. It was pointed out experimentally and theoretically that there exists a friction component which is directly related to hysteresis in the rubber bulk. This component is influenced by both macro- and micro-geometry (surface roughness) and is termed viscoelastic or hysteresis friction component. As the hysteresis has effect on both sliding and rolling friction the viscoelastic component of friction is extensively studied in the literature. In most cases, however, the focus is put on tires being in contact with rough concrete, asphalt, etc. road surface (tire application) because the contribution of viscoelastic component to friction is more significant when the counter surface is rough. Root-mean-square roughness of asphalt road surface is typically few hundred microns, while that of polished steel surface is typically few tenth microns. In many cases, however, viscoelastic bodies are paired with apparently smooth, hard surfaces (e.g. sealing application). Although the latter is of great importance in mechanical engineering practice only a few studies are available in the literature on the prediction of viscoelastic friction component. One of these studies came to the conclusion that the seemingly mild roughness of a highly polished steel surface may also give the dominant contribution to the friction, even for lubricated surfaces. Although apparently smooth surfaces seem smooth for human eye, in the reality, they are rough. The increasing magnification makes visible their real surface micro-topography. When the magnification is low, the rough surface seems quite smooth because the short wavelength roughnesses do not appear. In most cases, rough surfaces are considered to be isotropic, where their statistical properties are translational and rota-

tional invariant i.e. independent of the location and direction of line scans (1D surface roughness measurements). However, many engineering surfaces have anisotropic surface roughness (e.g. unidirectionally polished steel surfaces) yielding sliding direction dependent friction force. Another important character of rough surfaces is that the coarser scale asperities are covered with finer scale asperities (multi-scale character of rough surfaces) and the friction force predicted for a given surface roughness depends both on the shortest and on the longest wavelength components (the surface is considered to be rough between the longest and the shortest wavelength component only). The longest wavelength component of surface roughness is usually determined by the dimensions of the nominal contact area of the contacting bodies. The viscoelastic nature of material behavior complicates further the problem. In the rubbery region (at very small excitation frequencies), the rubber behaves as a soft, perfectly elastic material since its energy dissipation is negligible. On the other hand, in the glassy region (at very high excitation frequencies) it behaves as a stiff, almost perfectly elastic material because its energy dissipation is negligible in this state. However, in the transition region, the energy dissipation of rubber cannot be neglected while its stiffness increases with orders of magnitude with increasing frequencies. Due to its great practical importance the first topic addressed in this thesis is the numerical prediction and experimental investigation of surface roughness generated viscoelastic friction. The studies summarized here apply one of the most important/frequently used continuum mechanics-based method of numerical tribology, namely the finite element method. Using finite element method not only the detailed geometry of asperities but also the effect of large strains and viscoelasticity can be taken into consideration. Due to the huge CPU time and memory demand, however, it is practically impossible to consider all length scales of the surface roughness in a single FE model. Contrary to this fact the FE models help us to understand the role of viscoelastic friction while the knowledge gained from them will enable engineers to design viscoelastic components/machine elements with improved tribological behavior.

Reciprocating rubber seals as typical viscoelastic machine elements are widely used in mechanical engineering practice. In most engineering applications, rubber/metal sliding pairs are lubricated in order to decrease the friction force arising in dry case and hindering the damages of the contacting surfaces. In the presence of lubricant, rubber friction is influenced by the viscoelastic losses in the rubber, the boundary lubrication and the fluid friction. The lubrication diminishes adhesion and decreases the contribution of surface roughness generated viscoelastic friction because lubricant fills out the valleys of surface roughness i.e. seemingly smoothes the rough surface. In the case of full film lubrication, there is a continuous lubricating film with load carrying capacity between the contacting surfaces which does not make it possible to come into direct, asperity type contacts. In this case, the total normal load is carried by the lubricating film. Contrary to this, in mixed lubrication, the lubricating film is not able to separate surfaces from each other completely i.e. local solid contacts can be formed among asperities. As a consequence, one part of the normal load is carried by the lubricating film while the rest is carried by solid contacts. To predict the lubrication performance of a reciprocating seal engineers need effective and accurate models and algorithms. In the last two decades, intensive development was observable in the numerical modeling of lubrication of reciprocating seals. Main aims of the research work were, among others, to predict the thickness of the lubricant film, the pressure distribution due to hydrodynamic effect and solid/solid contact, the friction resistance (friction force), the amount of leakage which can be defined as the difference between fluid transport during outstroke and instroke. Thanks to the research efforts the latest numerical models are able to take into consideration not only the seal deformation, the effect of surface roughness and the pressure dependent viscosity but also the cavitation. The second part of the thesis concentrates to the implementation and application of a very recent stochastic, one-dimensional, steady-state mixed friction model.

Numerical methods of tribology can be divided into two parts. One part of methods uses the continuous approach (e.g. finite element method) while another part of them follows discrete approach (e.g. discrete element method, molecular dynamics simulation). In the last few decades, the importance of discrete approach, similarly to other fields of science, continuously increases. Continuum mechanics-based numerical methods are widely used to model frictional contact of rough surfaces, flow of lubricant, etc. while the discrete element method (macro- and micro-scale) and the molecular dynamics simulation (atomic- or nano-scale) can be used to model solids, liquids and gasses. Due to the large CPU time, however, the time scale and space scale that can be modeled are strongly limited in the discrete modeling approach. By combining the continuous and discrete approach, however, it is possible to create multi-scale (time- and space scale) numerical models for contact mechanics problems. Consequently the main aim of the community of numerical tribology is to couple the continuous and the discrete approaches. In accordance with these efforts the third part of the thesis concentrates on the implementation of three-dimensional discrete element method and its application for wall friction prediction in hoppers/silos containing viscoelastic granular material.

2. Outline of the thesis

In Chapter 3, the topics addressed in this thesis are collected. After highlighting their practical importance some related industrial R&D projects are presented. In order to characterize the very complex frictional behavior of viscoelastic bodies Chapter 4 starts with the discussion of dry and lubricated rubber friction. Then the physical processes associated with rubber friction are introduced and described briefly. As a next step the viscoelastic friction predictions are reviewed briefly (see Chapter 4.2) which is followed by continuum mechanics-based computations. Main aim of the FE models presented in Chapter 4.3 is to investigate the role of the surface roughness generated viscoelastic friction. For the sake of completeness measurement results on apparently smooth surface generated viscoelastic friction are cited and discussed in Chapter 4.4. Within the frame of numerical modeling of mixed elastohydrodynamic lubrication (Chapter 4.5), after a short literature review, the focus is placed on the relation between the mean interfacial separation and the contact pressure originating from Greenwood-Williamson's as well as from Persson's contact theory. Then a mixed friction model is presented and implemented in order to investigate the tribological behavior of O-rings and wiper blades. In Chapter 5, the focus is placed on the numerical modeling of wall friction in nonaxisymmetric hoppers/silos using discrete modeling approach. The first part of the chapter gives insight into the implementation of a three-dimensional explicit discrete element code at which material properties are incorporated into the contact laws. The computer code is composed of classical Newtonian dynamic model for the solution of equations of particle dynamics (discrete element computation) and for the visualization/evaluation of simulation results. In the second part of the chapter, the discrete element code developed is applied for predicting the role of static and dynamic wall friction in three-dimensional containers containing mono-sized, spherical, cohesionless viscoelastic particles. Finally, in Chapter 6, the new scientific results are summarized in compact form.

The thesis is closed by three appendixes. Appendix A gives a detailed description on the theories used here for finite element modeling of time independent hyperelastic and small/large strain linear viscoelastic material behavior. The way of parameter identification and extension of the viscoelastic material model to viscoplasticity are also summarized briefly. In Appendix B, the spectrum of the stationary stochastic surface roughness is introduced and characterized. For the sake of clarity the computation of surface roughness spectrum is also described. Appendix C contains the characterization and modeling of macro-scale viscoelastic material behavior of an ethylene-propylene-diene-monomer (EPDM) rubber which is

the typical material of rubber seals built into real brake cylinders and is used in the majority of FE friction predictions of this thesis.

3. Topics addressed in the thesis

3.1. Practical importance of the topics

The title of the thesis indicates clearly that topics addressed here are directly related to the numerical tribology. Similar to other fields of sciences, nowadays, the tribology as the science of friction, wear and lubrication cannot be imagined without computer simulations. In this thesis, three different topics are addressed: (a) FE prediction of apparently smooth surface generated viscoelastic friction, (b) numerical modeling of mixed elastohydrodynamic lubrication (EHL) of reciprocating rubber seals and components, (c) implementation of the three-dimensional discrete element method and its application for the prediction of wall friction and static/dynamic wall pressure.

Investigation of dry and lubricated friction of viscoelastic bodies is of great practical importance because many everyday life-related components (tire of automobiles, bicycles, motorbikes, agricultural machines; shoe sole; windscreen wiper; etc.) and important machine elements (seals, rollers, conveyor belts, guiding shoes, etc.) are made of rubber or rubber-like material. The friction relating to these components affects, among others, the energy consumption, the fuel consumption, the CO₂ emission, the amount of lubricant needed, the slip and fall accidents causing human injuries/deaths, the occupational safety and health, the traffic safety, the friction related control and service problems, the friction related vibration and noise generation, the environment friendly design of rubber products, the reduction of environmental impact, etc. It is worth to mention that real micro topography (surface roughness) of surfaces plays critical role not only in dry and lubricated friction of bodies but also in additional physical phenomena, such as wear and thermal/electrical conductance between surfaces. Although rubber friction has wide literature relative little information is available on apparently smooth surface generated viscoelastic friction. Majority of studies dealing with hysteresis friction focuses on tire friction where the RMS roughness of the road surface is bigger with orders of magnitude than that of apparently smooth surfaces frequently used in sealing applications. In case of dynamic seals, however, one of the main uncertainties is the friction-connected energy loss contribution arising from micro hysteresis. Consequently it is essential to get better insight into the mechanism of hysteresis friction and give reliable prediction for the hysteresis component of rubber friction. Accurate prediction of micro hysteresis friction makes the differentiation and quantification of other friction mechanisms (contribution to rubber friction from macro hysteresis, adhesion, rubber wear, etc.) possible. Additionally, the knowledge gained from theoretical and/or experimental works will enable engineers to design sliding/rolling viscoelastic components with prescribed (decreased or increased) friction. At the same time numerical tribology helps engineers to understand the causes and consequences of friction and to develop design tools with which the tribological aspects can be taken into consideration even in the design phase. One part of the research work (viscoelastic friction predictions, material characterization and parameter identification, surface roughness characterization) presented in this thesis is directly related to the operation of automobile brake systems. In a typical automobile brake system the force exerted on the brake pedal is converted into hydraulic pressure in the master cylinder. A modern master cylinder contains two plungers; each of them makes a separate brake circuit to operate. The brake plunger moves forward when the driver pushes the brake pedal and goes back in its initial position as the pedal is released. The primary plunger is operated through the brake pedal while the hydraulic pressure between the primary and secondary plunger forces the secondary plunger to press the fluid in its circuit. As the brake plungers are in contact with rubber seals the resulting friction force

has to be overcome when they move. Due to the non-zero frictional resistance the hydraulic pressure in the two separate brake circuits cannot be exactly the same. To minimize this pressure difference the friction force at the plunger/rubber seal contact has to be kept as low as possible.

Reciprocating hydraulic rod seals are widely used in different industrial applications and they operate frequently in the boundary lubrication or the mixed friction regime. In the last few decades, huge effort was made in the literature to minimize wear, friction resistance (friction force) and leakage (seals with less leak rate or possibly zero leakage). To predict the tribological behavior of rubber seals engineers need effective and accurate models and algorithms (design tools) with which they can test different what-if scenarios and seal geometries, perform sensitivity analysis, optimize the geometry, surface roughness and surface treatment of rubber component and its counterpart, eliminate or minimize time consuming and expensive measurements, reduce the number of prototypes, simulate real engineering problems, and understand the effect of different physical processes on the tribological behavior. Furthermore mixed friction simulations contribute to the better designing of rubber component and reduce the time to market. Numerical models are particularly useful because they usually allow engineers to analyze more complex sealing problems where the frictional heat generation, thermal expansion, nonlinear material behavior, and temperature dependent material properties of the seal, seal wear, texturing and surface treatment of the seal, etc. play important/decisive role. Establishment of such numerical models is, however, very challenging due to the fact that the frictional loss of seals is affected, among others, by seal geometry, surface roughness of contacting surfaces, material of contacting components, texturing, coating and antifriction treatment of contacting surfaces, lubricant, temperature, etc.

In order to improve the tribological properties it is essential to understand the interrelation between tribological behavior at macro and micro/nano-scale. Due to the lack of knowledge on scale dependent tribological behavior, in the majority of cases, the so called “trial and error” approach prevails in the present design practice of sliding systems. Numerical methods of tribology, however, allow us to change this. To predict friction, study contact conditions and simulate wear at macro-, micro- and nano-scale numerically both continuum (e.g. finite element method, boundary element method) and discrete methods (e.g. discrete element method, molecular dynamics simulation) can be used. As there exists no a generally applicable simulation method for multi-scale (time- and space-scale) systems, in many cases, it is needed to couple these methods. At this point, it must be mentioned that the three-dimensional discrete element computation algorithm and program developed and implemented by the author of this thesis can be used for multi-scale systems and, after minor modification, for MD simulations. At the same time the computer code mentioned may be extended freely and with or without modifications can be used for wear simulation and for research in material science, fracture mechanics, rheology of particulate materials, soil mechanics, etc.

3.2. Related industrial R&D projects of the author

Beside direct application of the techniques and methods presented in this thesis the indirect application of those has also practical importance. In order to prove this, two different practical problems are mentioned here which emerged in the industrial sector and solved by the author of this thesis within the frame of industrial R&D projects. The first problem was connected with the sealing capability of soft, viscoelastic gaskets used in the gas industry and the focus was placed on the modeling and analyzing of stress relaxation caused by the viscoelastic nature of gaskets. A considerable part of such gaskets is made of rubber or rubber-like material and, as a good approximation, shows thermorheologically simple material behavior. As it is well known the viscoelastic material behavior yields decreasing clamping force (it is the force that pushes the soft gasket against the counter surface in order to eliminate leakage

through the small channels formed between the contacting rough surfaces) as the time elapses. If the magnitude of clamping force falls below a critical value the gasket starts to leak. In most cases, the critical value of clamping force can only be determined experimentally due to the large number of influencing factors. The leakage is dangerous and, at the same time, causes financial losses for the gas suppliers. Nowadays the propensity of gas suppliers to minimize gas losses increases due to the high energy prices. To sum it up it can be concluded that research efforts on reduction of leakage are of great practical importance because the gas saving and the accompanying money saving can be considerable due to the huge number of gaskets built into union joints of gas-meters and the high energy prices. Within the frame of the R&D project, it was pointed out that, based on the master curves of different gasket materials it is possible to estimate the necessary frequency of gasket replacements and to rank soft gaskets available on the market. The second industry induced problem was related to the modeling of fluid/structure interaction (FSI) which is arisen also in simulation of soft elastohydrodynamic lubrication of rubber seals. The overall aim was to connect CFD (Computational Fluid Dynamics) and FE structural analysis through transferring contact pressure distribution computed by Ansys Fluent to MSC.Marc for static stress analysis. In order to solve this problem the author of this thesis developed computer algorithm and program to convert the output pressure distribution of CFD into an approximately equivalent input pressure distribution for FE analysis.

4. Dry and lubricated sliding friction of rubbers and rubber-like (viscoelastic) materials

Nowadays, major share of seals subjected to sliding friction made of rubber or rubber-like (viscoelastic) material. Although these seals are widely used in the industry, the impact of time (load frequency)-and temperature-dependent material behavior on the friction force is not satisfactorily understood. To overcome this difficulty numerous theoretical and experimental studies dealt with the physical background of rubber friction in the last years and decades.

4.1. Separable rubber friction contributions

Pioneering work of Grosch [1] has shown that rubber friction force and energy dissipation arise, first of all, from interfacial adhesion and hysteresis losses in the rubber itself. Generally, it can be concluded that interfacial adhesion plays important role at clean, dry surfaces and at small sliding speeds. Contrary to this, in case of lubricated surfaces and high sliding speeds, the friction dissipation is due primarily to hysteresis losses in the rubber. Furthermore, it has been found that both adhesion and deformation (hysteresis) losses are directly related to the viscoelastic properties of the rubber.

As reported by Lorenz et al. [2] several different physical processes contribute to rubber friction (see Fig. 4.1). (a) The substrate asperities deform the rubber which, during sliding, gives rise to energy dissipation in the bulk of the rubber (pink light dotted area). (b) Close to the opening crack tips very large viscoelastic deformations may occur resulting in locally very large energy dissipation (pink heavy-dotted area). (c) There will also be a contribution to the energy dissipation from shearing a thin solid or liquid or mixed contamination film (green area) on the rubber surface and/or on the substrate surface. In the absence of such a film direct bonding between the rubber molecules and the substrate, followed by viscoelastic deformation and bond breaking, will also contribute to the energy dissipation and the friction force. (d) In addition, a contribution to rubber friction will arise from wear processes, *e.g.*, the energy necessary to propagate cracks in the rubber surface region resulting in the removal of small rubber particles. As it is mentioned by Lorenz et al. [2], in most practical applications, rubber

friction is usually modeled using Amontons's law with sliding velocity (v) and pressure (p) dependent apparent coefficient of friction ($\mu(v, p)$). However this is a phenomenological approach where different physical processes of rubber friction are not described and modeled. Furthermore [2] mentions that the friction force, in case of a rubber block sliding on a concrete surface, is, among others, due to the combined effect of asperity-induced viscoelastic bulk deformation, opening cracks and shearing of a thin viscous film at the interface. In other words, only a fraction of the energy dissipated during sliding of a rough surface on rubber is due to asperity induced viscoelastic losses.

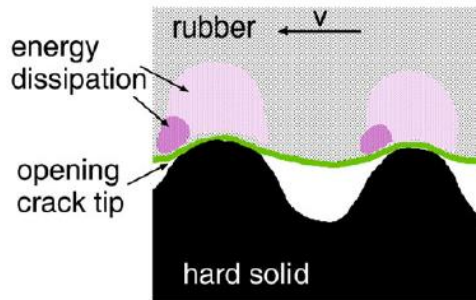


Fig. 4.1. Asperity level physical processes contributing to rubber friction [2]

The contribution of different components to the friction force depends on the macro geometry, detailed surface micro-topography, relative tangential velocity, cleanliness of surfaces, temperature, material and surface properties of rubbing bodies, applied normal load, filler material and content, lubricant and its additives, and surface treatment/coating of the harder counterpart and/or the rubber surface. The interaction of friction mechanisms and complexity of physical processes (complex nature of rubber friction), however, make the friction prediction and the modeling of physical processes associated with rubber friction very challenging. Consequently the applicability and prediction capability of analytical and/or numerical models have been developed so far are limited and, in many cases, the different scales of tribological processes may be modeled only by combining discrete methods (e.g. discrete element method, molecular dynamics simulation) and numerical methods of continuum mechanics (e.g. finite element method).

4.1.1. Dry friction

Nowadays, it is commonly accepted that basically four mechanisms are responsible for rubber friction in dry case. As reported by Smith [8] rubber friction is controlled by adhesion, macro hysteresis, micro- or surface roughness generated hysteresis, and cohesion (friction contribution from rubber wear). When rubber slides on smooth clean surface the rubber friction is due to mainly adhesion. This is the case at rubber/glass sliding pairs where the adhesive wear predominates. In case of clean, rough counter surface the rubber friction is mainly due to adhesion (especially at low sliding speeds) and energy dissipation in the rubber (viscoelastic friction contribution) as emphasized by Grosch [1], Persson [3] and Klüppel and Heinrich [9]. The viscoelastic friction comes into being when the rubber is subjected to cyclic deformation by the macro and/or micro geometry (surface roughness) of the hard, rough substrate [3, 9].

4.1.2. Lubricated friction

In most engineering applications (e.g. sealing applications), sliding components made of rubber or rubber-like material are lubricated in order to decrease the friction force. In the case of fluid friction (full film lubrication), friction force comes from the shearing of a con-

tinuous fluid film. This is the viscous component of friction which can be interpreted as energy loss due to the viscous nature of lubricant. At the same time, in regions where a very thin lubricating film covers the solid, the friction force comes partly from the shearing of this thin boundary layer. Consequently, in lubricated case, energy dissipation occurring in the sliding process is due to hysteresis losses in the rubber, boundary lubrication and fluid friction. The effect of adhesion usually can be neglected for the lack of direct contacts of solids. (Note: In many cases, the lubricant cannot eliminate the adhesion completely.) Furthermore the lubrication decreases the contribution of surface roughness to hysteresis friction because lubricant fills out the valleys of rough surfaces (smoothing effect of the lubricant) lowering the penetration of the rubber into these regions.

From engineering point of view reciprocating rubber seals are of primary importance because they are frequently used machine elements. During operation most of them slide on (apparently) smooth hard (compared to rubber) counter surface in presence of lubricant. Seals have smooth surface but, as reported by Salant et al. [41], the surface of harder counterpart is usually even smoother in order to reduce friction, rubber wear and wear induced leakage. It is well known that reciprocating rubber seals operate frequently in boundary and mixed lubrication regime. However different explanations exist in the literature for the friction contribution arisen in the boundary lubrication regime. On the one hand, Campbell [42] states that the friction is determined predominantly by interaction between the solids and between the solids and the liquid. Bulk flow properties of the liquid play little or no part in friction. In other words, the friction contribution arisen in the boundary lubrication regime is considered to be due to the shearing of a thin boundary lubricant layer separating contacting surfaces or shearing of the interface between the boundary layer and the solid surfaces. Shear strength of the boundary lubricant layer is influenced by both properties of the contacting surfaces and those of the lubricant. Its magnitude can only be determined by experiments conducted at sufficiently low sliding velocity where the hydrodynamic effect is negligible. Persson et al. [43] pointed out that the applied normal pressure and the adhesion may induce solid/solid contact between the adhered boundary lubricant islands (discontinuous boundary lubricant layer) causing relatively high coefficient of friction. In the boundary lubrication regime, applied normal load is carried by asperity contacts and closed lubricant pools formed in the roughness valleys of harder surface. On the other hand, in the studies of Mofidi et al. [44] and Wohlers et al. [45], the importance of micro hysteresis friction component is emphasized in case of boundary lubrication. The authors hypothesized that the friction contribution arisen in boundary lubrication regime is mainly due to surface roughness generated hysteresis (micro-hysteresis). The reason why this was hypothesized is that the very thin boundary layer formed typically from few layers of lubricant molecules makes solid type asperity contacts possible. In contrast, Smith's theory [8] states that if the adhesion propensity is very low (this is the case when adhesion eliminating boundary layer separates contacting surfaces) the micro hysteresis friction will disappear. Consequently Smith's theory is based on "adhesion-related surface deformation hysteresis" where the decreasing adhesion propensity results in decreasing micro hysteresis friction. Additionally Smith assumes that the micro hysteresis friction contribution is practically independent of the nominal contact pressure.

The windscreen wiper application is particularly interesting because the lubricant is water. It is well known that the water causes perceptible reduction in sliding friction by creating a thin lubricant film between the contacting surfaces. This proves that the water has significant friction reducing effect although its viscosity is low. As reported by Bódai and Goda [10] the lower friction measured in wet case is probably due to the following process. At very low sliding velocities the real contact area is practically the same as in dry case. However, within the asperity contact regions the surfaces are not perfectly dry. They are covered with a very thin water film (hydrophilic solid possesses high surface free energy) which does not

allow the formation of adhesion bonds (boundary lubrication). Results of [10] indicate that, in the boundary lubrication regime, the coefficient of friction depends strongly on the magnitude of normal load. By increasing the sliding velocity the water film, due to the increasing fluid pressure, becomes thicker which results in friction force to be controlled by fluid film friction and boundary layer friction. Due to the thicker water film the importance of real contact area is much less in the mixed friction regime than in the boundary lubrication state.

4.1.3. Viscoelastic component of rubber friction

Basically, both the macro and the micro deformations can cause energy dissipation. As reported by Felhős et al. [11], in case when a smooth steel ball slides or rolls over a rubber plate the viscoelastic friction is due to macro deformations caused by the ball. During sliding or rolling, work is done as the ball moves forward. This work is required to deform the rubber in front of the ball. Simultaneous with this elastic energy is recovered from the rear. Since rubber has viscoelastic material behavior it shows hysteresis and thus one portion of the work done is lost which can be considered as the work of the hysteresis friction force. When a rubber component slides on a hard, rough solid the surface asperities of the hard surface exert oscillating forces on the rubber surface leading to energy dissipation via the "internal friction" of the rubber (micro-hysteresis). In respect of asperity induced energy dissipation (micro hysteresis component of rubber friction), Lorenz et al. [2] emphasize that most of the energy dissipation occurs in a volume element of order d^3 , where d denotes the diameter of an asperity contact region. Furthermore the authors note that in order to have a large asperity induced contribution to the friction, the excitation frequency caused by the sliding asperities should be close to that at which the maximum of the loss factor/tangent ($\tan(\delta)$) curve appears and the $\tan(\delta)$ should be as large as possible. Correlation of loss factor with the viscoelastic friction force is also mentioned, among others, by Hegmon [4], Moore [5], Kummer [6] and Heinrich et al. [7]. Lorenz et al. [2] concluded that the viscoelastic or complex modulus $E(\omega)$ involved in Persson's [3] hysteresis friction theory should be measured at as large strain (or stress) as possible because the strain (or stress) in the vicinity of an asperity contact region, will in general be very high and real rubber materials, in particular filled rubbers, exhibit non-linear rheological properties. The surface roughness generated viscoelastic component of rubber friction is described qualitatively by Achenbach and Frank [22].

4.1.4. Adhesion component of rubber friction

Adhesion component of rubber friction is an area of real contact related phenomenon. It is convenient to express adhesion friction as the frictional shear stress depending, among others, on sliding velocity and temperature multiplied with the real area of contact. According to Schallamach's concept [15] the frictional shear stress is due to stretching and debonding of rubber molecules. In [13], Koenen et al. found that the apparent coefficient of friction of wiper blade sliding on dry glass is proportional to the loss factor ($\tan(\delta)$) of the rubber. This finding is in accordance with that of Grosch. In [1], Grosch has pointed out experimentally that adhesion is directly related to the viscoelastic properties of the rubber. At the same time, according to Le Gal et al.'s theory [14] the adhesive component of rubber friction depends not only on the real contact area but also on the sliding velocity, contact pressure and temperature dependent shear strength of adhesive contact. Due to the large number of influencing parameters the shear strength of adhesive contact can be determined from measurements only. If the sliding velocity is lower than the so called critical one then the shear strength increases with increasing sliding velocity. Above the critical sliding velocity the shear strength is practically constant. In respect of a given rubber, there is a close correlation between the critical sliding velocity and the glass transition temperature (T_g). Generally, it can be stated that lower the

glass transition temperature the higher the critical sliding velocity. The works cited above show clearly that the rubber formulation (rubber compound recipe) plays critical role in rubber friction. Additionally it is worth to mention that when viscoelastic solid slides on rough hard counterpart the contribution to the total friction from the area of real contact (adhesion component) is larger while the viscoelastic contribution (hysteresis component) is smaller for less rough surface than for more rough surface. In the simplest numerical friction predictions, contribution of adhesion to the friction force is modeled using nonzero input coefficient of friction.

4.2. Viscoelastic friction predictions

The evolution and the current state of viscoelastic friction prediction are discussed in depth by Pálfi [16] and Bódai [17]. Consequently only the latest results of analytical and numerical hysteresis friction predictions are summarized here briefly.

Hysteresis friction theories of Persson [3] (friction theory of randomly rough surfaces) and Klüppel and Heinrich [9] are based on the dissipated energy induced by a rigid surface being rough on many different length-scales and are given in frequency domain using a Fourier transformation. As an example Fig. 4.2 illustrates a rough surface at which roughness occurs on two length-scales. The rough surface being considered usually as self-affine is involved in the theories through the surface roughness spectrum (see Appendix B). Below the so-called smallest cut-off wavelength (see Section 4.5.2) the influence of roughness on the hysteresis friction is neglected. The interesting length-scales usually range from the millimeter to the micron scale. According to these theories and former theoretical and experimental works the hysteresis friction depends on the excited rubber volume (volume subjected to deformation) and the dissipated energy density. In many cases, the excited rubber volume is characterized by a mean surface layer thickness (see Klüppel and Heinrich's [9] and Lindner et al.'s [19] studies). The theory presented by Lindner et al. [19] is similar to that of Klüppel and Heinrich [9] but is described in time domain. The constitutive behavior of rubber was modeled phenomenologically using a three-parameter Standard-solid model while the surface roughness effect was taken into account through measured surface profiles. Fig. 4.3 shows a Standard-solid model excited by a moving surface profile.

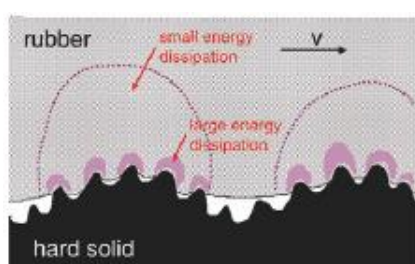


Fig. 4.2. Rough surface being rough on two length-scales (To get the total energy dissipation during sliding one needs to sum up the contribution from asperity-induced deformations of the rubber on all (relevant) length-scales.) [2]

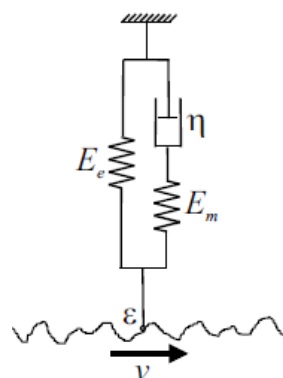


Fig. 4.3. Standard-solid model excited by a moving surface profile as an approximation of the real physical hysteresis friction process [19]

In [20], Bui and Ponthot investigate the interaction between a soft rubber asperity and its hard counterpart by a two-dimensional finite element model. The analysis is aimed to esti-

mate the influence of adhesion between surfaces and the energy losses arising from the deformation of rubber to the sliding resistance. The authors use a large strain Standard-solid model for describing the viscoelastic material behavior of rubber. During the FE contact simulations, the magnitude of friction force is computed as the sum of horizontal reaction forces of the rubber asperity. However hysteresis losses and their distribution in the rubber are not computed directly.

The contribution of roughness on different length-scales may be involved in FE prediction of hysteresis friction, for example, by assuming that the coefficient of friction belonging to different length-scales are additive. The hysteresis friction predictions of Nettingsmeier and Wriggers [21] are based on this assumption. It is postulated that, as a first step, the apparent coefficient of friction should be computed at the smallest length-scale then it should be added locally to the contact elements of the superior scale. In other words, the contact problem at the superior scale is solved by using the coefficient of friction computed at the smallest length-scale as an input coefficient of friction at the superior scale. At the same time, in the FE model reported by Nettingsmeier and Wriggers [21], only the first term of the Fourier series of a surface profile i.e. a sine wave was built in.

Palasantzas and De Hosson [23], in their recent theoretical work dealing with the prediction of hysteresis friction in presence of a liquid layer between a self-affine rough surface and a sliding rubber surface, pointed out that with smoothing of the substrate features, which are replicated on the rubber body, the apparent coefficient of friction drops very drastically. Remarkable apparent coefficients of friction are obtained for the cases when the length-scale below which the roughness is smoothed out is small. Based on this study it can be concluded that any liquid layer or layer of contaminants having smoothing effect with respect to the surface roughness can modify drastically the value of the viscoelastic friction predicted by the theoretical model of Persson [3]. As found by Lorenz et al. [2] on contaminated road surfaces the smallest relevant length-scale of the roughness may be determined by the nature of the contamination. In [2], where the friction force acting on a rubber block sliding on a concrete surface was investigated both experimentally and theoretically, the smallest relevant wavelength used in the hysteresis friction theory was $0.2 \mu\text{m}$ which was consistent with the size of the (smallest) wear particles which were in the order of magnitude of a few micrometers.

In [24], Westermann et al. performed an experimental study to evaluate the predictive capability of the models of Persson [3] and Klüppel/Heinrich [9]. The apparent coefficient of friction of rubber/road asphalt contact pairs was measured under dry conditions and at a nominal contact pressure of 0.4 MPa. The measured data were then compared with the predictions of the two friction theories. The main conclusion was that, at a sliding velocity above 10 mm/s, both models overestimate the measured friction force. As a possible cause, the flash temperature effect being not included in the models was mentioned.

In a very recent contribution of Scaraggi and Persson [25], rolling friction of a smooth hard cylinder rolling on a flat surface of a linear viscoelastic solid is studied using a numerical approach and an analytical theory. For the unfilled rubber, the authors found perfect agreement in respect of the two theories while some small difference was pointed out for the filled rubber.

In the work of Nguyen et al. [26] the hysteresis contributions to friction arising from localized viscoelastic dissipation at the nano-asperity scale are studied quantitatively. The manufacturing technique adopted by the authors makes it possible to prepare surfaces covered with various densities of spherical asperities with well-defined sizes and height distribution. It is noted that to some extent, such surfaces are reminiscent of the model surfaces considered in the rough contact theory by Greenwood and Williamson [27], in which asperities with spherical summits are assumed to be statistically distributed along the vertical direction. (For additional details on the GW theory see Section 4.5.2.) The authors emphasize that such patterned

surfaces are of particular interest for rubber friction studies because they offer the possibility to study the effect of roughness experimentally at a given length-scale. An order of magnitude agreement is obtained between experimental and theoretical results (the theory overestimated the hysteresis friction significantly) which indicates that the calculation of viscoelastic dissipation within the contact is very sensitive to the geometrical details of the rigid asperities. (There is a huge difference in the strain rate at the periphery and at the center of an asperity contact region.) As it is noted by Nguyen et al. [26] this result highlights the problem of the accuracy of the current theoretical predictions of hysteresis friction in the much more complex case of statistically rough surfaces. According to the knowledge of authors it is likely that the associated spectral description of the surfaces makes only an order-of-magnitude estimate of the hysteresis friction force possible. It is also mentioned that their contact model, as others, is based on a small strain linear viscoelastic description of the rubber behavior. The final conclusion of this study is that the effect of large strains should be taken into consideration in the different friction theories.

4.3. Finite element modeling of viscoelastic friction

FE-based friction predictions presented in this chapter has been carried out by the author of the thesis jointly with others (PhD students, researchers). The main aim of this chapter is to summarize briefly the most important findings of the related numerical studies. Instead of modeling viscoelastic material behavior, as often made in the literature, in simplified form viscoelastic solids characterized by very large number of relaxation times are used here. This approach allowed us to predict viscoelastic friction component quantitatively. The relaxation time and the importance of the large number of relaxation times are explained in Appendix A. In majority of the simulations, material properties of carbon black filled ethylene-propylene-diene-monomer (EPDM) rubber (see Appendix C) were used because EPDM is a frequently used material for reciprocating seals being built, among others, in piston rod sealings of real hydraulic brake cylinders. Contrary to the surface roughness spectral density-based theoretical predictions the elaborated FE technique makes the accurate modeling of asperity geometry and real rubber behavior (very large number of relaxation times, hyperelasticity, strongly temperature dependent material properties) possible on several length-scales. At the same time it must also be emphasized that all length-scales of the surface micro topography contribute to the friction. However they contribute to the friction not equally because both the excitation frequency ($\omega=v/\lambda$, where v is the relative tangential velocity between the rubber and the harder, rough counter surface, and λ is the wavelength of a given roughness component) and the excited volume are different length-scale by length-scale. Due to the huge CPU time and memory demand, however, it is practically impossible to consider all length-scales of surface roughness (from micro- to nano-level) in a single FE model. If the surface roughness is modeled in form of a single sine wave, then the roughness exists on a single length-scale. Superposition of two sine waves having given amplitude, wavelength and phase position results in a surface roughness model having roughness on two length-scales, and so on. Finally, it must be noted that penetration of rubber into valleys of the harder, rough counter surface may be induced by both the applied normal load and the adhesion (adhesive forces). The latter, however, is not taken into consideration in the simulations presented here. The flowchart of the finite element-based viscoelastic (hysteresis) friction predictions can be seen in Fig. 4.4.

In order to model viscoelastic behavior in FE environment spring-dashpot models are widely used because the most commercial FE software packages offer built-in fitting algorithms for parameter identification and graphical user interface for the specification of model parameters. However, the quality of fitting is not presented and analyzed in most cases. In many cases, model parameters are determined from a fit to the storage modulus master curve

without investigating the quality of fitting with respect to loss modulus and loss factor (loss tangent). However, as it will be presented in this section and in Appendix C, in case of viscoelastic friction predictions, it is of primary importance to reach good agreement for both storage modulus and loss modulus (loss factor) master curve, because both the stiffness and internal dissipation of rubber-like materials influence the hysteresis component of friction. At micro-level, where the hysteresis friction is due to the real micro-topography (surface roughness) the contact problem has to be modeled at asperity level as it is reported by Persson [3] and Klüppel and Heinrich [9]. By using FE technique, in addition to the material model of the rubber a surface model replacing the real, measured rough surface is also needed. As a possibility the micro-topography measured by AFM, contact profilometer (diamond stylus profilometer) or optical technique can be replaced, for instance, with spline surface fitted on the measurement results. As an alternative, the measured micro-topography can be decomposed into harmonic components by using the discrete Fourier transformation. This approach allows engineers to estimate the contribution of each component to the viscoelastic friction.

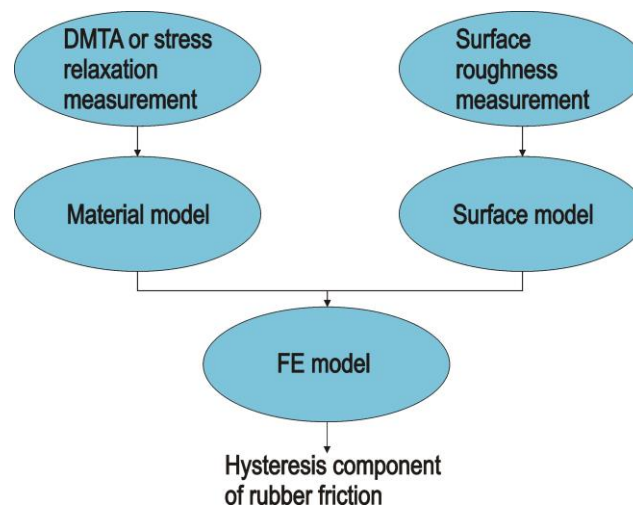


Fig. 4.4. Flowchart of the finite element-based viscoelastic friction prediction [12]

4.3.1. Two-dimensional single asperity contact model for the simulation of asperity-asperity interaction: Qualitative analysis

Here the asperity-asperity interaction is simulated qualitatively using a two-dimensional plane strain FE model (see Fig. 4.5) in which both the stationary and the moving asperities are modeled by cylinders. Notwithstanding that the radius of cylinders is greater than the radius of curvature of typical asperities it is believed that the FE simulations performed by Soós and Goda [28] are able to capture the essential characteristics of the asperity-asperity interaction. For the sake of clarity it must also be noted that such a single asperity contact model does not take into consideration the interaction between the asperities located on the same surface. The interfacial adhesion is neglected and the material behavior is modeled by using the simplest description of rubber rheology i.e. the small strain linear viscoelastic Standard-solid model (see Appendix A) with glassy modulus of 7.5 MPa and relaxed modulus of 1.5 MPa. Contrary to the broad relaxation spectrum of real rubber-like materials the material model used has a single relaxation time ($\tau = 5.58 \cdot 10^{-3}$ s) only. These material model parameters result in practically zero loss modulus (E'') and loss factor ($\tan \delta$) at excitation (angular) frequencies lower than 0.1 rad/s or higher than 10^5 rad/s. The peak value of loss modulus and loss factor curves appears at an excitation (angular) frequency of about 100 rad/s, which corresponds to sliding speed of $v \cong 8$ mm/s ($f \cong v/2R$, where f denotes the

excitation cyclic frequency in [Hz]). The simulations have been performed under approximately constant mean normal force as well as constant overlap ($s = 0.0378 \text{ mm} = \text{const}$). In the former case, the actual magnitude of overlap was determined by the fact that the mean normal force (\overline{F}_y) to be kept approximately constant during the simulations independently of sliding speed. To compute the mean normal force reaction forces in y-direction were averaged over a cycle of contact.

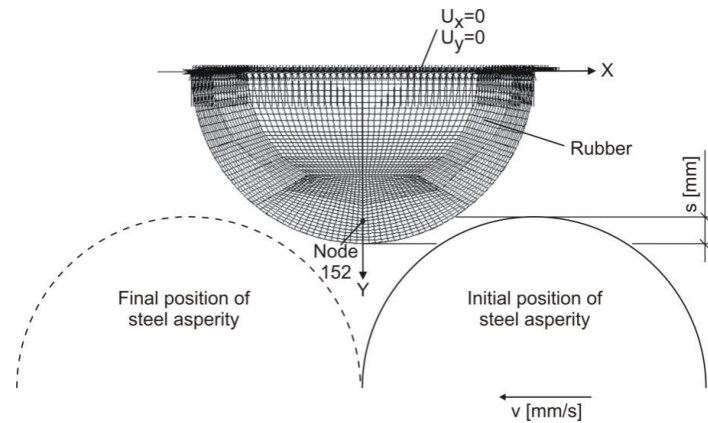


Fig. 4.5. Two dimensional (plane strain) FE model. Asperities of contacting rough surfaces are replaced with cylinders having radius of $R=0.25 \text{ mm}$ and the steel asperity is modeled as a perfectly rigid body with velocity varied between 0.1 mm/s and 100 mm/s . u_x and u_y denote displacement in x- and y-direction. [28]

During the mechanical interaction, work is done as the steel cylinder moves forward. This work is required to deform the rubber in front of the hard asperity. At the same time elastic energy is recovered from the rear. Since rubber has viscoelastic material behavior it exhibits hysteresis and thus one portion of the work done is lost. If the interfacial adhesion and the friction at steel/rubber interface caused by physical processes other than adhesion are neglected (the input coefficient of friction was set to 0), hysteresis is the only source of frictional work. If the rubber were ideally elastic the elastic energy recovered would be identical the work done to deform rubber and no energy would be lost. In this case, the frictional work would be zero. Fig. 4.6 shows the normal force F_y (reaction force in y-direction) and tangential force F_x (reaction force in x-direction) as a function of the position of steel asperity. At smaller sliding speeds rubber is less stiff (excitation frequency dependent material behavior of rubber) thus to obtain approximately the same mean contact normal force a larger overlap is required. By increasing the sliding speed the elastic modulus of rubber increases and the overlap - to obtain approximately the same mean force - decreases due to the increasing excitation frequency. In Fig. 4.6a, each curve has the same tendency, that is, the absolute value of the force increases as the steel asperity moves toward the center of rubber one, reaches a maximum and then falls to zero. As it can be seen, both at small and high sliding speeds the curves, as a good approximation, are symmetrical. The reason for this is that the rubber behaves elastically at very low (rubbery region) and very high excitation frequencies (glassy region). At sliding speeds between the rubbery and the glassy region (for example at 2.5 mm/s) the curves of normal force are asymmetrical. The force reaches its maximum before the centers of asperities would be in the same horizontal position ($x=0$). When rubber behaves elastically the tangential force curves (see Fig. 4.6b) resemble a sine wave. In these cases, the average value of tangential force, over a cycle of contact, is zero. In the viscoelastic region (for example at $v=2.5 \text{ mm/s}$) force curves lose their sine wave form. Therefore, the average

tangential force and hereby the apparent friction force will be zero no longer. Here the apparent friction force is defined as the mean value of the tangential force over a cycle of contact.

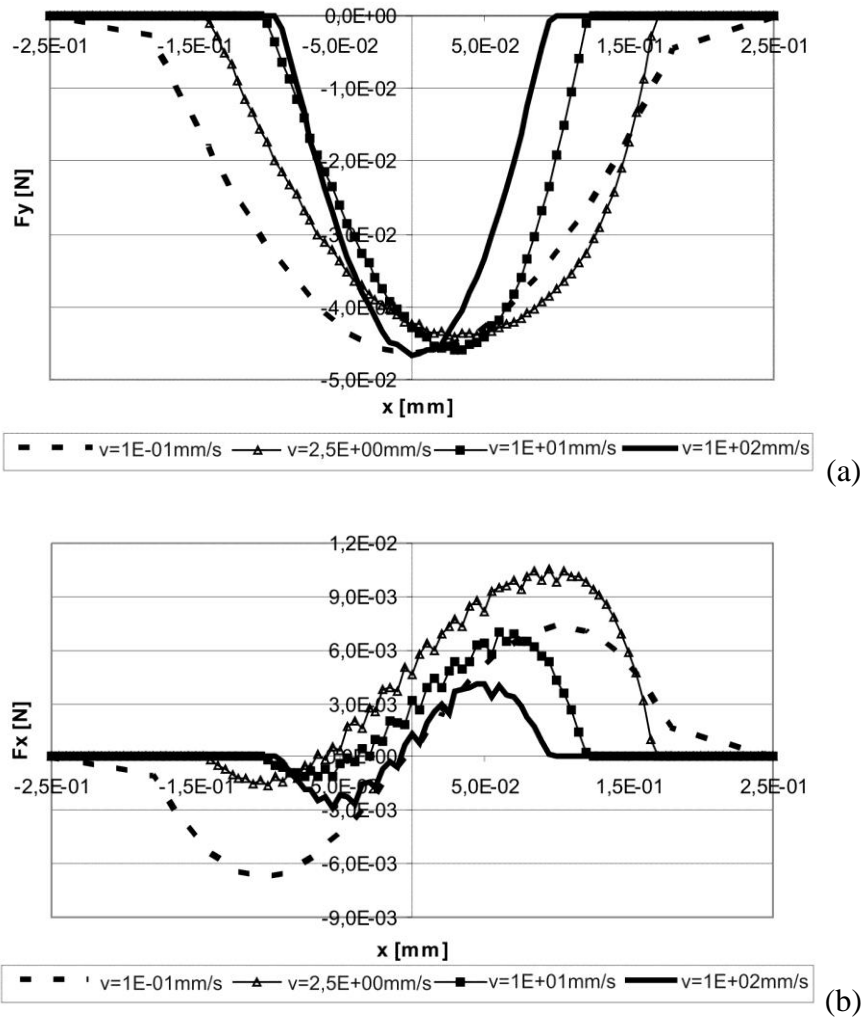


Fig. 4.6. (a) Normal force F_y and (b) tangential force F_x as a function of horizontal position of steel asperity at different sliding speeds (approximately constant mean normal force) [28]

Figs. 4.7a-b show similar tendencies for sliding speed dependency of the average apparent friction force and the apparent coefficient of friction. Amount of energy loss and hence magnitude of the apparent friction force and apparent coefficient of friction are, as anticipated, very small at low ($v < 0.1$ mm/s) and high ($v > 10^3$ mm/s) sliding speeds due to the quasi-elastic material behavior. Between these speed domains the rubber used shows rate-dependent material behavior (viscoelastic region). As it can be seen in Fig. 4.7a the energy loss and the apparent friction force are much greater in case of constant overlap than in case of approximately constant mean normal force. At the same time, the difference in apparent coefficient of friction is somewhat smaller. The cause of this is that the apparent coefficient of friction is defined, in conventional sense, as $\mu = \overline{F_x} / \overline{F_y}$. In case of constant overlap, both the tangential and the normal force increase with increasing sliding speed while, in case of approximately constant mean normal force, the increasing sliding speed has an influence on the magnitude of tangential force only. Since the rubber becomes stiffer with increasing sliding speed, the mag-

nitude of overlap and the size of contact area have to vary in case of approximately constant mean normal force.

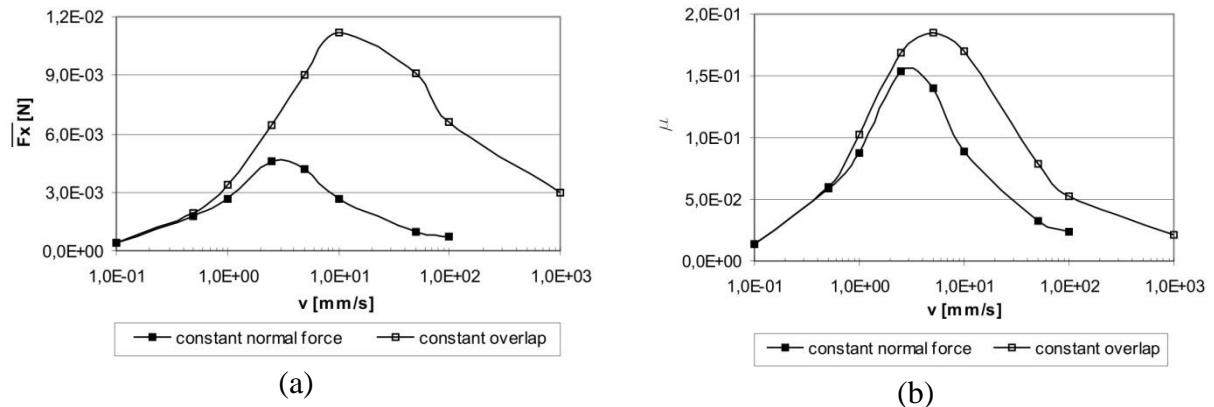


Fig. 4.7. Variation of (a) the average apparent friction force and (b) the apparent coefficient of friction as a function of sliding speed [28]

4.3.2. Two-dimensional single asperity contact model for the simulation of hard, ideally smooth asperity sliding on smooth rubber plane

Here the asperity sliding on ideally smooth rubber plane (thickness = 2 mm) has a radius of 0.25 mm (see Fig. 4.8a). The asperity is squeezed against an EPDM rubber plane (see Appendix C) with prescribed vertical displacement of 0.042 mm which is kept constant during the simulation. Sliding speed of the asperity ranges from $5 \cdot 10^{-6}$ to $5 \cdot 10^7$ mm/s.

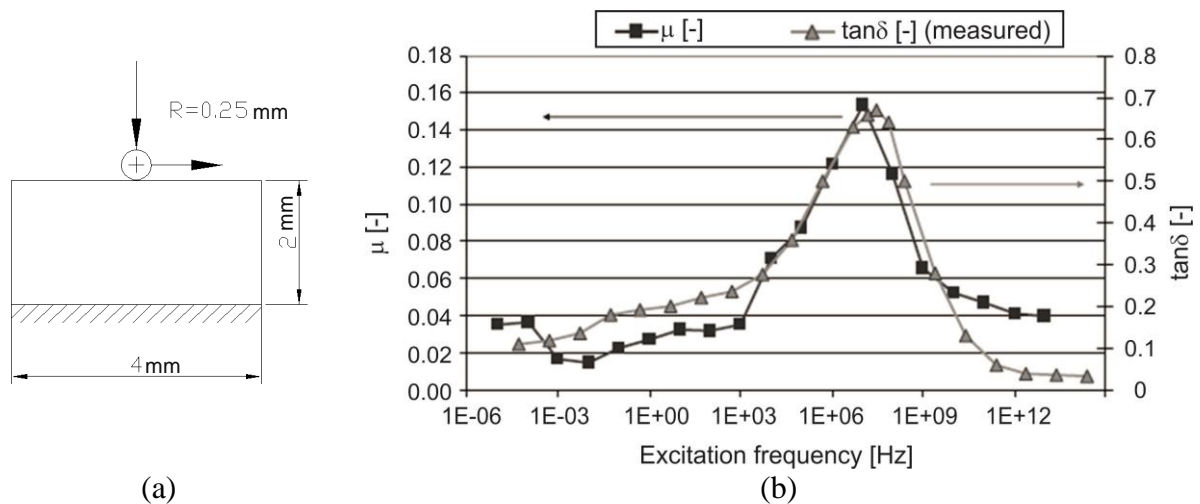


Fig. 4.8. (a) Hard smooth asperity sliding on ideally smooth rubber plane and (b) comparison of computed apparent coefficient of friction and loss factor (tangent) measured by DMA as a function of excitation frequency. As it is represented schematically the bottom of the rubber plane is fixed. [29]

FE analysis has been performed under plane strain condition and by using a 15-term generalized Maxwell-model connected parallel to a nonlinear spring (glassy modulus = 2220 MPa, relaxed modulus = 12.3 MPa). Parameters of the material model were determined from a fit to measured storage modulus master curve and, together with all details of the FE models, can be found in the works of Békési and Goda [29, 30]. Fig. 4.8b shows the apparent coefficient

of friction vs. excitation frequency curve and its comparison with the measured loss factor ($\tan\delta$) vs. excitation frequency curve. The excitation frequency is defined as sliding speed divided by two times the asperity radius while the apparent coefficient of friction is computed based on the system of reaction forces. As the input real coefficient of friction was set to zero, Fig. 4.8b shows the viscoelastic component of rubber friction. As expected both the magnitude and the variation of the apparent coefficient of friction are in good agreement with those of loss factor (loss tangent).

4.3.3. Two-dimensional single asperity contact models for the simulation of hard, rough asperity sliding on smooth rubber plane

Main aim of this subsection is to study the effect of multi-scale nature of engineering surfaces on viscoelastic friction. The FE model used has been constructed based on the study by Archard [31]. Archard's multi-scale surfaces are composed of rough hemispherical asperities where the larger hemispherical asperities are covered with smaller ones which are also covered with even smaller hemispherical asperities, and so on. In Archard's two-scale model, it is assumed that the load on each fine scale asperity is equal to the ratio of the load supported by a small portion (an annulus of radius r with width dr) of the coarser scale contact area and the number of fine scale asperities within the investigated portion of the coarser scale contact area. Additionally, fine scale asperity peaks are considered to displace independently of the coarser scale deformation and the deformation of the neighboring asperities. In FE simulations of Békési and Goda [29, 30], a two-scale surface has been introduced which consists of smaller cylindrical asperities with radius of 0.03 mm located on top of a larger one with radius of 0.25 mm (see Fig. 4.9). The distance between two neighboring fine scale asperities is 0.06 mm. All the other characteristics of the FE model are the same as in the problem when a cylindrical asperity with radius of 0.25 mm slides on an ideally smooth rubber plane (see Section 4.3.2). In contrast with Archard's model both the effect of fine scale asperities on the stress distribution and the coarser scale deformation together with the interaction between neighboring fine scale asperities are taken into account in the FE model. As it can be seen in Fig. 4.10a the contact area is discontinuous because the rubber is unable to fill out the valleys of the rough surface completely under the conditions studied here. Finally, comparison of viscoelastic friction generated by the one- (smooth asperity) and the two-scale surface (rough asperity) can be seen in Fig. 4.10b. FE results show that the two-scale surface generates about two times higher apparent coefficient of friction than the one-scale surface. Large contribution of small or fine scale asperities to viscoelastic friction may be explained by the higher strain rates.

Two-dimensional FE models are presented by Pálfi et al. [32] in order to predict the hysteresis rubber friction generated by a sinusoidal hard asperity with multi-scale nature. The characteristic wavelengths and amplitudes are determined from surface roughness measurements (measurements using diamond stylus profilometer and atomic force microscope) of the plunger of a TRW brake cylinder using 3D parameter-based technique, slicing method and surface roughness spectrum analysis (see Appendix B). During operation this plunger is in sliding contact with rubber seals in presence of brake fluid. In order to describe large strain viscoelastic material behavior of the EPDM rubber filled with carbon black, two-parameter Mooney-Rivlin material law combined with 40-term generalized Maxwell-model has been used. Parameters of the material model have been determined from a fit to the storage modulus master curve using the software ViscoData [33]. Then the Maxwell-parameters were manually adjusted to the $\tan(\delta)$ master curve, using a trial-and-error technique, to improve the agreement between the measured and the simulated $\tan(\delta)$ curve (see Appendix C). Temperature-dependency of the material behavior is taken into consideration by constructing master curves at temperature of -50, 25, and 150°C. In order to study the effect of multi-scale nature

of engineering surfaces on viscoelastic friction three different roughness models (one-, two- and three-scale surfaces) were constructed and studied.

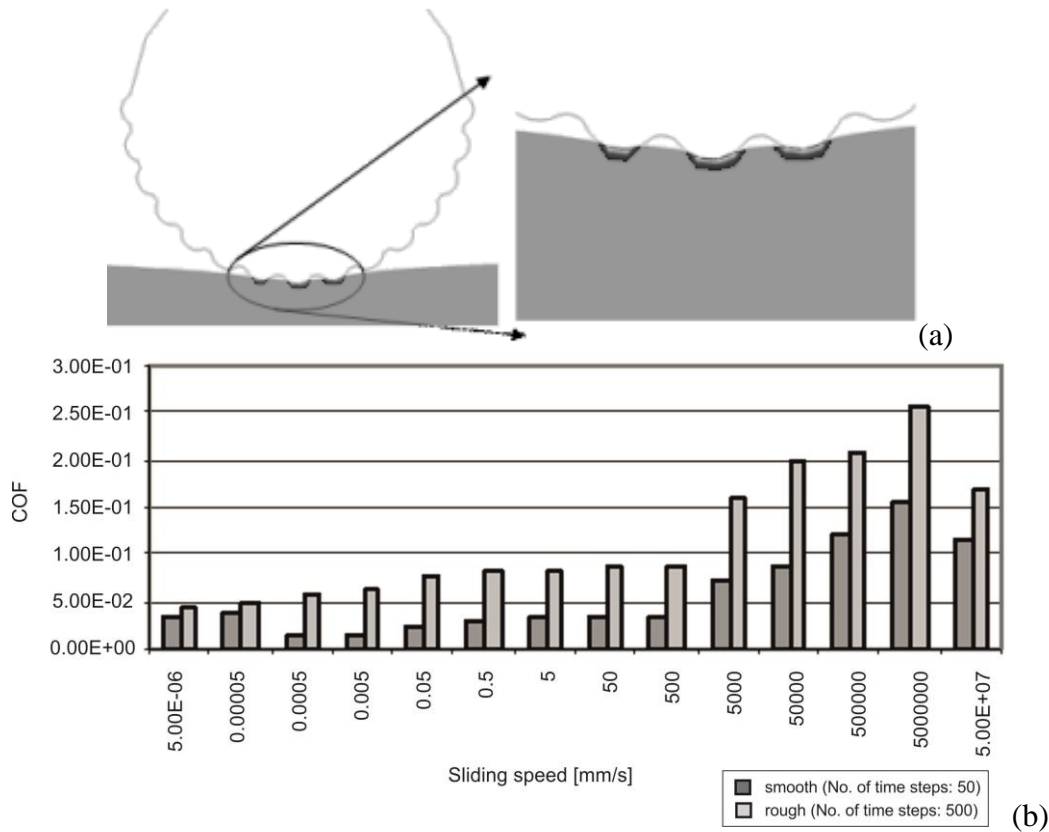


Fig. 4.9. (a) Hard, rough asperity modeled as two-scale surface sliding on a smooth rubber plane (EPDM rubber with unknown chemical composition from TRW Automotive, see Appendix C) and (b) the variation of viscoelastic (apparent) coefficient of friction computed at different sliding velocities. In case of “smooth” surface, there are no fine scale asperities on top of the coarse scale asperity. [29]

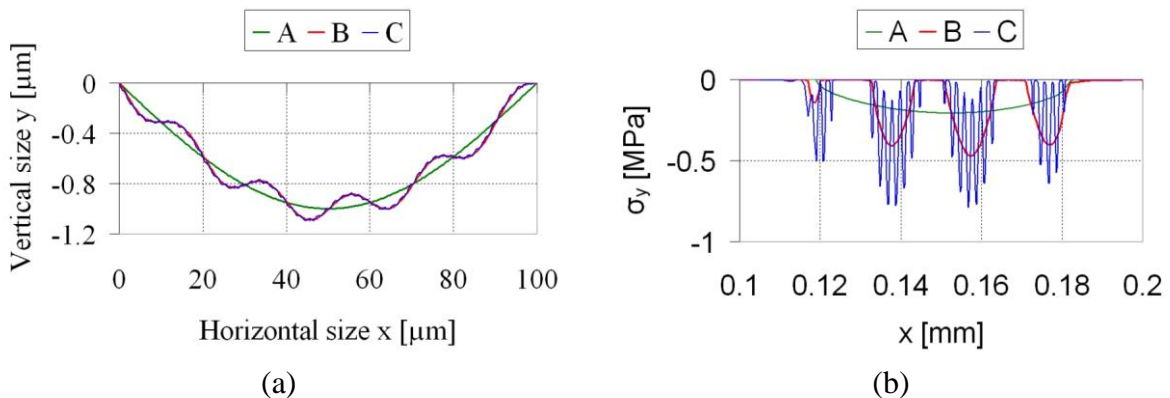


Fig. 4.10. (a) Roughness models studied and (b) the distribution of normal stress component σ_y (contact pressure distribution) [32]

In the first model, the counter-surface was composed of a single sinusoidal asperity (referred as ‘A’) with wavelength of 200 μm and amplitude of 1 μm (amplitude/wavelength= 0.005) and without smaller length-scale asperities. In the second model, the sine wave with a wavelength of 20 μm and amplitude of 0.1 μm (amplitude/wavelength= 0.005) was superimposed on the asperity ‘A’ (referred as ‘B’). Finally, in the third model, a sine wave with a wave-

length of $2\ \mu\text{m}$ and amplitude of $0.01\ \mu\text{m}$ (amplitude/wavelength = 0.005) was superimposed on counter-surface ‘B’ (referred as ‘C’). Surfaces ‘A’, ‘B’ and ‘C’ can be seen in Fig. 4.10a. In all the FE simulations presented here, the counter-surface is pressed against a rubber block with constant penetration depth of $0.002\ \text{mm}$, and moves with a sliding speed of $0.1\ \text{mm/s}$. Like in the former cases bottom of the rubber block was fixed and the input real coefficient of friction was set to zero. In Fig. 4.10b, it can be seen that the rubber is not able to fill out the valleys of the rough counter-surface. The real area of contact becomes smaller and smaller as the number of length-scales involved in the roughness model increases. This finding is in accordance with the prediction of Archard’s [31] as well as Persson’s [3] model. The ratios of the real (A_r) and the nominal contact area (A_n) and the predicted viscoelastic (apparent) coefficient of friction are depicted in Fig. 4.11a. The apparent coefficient of friction was calculated as the ratio of tangential and normal reaction force. At room temperature the normal (vertical) reaction force was $F_n = 0.0131, 0.0135$ and $0.0136\ \text{N}$ for surfaces ‘A’, ‘B’ and ‘C’. The slight difference in normal force is due to the fact that FE simulations are performed with constant penetration depth. These results prove that the real area of contact is overestimated while the viscoelastic (apparent) coefficient of friction is underestimated if small scale components of surface roughness are neglected i.e. not involved in FE models.

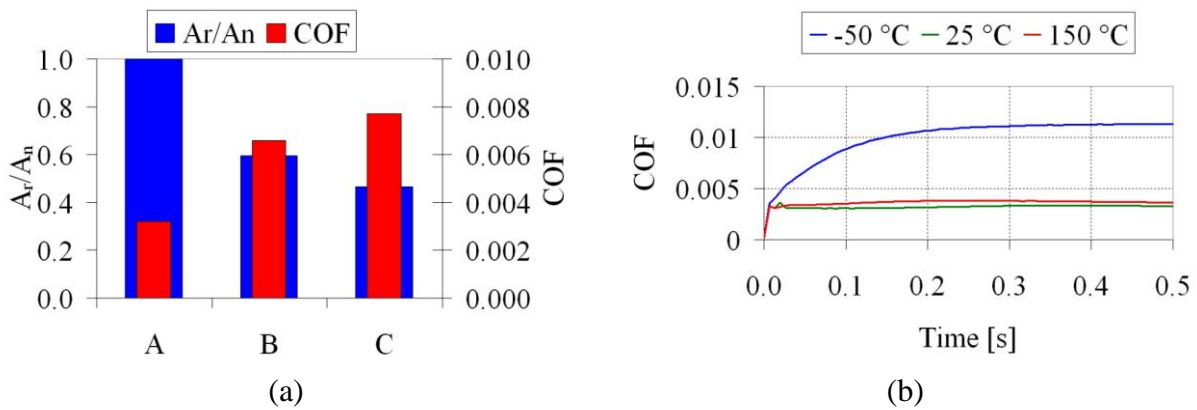


Fig. 4.11. (a) Ratios of real and nominal contact area and the predicted viscoelastic (apparent) coefficients of friction for surface ‘A’, ‘B’ and ‘C’ ($\mu_A = 0.0032$, $\mu_B = 0.0066$, $\mu_C = 0.0077$) at room temperature as well as (b) predicted apparent coefficient of friction vs. time curves at three different temperatures for surface ‘A’ [32]

In order to test the effect of temperature on viscoelastic friction FE simulations have been performed with surface ‘A’. The apparent coefficient of friction vs. time curves can be seen in Fig. 4.11b. The results show that, in case of 150°C , the apparent coefficient of friction predicted is slightly higher than at 25°C . However, at the lowest temperature, the apparent coefficient of friction is more than three times higher than at room temperature. This can be explained by the fact that, at the excitation frequency induced by surface ‘A’, the loss factor is much higher at -50°C than at higher temperatures (low temperature shifts master curves towards lower frequencies), while the excited volume is the same. This proves that the viscoelastic friction component may be particularly important at low temperatures.

4.3.4. Two-dimensional FE model for the simulation of hard sinusoidal one-scale surface sliding on smooth rubber plane

In one of the works of Békési and Goda [29], the viscoelastic friction generated by a sinusoidal hard surface having amplitude of $A = 1\ \mu\text{m}$ and wavelength of $\lambda = 200\ \mu\text{m}$ (see Fig. 4.12a) is studied in 2D under plane strain condition. Amplitude and wavelength of the surface

were extracted from surface roughness measurements of the brake plunger of TRW having apparently smooth surface. As the input coefficient of friction was set to zero the friction predicted is due to hysteresis. FE simulations have been performed at a sliding velocity of 1 mm/s and under nominal contact pressure of 5, 0.5 and 0.05 MPa. The hard surface is squeezed against an EPDM rubber plane with unknown chemical composition (see Appendix C). Parameters of the 15-term viscoelastic model were determined from a fit to measured relaxation modulus master curve. The Mooney-Rivlin material model parameters used were the followings: $C_{10}=320$ MPa, $C_{01}=80$ MPa. Fig. 4.12b shows the apparent coefficient of friction as a function of nominal contact pressure. It is worth to mention that at the highest pressure the rubber fills out completely the valleys of the hard surface. Although the apparent coefficient of friction increases with increasing pressure even its highest value is lower than 0.0025. The reason why the apparent coefficient of friction is very low is that the ratio between the amplitude and the wavelength of the surface roughness component studied ($A/\lambda=0.005$) and the excited rubber volume are very small. Békési and Goda [29] worked both with and without input real coefficient of friction. Firstly, the input real coefficient of friction was set to 0.1 and the computations were carried out at sliding velocity of 10 mm/s and under nominal contact pressure of 0.2 MPa. Then the input real coefficient of friction was set to zero and the computations were repeated. With nonzero input real coefficient of friction the mean apparent coefficient of friction is 0.1023 while its value without input real coefficient of friction is 0.0028. The difference is about the input real coefficient of friction of $\mu=0.1$.

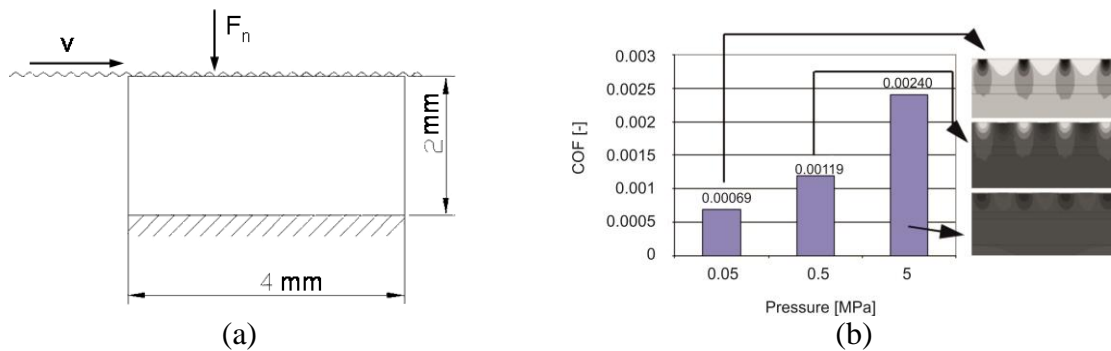


Fig. 4.12. (a) Sinusoidal hard surface with amplitude of $1 \mu\text{m}$ and wavelength of $200 \mu\text{m}$ sliding on smooth rubber plane, and (b) the viscoelastic (apparent) coefficient of friction predicted. As it is represented schematically bottom of rubber plane is fixed. [29]

The effect of wavelength and amplitude was studied by Pálfi et al. [32]. Two-dimensional FE models have been presented in order to predict the hysteresis rubber friction generated by hard sinusoidal surface with varying amplitude and wavelength. The rubber block with a height of 2 mm and width of 4 mm was made of EPDM filled with carbon black (TRW Automotive, see Appendix C) and modeled with 4000, 2D plain strain finite elements where the nodes on the bottom of the rubber block were fixed. Between the contacting surfaces there was no prescribed real coefficient of friction. Parameters of the material model (two-parameter Mooney-Rivlin model (see Appendix A.3) combined with 40-term generalized Maxwell-model) have been determined from a fit to the storage modulus master curve using the software ViscoData [33]. Then the Maxwell-parameters were manually adjusted to the $\tan(\delta)$ master curve, using a trial-and-error technique, to improve the agreement between the measured and the simulated $\tan(\delta)$ curve (see Appendix C). The first asperity, referred as 1x200, has a wavelength of $\lambda=200 \mu\text{m}$ and amplitude of $A=1 \mu\text{m}$ ($A/\lambda=0.005$). Then it was replaced with another, referred as 2x200, that had a wavelength of $200 \mu\text{m}$ and an amplitude of $2 \mu\text{m}$ ($A/\lambda=0.01$). Finally a sinusoidal surface with a wavelength of $400 \mu\text{m}$ and amplitude

of $1\ \mu\text{m}$, referred as 1x400, was studied ($A/\lambda=0.0025$). The sliding speed was $v=1\ \text{mm/s}$ while the nominal contact pressure was $0.5\ \text{MPa}$. The calculated values of the apparent coefficient of friction as a function of time can be seen in Fig. 4.13. As it can be seen the larger amplitude ($A=2\ \mu\text{m}$) produces about 5 times higher viscoelastic friction with the same wavelength of $200\ \mu\text{m}$. This proves that sinusoidal surfaces generating higher viscoelastic friction are characterized at a given wavelength by higher amplitude per wavelength value.

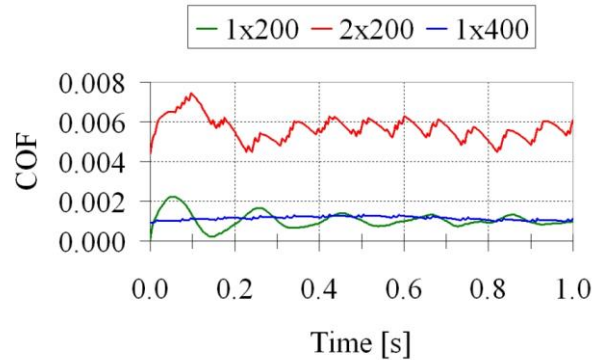


Fig. 4.13. Calculated apparent friction vs. time curves in case of different amplitudes and wavelengths (COF denotes the apparent coefficient of friction computed). The apparent coefficient of friction is calculated as the ratio of the total horizontal and vertical reaction force.

[32]

4.3.5. Two-dimensional FE model for the simulation of hard, multi-scale sinusoidal surface sliding on smooth rubber plane

Like in the study of Wriggers and Reinelt [34] real surface roughness is approximated here by a superposition of sine waves with different amplitudes and wavelengths (multi-scale model). Wriggers and Reinelt assumed that the different (length-) scales of surface roughness can be separated when calculating viscoelastic friction. The smaller scale roughness generated viscoelastic coefficient of friction is used as input coefficient of friction at the next larger scale. The proposed technique used scale by scale makes it possible to solve the problem of scale transition (interaction of scales). In [34], an abrasive paper surface being in frictional contact with an elastomer counterpart was modeled through the superposition of three as well as four sine waves (amplitudes of sine waves were 15 , 6 , 3 , and $2\ \mu\text{m}$ while the corresponding wavelengths were 180 , 78 , 31 , and $21\ \mu\text{m}$). The amplitude per wavelength values of the harmonic components were 0.083 , 0.077 , 0.097 and 0.095 , respectively. Although approximation of surface roughness is similar the viscoelastic solid used is drastically different from that of Pálfi et al. [35]. In [34], a very simple viscoelastic solid characterized by 6 relaxation times was used while, in Pálfi et al. [35], a real viscoelastic solid characterized by 40 relaxation times is studied. Consequently FE simulation reported by Wriggers and Reinelt [34] can be considered as a qualitative analysis for the viscoelastic friction. (For additional details on the importance of number of relaxation times see Appendix C.)

In order to examine the hysteresis portion of the coefficient of friction when smooth rubber block (carbon black filled EPDM rubber of TRW, see Appendix C) slides on a hard, rough surface, two-dimensional FE models were constructed by Pálfi et al. [35]. The microscopic surface roughness of the hard counter surface was modeled by two different sine waves (counter surface A and B) having a wavelength of $100\ \mu\text{m}$ (amplitude= $4\ \mu\text{m}$) and $11.11\ \mu\text{m}$ (amplitude= $1\ \mu\text{m}$) and by their combination (counter surface A+B) where the counter surface B was superimposed on counter surface A. Consequently the amplitude per wavelength ratio for surface A and B is 0.04 and 0.09 , respectively. Fig. 4.14 shows the three different surface

roughness models used in [35]. In order to emphasize the difference among the models they were depicted in a single graph by using different scale in the horizontal and vertical directions. The sliding speed was considered to be 10 mm/s. With the help of surface roughness spectrum analysis of a measured rough surface, one can determine the wavelengths and amplitudes of its harmonic components. Using the harmonic components of the measured rough surface one by one and their combination one can examine the contribution of each component of the surface roughness (from micro- to nano-level) to the hysteresis friction. Due to the periodicity in the surface roughness it is sufficient to model a small, repetitive segment of the rubber. Naturally, for such a small model the condition of repetition has to be applied as boundary condition. Due to the repetitive symmetry the length of the 2D plane strain FE model in sliding direction was the wavelength of the corresponding harmonic component of the rough surface. According to this the length of the FE models for counter surface A, B and A+B was 100 μm , 11.11 μm , and 100 μm , respectively. The length of the rigid counter surface is larger than the wavelength of the irregularity. Its length was specified to insure continuous contact with the rubber during the simulation. It means that the rigid counter surface is composed of identical irregularities having a wavelength of 100 or 11.11 μm , thus many irregularities make a contact with the rubber during the simulation. The modeled rubber segment had a height of 500 μm to ensure that the load application zone (upper part in Fig. 4.15), which was defined to remain perfectly horizontal during the simulation, may not be able to affect the contact zone (lower part in Fig. 4.15). In the contact zone between the rubber and the rigid counterpart, the FE mesh consisted of elements having a size of 0.25 μm in x-direction. The element size of 0.25 μm was obtained from sensitivity analysis. The rubber part was considered to obey the large strain linear viscoelastic material behavior and discretized by QUAD80 elements [36], while the rough counter surface was modeled as an analytical rigid surface. The sliding contact between the rubber and the counter surface was modeled as follows. As a first step the rubber segment was squeezed with a pressure of $p=1$ MPa against the counter surface. During the indentation the relative tangential velocity between contacting bodies was zero. At the end of the loading the uniform acceleration phase of the rubber block began. It took up to sliding speed of 10 mm/s. During the acceleration phase the counter surface was fixed in vertical direction and the nodes on the lateral walls of the rubber were forced to move identically. The phase of uniform horizontal motion with constant speed of 10 mm/s began after the acceleration phase had finished. In the course of steps 2 and 3 (acceleration and motion with constant speed) nodes on the lateral walls moved horizontally in the same way (constraint equations have been defined for this purpose), in order to model a finite rubber sample being composed of identical sections, while pressure was applied on the top wall (see Fig. 4.15). Furthermore the same condition has been imposed for the vertical displacement of the nodes at both lateral walls. Fig. 4.15 shows the deformed shape of the FE model, according to the boundary conditions discussed above. The real rubber rheology was taken into consideration through 40-term generalized Maxwell-models connected parallel with two-parameter Mooney-Rivlin model (see Appendix C). Like in all the cases presented in this thesis FE models were constructed and solved in MSC.Marc. Since the magnitude of the apparent friction force is sum of the horizontal component of the reaction forces the apparent coefficient of friction (μ_{Force}) was defined as the ratio of the total horizontal and vertical reaction force.

Table 4.1 shows the apparent coefficients of friction at three different temperatures computed by viscoelastic material models with different parameters and zero input real coefficient of friction at the contact interface ($\mu_{\text{interface}}=0$). The apparent coefficient of friction (COF) computed for counter surface A is the highest at $T=25^\circ\text{C}$ while it is the lowest at -50°C . It first rises as the temperature increases, then, having reached a peak value, it begins to fall. Similar tendency can be observed for counter surface B, however, in case of material model

fitted to loss tangent, the highest COF can be observed at 150°C. In case of counter surface A+B, the viscoelastic friction for all the temperatures is greater than at counter surfaces A or B separately. Its maximum appeared at T=25°C while at -50°C nearly identical hysteresis COF can be computed. At T=25°C and 150°C the highest COF is generated at counter surface A+B, followed by counter surface B and then by counter surface A. The higher apparent coefficients of friction obtained for surface B can be explained by the higher amplitude per wavelength ratio.

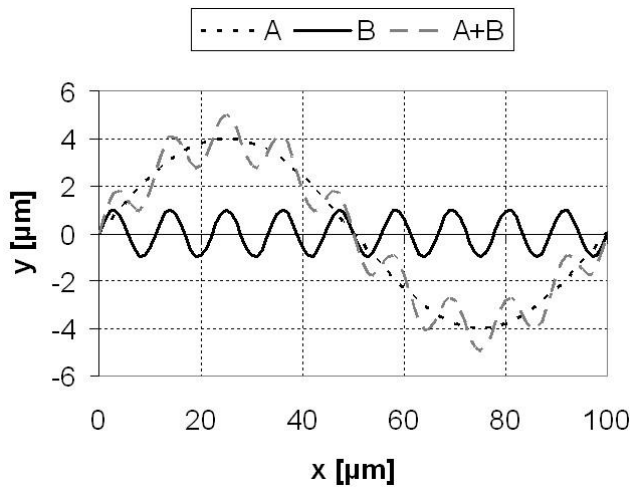


Fig. 4.14. Surface roughness models used in [35]

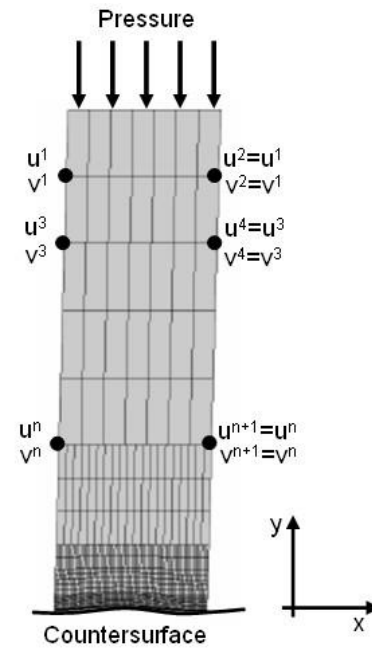


Fig. 4.15. Deformed shape of the FE model and the applied boundary conditions (u – displacement in x-direction; v – displacement in y-direction) [35]

	T [°C]	μ_{Force}			h [μm] (average penetration depth)		
		A	B	A+B	A	B	A+B
Material model fitted to E' curve	-50	0.025	0.028	0.028	0.70	0.09	0.97
	25	0.044	0.062	0.092	4.83	0.71	5.52
	150	0.038	0.059	0.075	5.32	0.80	6.07
Material model fitted to tan(δ) curve	-50	0.028	0.026	0.030	0.48	0.06	0.72
	25	0.054	0.071	0.119	5.67	0.87	6.44
	150	0.046	0.085	0.111	7.12	1.39	8.26

Table 4.1. Average steady-state apparent coefficient of friction and the average penetration depth at different temperatures in case of 40-term viscoelastic models ($\mu_{interface}=0$) [35]

4.3.6. Three-dimensional FE model for the simulation of hard, apparently smooth surface sliding on smooth rubber plane

In order to examine the effect of sliding speed and temperature on the surface roughness generated viscoelastic (hysteresis) friction a three-dimensional FE model has been constructed by Pálfi et al. [32, 37]. The hard counter surface modeled the measured microtopography of the plunger of a brake cylinder (TRW Automotive, Spain) through a NURBS surface. The NURBS surface was fit to data of surface roughness measurements (scanned area= 1x1 mm², resolution= 1 μm, see Fig. 4.16).

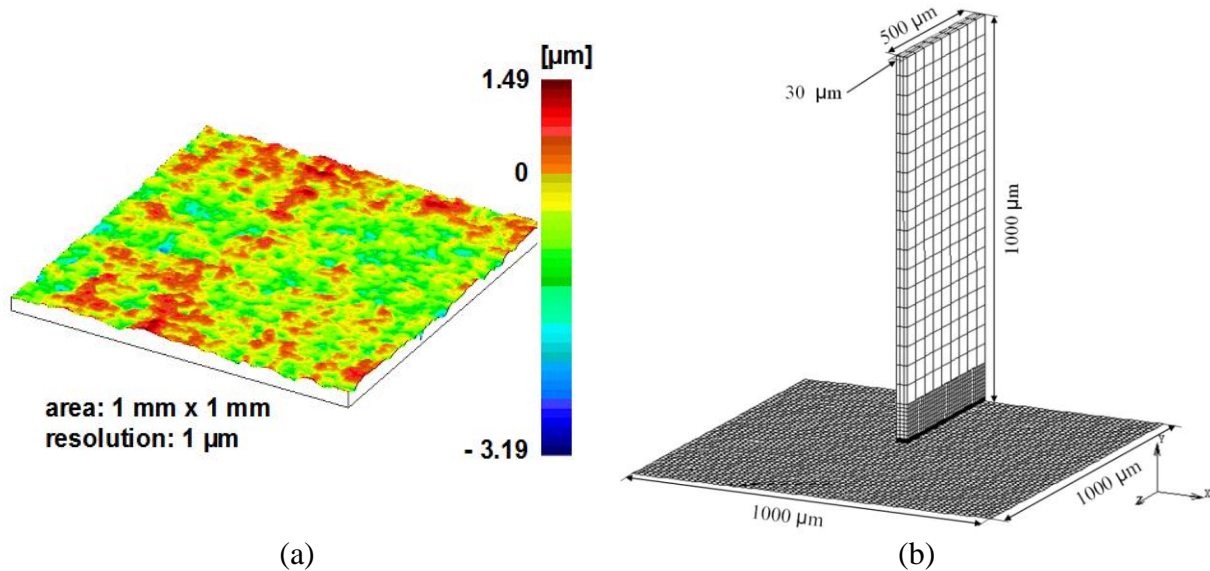
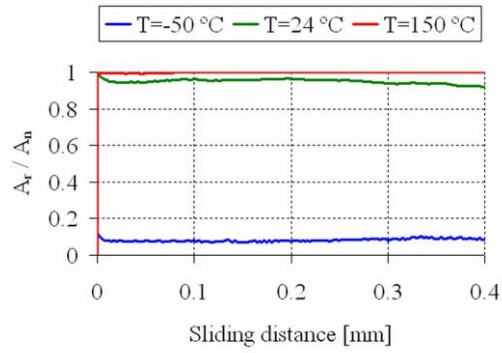
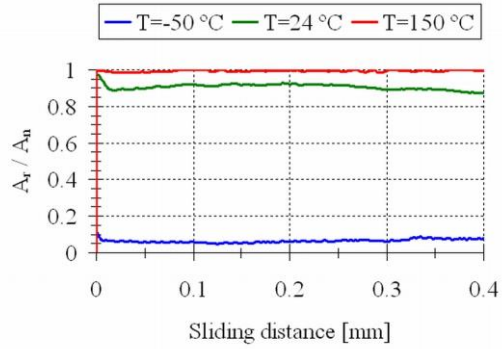


Fig. 4.16. (a) Surface topography of the brake plunger of TRW Automotive measured by diamond stylus profilometer and (b) the three-dimensional FE model. The rigid counter surface moves in negative z -direction. [32]

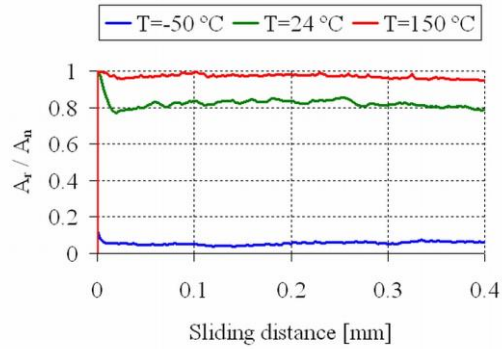
For the sake of simplicity and to avoid unmanageably large amount of nodes and computation time smaller length-scales of measured surface roughness were not involved in the FE model. According to this the NURBS surface was fit to 100 x 100 measured points only where the lateral distance between two neighboring points was 10 μm. To reduce the CPU time only a small rubber (EPDM rubber of TRW Automotive, see Appendix C) segment (30 μm x 500 μm x 1000 μm) has been modeled (see Fig. 4.16b). For discretization eight-noded incompressible Hermann type elements were used [36]. Lateral walls of the rubber segment that are parallel to the x - y plane were fixed in direction z . Furthermore nodes on the upper plane of the rubber segment were constrained in x -, y - and z -direction. As it can be seen in Fig. 4.16b the modeled rubber segment is high enough (1000 μm) thus the constraint conditions used on the top of the rubber segment practically does not influence the solution of the contact problem. The average element size in the contact zone was 2 μm. The sliding contact between the counter surface and the rubber was modeled as follows. As a first step the rigid surface was pressed with a pressure of $p=1$ MPa against the rubber using incremental technique meanwhile the relative tangential velocity between contacting bodies was zero. Then the rough surface was moved in negative z -direction with prescribed sliding speed ($v=1, 10$ and 100 mm/s). Fig. 4.17 shows the contact state and the distribution of normal stress component σ_y at three different temperatures. The areas in contact are visualized by red color while the purple area indicates the non-contacting part of the nominal contact area. The figure shows clearly that as the temperature rises the real area of contact becomes larger and larger.



(a)

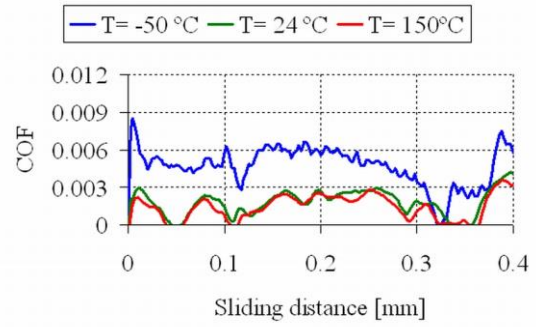


(b)

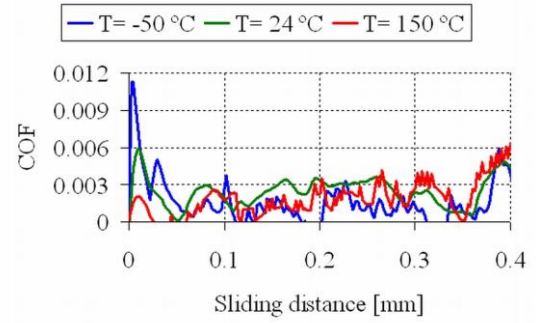


(c)

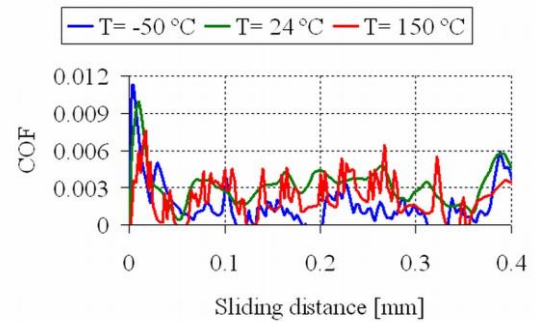
Fig. 4.18. Ratio of real (A_r) and nominal contact area (A_n) at three different temperatures and sliding speeds: (a) $v=1$ mm/s, (b) $v=10$ mm/s, and (c) $v=100$ mm/s [32]



(a)



(b)



(c)

Fig. 4.19. Viscoelastic (apparent) coefficient of friction computed at three different temperatures and sliding speeds: (a) $v=1$ mm/s, (b) $v=10$ mm/s, and (c) $v=100$ mm/s [32]

4.3.7. Three-dimensional FE modeling of viscoelastic friction at macro-scale

As a first step the influence of sliding speed and temperature on the viscoelastic friction for a smooth, reciprocating steel bearing ball with diameter of 2 mm sliding on a smooth EPDM (TRW Automotive, see Appendix C) rubber plate ($10 \text{ mm} \times 4 \text{ mm} \times 2 \text{ mm}$) is investigated numerically by Pálfi et al. [38]. The ball was forced to perform reciprocating motion with an amplitude of $A = 0.3 \text{ mm}$ at different, sinusoidally varying speeds through six cycles. The normal force was $F_n = 100 \text{ mN}$ while the peak values of the sinusoidally varying sliding speeds were $v_{\max} = 0.01, 0.1, 1, 10, \text{ and } 100 \text{ mm/s}$. Figs. 4.20 and 4.21 show the FE model as well as the displacement control curve of the ball. The time and temperature dependent material behavior of the rubber is modeled by 15-term and a 40-term generalized Maxwell-models connected parallel with a two-parameter Mooney-Rivlin model. One part of the material models were constructed by fitting to storage modulus master curves determined by DMTA meas-

urements and pertaining to temperature of -50 , $+25$ and $+150^\circ\text{C}$, respectively. The rest of the material models were originated from the former ones through manual modification of the model parameters in order to describe the measured loss factor master curve more accurately. As it can be seen in Appendix C such material models cannot describe the storage modulus and the loss factor master curve with the same accuracy within the entire frequency range, therefore care must be taken at what excitation frequency and at what temperature the material model is used.

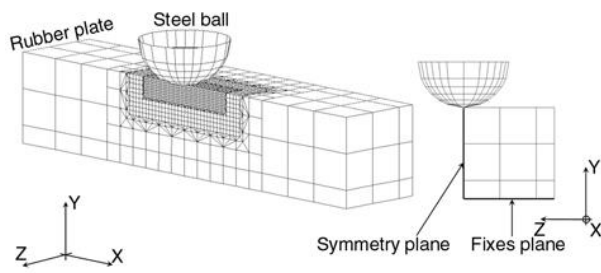


Fig. 4.20. FE model of a steel ball sliding on a rubber plate (only half of the rubber plate is modeled due to the symmetry) [38]

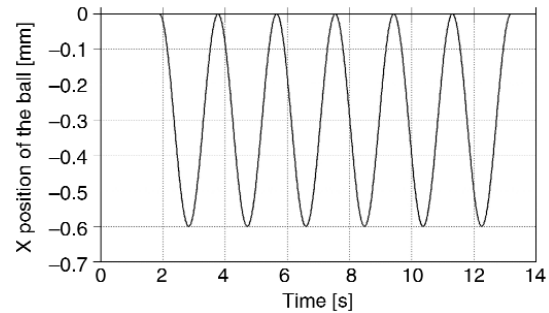


Fig. 4.21. x coordinate of the moving ball in function of time ($v_{\max} = 1$ mm/s) [38]

The FE model was built and solved in MSC.MARC [36]. The rubber plate was discretized by using incompressible elements, whereas the steel ball was modeled as an ideally rigid component. As due to the symmetry only half of the rubber plate was modeled the nodes in the symmetry plane were fixed in z -direction (Fig. 4.20). The bottom of the rubber plate was fixed, i.e. the nodes on this plane were constrained in x -, y - and z -direction. The simulation was realized as follows. As a first step the steel ball was pressed downwards (in negative y -direction) into the rubber plate with the force specified by using incremental technique. After the load reached its final value the ball was drawn horizontally (in negative x -direction) with sinusoidally varying speed. The reciprocating motion last six cycles with amplitude of $A = 0.3$ mm. Fig. 4.21 shows the position of the ball as a function of time in the case of a maximum sliding speed of 1 mm/s. The excitation cyclic frequency induced by the ball performing reciprocating motion can be estimated as $f = \omega/2\pi = v_{\max}/2\pi A$, where ω is the angular frequency. The grey band in Appendix C indicates the range between the lowest and the highest cyclic frequency. Tables 4.2 and 4.3 show the penetration depth (h), the radius of the contact area (a) computed by FE technique and the apparent coefficients of friction ($\mu_{\text{hysteresis}}$) induced by hysteresis. As it can be seen the penetration depth of the ball reduces as the speed increases, due to the fact that the complex modulus of the rubber rises as the speed increases. For the 15- and 40-term material models fitted to the storage modulus (see Appendix C) the values of the penetration depth were approximately the same, but for the 40-term material model fitted to the loss factor (see Appendix C), the values of penetration depth are much bigger because the material model underestimates the storage modulus curve within the interesting cyclic frequency range. As the tables show the biggest penetration depth values appears at $T = 150^\circ\text{C}$ where the storage modulus of the rubber is the lowest. With respect to the apparent coefficient of friction computed it can be concluded that the FE simulations incorporating material models fitted to the storage modulus underestimate hysteresis friction because at $T = 25$ and 150°C these material models give much lower loss factor values than the DMA measurements (see Appendix C). Consequently the apparent coefficient of friction values seen at $T = 25$ and 150°C in Table 4.2 can be considered as rough lower estimations of the reality. At $T = -50^\circ\text{C}$, however, there is a close agreement between the measured and simulated (material model

fitted to the storage modulus master curve) storage modulus and loss factor curves thus the apparent coefficient of friction computed is a good approximation of the reality.

Temperature [°C]	v_{\max} [mm/s]	0.01	0.1	1	10	100
-50	h [μm]	6.70	5.38	5.11	3.55	4.20
	a [μm]	83.65	73.32	71.45	59.60	64.71
	$\mu_{\text{hysteresis}}$	0.0120	0.0080	0.0050	0.0020	0.0007
25	h [μm]	25.94	25.60	24.59	22.78	20.65
	a [μm]	161.04	159.85	156.82	150.93	143.71
	$\mu_{\text{hysteresis}}$	0.0041	0.0078	0.0087	0.0106	0.0111
150	h [μm]	25.90	25.90	25.88	25.56	24.74
	a [μm]	160.94	160.94	160.89	159.86	157.30
	$\mu_{\text{hysteresis}}$	0.0004	0.0010	0.0031	0.0079	0.0088

Table 4.2. Values of the penetration depth (h), radius of the contact area (a) and the hysteresis or apparent coefficient of friction in case of 40-term Maxwell-model fitted to the measured storage modulus master curve [38]

Temperature [°C]	v_{\max} [mm/s]	0.01	0.1	1	10	100
-50	h [μm]	9.74	6.62	4.02	2.54	1.82
	a [μm]	98.68	81.35	63.38	50.40	42.72
	$\mu_{\text{hysteresis}}$	0.0210	0.0180	0.0070	0.0030	0.0008
25	h [μm]	42.51	36.28	30.79	25.79	21.61
	a [μm]	206.18	190.48	175.48	160.60	147.02
	$\mu_{\text{hysteresis}}$	0.0203	0.0177	0.0184	0.0176	0.0173
150	h [μm]	57.22	55.37	49.44	42.51	36.28
	a [μm]	239.22	235.32	222.34	206.18	190.48
	$\mu_{\text{hysteresis}}$	0.0208	0.0237	0.0279	0.0212	0.0177

Table 4.3. Values of the penetration depth (h), radius of the contact area (a) and the hysteresis or apparent coefficient of friction in case of 40-term Maxwell-model fitted to the measured loss factor master curve [38]

When using the 40-term material model fitted to the storage modulus master curve the highest apparent coefficient of friction ($\mu_{\text{hysteresis}} = 0.012$) appears at $T = -50^\circ\text{C}$ and $v_{\max} = 0.01 \text{ mm/s}$. At higher speeds the apparent coefficients of friction obtained at $T = 25^\circ\text{C}$ are higher than those at $T = -50$ and 150°C and are increased as the sliding speed increases. In case of 40-term viscoelastic model fitted to the loss factor master curve the apparent coefficients of friction obtained at $T = 150^\circ\text{C}$ are higher than those appearing at $T = -50$ and 25°C . At this point it must be mentioned that the 40-term model fitted to the loss factor master curve gives realistic loss factor but underestimates the measured storage modulus (see Appendix C). The inaccuracy caused by the underestimation is most critical at $T = 150^\circ\text{C}$ but its degree decreases as the sliding speed increases. Due to the underestimated storage modulus the apparent coefficient of friction values seen at $T = 25$ and 150°C in Table 4.3 can be considered as rough upper estimations of the real values. The comparison of measured and simulated storage modulus and loss factor curves in Appendix C shows, however, clearly that the apparent coefficient of friction obtained at $T = 25^\circ\text{C}$ and $v_{\max} = 100 \text{ mm/s}$ (see Table 4.3) is a good approximation of the real value. It is worth to mention that its value is more than 50% higher than the one obtained by the 40-term model fitted to the storage modulus master curve (see Table 4.2).

Sliding friction of a hard ball on viscoelastic solid has been studied analytically by Greenwood and Tabor [39]. They have shown that the viscoelastic friction contribution is inversely proportional to the viscoelastic (complex) modulus of rubber and directly proportional to the average contact pressure and the fraction of the input elastic energy which is lost due to internal damping. FE results of Pálfi et al. [38] proved that the latter is larger than the loss tangent and, at each temperature, follows the changes in it due to the change in the fre-

quency. According to this the Greenwood-Tabor formula can be used for qualitative prediction of viscoelastic friction component if the fraction of the input elastic energy lost due to internal damping is replaced with $\tan\delta$. Theoretical work of Persson [40] for rolling friction of a spherical ball on viscoelastic solid supports also this finding. Persson's comment on number of relaxation times requested when using the Prony-series representation of the viscoelastic modulus, however, must be criticized. Persson states that it is usually enough to include $n \approx 15$ relaxation times ($\tau_i, i = 1 \dots 15$) if $\tau_{i+1} \approx 10\tau_i$. Contrary this, in Appendix C, it is demonstrated clearly that viscoelastic models with 15 relaxation times yields strongly oscillating loss tangent-cyclic frequency curve if the fitting is realized over a wide range of frequencies.

Validation of the simulation results, as demonstrated by Felhős et al. [11], is simpler at macro-scale than at micro- or nano-scale. In this study, it is found that there is a good agreement between predicted and measured hysteresis friction in case of steel ball rolling on an EPDM rubber plate (see Fig. 4.22a and b). Furthermore it can also be concluded that the FE model would give the same hysteresis friction for rolling and sliding. This is not surprising because as it is mentioned by Greenwood and Tabor [39], in the presence of lubricant, most of the (sliding) friction force is assumed to be due to hysteresis in the rubber bulk if the thickness of the lubricant film is larger than the amplitude of the roughness. In dry case, however, the rolling friction is lower because the additional surface-shear existing in sliding is absent. At the same time the sub-surface stresses consist of a large hydrostatic component superposed on shear in both cases.

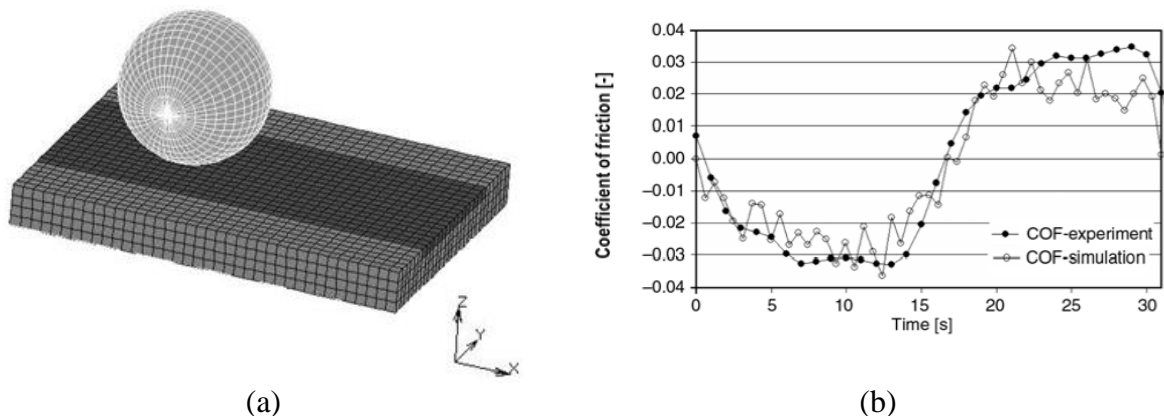


Fig. 4.22. (a) FE model of a steel ball rolling on a rubber plate and (b) comparison of measured and computed (simulated) apparent coefficient of friction in case of 15-term generalized Maxwell-model combined with two-parameter Mooney-Rivlin material law and fitted to storage modulus master curve ($T=20^\circ\text{C}$, diameter of rolling steel ball=14 mm, amplitude of reciprocating motion=25.06 mm, cyclic frequency=1/30 Hz, normal load=140 N) [11]

As it has already been mentioned (see Appendix C) if the 15-term generalized Maxwell model is fitted to measured storage modulus master curve spanning more than 15/2 decades of time (see the work of Felhős et al. [11]) then the material model yields oscillating loss factor (loss modulus) curve. This oscillation, however, can be decreased by (a) using increased number of Maxwell elements, (b) fitting the 15-term model over a narrower frequency range or (c) using other relaxation times. The results prove that rolling friction of rubbers is directly interrelated to its viscoelastic nature. In [40], Persson came to the same conclusion when calculating the rolling friction for a hard cylinder or spherical ball rolling on a flat surface of a viscoelastic solid.

4.4. Experimental investigation of apparently smooth, hard surface generated viscoelastic friction on the basis of literature results

This chapter is based on the findings of Goda [131] and its main objective is to investigate the contribution of micro-hysteresis to rubber friction in case of apparently smooth surfaces. In order to attain this objective it is needed to reanalyze measurement results of Mofidi et al. [44], and compare them with additional test results. Like in [44], friction test results reported for nitrile butadiene rubber (NBR) are in the focus of this work because, contrary to its great practical importance, surprisingly little attention is paid in the literature to oil lubricated sliding friction of NBR squeezing against (apparently) smooth steel surface.

Nowadays considerable effort is made in the literature to study the role of micro hysteresis component of rubber friction both theoretically and experimentally. Accurate prediction of micro hysteresis friction contributes to the differentiation and quantification of friction mechanisms (contribution to rubber friction from macro hysteresis, adhesion, rubber wear, etc.). Furthermore, the knowledge gained from theoretical and/or experimental works enables engineers to design rubber components or rubber friction related tribological systems with improved tribological behavior. Several studies and results prove that the micro hysteresis friction may be dominant when the rubber slides on rough (silicon carbide paper) or very rough surface (asphalt road surface). At the same time, the combined experimental (see Fig. 4.23) and theoretical study of Mofidi et al. [44] on surface roughness generated friction showed that micro-hysteresis may give the dominant contribution to rubber friction even in case of lubricated, apparently smooth surfaces.

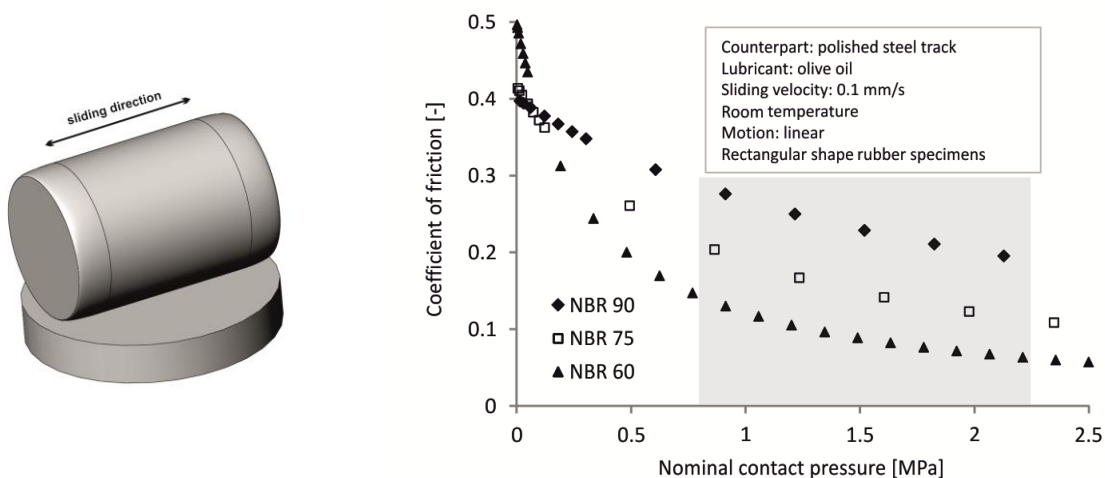


Fig. 4.23. Test configuration used in [44]. The figure is taken from [131].

Fig. 4.24. Apparent coefficient of friction vs. nominal contact pressure (back-calculated from [51]). The shaded area represents the range of nominal contact pressure values appeared at room temperature in [44]. The figure is taken from [131].

Wohlers et al. [45] emphasize also the importance of micro-hysteresis for the case when rubber slides on apparently smooth steel surface. Mixed friction of reciprocating O-rings was analyzed numerically as well as experimentally and it was concluded that, in the boundary lubrication regime, the friction force can be explained by Persson's micro hysteresis friction theory [3].

Conclusion drawn by Mofidi et al. [44] is very interesting especially in the light of the fact that the friction of NBR specimens studied was complicated by very unfavorable lubrication

tion condition, frictional heating and wear. In [44], the viscoelastic (hysteresis) friction contribution was calculated by using Persson's friction theory [3] which is based on spectral description of the surface roughness and a new contact theory. The latter is investigated in depth in section 4.5.2. However, in [26], Nguyen et al. pointed out that the computed viscoelastic contribution is very sensitive to the geometrical details of rigid asperities and hence the spectral description of surface roughness does not allow us to predict micro hysteresis contribution accurately. At the same time, in a very recent paper, Fina and his co-authors [46] found that, in case of rough surfaces, Persson's model predicts correctly the peak value of hysteresis (or apparent) coefficient of friction and the sliding velocity at which it appears but results are in poor correlation for the shape of the hysteresis friction master curve. The latter implies that the computed apparent coefficients of friction, excepting the peak value and the ones in its small vicinity, differ considerably from the measured values. However it must be mentioned that Fina et al. [46] did not consider friction test results for smooth surfaces. Persson's theory may also be criticized for the small strain linear viscoelastic description of rubber behavior incorporated in it because does not allow researchers to take into consideration neither the effect of large strains nor the strain amplitude dependence of the storage modulus and the loss factor of rubber. The influencing effect of strain on rubber viscoelastic properties was studied, among others, by Wang et al. [47]. Contrary to its great importance the effect of strain on the rubber viscoelastic properties is usually neglected in the hysteresis friction predictions because there is no consensus in the literature in respect of strain at which DM(T)A (dynamic mechanical (thermal) analysis) tests should be performed. Arbitrary choosing of strain value, however, may cause serious uncertainty in hysteresis friction predictions. In [48], Mokhtari et al. performed friction tests at $T=27^{\circ}\text{C}$ to study the friction process between dry rubber disks (carbon black- and silica-reinforced BR and S-SBR elastomers) and smooth (polished, $R_a=0.52 \mu\text{m}$) or rough ($R_a=2.28 \mu\text{m}$) granite balls with diameter of 30 mm. The sliding velocity and the nominal contact pressure were 5 mm/s and 0.4 MPa, respectively. In dry case, the smooth surface produced higher friction force than the rough one. In order to estimate the contribution of micro hysteresis component to rubber friction the tests were repeated in presence of lubricating oil having dynamic viscosity of 78 mPas at 20°C . In case of smooth ball, it was found that a thin boundary lubricant layer decreases the coefficient of friction drastically (from 1.55 to 0.05 for 85 phr silica-filled rubber). This experimental finding and additional calculations proved that the high friction force cannot be explained by the micro-hysteresis component of friction. It was also concluded that the real area of contact is 3-5 times greater when the smooth ball is in contact with the rubber. Additionally, it was pointed out that wear debris attached to the granite surface decreases the surface roughness (smoothing effect of the adhering wear debris) and increases the real area of contact.

4.4.1. Unlubricated frictional behavior of nitrile butadiene rubber (NBR)

Firstly, the most important conclusions of friction tests conducted on rubber sliding on dry, apparently smooth harder surfaces will be reviewed. According to the aim of this study, most of them refer to nitrile rubber.

From the friction test results analyzed by Smith [8] it can be concluded that when the rubber block slides on dry and smooth glass surface with a velocity lower than 1 mm/s (negligible frictional heat generation) the sliding friction coefficient is dominated by adhesion and usually load dependent i.e. decreases with increasing applied normal pressure (nominal contact pressure). At the same time, rubber frictional resistance to sliding on dry, smooth track can be reduced by using rougher rubber specimens (smaller real contact area at low loads). Friction reducing effect of rubber roughening, however, completely disappears at high loads (entirely flattened rubber asperities).

In one part of the dynamic friction tests of Grosch [1], flat NBR specimens (containing various amount of carbon black) of 25.4 x 25.4 x 6.3 mm (length x width x thickness) were pressed against dry, polished stainless steel track moving with constant velocity under controlled ambient temperature (varied between -50 and 100°C). The velocity ranged from 10⁻⁵ to 30 mm/s while the highest normal pressure was 0.054 MPa. Grosch came to the conclusion that the dry friction of NBR specimens on a smooth surface is due to interfacial adhesion. He pointed out that under constant load and temperature the apparent coefficient of friction first increases then decreases with increasing sliding velocity. Additionally he was able to identify experimentally the sliding velocity at which the apparent coefficient of friction reached its maximum value (adhesion hump). The highest apparent coefficient of friction at T=20°C was about 2.4 which appeared at a sliding velocity of ≈ 10 mm/s in case of NBR containing no carbon black. Increasing carbon black content resulted in reducing apparent coefficient of friction (at 50 phr carbon black the peak value was half as high as at zero carbon black content) and a slight shift of adhesion peak towards lower velocities (from 1 to 0.1 mm/s) in case of smooth glass counter surface. This tendency was explained by the fact that the addition of carbon black to NBR shifts slightly the peak value of the loss modulus towards lower frequencies and flattens the loss curves (loss modulus and loss factor). At the same time, on increasing carbon black content the hysteresis friction appeared to decrease more rapidly than the adhesion component. When replacing polished steel surface with a rough silicon carbide paper (particle size ≈ 0.1 mm, average spacing between abrasive particles ≈ 0.14 mm) a hysteresis peak (hysteresis hump) appeared beside the adhesion peak (adhesion hump) in the apparent coefficient of friction vs. sliding velocity (master) curve. However the dusting of rough surface with magnesium oxide powder eliminated the adhesion peak and reduced the hysteresis peak. The adhesion-reducing powder resulted in an adhesion component being almost independent of the velocity and the temperature. The cyclic frequency at which the maxima of loss modulus (E'') of NBR appeared was $2 \cdot 10^6$ Hz at temperature of 30°C. It is worth to mention that both the magnitude and the location of adhesion peak in apparent coefficient of friction vs. sliding velocity curve were about the same for NBR/polished steel and NBR/wavy glass sliding pair. The waviness on the glass was needed to enhance the reproducibility of measurement results. The apparent coefficient of friction of NBR (with 0, 20 and 50 phr carbon black content) measured on dry wavy glass surface at T=20°C and sliding velocity of 10 mm/s was 2.3, 1.9 and 1, respectively. Increasing the temperature from 20 to 80°C decreased the adhesion (apparent) coefficient of friction from 2.3 to 1.5 for unfilled NBR sliding on wavy glass surface at a sliding velocity of 10 mm/s. When NBR specimens rubbed against polished steel counter surface no hysteresis peak appeared in Grosch's apparent coefficient of friction vs. sliding velocity master curve. It is due to the fact that the wavelength of the roughness component which would be able to excite the rubber surface with frequency of $2 \cdot 10^6$ Hz (frequency belonging to the maxima of loss modulus) is unrealistically low i.e. is in the nanometer range. At the same time the longer wavelength roughness components are unable to generate considerable hysteresis due to the lower loss modulus.

Friction behavior of NBR (with 76.1 Shore A hardness and unknown carbon black content) paired with steel surfaces of different surface roughness was studied at T=22°C and under unidirectional dry sliding conditions by Mofidi and Prakash [49]. Experiments were conducted using a block-on-ring configuration where a rubber block of 16 x 4 x 2 mm (length x width x thickness) was pressed against the external cylindrical surface of a rotating steel ring with external diameter of 35 mm, and internal diameter of 19 mm. Three sets of bearing steel rings with different ranges of surface roughness (fine, medium and rough) were used. The arithmetic mean roughness (R_a) ranged between 0.15 and 0.3 μm for fine, 0.35 and 0.55 μm for medium, 0.5 and 0.7 μm for rough steel surface. The width of the nominal contact

area was 4 mm while the sliding velocity was 18 mm/s. At very low cyclic frequency (relaxed state) and room temperature the modulus of rubber specimens was about 10 MPa. The apparent coefficient of friction decreased continuously during the test until a steady state value but the decrease was most intensive in the first 15 min (running-in period). At low load (nominal contact pressure is about 0.24 MPa) the apparent coefficient of friction measured at $t=15$ min was 1.4 and 0.9 for fine/medium and rough steel surface, respectively. At higher load (nominal contact pressure is about 0.75 MPa) the apparent coefficient of friction measured at the end of the running-in period was about 1 for medium rough steel. The steady state apparent coefficient of friction for medium rough steel and at the higher load was 0.6 while at the lower load was 1.2 (fine surface), 0.75 (medium rough surface), and 0.65 (rough surface). Based on these results, it can be concluded that the increasing nominal contact pressure and surface roughness decreases the apparent coefficient of friction. The transition from fine to medium rough surface resulted in significant reduction in the steady state apparent coefficient of friction but the further increase in surface roughness between the medium rough and the rough surface was accompanied with a slight decrease in the dry apparent coefficient of friction. Although measurement results are consistent with those of Grosch [1] the authors assumed that the micro hysteresis component is the most dominant component of steady state sliding friction. Unfortunately, the reason why it was assumed is not explained in the study of Mofidi and Prakash [49]. Finally, the authors mentioned that when an unlubricated rubber slides against the same counter face repeatedly, a decrease in friction may occur until a complete layer of material is deposited from the rubber onto the opposing surface.

In case of rubber block - made from tread rubber having unknown chemical composition - sliding on dry, apparently smooth, unidirectional polished steel track (RMS roughness $\approx 0.08 \mu\text{m}$ from the 2D data and $\approx 0.5 \mu\text{m}$ from the 1D line scan data) with velocity of 0.2 mm/s (sliding direction is orthogonal to the polishing direction) and at room temperature Carbone et al. [50], however, found experimentally that the sliding friction coefficient is practically load- or nominal contact pressure-independent. More precisely the sliding friction coefficient increases slightly with increasing normal load or nominal contact pressure. This finding is consistent with that of Hurry and Prock reported in 1953 for rubber belting/polished steel (RMS roughness = $0.3 \mu\text{m}$) sliding pair (see Smith's book [8] for a short summary on test results). Their variable-load friction tests conducted at constant velocity of 0.25 mm/s resulted in constant sliding friction coefficient. Carbone et al. hypothesized that if adhesion was the dominant friction component the apparent coefficient of friction would decrease with increasing normal load. According to the authors' knowledge this fact emphasizes the importance of micro hysteresis friction contribution even for dry, apparently smooth surfaces. They, however, did not mention that surface free energy of rubbers has an effect not only on the magnitude but also the tendency of the adhesion component of rubber friction. As concluded by Smith [8] decreasing surface free energy yields smaller variation in dry apparent coefficient of friction as the applied normal load increases.

4.4.2. Frictional behavior of nitrile butadiene rubber (NBR) under oil lubricated condition

One of the earliest experimental studies in this category is the work of Denny [51]. His main conclusion was that in addition to the adhesion component of rubber friction, an additional contribution of comparable magnitude may arise due to the roughness of the track surface. Among others the friction of NBR with 60, 75 and 90 Shore A hardness was measured at constant sliding velocity of 0.1 mm/s and against various lubricated apparently smooth track surfaces. The velocity dependence of friction was negligible below this sliding velocity. At the same time the low sliding velocity implies that the effect of frictional heat generation on

friction force can also be neglected. The size of the rectangular shape rubber specimens varied from 5 mm thick and 10000 mm² area to 1 mm thick and 8 mm² area. In relation to the load effect he found that the apparent coefficient of friction decreases with increasing pressure and depends only on the nominal contact pressure and not on shape or size of the specimen (see Fig. 4.24). When NBR 75 slides on olive oil lubricated polished steel track under nominal contact pressure of 0.25 and 0.75 MPa the apparent coefficient of friction was 0.31 and 0.22, respectively. The back-calculated frictional shear stress vs. nominal contact pressure curve (see Fig. 4.25) shows clearly that, in case of NBR 60, the frictional shear stress (friction force per unit nominal contact area) reaches a practically constant value with increasing contact pressure. The constant friction force suggests that the magnitude of real contact area saturated i.e. reached a practically normal load independent value. Probably the magnitude of real contact area cannot reach the magnitude of nominal contact area because in case of complete contact the oil should be squeezed out entirely. The pressure inducing complete contact, as seen, becomes higher and higher with increasing rubber hardness.

Measurement results showing the effect of track surface roughness are particularly interesting. Friction tests on NBR 90 against light mineral oil lubricated polymethyl methacrylate (PMMA) track surfaces with $R_a=0.01$ (0.01), 0.13 (0.25), 0.2 (0.38), 0.38 (1.37) and 0.38 (1.62) μm (values without and with brackets are valid along and across finishing marks) showed that at any contact pressure between 0.01 and 10 MPa the apparent coefficient of friction increases as the track surface becomes rougher (see Fig. 4.26). Measured R_a values indicate anisotropic surface roughness which is in accordance with the fact that they were prepared by unidirectional abrasion with emery cloth of various grades.

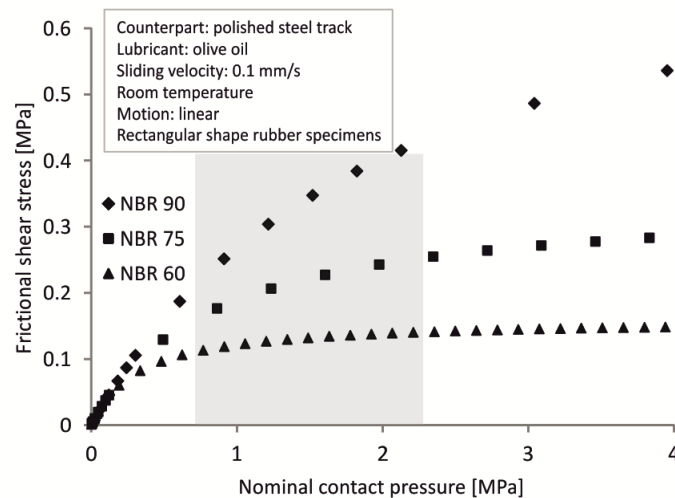


Fig. 4.25. Mean frictional shear stress vs. nominal contact pressure (back-calculated from [51]). The shaded area represents the range of nominal contact pressure values appeared at room temperature in [44]. The figure is taken from [131].

Fig. 4.27 depicts the variation of the apparent coefficient of friction in function of nominal contact pressure for NBR 90 sliding on smooth PMMA track. In respect of track material Denny mentioned that when replacing steel track with PMMA the apparent coefficients of friction became about 60% higher. The latter allows us to estimate the apparent coefficient of friction for NBR 90/smooth steel sliding pair under oil lubrication (see Fig. 4.27). As the track is smooth Denny hypothesized that friction is due to friction mechanism other than micro-hysteresis. In order to represent the effect of track roughness on the apparent coefficient of friction Denny subtracted the coefficients of friction measured on smooth track ($R_a=0.01$ μm) from the ones measured on rougher tracks.

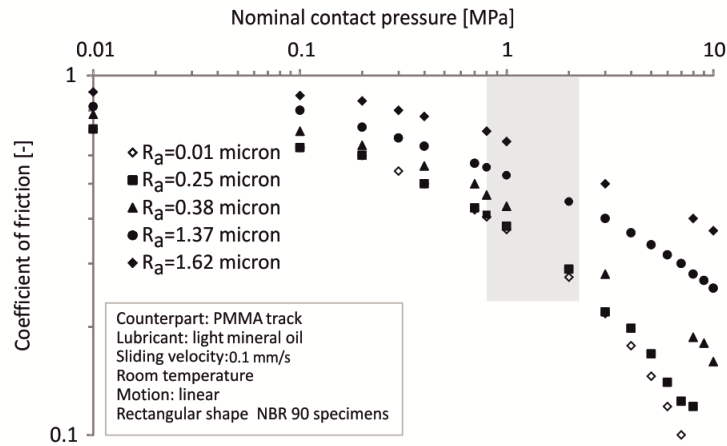


Fig. 4.26. Variation in apparent coefficient of friction as a function of nominal contact pressure in log-log scale when sliding across finishing marks (based on [51]). The shaded area represents the range of nominal contact pressure values appeared at room temperature in [44]. The figure is taken from [131].

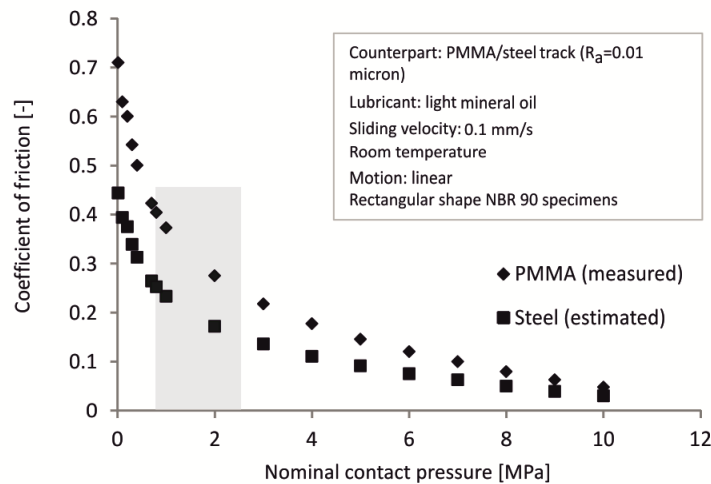
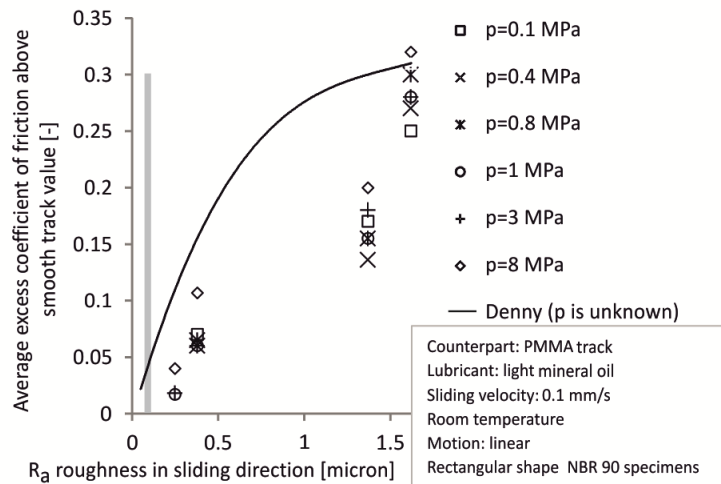


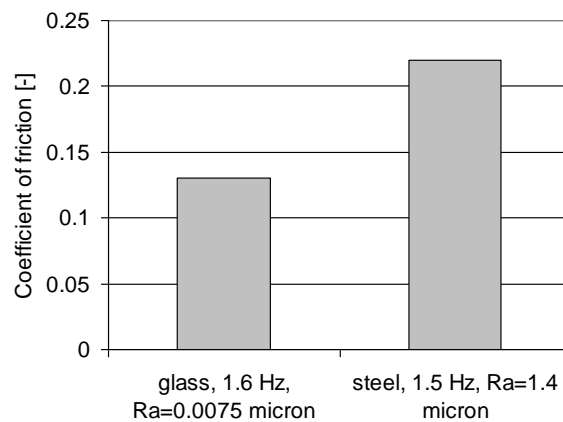
Fig. 4.27. Variation in apparent coefficient of friction as a function of nominal contact pressure for smooth PMMA and steel track (based on [51]). The shaded area represents the range of nominal contact pressure values appeared at room temperature in [44]. The figure is taken from [131].

In the study of Denny [51], the difference is termed average excess coefficient above smooth track value (contribution of surface roughness to the apparent coefficient of friction). Fig. 4.28a shows the contribution of surface roughness back-calculated from [51] (data points) and as reported in [51] (solid line) in function of track roughness along direction of sliding. In Denny's opinion, the solid line can be considered as a largely pressure independent upper limit for the average excess coefficient above smooth track value. This statement is based on the fact that friction test results complicated with neither frictional heat generation nor elastohydrodynamic effects showed only slightly increasing track roughness effect on rubber friction as the nominal or mean contact pressure increased (see Fig. 4.28a). Denny pointed out also experimentally that the increasing rubber roughness decreases the apparent coefficient of friction at lower nominal contact pressure but has no effect at higher loads. When NBR 75 slides on light mineral oil lubricated, smooth PMMA surface with $R_a = 0.01 \mu m$, the rubber roughness has effect on the apparent coefficient of friction only when nominal contact pressure is lower than ~ 0.3 MPa. From engineering point of view Denny's work is of

great importance because he pointed out also that sliding friction is higher across the finishing marks than parallel to them (sliding direction sensitivity of the friction when rubber slides on grooved surfaces) and the effect of undulation in sliding direction on the friction force is greater than that of the overall height of the asperities. Using a combined experimental and theoretical approach Carbone et al. [50] came to the same conclusion in their recent study. Two possible energy dissipating (friction) mechanisms were mentioned by Denny to explain the track roughness introduced friction force contribution: the material tearing out and the hysteresis in the path of track asperities. Finally, Denny's friction tests show clearly that the harder the rubber is the higher the apparent coefficient of friction is under oil lubrication.



(a)



(b)

Fig. 4.28. (a) Variation of back-calculated average excess coefficient of friction above smooth track value with track roughness along direction of sliding (based on [51]). Data points represent back-calculated values while solid line is from Denny's original publication (see [51]). In the original publication, only the solid line was reported. The shaded area represents the R_a value appeared in [44]. The figure is taken from [131]. (b) Apparent coefficients of friction of lubricated rubber/glass and rubber/steel sliding pairs measured at room temperature. (Based on the results of [56].) Oil viscosity=65.9 mm²/s. The figure is taken from [35].

Before going on the discussion of lubricated frictional behavior of NBR rubbers it is worth to cite the work of Rana et al. [56]. They developed an experimental reciprocating rig to study the contact conditions of an elastomeric seal with a hard surface at room temperature. The stroke length, stroke speed and the load on the rectangular seal was varied. The counter surfaces included smooth glass ($R_a=0.0075 \mu\text{m}$) and steel having a mean surface roughness of

$R_a=1.4 \mu\text{m}$. The tests were carried out at a mean surface pressure of $p \approx 3 \text{ MPa}$ in dry and lubricated conditions. The stroke length was 5 mm, while the reciprocating frequency varied between 1.5 and 11 Hz. The velocity of the slider changed with time in a sinusoidal manner since rotary motion was converted into linear. A reciprocation frequency of 1.5 Hz implied an average stroking speed of 15 mm/s with a peak velocity of 47 mm/s. They concluded that the reciprocating with a rough steel plate increases the friction due to the interaction of hard steel asperities with soft rubber ones. Apparent coefficients of friction computed based on the measured friction force values of Rana et al. [56] can be seen in Fig. 4.28b. Measured COFs show clearly that the higher surface roughness of steel causes higher sliding friction due to the increased hysteresis friction. The increase in rubber friction is about 0.1. It is worth to mention as the sliding speed is low neither the hydrodynamic effect nor the frictional heat generation play role in the measured sliding behavior of rubber.

The frictional behavior of nitrile butadiene rubber (NBR) with 76.1 Shore A hardness, arithmetic surface roughness of $R_a \approx 0.08 \mu\text{m}$ and relaxed modulus of about 10 MPa (measured at room temperature) sliding against steel surface ($R_a \approx 0.38 \mu\text{m}$) was studied under unidirectional paraffinic oil lubricated conditions by Mofidi and Prakash [52]. The same block-on-ring test configuration was used as in their former study [49] but the steel ring had anisotropic surface roughness with finishing marks (grooves) parallel to the sliding (circumferential) direction. All the tests were performed at room temperature ($T=22^\circ\text{C}$) and after an initial running in phase taking 50 min at a sliding velocity of 18.33 mm/s. The nominal contact pressure was 0.37 MPa and the sliding velocity used in the test phase was set to 0.24, 0.33, 0.58, 1.03, 1.83, 3.26, 5.79, 10.3, 18.33, and 32.58 mm/s. The friction test phase took 10 min at each sliding velocity. The measured apparent coefficient of friction decreased with increasing sliding velocity showing the transition from the boundary to mixed and from the mixed to elastohydrodynamic lubrication regime (see Fig. 4.29). It is worth to mention that as the sliding direction was parallel to finishing marks of steel surface the real roughness in the direction of sliding was likely significantly smaller than $0.38 \mu\text{m}$.

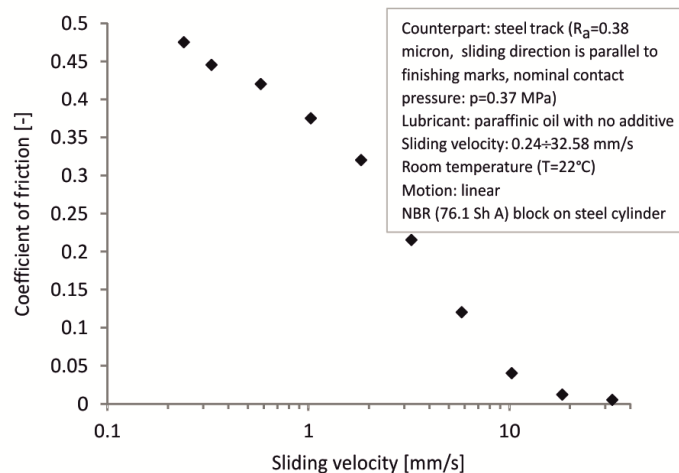


Fig. 4.29. Variation in apparent coefficient of friction as a function of sliding velocity (based on [52]). The figure is taken from [131].

In order to test the tribological behavior of sliding rubber components, in many cases, a special test rig is used where a metallic cylinder performing reciprocating motion with given amplitude and frequency is squeezed against a rubber sample (see the studies of Mofidi et al. [44, 53] and Fernandez-Diaz [54] and Fig. 4.23). In [53], a steel cylinder with diameter of 15 mm and length of 22 mm was reciprocated along its axis of revolution against curved (cylinder-

on-curved sample i.e. CoCS) and flat (cylinder-on-flat sample i.e. CoFS) NBR samples. The curved rubber samples were used to eliminate completely the edge effect. The specimen thickness was 6 mm and all the tests were performed at temperature of $T=26^{\circ}\text{C}$. Apparent coefficients of friction measured at 60 (CoCS) as well as 30 min (CoFS) and in presence of lubricant (uncontaminated polyol and complex ester) can be seen in Fig. 4.30.

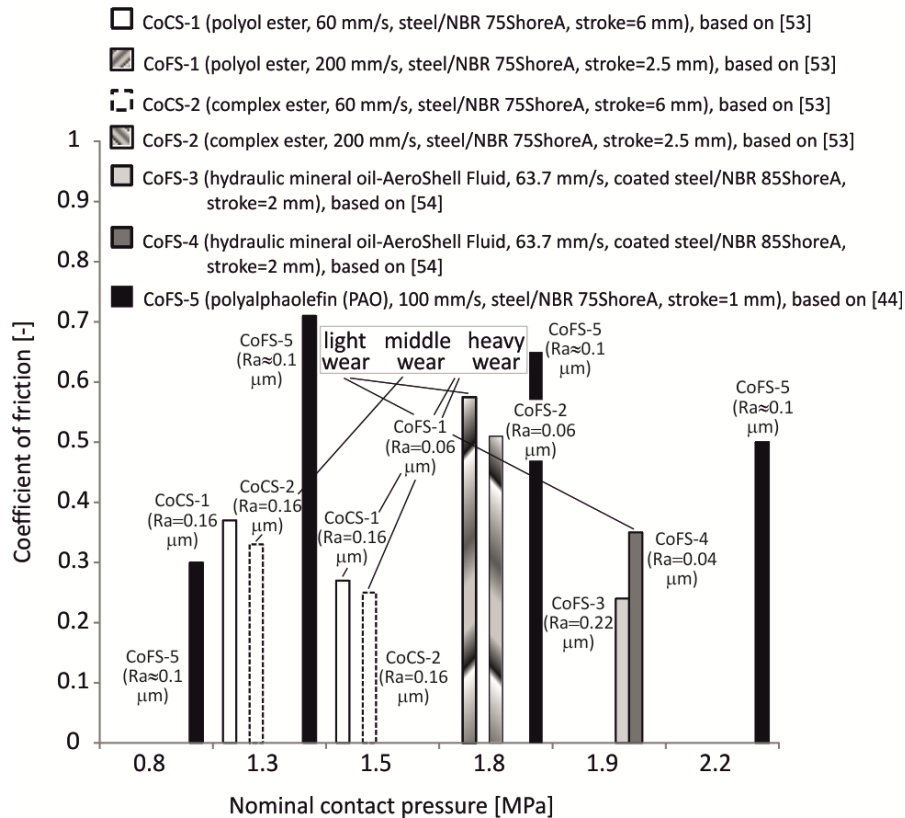


Fig. 4.30. Variation in apparent coefficient of friction as a function of nominal contact pressure for uncoated/coated steel cylinder reciprocating against lubricated NBR samples at room temperature (based on [44], [53] and [54]). The figure is taken from [131].

The lubrication was realized in a way that a small amount of lubricant was applied to the contacting surfaces prior to the tests. In case of cylinder-on-curved sample test configuration, independently of the lubricant used, the apparent coefficient of friction decreased with about 0.1 as the mean contact pressure increased from 1.3 to 1.5 MPa. However, this was accompanied by enhanced wear (roughening rubber surface). In cylinder-on-flat sample test configuration rubber samples were paired with smoother steel cylinder and showed less wear but much higher apparent coefficients of friction. The latter indicates that the lubrication conditions were more favorable (larger stroke, rougher counter surface, no edge effect) in CoCS test configuration (mixed friction) than in CoFS one (boundary lubrication). In the CoFS test configuration, the boundary lubricating film was likely very thin (few layers of lubricant molecules) thus it was unable to reduce the rubber-steel asperity contact i.e. the micro hysteresis component of friction. The effect of lubricant on the apparent coefficient of friction, the presence of wear, and the very smooth counter surface, however, imply that the high apparent coefficient of friction values ($\mu \approx 0.5-0.6$) cannot be completely due to micro-hysteresis. Finally, Fig. 4.31 shows the ambient temperature dependency of measured apparent coefficient of friction for lubricated fluorocarbon rubber (FKM), nitrile butadiene rubber (NBR) and hydrogenated nitrile butadiene rubber (HNBR). The apparent coefficient of friction decreases as the ambient temperature increases but the change is very small. Contrary to Mofidi et al.'s finding [44] it

was found that ambient temperature has little effect on friction. This result will be of great importance when analyzing Mofidi et al.'s findings in depth.

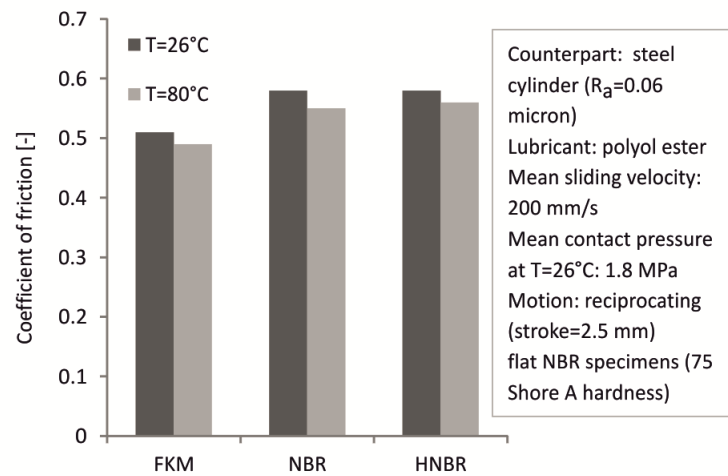


Fig. 4.31. Variation in apparent coefficient of friction as a function of ambient temperature for uncoated steel cylinder reciprocating against lubricated FKM (fluorocarbon rubber), NBR (nitrile butadiene rubber) and HNBR (hydrogenated nitrile butadiene rubber) samples (based on [53]). The figure is taken from [131].

In Fernandez-Diaz et al.'s study [54], coated steel cylinders (diameter=19 mm, length=33 mm) with different R_a roughness were reciprocated along their axis of revolution against oil lubricated NBR samples (85 Shore A hardness, length or size in sliding direction=8 mm, width=15 mm, thickness=8 mm). Using high velocity oxygen fuel coating and hard chromium plating processes a thin layer of different materials (AlBronze, NiCrBSi, WCCoCr, chromium) was made onto the steel cylinders. Then the coated cylinders were subjected to surface modification processes, such as grinding and grinding+superfinishing, in order to reach the desired surface roughness ($R_a = 0.2\text{-}0.23 \mu\text{m}$ for grinded surface, $R_a = 0.03\text{-}0.04 \mu\text{m}$ for grinded+superfinished surface). The ambient temperature, average sliding velocity, applied normal load, and stroke was $T=25^\circ\text{C}$, $v=63.7 \text{ mm/s}$, $F_N=100 \text{ N}$, and $s=2 \text{ mm}$, respectively. Test duration was 30 min and the sliding pairs were lubricated with AeroShell Fluid 41 hydraulic mineral oil. Friction test results showed that the apparent coefficient of friction, independently of the material of the coating, increases with decreasing R_a roughness. The apparent coefficient of friction was about 0.33-0.36 for grinded+superfinished and 0.23-0.25 for grinded surfaces independently of the material of the coating. The experimental finding that surfaces with same R_a roughness yields the same apparent coefficient of friction independently of the material of the coating may be interpreted as the indicative of dominating micro-hysteresis. At the same time as no results are available for dry surfaces in [54] the real contribution of micro-hysteresis to rubber friction cannot be estimated reliably. It must be, however, mentioned that the measured apparent coefficients of friction values are considerably lower than those of Mofidi et al. [44] due to the more favorable lubrication conditions.

In [44], Mofidi et al. came to the conclusion that micro-hysteresis generated by the roughness of a highly polished steel surface may give the dominant contribution to the lubricated friction. They mentioned that this is particularly valid at low sliding velocities (negligible hydrodynamic effect and frictional heat generation) and low temperatures (enhanced hysteresis). In their friction tests, a steel cylinder (diameter = 15 mm, length = 22 mm, RMS roughness $\approx 0.1 \mu\text{m}$) was reciprocated (stroke = 1 mm, cyclic frequency = 50 Hz, average sliding velocity $\approx 100 \text{ mm/s}$) against NBR discs (75 Shore A hardness, RMS roughness prior

to tests $\approx 0.4 \mu\text{m}$) at room ($T=25^\circ\text{C}$) and elevated temperatures ($T=40$ and 80°C). The cylinder reciprocated longitudinally i.e. along its axis of revolution (see Fig. 4.23). Unfortunately sizes of the rubber samples used were not reported by Mofidi et al. [44]. However majority of measurement results reported in [44] for non-aged and aged rubber samples can also be found in an another study of Mofidi et al. [55] where rubber discs with diameter of 25 mm and thickness of 4 mm were used. This proves that the same rubber discs were used in both studies. In order to avoid the edge effects edges of steel cylinder were well-rounded (see Fig. 4.23). Measurement results are represented in Figs. 4.32 and 4.33. As Mofidi et al. did not provide nominal contact pressure values they were estimated by me based on the data being available and using the Hertz theory. Friction tests of Mofidi et al. [44] on non-aged samples in different lubrication oils of different viscosities showed that the lubricant has only slight effect on the apparent coefficient of friction at $T=40^\circ\text{C}$. (The influence of lubricant on the friction will be discussed in depth in the next section.) Consequently the authors came to the conclusion that the rubber friction is not (mainly) due to shearing a thin viscous layer, but due to the internal friction of the rubber. The significantly lower apparent coefficient of friction at normal load of 20 N (see Fig. 4.32) was explained as follows. At small load the initial molding grooves on the rubber surface are not fully flattened thus they are able to store lubricant. When the molding grooves oriented parallel to the reciprocating direction of the steel cylinder they flatten completely and most of the lubricant squeezes out from the contact region resulting unfavorable lubrication. However it is worth to mention that apparent coefficients of friction measured by Mofidi et al. [44] at higher loads are much higher than the values measured by Denny [51] and Mofidi and Prakash [52]. The apparent coefficient of friction measured at normal load of 20 N (small load), however, is consistent with Denny's friction test results (see Figs. 4.24 and 4.25). The decrease in apparent coefficient of friction at higher ambient temperature (see Figs. 4.32 and 4.33) was explained by the temperature dependence of the internal friction (decreasing internal friction with increasing temperature) of the rubber.

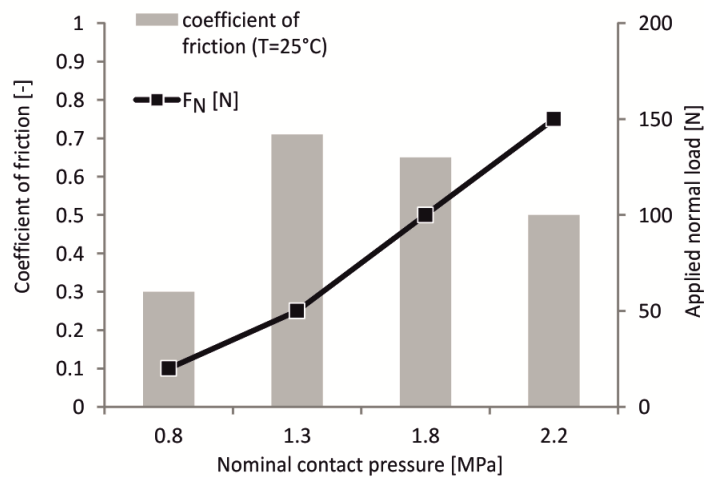


Fig. 4.32. Measured apparent coefficient of friction in function of estimated nominal contact pressure ($T= 25^\circ\text{C}$, lubricant: polyalphaolefin with dynamic viscosity of $\eta_{40^\circ\text{C}} = 4.4 \cdot 10^{-3}$ Pas, RMS roughness of steel surface $\approx 0.1 \mu\text{m}$, rubber specimen: NBR 75 Shore A hardness, test duration: 15 min, average sliding velocity ≈ 100 mm/s, stroke = 1 mm) (based on [44]). The figure is taken from [131].

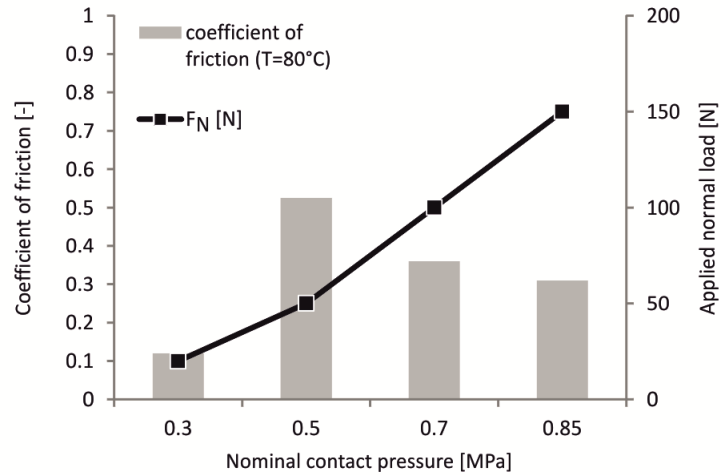


Fig. 4.33. Measured apparent coefficient of friction in function of estimated nominal contact pressure ($T=80^{\circ}\text{C}$, lubricant: polyalphaolefin with dynamic viscosity of $\eta_{40^{\circ}\text{C}} = 4.4 \cdot 10^{-3}$ Pas, RMS roughness of steel surface $\approx 0.1 \mu\text{m}$, rubber specimen: NBR 75 Shore A hardness, test duration: 15 min, average sliding velocity ≈ 100 mm/s, stroke = 1 mm) (based on [44]). The figure is taken from [131].

4.4.3. Critical discussion of the most important literature results

Findings of Mofidi et al. have been used in this study for comparison with experimental data taken from the literature. The evaluation of Mofidi et al.'s test results, however, is complicated by the fact that the nominal contact area varies as a function of the applied normal load and no information on wear and deformation of rubber due to the friction force is available in the study of Mofidi et al. [44]. For the sake of completeness, in this section, the effect of hysteresis, adhesion, rubber roughness, wear, ambient temperature, lubricant, frictional heating and rubber elasticity on rubber friction will be discussed in depth.

It is very interesting to compare Persson's [3] (micro hysteresis) theory with that of Smith [8]. Persson considers micro hysteresis friction to be adhesion and applied normal pressure dependent phenomenon but, in his predictions, the effect of adhesion is not taken into account. According to his opinion if the roughness is large enough (this is not the case for apparently smooth surfaces) the increase in the hysteresis contribution to the friction from the adhesion induced increase in the contact area may be very small [50]. The larger the roughness is the smaller the adhesion-induced increase is in the micro hysteresis friction contribution. Smith's theory contrasts strongly with this because he assumes an adhesion dependent micro hysteresis friction contribution which is apparently independent of the applied normal pressure (see the largely nominal contact pressure independent results of Denny in Fig. 4.28a). In his theory, the penetration of the rigid asperities into the rubber surface is controlled by the adhesional interaction between the surfaces and the increasing applied normal pressure does not measurably increase the hysteresis friction contribution due to the small micro asperity depth of the harder, apparently smooth surface. Smith concluded that higher the adhesion larger the micro hysteresis friction contribution.

In [44], Mofidi et al. studied the effect of micro hysteresis friction in the presence of lubricant but the conditions for adhesion-eliminating lubricant film formation were unfavorable. The very high apparent coefficients of friction reported prove that there was no continuous adhesion-eliminating boundary lubricant layer between contacting surfaces. As it is known a discontinuous boundary lubricant layer, however, cannot eliminate adhesion entirely but can reduce its effect. It must also be mentioned that as the cylinder was smooth a relative-

ly large real area of contact was formed in the tests of Mofidi et al. [44]. Adhesive component of rubber friction depends not only on the real area of contact but also on the sliding velocity, contact pressure and temperature dependent shear strength of adhesive contact. For the first sight it seems that the sliding velocity dependency of friction does not play role in [44] because the amplitude and frequency of the reciprocating motion were kept constant during friction tests. The real sliding velocity, however, may differ from the theoretical one (especially at higher temperatures) as it will be pointed out at the end of this section. As it is well known adhesion component of friction originates from interaction of contacting surfaces, acts at the interface of the contacting bodies and is directly correlated to the real area of contact. As reported by Smith [8], in case of apparently smooth surfaces, adhesive friction may be very high because the smoothness of the paired, harder surface promotes adhesion. Contrary to the very unfavorable lubrication conditions Mofidi et al. made no mention of the possible development of adhesive friction and did not provide measurement results for dry surfaces. Without dry results, however, the real contribution of micro hysteresis component to rubber friction cannot be estimated reliably.

Importance of rubber roughness is emphasized, among others, by Salant et al. [41], Rana et al. [56] and Arnold et al. [57]. Studies cited by Rana et al. [56] shows clearly that the roughness of metal surfaces does not affect the friction much if its roughness is significantly lower than the seal roughness. It was found experimentally that when oil-lubricated smooth metal surface is reciprocated with a rough elastomeric seal at a velocity lower than 100 mm/s mixed friction or boundary lubrication dominates the friction. Arnold et al. [57] emphasize also the importance of rubber roughness and point out that roughening a rubber surface decreases its adhesion-friction-force-development potential when sliding on smooth materials. In the friction tests of Mofidi et al. [44], the RMS roughness of rubber surface prior to tests was about $0.4 \mu\text{m}$. Although experimental results show clearly that rubber roughness and surface energies of the contacting bodies have considerable effect on the friction force the common practice in friction prediction is not in accordance with this. Effect of rubber roughness and surface energies is, almost without exception, neglected in friction force predictions.

Albeit rubber wear (deposited rubber layer on the metal surface, damage of rubber surface, etc.) has considerable effect on friction neither microscopic images on worn surfaces nor surface roughness measurements are presented by Mofidi et al. [44]. The real area of contact reduction and the smoothing effect of wear debris may also be mentioned among the effects of rubber wear. Effect of lubricant on the rubber friction can be appear in different forms such as frictional resistance due to the lubricant viscosity, change in the frictional resistance due to the change in lubricant viscosity, real area of contact and surface roughness reduction due to lubricant pool formation in the roughness valleys of harder, rough surface, formation of adhesion eliminating boundary layer, development of capillary forces, decreasing friction and increasing separation of contacting surfaces due to the increasing hydrodynamic effect, etc. An important consequence of the latter is the decreasing adhesive and micro hysteresis friction. At the same time while both the hydrodynamic effect and the closed fluid pools decrease the real (solid-solid) area of contact while the squeezing effect increases it.

Very little information is available in the literature on the effect of ambient temperature on apparently smooth steel surface generated micro-hysteresis. Studies of Mofidi et al. [44, 53] are exceptions of this. Their results show that the friction force for apparently smooth steel surface sliding on lubricated nitrile rubber decreases with increasing ambient temperature. Although the cylinder on flat sample test configuration was used in both cases, conditions were not exactly the same. As in [44] disc shaped NBR 75 Shore A specimens were used in [53] but the thickness was 6 mm instead of 4 mm. Additionally lubricating oil (polyol ester in [53] and polyalphaolefin in [44]), test duration (30 min in [53] and 15 min in [44]), mean sliding velocity (200 mm/s in [53] and 100 mm/s in [44]), stroke (2.5 mm in [53] and 1

mm in [44]), and applied normal load (200 N in [53] and 20, 50, 100, 150, 300 N in [44]) were also different. Mean sliding velocity of 200 mm/s implies that friction processes are complicated with frictional heat generation yielding real contact temperature higher than the ambient one. At the same time the higher velocity increases the frequency with which the rubber surface is excited. While the latter increases the former (higher contact temperature) decreases the micro-hysteresis, nevertheless, at room temperature, the apparent coefficients of friction reported by Mofidi et al. in [44] and [53] are consistent (they are close to 0.6). However, the decrease in apparent coefficient of friction due to an increase in the ambient temperature from 25°C to 80°C is much smaller in [53] than in [44] (see Figs. 4.31, 4.32 and 4.33). The small change in the apparent coefficient of friction (see Fig. 4.31) does not reflect the strongly temperature dependent properties of rubber. In other words, the temperature dependent micro-hysteresis, contrary to [44], has little contribution to rubber friction in [53]. It is worth to mention that while the apparent coefficients of friction measured at room temperature are similar, the ones observed at elevated temperature are drastically different in [53] and [44]. At room temperature the apparent coefficients of friction reported are in accordance with each other and indicate boundary lubrication. Unfortunately, in [44], no measurement results are available on the temperature dependency of apparent coefficient of friction for polyol ester. However friction test results of [44] show clearly that the apparent coefficient of friction is 0.66 for polyol ester and about 0.5 for polyalphaolefin at $T=40^{\circ}\text{C}$. Contrary to this significant difference in apparent coefficient of friction Mofidi et al. concluded that the lubricant has negligible influence on the friction in their tests. As it is demonstrated in Smith's book [8], the adhesion friction force is also lower at higher temperatures because both the hysteresis and adhesion component of rubber friction are directly related to viscoelastic properties of rubber. According to Grosch [1], the expected sliding velocity and temperature dependence of rubber friction under constant normal load and on a given surface can be described by a friction force-sliding velocity master curve and the Williams-Landel-Ferry (WLF) equation (see Appendix A.4). Consequently, the increasing ambient temperature decreases both the hysteresis and adhesion component of friction.

In [44], it is assumed that the friction measured is due to the internal friction (hysteresis) of the rubber and the drop in the apparent coefficient of friction for large loads (applied normal load ≥ 100 N) is most likely due to the increasing frictional heat generation caused by the internal friction in the rubber. The frictional heat fluxes (heat energy production per unit area and unit time) defined as $\mu \cdot p \cdot v$, where μ , p and v denote apparent coefficient of friction, mean contact pressure, and sliding velocity, however, do not support the increasing frictional heating because they are nearly equal for loads larger than or equal to 100 N. The cause of this is that the increasing mean contact pressure is accompanied by decreasing apparent coefficient of friction.

As the rubber has very low elastic modulus the friction force may be able to deform the rubber sample. This may cause that in certain part of the stroke the displacement of the rubber surface measured in sliding direction equals to that travelled by the cylinder (sticking phase). At high temperatures where the rubber has low modulus the effect of sticking on rubber friction may be particularly important. In order to prove this a simple, three-dimensional, linear elastic finite element model has been developed (see Fig. 4.34a). The bottom of the rubber sample was fixed while the displacement of the nodes being in the symmetry plane was restrained perpendicularly to the symmetry plane (symmetry condition). Like in friction tests of Mofidi et al. [44] the steel cylinder was pressed against the rubber sample with a given normal load (due to the half model only half of the applied normal load must be used in the FE model) and reciprocated with cyclic frequency of 50 Hz and amplitude of 0.5 mm. Normal load, apparent coefficient of friction and elastic modulus concerning excitation frequency of 50 Hz were specified based on [44]. Fig. 4.34b shows the x-position of the center point of the

rubber sample being in contact with the cylinder as a function of the x-position of the cylinder in the first cycle.

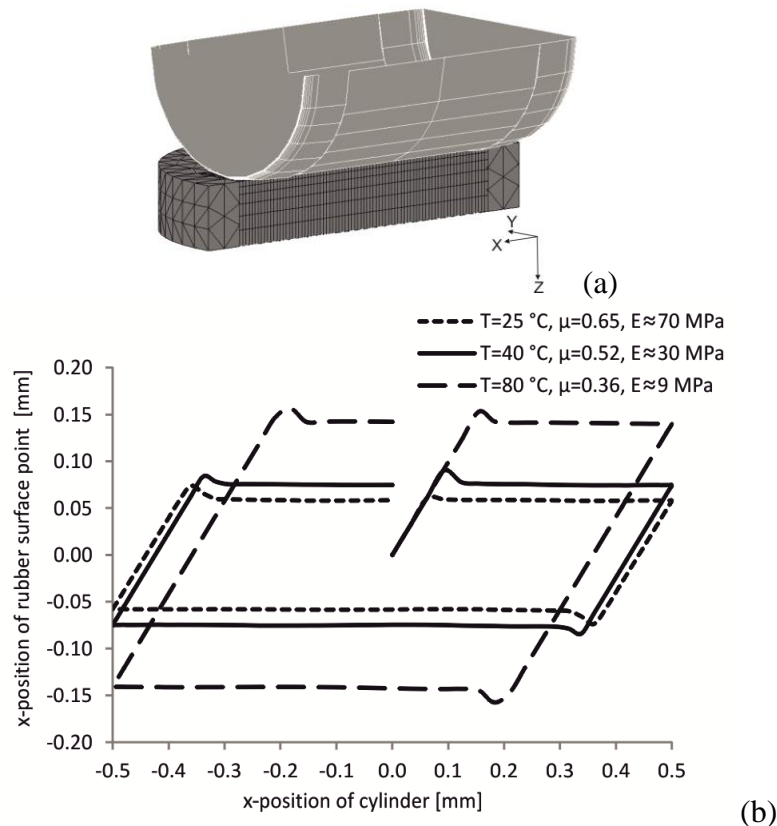


Fig. 4.34. (a) FE model of Mofidi et al.'s test configuration. Restraints are not visualized and due to the symmetry only half of the rubber disc is modeled. The figure is taken from [131]. (b) Position of the center point of rubber sample being in contact with the cylinder as a function of position of the cylinder. Applied normal load referring to the complete rubber sample is $F_N = 100$ N. The figure is taken from [131].

The FE results prove that the effect of sticking may be considerable, especially at higher temperatures where the modulus is very low. Based on these results not only the real sliding distance and real mean sliding velocity but the real frictional heat flux can also be determined. Finally, it is worth to mention that the sticking phase indicated by the simulation was the longest in the center point of the contact area.

As a last point, it must be mentioned that the effect of stresses and frictional heat generation on the mechanical properties of the rubber should also be considered when studying rubber friction. In [133], Mokhtari and Schipper pointed out that a tribo-modified surface layer with degraded elastic modulus exists on the top of a rubber surface being in contact with a rigid counter surface. Furthermore it was found that the thermal and stress-induced degradation of a thin rubber layer becomes more intensive as the contact pressure and sliding velocity increases. However, as demonstrated by Mokhtari et al. [134], excessive wear can prevent the formation of such layer. Additionally, it was also concluded that the degradation of rubber matrix at the surface does not affect the real area of contact but change the frictional shear stress required to shear a thin surface layer (adhesion component of rubber friction) and micro-hysteresis substantially.

4.4.4. Conclusions

Micro hysteresis component of rubber sliding friction generated by harder, apparently smooth track surfaces is studied here. Experimental and theoretical results of Mofidi et al. [44] obtained at room and elevated temperature suggest that the friction of nitrile rubber sliding on apparently smooth steel surface may be dominated by micro-hysteresis. These friction test results, however, were not compared with similar results taken from the literature. A possible reason for this is that the little experimental result available in this category (almost without exception) focuses on the room temperature behavior only. Here an attempt has been made to collect and analyze experimental results on micro-hysteresis generated by apparently smooth surfaces. Additionally, friction test results of Mofidi et al. [44] obtained at $T=25$ and 80°C has also been reanalyzed and compared to literature results. The apparent coefficient of friction decreased with increasing ambient temperature in all the cases but the change in friction was drastically different. In other words, the temperature dependent micro-hysteresis-based explanation of Mofidi et al. for the temperature dependency of apparent coefficient of friction is not of universal validity in case of apparently smooth surfaces. The contribution to the friction from the area of contact and rubber wear was not analyzed by Mofidi et al. [44], but due to the very unfavorable lubrication conditions it seems possible as well that the coefficient of friction measured is, at least in part, due to these phenomena. The present study shows clearly both the weak points of already existing friction tests and the need for a comprehensive testing program on the apparently smooth surface generated hysteresis contribution to rubber friction. Additionally it is found that none of experimental results discussed here proves the dominancy of micro-hysteresis for the sliding pair of Mofidi et al. and the real contribution of micro-hysteresis is likely considerably lesser than suggested in [44]. All of these prove that the role of micro-hysteresis is not fully understood for apparently smooth surfaces.

4.5. Numerical modeling of mixed friction of sliding rubber components using stochastic modeling approach

4.5.1. State of the art

Reciprocating rubber seals are commonly used viscoelastic machine elements, which, in many cases, operate in the mixed elastohydrodynamic lubrication (EHL) regime. As it is well known, in the mixed-EHL regime, both the hydrodynamic effect and the surface roughness contribute to the frictional effect characterized by the forces acting against the motion. In case of reciprocating rubber seals, the prediction of friction force, leakage rate (the difference between fluid transport during outstroke and instroke) and wear rate is the main motivation for modeling. In the field of numerical modeling of lubrication an intensive development was observable for both stochastic and deterministic modeling approach in the last few decades. Compared to lubrication between ideally smooth sliding surfaces the stochastic model proposed by Patir and Cheng [58] (it is termed PC model in the literature) for modeling lubrication between rough sliding surfaces brought a decisive improvement. In the PC model, the transition from smooth surface lubrication to rough surface one is solved by introducing flow factors in the Reynolds equation. These factors have been determined from separate deterministic models using elementary rough surfaces by Patir and Cheng [58]. Weak point of the PC model is that the three-dimensional surface topography is characterized by two parameters (surface descriptors) only. As reported by Czifra et al. [60] these parameters, namely the standard deviation of the profile heights (RMS roughness) and the roughness orientation, do not allow analysts to describe precisely the real micro-topography. Contrary to the stochastic modeling approach the deterministic one where rough surfaces are modeled as realistic as

possible provides more realistic localized (non-averaged) pressure/film thickness distribution and peak values (see studies of Ren et al. [61] and Minet et al. [62]). In this case, the main problem is the strongly limited area of modeled rough surfaces which is usually much smaller than the entire sealing zone. It must also be mentioned that the lubrication problem between rough sliding surfaces is essentially transient (time-dependent) due to the relative motion of the asperities in contact. The lubrication problem of rough surfaces, however, may be transformed into an equivalent stationary lubrication problem consisting of an ideally smooth surface being in motion with constant velocity and a rough surface (combination of the two rough surfaces) being at rest [41].

In the past decade, great effort was taken to develop numerical models for the analysis of mixed friction in reciprocating rubber components. In a recent paper of Salant et al. [41], a one-dimensional stochastic approach has been developed for rough surface mixed EHL in reciprocating rod seals. It is based on Greenwood and Williamson's contact model [27] and Patir and Cheng's stochastic lubrication model [58, 59]. On the contrary Persson and Scaraggi [63] use a very recent contact theory for the same purpose which was developed for the contact between a rigid solid with isotropic surface roughness on many different length-scales (self-affine fractal surface) and an elastic block with flat surface. The models consist of coupled fluid mechanics, deformation mechanics, and contact mechanics analyses. The fluid mechanical analysis deals with the solution of the Reynolds equation, while the deformation of rubber component is computed numerically through the use of influence coefficients (see Section 4.5.3 and the study of Salant et al. [41]) or analytically by applying the theory of elasticity (see study of Persson and Scaraggi [63]). Both mixed friction models take into consideration the effect of cavitation and consider the fluid to be Newtonian. Cavitation usually occurs in the regions of diverging gap where the gap between the contacting surfaces expands. Hydrodynamic pressure is achieved until the gap expands to a level where the lubricant does not occupy the complete gap and cavitates. In the cavitated region, a gas-lubricant mixture fills out the gap between contacting solid surfaces. The cavitation model in Salant et al.'s algorithm [41] assumes the conservation of the lubricant mass, the continuity and a constant contact pressure (cavitation pressure) i.e. a zero pressure gradient in the cavitated region. Due to the asperity type contact model incorporated in Salant et al.'s model it is possible to study both the full film and the mixed lubrication in reciprocating seals. In the case of full film lubrication, there is a continuous lubricating film with load carrying capacity between surfaces which does not make it possible for surfaces to come into direct, solid-solid contact. In such a case, the total normal load is carried by the lubricating film. Contrary to this, in mixed lubrication, the lubricating film is not able to separate surfaces from each other completely i.e. local solid contacts can be formed among asperities. As a consequence, one part of the normal load is carried by the lubricating film while the rest is carried by asperity contacts. The effect of asperity type contact on the friction force is taken into account by an empirical coefficient of friction in Salant et al.'s model [41].

4.5.2. Separation of nominally flat rough surfaces in contact: Greenwood-Williamson's contact theory vs. Persson's contact theory

When studying the contact between two nominally flat rough surfaces the separation is of primary importance. (The distance between the mean surface heights or mean planes of the nominally flat surfaces is referred to as the separation.) At the same time there is no consensus in the literature on how this separation should be computed. In this section, the frictionless static (non-sliding) contact between elastic, rough solids is studied using Greenwood and Williamson's and Persson's contact mechanical theories. The review of the theories is based on Greenwood and Williamson's and Persson's original papers.

Contact theory of Greenwood and Williamson [27] is one of the most well-known and the most frequently used theories of contact mechanics. As reported by Johnson [66] “in the frictionless contact of elastic solids the contact stresses depend only upon the shape of the gap between them before loading. The system may then be replaced by a flat, rigid surface in contact with a body having an effective modulus and a profile which results in the same undeformed gap between the surfaces” (Fig. 4.35a). The effective elastic modulus (composite contact modulus) E' is defined as

$$\frac{1}{E'} = \frac{1-\nu_1^2}{E_1} + \frac{1-\nu_2^2}{E_2}, \quad (4.3)$$

where 1 and 2 denote the one and the other surface. When highly elastic rubber-like material (denoted by 2) slides on hard surface $E' = E^*$ is approximately equal to $\frac{E_2}{1-\nu_2^2}$. In [27],

Greenwood and Williamson studies the contact between a rigid plane (rigid smooth surface) and a nominally flat rigid surface covered with large number of elastic asperities under the assumption that the summits of the asperities are spherical and have the same radius R and the height of the summits (z) varies randomly (Fig. 4.35b). In such a case, the normal force F_N acting on the rigid plane is supported by those asperities whose heights are greater than the separation, denoted by d , between the smooth rigid plane and the reference plane of the rough surface (mean surface height). The probability that a summit has a height between z and $z+dz$ above the reference plane of the rough surface is $\phi(z)dz$ where $\phi(z)$ is the probability density function.

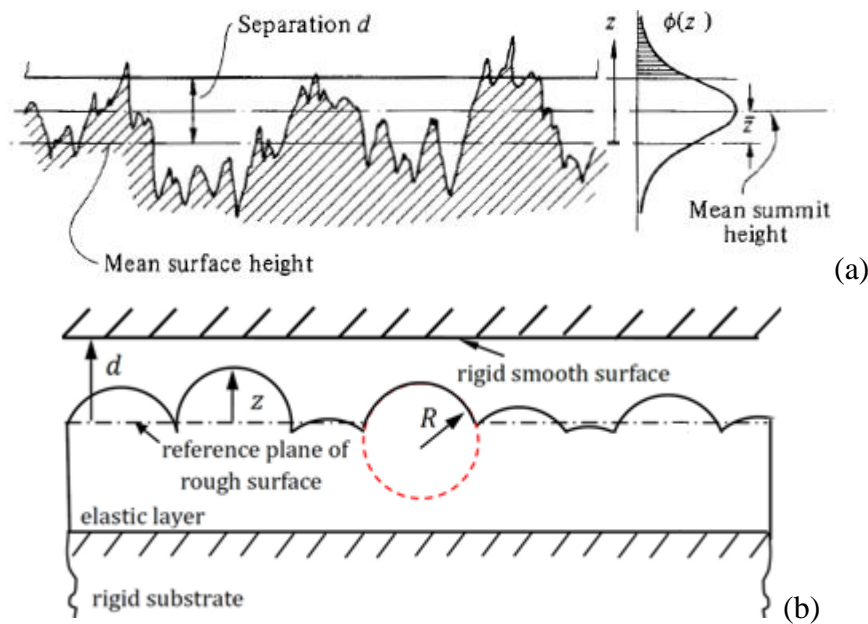


Fig. 4.35. (a) Contact of a rough surface with a smooth flat [66] (At the representation of the measured profile larger magnification is used in the normal than in the tangential direction.), (b) Greenwood and Williamson’s spherical asperity summits with a constant radius R [140]

The probability of making contact at any given summit of height z is [27]

$$prob(z > d) = \int_d^{\infty} \phi(z) dz, \quad (4.4)$$

while the expected number of summits in contact at a separation d is given by [27]

$$n = N \int_d^{\infty} \phi(z) dz. \quad (4.5)$$

In Eq. 4.5, N denotes the total number of asperities in the nominal or apparent contact area A_n . (Note: the correct form of Eq. 4.4 would be $prob(z > d) = \int_d^{\infty} \phi(z') dz'$ but as it has already been mentioned the equations are presented in the form in which they were originally reported.) If the i th summit height denoted by z_i exceeds the separation d then the i th summit is in contact with the rigid plane and is compressed by $\delta_i = z_i - d$. From the Hertz equation for the contact between a sphere and a flat rigid plate ($\delta = \frac{a^2}{R} = \left(\frac{9F_N^2}{16RE'^2} \right)^{1/3}$ where a is the radius of the contact area and F_N is the normal force) the circular contact area of the i th summit (A_i) and the force required to compress it (F_{Ni}) can be expressed as

$$A_i = a_i^2 \pi = \delta_i R \pi = (z_i - d) R \pi, \quad (4.6a)$$

and

$$F_{Ni} = \sqrt{\frac{16RE'^2 \delta^3}{9}} = \frac{4}{3} R^{1/2} E' \delta_i^{3/2} = \frac{4}{3} R^{1/2} E' (z_i - d)^{3/2}. \quad (4.6b)$$

The total real area of contact and the total normal force required to compress the asperities in contact may be determined by summing the contact areas and normal forces of all the asperities in contact. Thus the expected total real area of contact is given by [27]

$$A = N \int_d^{\infty} (z - d) R \pi \phi(z) dz = \pi N R \int_d^{\infty} (z - d) \phi(z) dz, \quad (4.7)$$

while the expected total normal load is [27]

$$F_N = N \int_d^{\infty} \frac{4}{3} R^{1/2} E' (z - d)^{3/2} \phi(z) dz = \frac{4}{3} N E' R^{1/2} \int_d^{\infty} (z - d)^{3/2} \phi(z) dz. \quad (4.8)$$

Introducing the surface density of asperities ($\chi = N/A_n$) and describing heights in terms of the standard (or RMS) deviation σ of the height distribution ($z/\sigma = s$ and $d/\sigma = h$) the total real area of contact A and the total normal load F_N can be written as [27]

$$A = \pi \chi A_n R \sigma F_1(h), \quad (4.9)$$

and

$$F_N = \frac{4}{3} \chi A_n E' R^{1/2} \sigma^{3/2} F_{3/2}(h), \quad (4.10)$$

where A_n is the nominal contact area and

$$F_1(h) = \int_h^{\infty} (s - h) \phi^*(s) ds \quad (4.11)$$

$$F_{3/2}(h) = \int_h^{\infty} (s-h)^{3/2} \phi^*(s) ds. \quad (4.12)$$

In the equations, $\phi^*(s)$ denotes the normalized height distribution. If the rough surface has Gaussian height distribution, then $\phi^*(s) = \frac{1}{\sqrt{2\pi}} e^{-\frac{s^2}{2}}$ [27]. Using these results the nominal contact pressure can be expressed as

$$p = \frac{F_N}{A_n} = \frac{4}{3} \chi E' R^{1/2} \sigma^{3/2} F_{3/2}(h). \quad (4.13)$$

The latter equation can be used to compute the relation between nominal contact pressure p and normalized separation h .

Persson's contact mechanical theory [3] was originally developed for the contact of a rigid isotropic rough surface having fractal nature and a smooth rubber (viscoelastic) block. One of the most important characteristics of Persson's theory is that the rough surface considered has surface roughness on many different length-scales λ (asperities at multiple scales) which can be described by the surface roughness spectral density $C(q)$ where q denotes the magnitude of the wavevector ($q = 2\pi/\lambda$) i.e. the spatial angular frequency or the wave-number of the wave. In other words, for isotropic rough surfaces not the direction of the wave vector is important but its magnitude. Persson [3] assumed that between q_0 and q_1 the rough surface is a self-affine fractal surface with fractal dimension D_f (q_0 is the lower cut-off wavenumber and q_1 is the upper cut-off wavenumber) whose surface roughness spectral density can be approximated in the following form

$$C(q) \cong \frac{H}{2\pi} \left(\frac{h_0}{q_0} \right)^2 \left(\frac{q}{q_0} \right)^{-2(H+1)} = \frac{H}{\pi} \frac{h_{RMS}^2}{q_0^2} \left(\frac{q}{q_0} \right)^{-2(H+1)}, \quad (4.14)$$

where H is the Hurst exponent ($H = 3 - D_f$) and $h_0^2/2 = h_{RMS}^2$. $h_{RMS} \equiv \sigma$ denotes the RMS roughness of the rough surface ($h_{RMS}^2 = \frac{1}{N} \sum_{i=1}^N z_i^2$, where N is the total number of heights sampled and z_i is the i th height measured from the mean surface). Furthermore it was also assumed that there exists a roll-off wavenumber below which surface roughness spectral density is approximately constant (see Fig. 4.36 taken from Yang and Persson [67]). As it can be seen for a self-affine fractal surface the surface roughness spectral density has power-law behavior i.e. surface roughness spectral density is proportional to $q^{-2(H+1)}$ [67]. The computation of the surface roughness spectral density for measured surface height profiles is detailed in Appendix B. In order to investigate the surface roughness on many different length-scales rough surfaces are studied at different magnification ζ ($\zeta = q/q_0 = \lambda_0/\lambda$ where λ_0 is the roll-off wavelength of the surface roughness spectral density) in Persson's contact theory [3]. When the magnification is high, the surface is quite rough because there are many short-wavelength roughnesses as demonstrated by Yang and Persson [67]. When the magnification is low, the small scale components of surface roughness do not appear in the surface height profile thus the surface seems much smoother (see Fig. 4.37). Generally speaking, when a rough surface is studied at given magnification the surface is considered to be smooth on all length-scales shorter than λ .

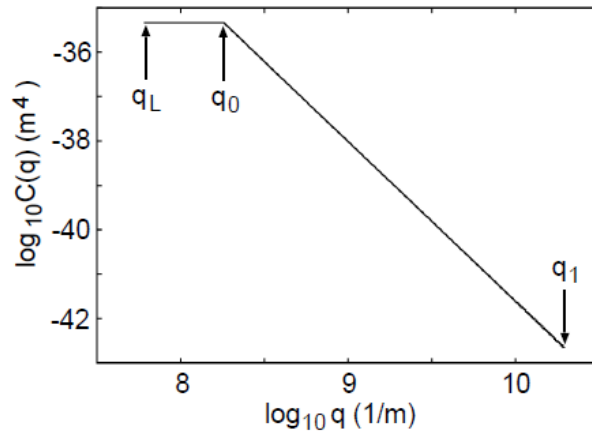


Fig. 4.36. Surface roughness spectral density ($C(q)$) of a self-affine fractal surface. q_L is the smallest surface roughness wavenumber. [67]

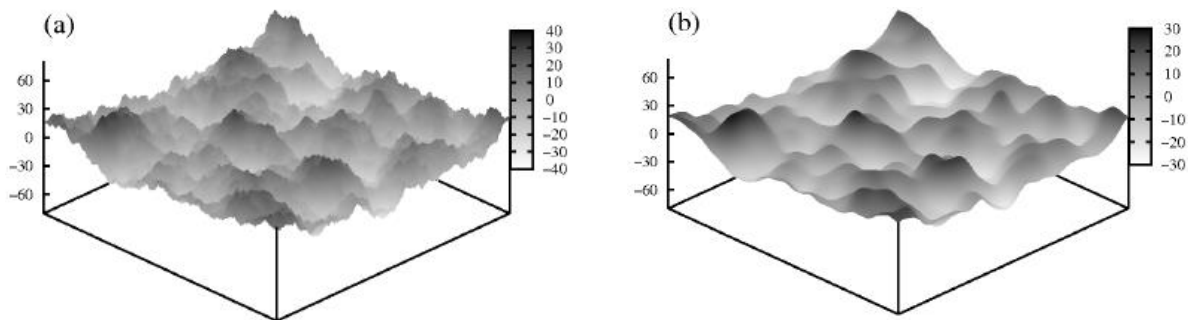


Fig. 4.37. Surface height profile of a mathematically generated self-affine fractal surface ($104 \times 104 \text{ nm}^2$ square surface area) with the root mean square (RMS) roughness of 1 nm : (a) high magnification ($\zeta = 216$), (b) low magnification ($\zeta = 4$) [67]

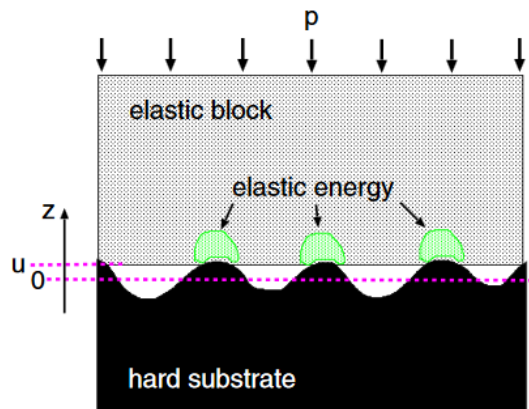


Fig. 4.38. An elastic block squeezed against a rigid rough substrate. The separation and the applied squeezing pressure are denoted by u (with $u \geq 0$) and p , respectively. In case of complete contact, $u = 0$ and $p = \infty$ [65].

The contact problem of an elastic block with a flat surface squeezing against a hard self-affine fractal surface (Fig. 4.38) is studied by Persson [3, 65], where the separation of contacting surfaces is denoted by u and is defined as the distance between the block and the mean plane (mean surface height) of the counter surface [67]. As it has already been mentioned this contact problem is equivalent with the one when two elastic solids with rough surfaces are squeezed together. Persson [67] assumes that the separation depends on the squeezing pres-

sure (as the applied squeezing pressure increases the separation between the surfaces decreases) and the elastic energy stored in the hard asperity-elastic block contact regions is equal the work done by the external pressure in displacing the lower surface of the block towards the rough counter surface, i.e. $\int_u^\infty p(u')A_0 du' = U_{el}(u)$ or $p(u) = -\frac{1}{A_0} \frac{dU_{el}}{du}$, where A_0 is the nominal contact area and $U_{el}(u)$ is the separation dependent elastic energy stored in the contact regions.

According to these there must be an interrelation between the elastic energy stored in the contact regions and the (separation dependent) applied squeezing pressure. In other words, if the dependence of the surface separation on the squeezing pressure is known then one can obtain the elastic energy stored in the asperity contact regions. In [65], Persson concluded that the elastic energy stored in the contact regions, in the simplest approximation, takes the form

$$U_{el} \approx A_0 E^* \frac{\pi}{2} \gamma \int_{q_0}^{q_1} q^2 P(q) C(q) dq, \quad (4.15)$$

where E^* is the effective elastic modulus ($E^* = E/(1-\nu^2)$), $P(q)$ is the relative area of real contact when the interface is studied at magnification ζ ($P(q) = A(\zeta)/A_0$, where $A(\zeta)$ denotes the real area of contact at a given magnification), and $C(q)$ is the surface roughness spectral density (see Appendix B). For perfect contact (high squeezing pressures) $P=1$ and, with $\gamma=1$, Eq. 4.15 is exact. For low squeezing pressures the parameter γ in Eq. 4.15 takes into account that the elastic energy stored in the contact region (per unit surface area), in general, is less than the average elastic energy (per unit surface area) for perfect contact. In case of elastic nonadhesive contact, the relative area of real contact may be written as [3]

$P(q) = \frac{2}{\sqrt{\pi}} \int_0^{s(q)p} e^{-x^2} dx$, where $s(q) = w(q, q_0)/E^*$ with

$$w(q, q_0) = \left(\pi \int_{q_0}^q q'^3 C(q') dq' \right)^{-1/2}, \quad (4.16)$$

and $\frac{\partial P}{\partial u} = \frac{2}{\sqrt{\pi}} s \frac{dp}{du} e^{-s^2 p^2}$. Combining $p(u) = -\frac{1}{A_0} \frac{dU_{el}}{du}$ with the equation for U_{el} and subse-

quently with the one for $\frac{\partial P}{\partial u}$ the applied squeezing pressure dependency of the separation may be written as [65]

$$u = \sqrt{\pi} \gamma \int_{q_0}^{q_1} \left[q^2 C(q) w(q, q_0) \int_p^\infty \left(\frac{1}{p'} e^{-[w(q)p'/E^*]^2} \right) dp' \right] dq. \quad (4.17)$$

In [65], Persson noted that the results of his theory differ drastically from those of Greenwood and Williamson's theory and the latter does not correctly describe the interfacial separation between contacting rough solids. However [65] does not quantify the difference therefore it is very difficult to imagine how big it is and how this difference depends on the contact pressure. At the same time the comparison is difficult because the two different contact models are based on different input parameters (surface descriptors). From scientific point of view such a comparison is of great importance because both contact models are widely used in the prediction of lubrication performance of sliding rubber components. Greenwood-Williamson's and Persson's contact theories have been compared quantitatively in a recent study of Bódai and Goda [64], where the separation (between an elastomer plate and a rigid flat) as a function of the applied squeezing pressure has been computed using the authors'

home-made computer code. The code was implemented in C++ and verified through the contact problem studied by Persson [65]. Computational results obtained by numerical integration had been compared to those of Persson and excellent agreement was found. When calculating with Persson's theory surface descriptors reported by Persson and Scaraggi [63] were used (RMS roughness is $1\mu\text{m}$, fractal dimension is $D_f = 2.2$, surface roughness is self-affine fractal for $q_0 < q < q_1$, where the lower wavenumber is $q_0 = 10^4 \text{ 1/m}$ and the upper one is $q_1 = 0.78 \cdot 10^{10} \text{ 1/m}$, Young modulus is $E = 10 \text{ MPa}$, Poisson's ratio is $\nu = 0.5$, $\gamma = 1$). The parameter γ shows the ratio of the elastic energy stored in the asperity contact regions (per unit surface area) and the average elastic energy (per unit surface area) for perfect contact [65]. In case of GW model, statistical parameters reported by Salant et al. [41] were used: RMS roughness is $1\mu\text{m}$, asperity radius is $R = 1\mu\text{m}$, asperity density is $\mu = 10 \cdot 10^{13} \text{ m}^{-2}$. The results are shown in Fig. 4.39 for nominal contact pressure ranging from 0.001 MPa to 2 MPa . Based on Fig. 4.39, it can be concluded that the difference in separation (distance between the mean plane of a nominally flat rough surface and a smooth flat) varies between one and four orders of magnitude if the nominal contact pressure is between 0.1 and 1 MPa . Additionally, the difference becomes smaller and smaller as the contact pressure decreases. This huge difference in the separation draws attention to the necessity of experimental testing of contact theories. At present the reliability of these contact theories is still an open question.

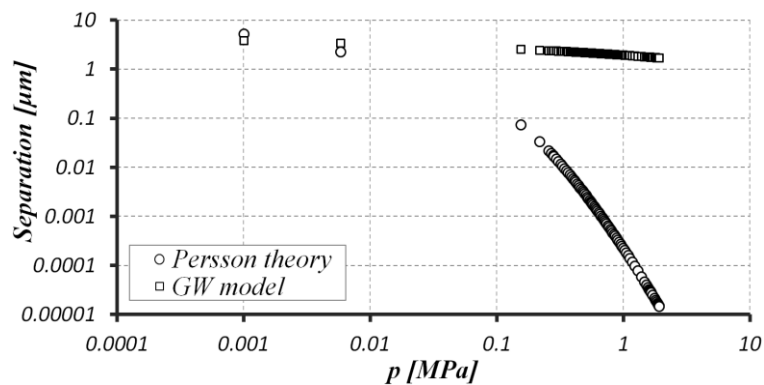


Fig. 4.39. Separation of contacting surfaces as a function of nominal contact pressure (applied squeezing pressure) in case of two different contact theories [64]

From application point of view it is extremely important to know the limitations of the contact theories used. As a last point, an attempt is made here to describe briefly the most important assumptions and limitations of the theories studied. Persson's contact theory has been developed for the contact between a rigid solid with isotropic surface roughness on many different length-scales (self-affine fractal surface) and an elastic block with flat surface. It is valid for surface roughness with translational and rotational invariant (i.e. isotropic) statistical properties only where 1D surface roughness spectral densities are independent of the location and direction of line scans. In [3], Persson developed a model based on his contact theory for the prediction of viscoelastic friction force generated by the surface roughness. From the characteristics of Persson's contact theory, however, it is clear that his viscoelastic friction theory results in sliding direction independent real area of contact and micro hysteresis friction force. In [50], Carbone et al. realized that many surfaces of practical interest have surface roughness with anisotropic statistical properties and sliding direction dependent frictional properties. In order to treat sliding direction dependency of rubber friction the authors extended Persson's theory to surfaces with anisotropic surface roughness. They pointed out that the micro hysteresis friction contribution may depend significantly on the sliding direction (in case of sliding friction orthogonal to the wear tracks the energy dissipation-based hys-

teresis friction is significantly higher than along them), while the real area of contact depends weakly on the sliding direction. On a uniaxial polished steel surface the real area of contact was a bit larger when sliding along the direction of the wear tracks than when sliding orthogonal to the wear tracks. The latter implies that adhesion component of rubber friction depends weakly on the sliding direction as the adhesive friction is a real area of contact related phenomenon. They carried out friction tests for rubber blocks sliding on dry unidirectionally polished steel surfaces at sliding velocity of 0.2 mm/s (negligible frictional heat generation) and found a good qualitative (but no quantitative) agreement between the experiment and the theory. It is also known that Persson's surface roughness spectral density-based modeling approach considers the multi-scale nature of engineering surfaces (asperities at multiple scales) but is developed for self-affine fractal surfaces only. For real engineering surfaces, however, the assumption of fractal nature (scale- or magnification-dependent surface roughness) is an approximation only. Furthermore the theory is not able to model real asperity geometry accurately. It has been pointed out by Czifra et al. [60] that the fractal dimension, which measures the complexity of the rough surface and characterizes the change in surface roughness with change in scale at which it is measured, does not characterize uniquely the surface finishing technique with which the surface is manufactured. In other words, fractal dimensions may be very similar even if they belong to two different surface finishing techniques. Consequently, rough surfaces with drastically different asperity geometry may have the same or very similar surface roughness spectrum. In the GW contact theory, the same radius of curvature is assigned to each asperity tip which is equal to the average radius of curvature of asperities of measured surface topography. The local asperity deformations are taken into account through the Hertz theory which implies that each asperity deforms independently of the neighboring asperities (interaction between laterally spaced asperities is neglected) and can be modeled as a spring having nonlinear force-body approach characteristic. Another weakness of the theory is that the multi-scale nature of rough surfaces is considered by a two-scale model where the longer wavelength waviness is taken into consideration through the height distribution of the smaller asperity tips (fine scale asperities). As it is known from the literature the Greenwood-Williamson statistical contact model can be modified in various ways if the Hertz-theory is replaced with another asperity deformation model. At this point it must be mentioned that the GW contact model is based on statistical parameters extracted from measured surface topography. These are the asperity density (χ), the RMS roughness (σ), and the asperity radius of curvature (R). In [68], however, it has been pointed out that both R and χ are quite sensitive to the choice of resolution (sampling length divided by the number of data points). The authors of [68] cite studies from the literature which prove that the choice of sampling resolution can bias the statistical parameters. Finally, it is worth to mention that the RMS roughness of the rough surface is dominated by the components of larger wavelength, thus small scale components have minor effect on it.

4.5.3. Salant et al.'s stochastic mixed friction model and its implementation

Overall aim of this chapter is to summarize briefly Salant et al.'s [41] stochastic mixed friction model and its implementation. The numerical model has been implemented in Visual C++ (**Mixed Friction Code for Hydraulic Reciprocating Rod Seals** or MFCforHRRS) by Goda [69]. The numerical model takes into consideration the effect of surface roughness, deformation of seal, pressure dependency of viscosity and cavitation, respectively. As an asperity type contact theory is incorporated into the model it can be used not only for full film but also for mixed lubrication. Typical outputs of the numerical simulation are the pressure distribution within the lubricating film, the amount of fluid flow transport during outstroke and

instroke (their difference defines the amount of leakage) and the magnitude of the apparent coefficient of friction.

As it is well known, the load carrying capacity can be built up in a hydrodynamic seal from the wedge-film and the squeeze-film actions. For the wedge-film action, among others, a relative tangential velocity between contacting surfaces while for the squeeze-film action a decreasing gap due to the normal approach of surfaces has to be existed. The pressure distribution in a thin viscous fluid film can be described by the classical Reynolds equation. Assumptions used in derivation of the classical, one-dimensional Reynolds equation are as follows. (a) The lubricant's flow is laminar. (b) The temperature is constant (isothermal case). (c) Contacting surfaces are rigid. (d) The lubricant is Newtonian, and the viscosity is constant across the lubricant film. (e) Inertial forces are small and can be neglected. (f) The weight of the lubricant can be neglected relative to other forces. (g) There is no slip at the lubricant/solid interface i.e. the lubricant adheres to the solid surfaces. (h) The film thickness is small. (i) The pressure across the film (in radial direction) and in the direction perpendicular to the sliding direction is constant. (j) Side-leakage is negligible. (k) The mass is conserved. Using these assumptions, the one-dimensional Reynolds equation governing the pressure in the lubricant film for compressible lubricant and at a given temperature can be written as [76]

$$\frac{\partial}{\partial x} \left(\frac{\rho \cdot h_T^3}{12 \cdot \eta} \frac{\partial p}{\partial x} \right) = \frac{1}{2} \frac{\partial}{\partial x} (\rho \cdot U \cdot h_T) + \frac{\partial}{\partial t} (\rho \cdot h_T), \quad (4.18)$$

where ρ is the lubricant's density which can be a function of pressure, h_T is the local film thickness ($h_T = h + \delta_1 + \delta_2$, where h is the local nominal film thickness and δ_1, δ_2 is the roughness profile (height of the surface) measured from the mean level (mean height) of surface profiles 1 and 2 as seen in Fig. 4.40), η is dynamic viscosity of the lubricant which can also be a function of pressure, p is the pressure in the lubricant film, x is the coordinate in axial or sliding direction, U is the relative tangential velocity and t is the time. If the lubricant is considered as incompressible, i.e. its density does not depend on the magnitude of the pressure, then the ρ can be eliminated from the Reynolds equation. In addition, if the tangential velocity is set to zero, then we obtain an ordinary differential equation that governs the squeezing of the lubricant in axisymmetric seals.

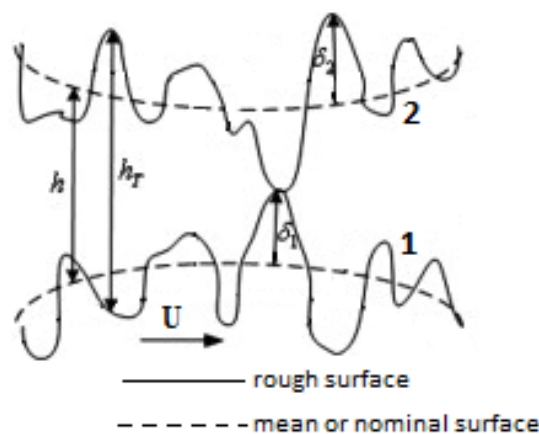


Fig. 4.40. Contact of rough surfaces (based on [141])

The steady state form of Eq. (4.18) i.e. when the film thickness does not varies in function of time, can be written as [76]

$$\frac{d}{dx} \left(\rho \cdot h_T^3 \frac{dp}{dx} \right) = 6 \cdot U \cdot \eta \frac{d(\rho \cdot h_T)}{dx}, \quad (4.19)$$

Eq. (4.19) is valid for large stroke length where the operational conditions do not vary during the stroke. It can also be used for the case when one of the contacting surfaces is considered to be rough (as it is the case in [41]) if the coordinate system is attached to the rough stationary surface. For an incompressible lubricant with pressure dependent viscosity the steady-state Reynolds equation has the form [76]

$$\frac{d}{dx} \left(h_T^3 \cdot e^{-\alpha \cdot p} \frac{dp}{dx} \right) = 6 \cdot U \cdot \eta_0 \frac{dh_T}{dx}, \quad (4.20)$$

where η_0 is the dynamic viscosity at ambient pressure and the pressure dependency of viscosity is given by the Barus formula ($\eta(p) = \eta_0 \cdot e^{\alpha \cdot p}$). α is the pressure-viscosity coefficient. Patir and Cheng [58] have performed numerical flow simulations for rough surfaces in order to obtain an averaged Reynolds equation which takes into consideration the effect of surface roughness on the lubricant flow through pressure and shear flow factors. These surface roughness specific flow factors depend on the directionality of the surface topography of mating surfaces and the nominal film thickness and characterize both the pressure induced fluid transport (pressure flow factors in the sliding direction and in the transverse direction) and the shearing effects (entrainment) induced fluid transport (shear flow factor). At the computation of the pressure flow factors the rough mating surfaces are considered to be stationary (surfaces without relative tangential displacement) with a macro-scale pressure gradient in the sliding direction and in the transverse direction. For instance, the pressure flow factor in the sliding direction can be found if the macro-scale pressure gradient is in the same direction and the average flow rate of mating rough surfaces with given separation is compared to that of idealized smooth surfaces with the same separation. For rough surfaces the average lubricant flow rate is a function of the local film thickness while, for idealized smooth surfaces, it is expressed as a function of the nominal film thickness and the flow factor. The flow factor can be determined from the condition that the average lubricant flow rate for these two cases must be the same. In other words, Patir and Cheng's "average flow model" replaces the flow between rough surfaces with an averaged flow between nominally smooth surfaces where the effect of surface roughness is taken into consideration through flow factors. The one-dimensional form of Patir and Cheng's average (ensemble-averaged) Reynolds equation valid for incompressible lubricant with pressure dependent viscosity can be written as [58]

$$\frac{d}{dx} \left(\phi_x \cdot h^3 \cdot e^{-\alpha \cdot \bar{p}} \frac{d\bar{p}}{dx} \right) = 6 \cdot \eta_0 \cdot U \left(\frac{d\bar{h}_T}{dx} + \sigma \frac{d\phi_{scx}}{dx} \right), \quad (4.21)$$

where ϕ_x is the non-dimensional pressure flow factor, \bar{p} is the average pressure, \bar{h}_T is the average gap or average film thickness (equals the expected or mean value of local film thickness h_T), σ is the RMS roughness, h is the local nominal film thickness defined as the distance between the mean levels of rough surfaces and ϕ_{scx} is the non-dimensional shear flow factor. In the studies of Patir and Cheng [58, 59], the flow factors have been expressed as empirical relations in terms of film thickness, RMS roughness and the length-to-width ratio of a representative asperity of a Gaussian surface. Patir and Cheng's average Reynolds equation is widely applicable since (a) instead of modeling rough surfaces deterministically the expected lubricant flow is predicted based on the separation only, the surface statistics and the operating conditions, and (b) the flow factors can be evaluated numerically for any rough surface.

The asperity scale and the macroscopic scale cavitation were incorporated into Patir and Cheng's average Reynolds equation by Harp and Salant [142]. In Harp and Salant model [142] (average Reynolds equation for cavitation), the asperity scale lubricant cavitation (inter-asperity cavitation) is induced by divergences associated with the roughness while the macroscopic cavitation is induced by the nominal divergence of mating surfaces and extends over a significant number of asperities. The dimensionless form of Eq. (4.21) valid for both cavitated and noncavitated lubricant flow between a stationary rough and a sliding perfectly smooth surface (dimensionless universal average Reynolds equation) is written by Salant et al. [41] as

$$\frac{d}{d\hat{x}} \left(\phi_x \cdot \hat{h}^3 \cdot e^{-\hat{\alpha} \cdot F \cdot \phi} \frac{d(F \cdot \phi)}{d\hat{x}} \right) = 6 \frac{\eta_0 \cdot U \cdot L}{p_a \cdot \sigma^2} \left(\frac{d}{d\hat{x}} \{ [1 + (1 - F)\phi] \cdot H_T \} + F \cdot \frac{d\phi_{scx}}{d\hat{x}} \right), \quad (4.22)$$

where \hat{x} is the dimensionless axial coordinate ($\hat{x} = \frac{x}{L}$, where L is the length of the solution domain in x- or axial direction), \hat{h} is the dimensionless local nominal film thickness ($\hat{h} = \frac{h}{\sigma}$), $\hat{\alpha}$ is the dimensionless pressure-viscosity coefficient ($\hat{\alpha} = \alpha \cdot p_a$), p_a is the ambient pressure, H_T is the dimensionless average (or expected) local film thickness ($H_T = \int_{-\hat{h}}^{\infty} (\hat{h} + \delta) f(\delta) d\delta$, where $f(\delta)$ denotes the probability density function of roughness [41]. H_T equals dimensionless local nominal film thickness if not in contact), F is the cavitation index and ϕ is an universal variable which has different interpretation in the liquid region and the cavitated region. In case of cavitation, it is assumed that only a fraction of the space between the mating surfaces is occupied by the lubricant; the rest is occupied by air pockets. Thus the average density in the cavitation zones is less than the density in the noncavitating zones. In the liquid (noncavitating) region,

$$\phi \geq 0, \quad F = 1, \quad \frac{P}{p_a} = F \cdot \phi, \quad (4.23)$$

where ϕ can be interpreted as dimensionless fluid pressure. In the cavitated region,

$$\phi < 0, \quad F = 0, \quad \frac{\rho}{\rho_c} = 1 + (1 - F)\phi, \quad (4.24)$$

where ρ is the density of the fluid-gas mixture, and ρ_c is the density of the fluid at cavitation pressure. The ratio $\frac{\rho}{\rho_c}$ can be interpreted as fractional film content. If the cavitation index is equal to zero, then Eq. (4.22) reduces to an expression of mass conservation with variable density. Three types of boundary conditions are used during the numerical solution of Eq. (4.22). If $\phi < 0$ ($\frac{\rho}{\rho_c} < 1$) and $F=0$ at the boundary the domain is termed starved, if $\frac{P}{p_a} = 1$ and $F=1$ the domain is flooded, and if $\frac{P}{p_a} > 1$ and $F=1$ the domain is pressurized.

In the model implemented, Eq. (4.22) is discretized and solved by iteration for ϕ and F using the control volume finite difference scheme of Patankar [143]. At the beginning of the iteration it is assumed that there is no cavitation inside the solution domain and the pressure is equal to the atmospheric pressure at these locations. The numerical model developed can be used for real reciprocating seals because, as it can be seen in the flow chart of the model (Fig. 4.40), it is able to take into account the effect of elastic deformation of the seal on the film

thickness and the flow factors. The reason why iteration is needed is that the pressure field induces elastic deformations in the seal that directly influence the film thickness. At the same time, the latter modifies the Reynolds equation used for the computation of a new pressure field. Additionally, two inner iterations are needed to calculate the locations of the cavitated regions and to handle non-linearity caused by pressure-dependent viscosity. In the latter case, the cause of iteration is that one wants to calculate pressure distribution at a given film thickness on the basis of the Reynolds equation which consists of a pressure-dependent viscosity. In order to determine the film thickness distribution, it is necessary to compute the elastic deformation of the rubber component normal to the common surface tangent. Like in [41] the influence coefficient method has been chosen for this purpose. This method states that the deformation at any location within the nominal contact area is proportional to the forces applied at every location. The “influence coefficients” are collected in the influence coefficient matrix (I). Coefficient I_{ik} of the matrix shows the normal displacement at the i th node due to a force (F) (corresponding to a unit pressure) applied at the j th node. Elements of the influence coefficient matrix were computed using a separate FE model.

The computational procedure shown in Fig. 4.41 can be summarized as follows. The computational scheme starts with the computation of the length of the sealing zone (nominal contact area) and the static contact pressure distribution by using the finite element method. Here it is assumed that the frictional stress or frictional traction (friction force per unit area) has little effect on the contact pressure distribution. Consequently the contact pressure distribution, which will be divided into fluid and asperity type contact pressure distribution, is determined for the frictionless case only (static contact pressure). Then the influence coefficients (elements of the influence coefficient matrix) are computed in a separate FE model. These FE models are not involved directly in the iterative computational procedure; they are used to provide input data for it only. The FE computations are followed by contact calculations (see Greenwood-Williamson contact model) to determine the static film thickness distribution that is also input data for the iterative procedure. The iterative computational procedure starts with an initial guess for the film thickness. Then the contact/fluid pressure distribution and the film thickness distribution are computed based on iterative scheme. When the converged solution is reached the iteration is stopped. Finally, the leakage rate and the average frictional stress are computed. In case of negligible fluid acceleration, there is no net force in axial (x-) direction i.e. the pressure forces and shear viscous forces acting on an infinitesimal volume of fluid equate each other. Substitution of Newton’s definition of viscosity into the equilibrium equation yields a differential equation for the relation between fluid pressure distribution and velocity distribution in (across) the fluid film. As the fluid velocity does not vary in circumferential direction the volumetric flow rate per unit circumferential length (q) can be computed by integrating the velocity distribution over the film thickness. Consequently, the nondimensional volumetric flow rate per unit circumferential length ($\hat{q} = 12\eta_0 q L / (p_a \sigma^3)$) or the instantaneous leakage can be found from (see [41])

$$\hat{q} = -\phi_x \cdot \hat{h}^3 \cdot e^{-\hat{\alpha} \cdot F \cdot \phi} \frac{d(F \cdot \phi)}{d\hat{x}} + 6 \frac{\eta_0 \cdot U \cdot L}{p_a \cdot \sigma^2} \left([1 + (1 - F)\phi] \cdot H_T + F \cdot \phi_{scx} \right). \quad (4.25)$$

The first term is the contribution of the pressure difference to the flow rate (pressure flow) while the second term is the contribution due to the shear flow, dragged by the moving rod.

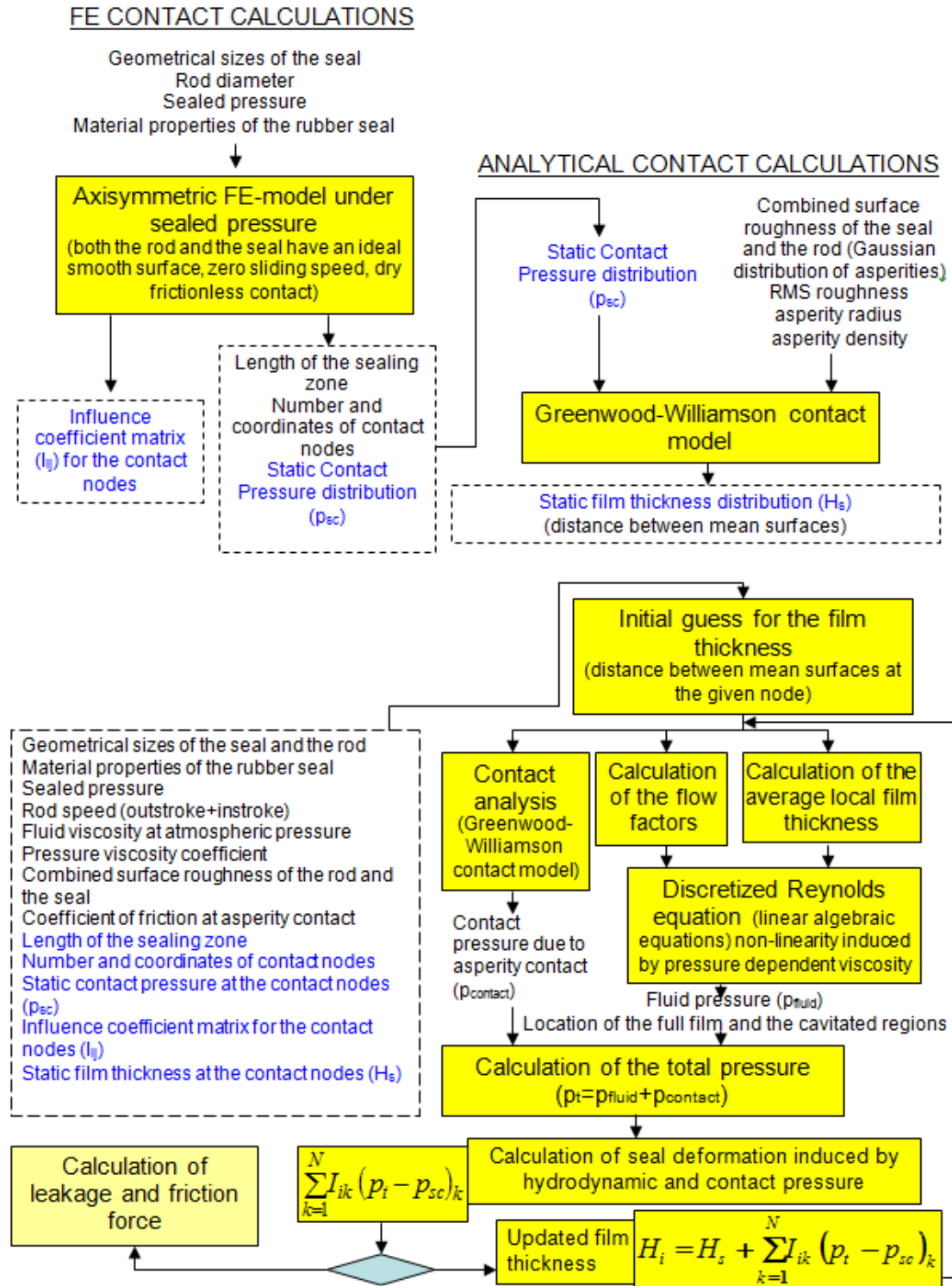


Fig. 4.41. Flow chart of the computational scheme [69]

The total frictional stress on the rod is the sum of the average viscous shear stress and the shear stress due to contacting asperities (see [41]).

$$(\hat{\tau}_{avg})_{total} = (\hat{\tau}_{avg})_{viscous} + (\hat{\tau})_{contact}, \quad (4.26)$$

where $(\hat{\tau}_{avg})_{total}$ is the dimensionless total frictional stress, $(\hat{\tau}_{avg})_{viscous}$ is the dimensionless average viscous shear stress ($(\hat{\tau}_{avg})_{viscous} = (\tau_{avg})_{viscous} / E$), and $(\hat{\tau})_{contact}$ is the dimensionless shear

stress due to contacting asperities ($(\hat{\tau})_{contact} = (\tau)_{contact} / E$). The dimensionless average viscous shear stress is

$$(\hat{\tau}_{avg})_{viscous} = -\frac{\hat{\sigma}}{\xi} \cdot e^{-\hat{\alpha} \cdot F \cdot \phi} \frac{\eta_0 \cdot U \cdot L}{p_a \cdot \sigma^2 \hat{h}} (\phi_f - \phi_{fss}) - \phi_{fpp} \frac{\hat{\sigma} \hat{h}}{\xi} \frac{d(F\phi)}{d\hat{x}} \quad (4.27)$$

where $\hat{\sigma}$ is the dimensionless RMS roughness ($\hat{\sigma} = \sigma R^{1/3} \chi^{2/3}$ where R denotes the asperity radius and χ denotes the asperity density), $\xi = R^{1/3} \chi^{2/3} EL / p_a$, and ϕ_f , ϕ_{fss} , ϕ_{fpp} are the shear stress factors to take into consideration the influence of the roughness on the viscous shear. The shear stress factors can be obtained numerically as described in the work of Patir and Cheng [59]. Finally, the dimensionless shear stress due to contacting asperities can be computed using an empirical coefficient of friction μ as

$$(\hat{\tau})_{contact} = -\mu P_c \left(\frac{U}{|U|} \right), \quad (4.28)$$

where P_c denotes the dimensionless contact pressure ($P_c = p_c / E$, where E is the elastic modulus of the rubber seal). Based on the numerical model presented above a computer code has been developed and implemented by Goda [69]. Main objective of the next chapters is to present briefly the verification problems with which the reliability of the code can be proved.

4.5.4. Verification problem: Ideal smooth flat surface in contact with combined sinusoidal/flat surface

The first verification problem is taken from the study of Sahlin et al. [70]. Fig. 4.42a shows the geometry of the contacting bodies examined. The stationary surface can be divided into two parts: its left half is a sinusoidal wave while its right half is an ideal smooth horizontal plane which is parallel to the ideal smooth counterpart with velocity of $U=0.25$ m/s=250 mm/s. Both the inlet and the outlet of the solution domain are flooded that is the cavitation index is $F=1$ and the pressure is equal to the atmospheric pressure at these locations. The wavelength of the sinusoidal wave is 10 mm while its amplitude is $5 \mu m$. In the numerical simulations, the cavitation pressure is assumed to be 0.1 MPa that is equal to the ambient or atmospheric pressure. In [69], the same problem was studied by Goda using his computer code. Fig. 4.42b shows Goda's [69] numerical results for the pressure distribution if the dynamic viscosity of the lubricant at atmospheric pressure is $\eta_0=0.04$ Pas and the pressure-viscosity coefficient is $\alpha=20 \cdot 10^{-9}$ 1/Pa. The solution domain was divided into equidistant control volumes. Altogether 201 grid points were located along the solution domain implying that the distance between two neighboring grid points is 0.5 mm. In order to obtain a grid independent solution computations were repeated with finer discretization, where the number of grid points was 401 and 801, respectively. Since both bodies are considered as ideal smooth, their RMS roughness is set to be three orders of magnitude smaller than the double of the amplitude of the sine wave in the numerical simulation. Goda's [69] pressure distribution seen in Fig. 4.42b is in good agreement with that of Sahlin et al. [70] (see Fig. 4.43). As it can be seen, pressure peaks become lower as the number of grid points increases. As the difference between the pressure distributions assigned to the two finer grids is very small the pressure solution with a number of grid points of 801 can be regarded as a grid independent solution. At the converging gaps full film lubrication occurs but, at the same time, diverging gaps can cause cavitation even in the left half of the solution domain. In the right half of the solution domain there is a continuous cavitated zone which results in zero load carrying capacity in

this region. Thus the load carrying capacity of the lubricating film is determined by the left half of the geometry.

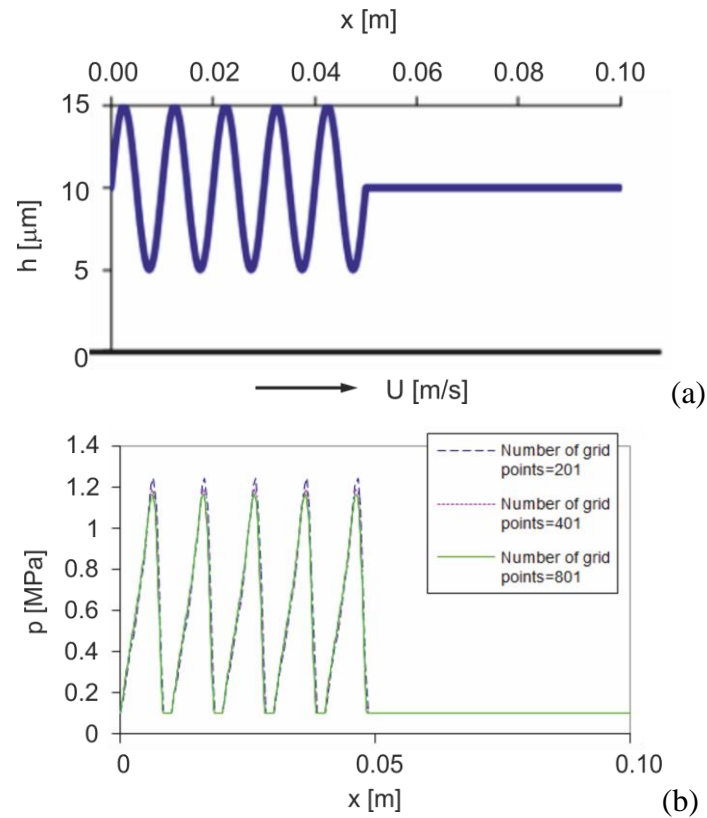


Fig. 4.42. (a) Sahlin et al.'s [70] lubrication problem and (b) the pressure distribution and location of the full film and the cavitated zones computed by Goda [69]

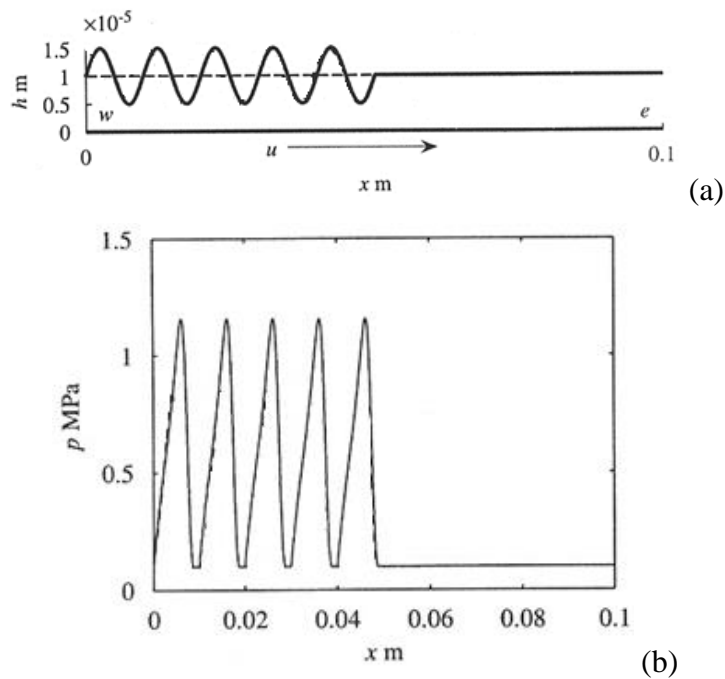


Fig. 4.43. (a) Geometries of the bodies involved in the lubrication problem of Sahlin et al. [70] and (b) the pressure solution across the domain [70]

Fig. 4.44 shows Goda's [69] numerical results for the fluid flow transport computed at different x coordinates. This flow transport, however, cannot be considered as leakage because leakage is defined as the difference between the fluid transport during outstroke and instroke. Fluid transport values presented in Fig. 4.44 belong to the case when the flat surface moves from left to right with constant velocity. The computed fluid transport shows some oscillation but this oscillation decreases as the number of grid points increases.

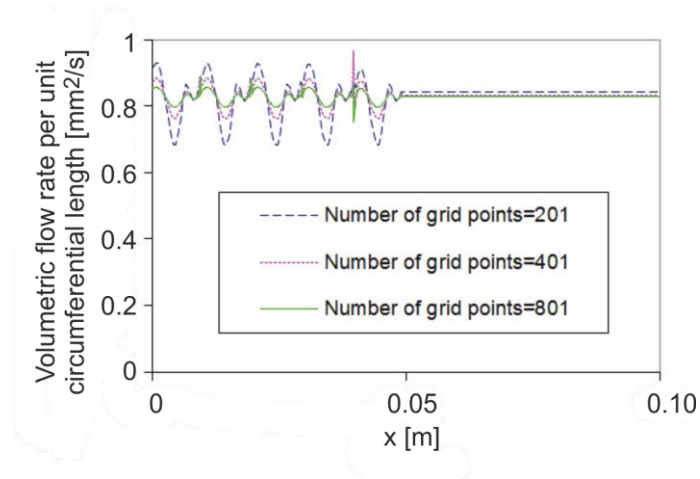


Fig. 4.44. Fluid flow transport computed by Goda [69]

4.5.5. Verification problem: Ideal smooth flat surface in contact with parabolic surface

The second verification problem is taken also from the study of Sahlin et al. [70]. Fig. 4.45a shows the geometry of the bodies involved. The stationary surface is an ideal smooth parabolic slider while the moving one is an ideal smooth flat counterpart. Both the inlet and the outlet of the solution domain are flooded i.e. the cavitation index is $F=1$ and the pressure is the atmospheric pressure at these locations. In the numerical simulations, the cavitation pressure is assumed to be 0.1 MPa that is equal to the ambient or atmospheric pressure. The moving surface has a velocity of $U=4.57 \text{ m/s} = 4570 \text{ mm/s}$.

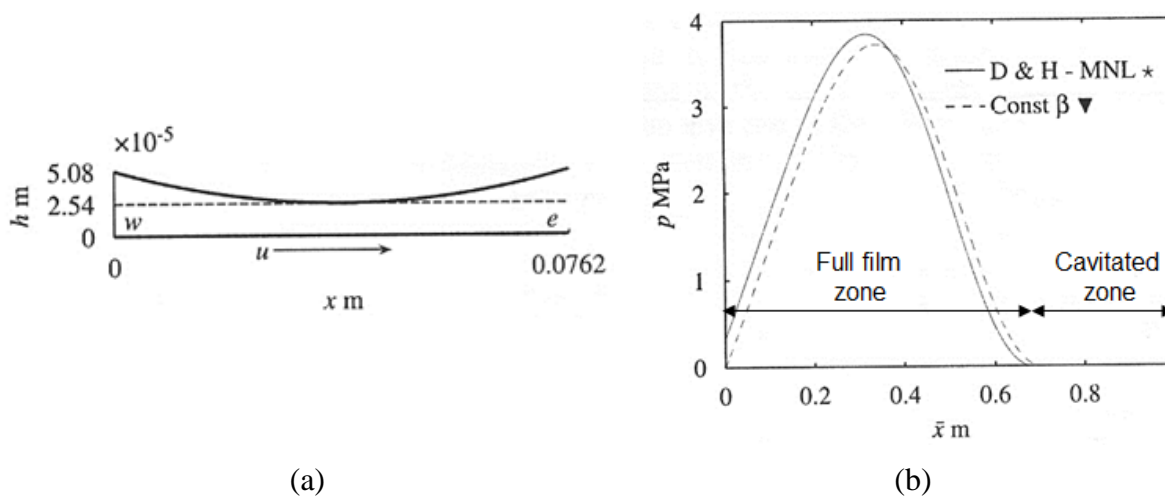


Fig. 4.45. (a) The geometry of the second verification problem including a parabolic slider and (b) the computed pressure distributions if the dynamic viscosity is $\eta = 0.039 \text{ Pas}$ (D & H-MNL and Const β denote compressibility models) [70]

The lubrication problem seen in Fig. 4.45a was also studied by Goda. Fig. 4.46 shows Goda's result for the grid independent pressure distribution if the dynamic viscosity of the lubricant at atmospheric pressure is $\eta_0=0.04$ Pas and the pressure-viscosity coefficient is $\alpha = 20 \cdot 10^{-9} 1/Pa$. The solution domain was divided into equidistant control volumes. Since both bodies are considered as ideal smooth their RMS roughness is set to be three orders of magnitude smaller than the height of the parabolic slider in the numerical simulation. Pressure distribution presented in Fig. 4.46 is in good agreement with the one reported by Sahlin et al. [70] (see Fig. 4.45b). At the converging gap full film lubrication occurs while the diverging gap can cause cavitation in the right part of the solution domain which yields lubricant film with zero load carrying capacity. Thus the load carrying capacity of the lubricating film is determined by the left portion of the geometry.

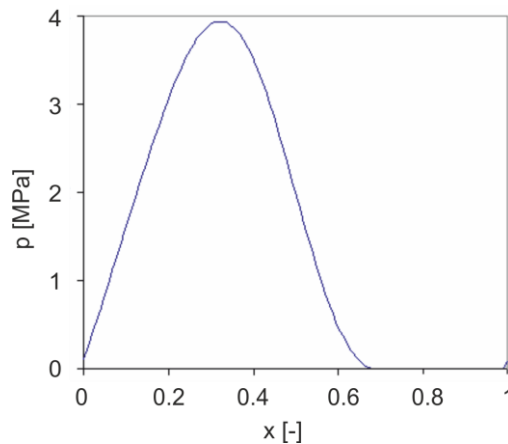


Fig. 4.46. Pressure distribution and location of the full film and the cavitated zone computed by Goda

4.5.6. Verification problem: Ideal smooth flat surface in contact with sinusoidal surface

As a next step the hydrodynamic lubrication problem of a rough solid/ smooth elastomer sliding pair proposed by Kozma [71, 72] is studied. Kozma replaced the roughness of the solid body with a sine wave and neglected the effect of cavitation. The main aim of the work done by Goda [69] is to study the effect of the cavitation and the pressure dependent viscosity on the hydrodynamic lubrication. As it is assumed by Kozma asperities of the solid body can contribute to develop hydrodynamic pressure between the sliding surfaces while the elastomer penetrates into the valleys of the solid surface due to the applied normal load. Furthermore it was assumed that, without normal load, (a) the elastomer surface is flat, (b) at the peaks of solid asperities the minimal film thickness is $h_0=0.1 \mu\text{m}$ and (c) the maximal film thickness is h_1 at the bottom of the valleys of the rough solid surface (see Fig. 4.47). Increasing the applied load the elastomer penetrates into the valleys of the solid surface lowering the maximal film thickness h_1 and increasing the hydrodynamic load carrying capacity. In other words, the contact geometry shown in Fig. 4.48 demonstrates the gap form between a rough, ideal rigid surface and a smooth, elastic rubber seal at a given normal load. The sine wave has a wavelength of $\lambda_1=100 \mu\text{m}$ or $\lambda_2=200 \mu\text{m}$ and amplitude, which is exactly the half of the h_1-h_0 value, 1, 0.75, 0.5, 0.25 or 0.125 μm . During the simulations, it is also assumed that the sliding velocity is $U=0.1 \text{ m/s}=100 \text{ mm/s}$, and the total length of the solution domain, in axial direction (direction x), is $L=2 \text{ mm}$ in all the cases studied. The gap form between the solid and the elastomer surfaces is defined, based on [71, 72], as

$$h(x) = h_0 + \frac{h_1 - h_0}{2} \left(1 + \cos \frac{2\pi}{\lambda} x \right). \quad (4.29)$$

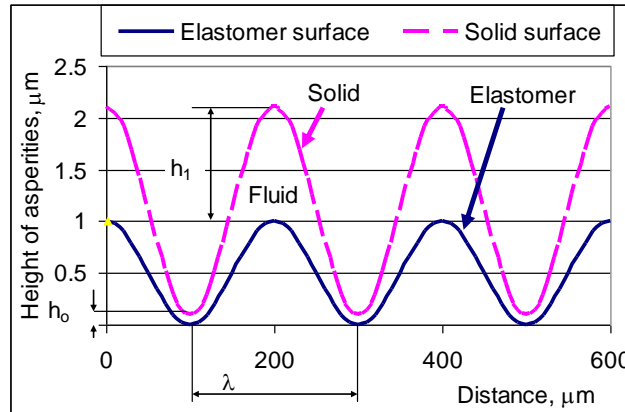


Fig. 4.47. Smooth elastomer surface penetrating into the valleys of a rigid, rough solid surface [71, 72]

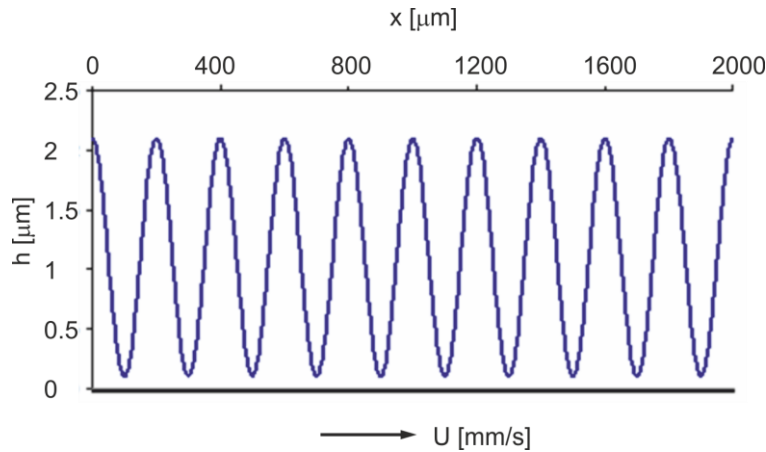


Fig. 4.48. Geometry of the lubrication problem for the case of $\lambda=200 \mu\text{m}$, $h_1-h_0=2 \mu\text{m}$ [69]

Fig. 4.48 shows the lubrication problem studied for the case of $\lambda=200 \mu\text{m}$, $h_1-h_0=2 \mu\text{m}$. In Goda's [69] numerical simulations, the cavitation pressure was assumed to be 0.1 MPa that is equal to the ambient pressure. Both the inlet and the outlet of the solution domain were flooded that is the cavitation index was $F=1$, and the pressure was $p=0.1 \text{ MPa}$ at these locations. Goda's numerical simulations have been performed under the following conditions: number of grid points is 801 which implies that the solution domain was discretized into 800 control volumes where the characteristic axial length of a single control volume was $2.5 \mu\text{m}$, both the flat plate and the sine wave had an ideal smooth surface i.e. their surfaces were regarded as ideal smooth at any magnification, dynamic viscosity of the lubricant at atmospheric pressure was $\eta_0=0.015 \text{ Pas}$ and the pressure-viscosity coefficient was $\alpha=20 \cdot 10^{-9} \text{ 1/Pa}$. The variation of the lubricant viscosity as a function of pressure is depicted in Fig. 4.49. As it can be seen, there is a viscosity increase of 22% as the pressure increases from atmospheric pressure to a pressure of 10 MPa. In order to model surfaces as ideal smooth ones their RMS roughness was set to be three orders of magnitude smaller than the double of the amplitude of the sine wave.

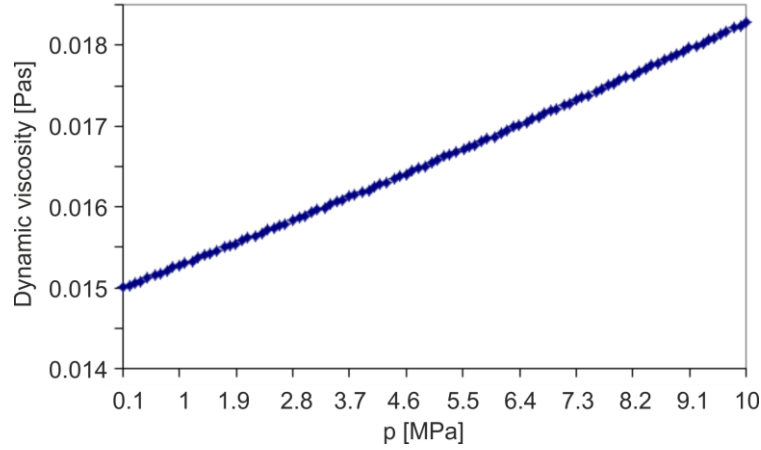


Fig. 4.49. Pressure dependency of the lubricant viscosity in Goda's simulations [69]

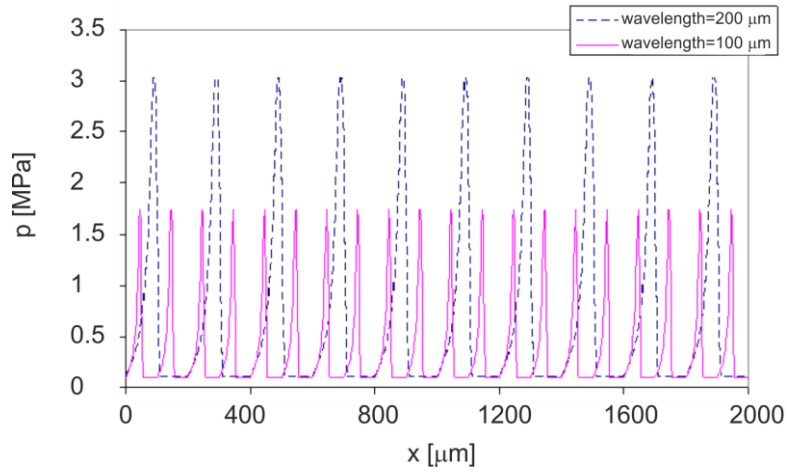


Fig. 4.50. Goda's computed pressure distribution for the case when $h_1-h_0=1 \mu\text{m}$ [69]

Fig. 4.50 shows the pressure distributions computed by Goda [69] for the cases when the sine wave has a wavelength of $\lambda=200 \mu\text{m}$, $\lambda=100 \mu\text{m}$ and an h_1-h_0 value of $1 \mu\text{m}$. Figs. 4.51-4.52 show Goda's [69] numerical results for the pressure distribution as a function of axial coordinate at different h_1-h_0 values for the cases of $\lambda=100$ and $200 \mu\text{m}$. As it can be seen, the extension of the lubricating film having load carrying capacity becomes larger as the amplitude of the sine wave decreases at a given wavelength. This implies that the cavitated zones become narrower as the amplitude reduces at a given wavelength. Finally, Fig. 4.53 shows Goda's [69] numerical results for the variation of the mean pressure as a function of h_1-h_0 and in case of two different wavelengths. Since the mean pressure can be interpreted as the load carrying capacity of the lubricating film we can come to the conclusion that, in the investigated range of h_1-h_0 , the load carrying capacity increases as the amplitude of the sine wave decreases and/or the wavelength of the sine wave increases. The mean pressure (\bar{p}) is obtained from the pressure distributions as follows:

$$\bar{p} = \frac{\int_0^L p(x) dx}{L}, \quad (4.30)$$

where L denotes the length of the solution domain. The integration in Eq. (4.30) was performed numerically under the assumption that pressure varied linearly between two neighbor-

ing grid points. The numerical results presented allow us to draw the following conclusions. (a) Tendencies of the mean pressure as a function of h_1-h_0 and wavelength are in good agreement with those of Kozma [71, 72]. (b) Load carrying capacity increases as the amplitude of the sine wave decreases and/or the wavelength of the sine wave increases. (c) Location of the cavitated zones are physically realistic and are in accordance with the anticipated ones. (d) Extension of the cavitated zones at a given wavelength becomes smaller as the h_1-h_0 value reduces.

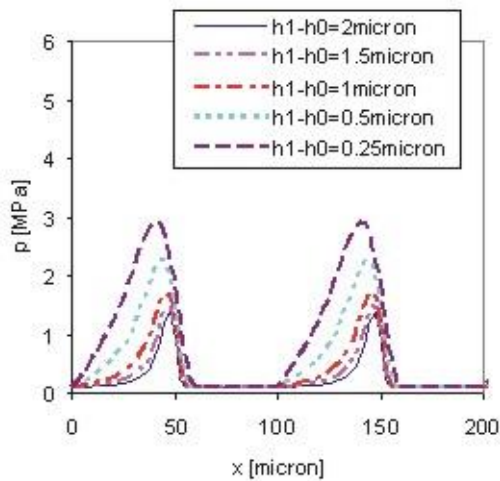


Fig. 4.51. Goda's pressure distributions for $\lambda=100 \mu\text{m}$ (only the first $200 \mu\text{m}$ segment of the solution domain is represented) [69]

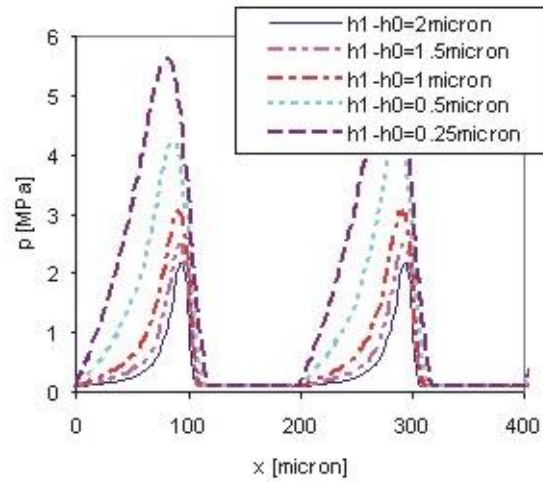


Fig. 4.52. Goda's pressure distribution for $\lambda=200 \mu\text{m}$ (only the first $400 \mu\text{m}$ segment of the solution domain is represented) [69]

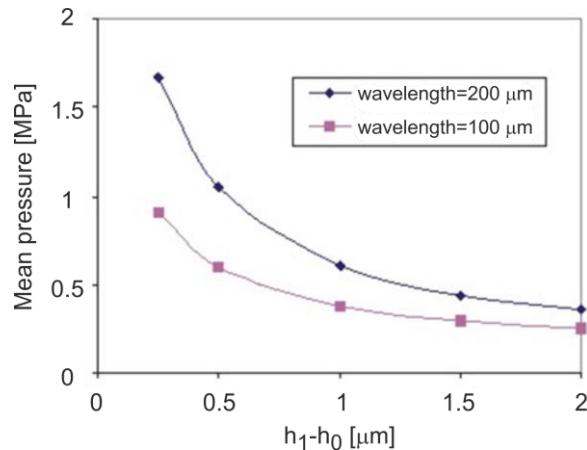


Fig. 4.53. Mean pressure computed by Goda as a function of wavelength and h_1-h_0 [69]

4.5.7. Windscreen wiper application

In this chapter, the steady-state elastohydrodynamic lubrication problem of wiper blade/glass contact is solved using Goda's mixed friction code. The lubrication problem and its solution were reported in Bódai and Goda [10]. Although there are studies dealing with the tribology of windscreen wipers in the literature (see studies of Koenen and Sanon [13], Deleau et al. [73], and Persson and Scaraggi [63]), only few authors (e.g. Koenen and Sanon [13]) made an effort to analyze the effect of real wiper blade geometry on the tribological behavior experimentally. Here it must be mentioned that even Koenen et al.'s [13] experi-

mental study presents only few results on the variation of apparent coefficient of friction as a function of sliding velocity, damping ratio of rubber, and the Stribeck parameter. At the same time no theoretical study taking into account the real geometry of wiper blade on tribological behavior is available in the literature. In order to fill these gaps a commercial wiper blade (SWF Duotec+) sliding on smooth glass surface was investigated experimentally and numerically by Bódai and Goda [10, 64, 75]. It is believed that these studies are able to highlight the unique behavior of wiper blade and contribute to the better understanding of tribological behavior of wiper lip/glass contact pairs.

In the windscreen wiper application, a rubber wiper blade slides on smooth glass surface in order to remove the water and/or contaminations from the windshield. From traffic safety point of view the windscreen wiper is of great importance because both the too thick water film and the presence of contaminants hinder the view of driver. The hyperelastic, time- and temperature-dependent material behavior of rubber (see Appendix A), the non-Hertzian contact and the presence of water make the tribology of windscreen wipers a challenging research area. Although sliding friction of rubber is an intensively studied research area, up to now scientists of the most respected journals in the field of tribology gave considerably less attention to the windscreen wiper application. The main objectives of the research efforts are to understand wiping action, improve wiping quality, reduce noise generation, and optimize tribological behavior of the rubber wiper blade, for instance, by using surface treatments and coatings. In one part of the investigations, a small piece of real wiper blade is studied (see e.g. Koenen and Sanon's [13] investigations), while, in the rest, the wiper blade for the sake of simplicity is replaced with cylindrical specimen (see e.g. Deleau et al. [73]). The few works available in this field of tribology, almost without exception, concentrate on dry and wet specimen-level investigations. At the same time, owing to the combined experimental and theoretical work of Bódai and Goda [64] the first structural-level results have also been appeared in the literature.

In many cases, sliding rubber components (e.g. rubber seals) operate in mixed friction state. With the development of tribology and computers, besides experimental investigations, different mixed friction models have been appeared in the literature to solve the elastohydrodynamic lubrication problem. In order to decrease the complexity of the model, usually it is assumed that material behavior of rubber obeys Hooke-law. For simple geometry the deformation of rubber surface is determined analytically, while the application of influence coefficient matrix is typical in cases when numerical method (e.g. finite element analysis) is used for the same purpose. However it must be mentioned that, at present, there is no commonly accepted contact theory for handling asperity interactions in mixed friction models. In most cases, the Greenwood- Williamson model is used but there are cases when other contact theory (e.g. Persson's theory) is preferred (see e.g. Persson and Scaraggi [63]). Unfortunately, the prediction of these contact models differs significantly (see Section 4.5.2 and Bódai and Goda [64]) especially as the contact pressure increases. It is interesting to mention that while mixed friction simulation of seals is extensively studied the adaptation of corresponding numerical models for windscreen wipers is considered as a new field of tribology. Besides the works of Bódai and Goda [10, 64, 75] only few studies, e.g. the study of Persson and Scaraggi [63] where the bended wiper lip is modeled by a rubber cylinder, are available in this field.

The profile of the wiper blade studied by Bódai and Goda [10] is shown in Fig. 4.54. At real windscreen wipers of passenger cars, each point of the wiper blade usually moves on circular path whose radius varies typically from $r=100..200$ mm (inner radius) to $R=600..800$ mm (outer radius). The typical sliding velocity of points close to the inner radius is approximately 150 mm/s. However, the sliding velocity at the outer radius is about one order of magnitude higher.

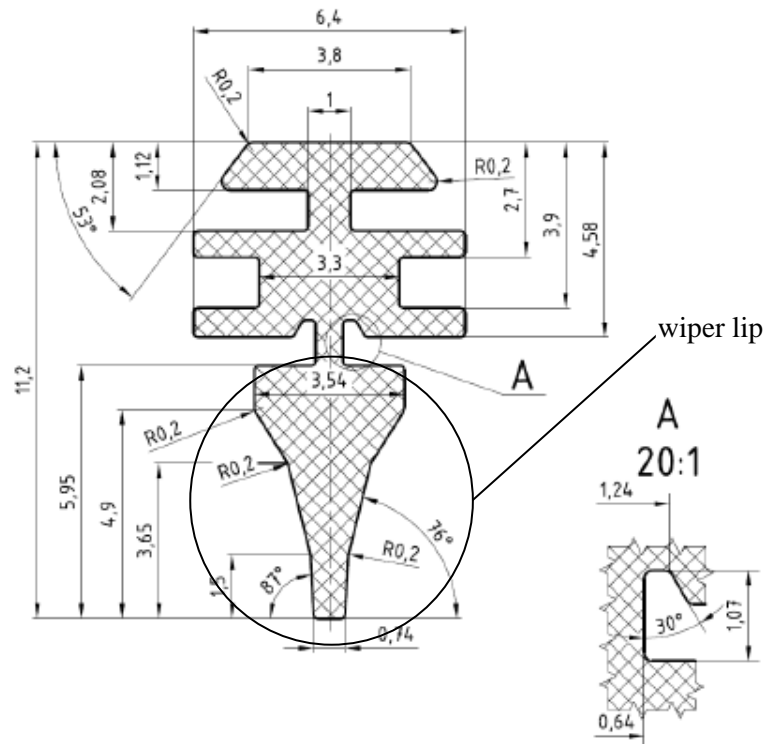


Fig. 4.54. Profile of the wiper blade studied (sizes are in [mm]) [17]

After analyzing operational conditions of real windscreen wipers (five different compact and subcompact passenger automobiles were investigated) it was found that the mean normal force per unit length is between 17.5 and 25 N/m. At this point it must be mentioned that, in the analyses, it was assumed that the pressure distribution is uniform along the length of the wiper blade. However this is an approximation because, in fact, the pressure distribution is not totally uniform. The investigations on speed of wiping showed that the mean sliding velocity, in the middle of the wiper blade, is about 600 mm/s for slow wiping and 1050 mm/s for fast wiping.

According to the work of Allen [74] the average contact angle (the angle at which the liquid/vapor interface meets the solid surface) between the clean glass surface and a water drop - identified by sessile drop test - is less than 30° thus the water is able to wet the glass surface. In other words, the clean glass surface is highly hydrophilic. A contact angle less than 90° usually indicates that the solid is hydrophilic and the water wets the solid. This good wettability is one of the essential elements of the hydrodynamic effect. As it is well known the increased wetting establishes boundary layer lubrication condition that eliminates solid-solid contact of the rubber with the glass.

The small strain viscoelastic behavior of the rubber wiper blade was studied by dynamic mechanical analysis (DMA). The DMA test (see Bódai and Goda [10]) was performed in compression mode with strain amplitude of 0.01%. The static preload acting on the specimen (21.7 x 3.75 x 1.32 mm) was 0.1 N. The temperature-dependent ($T_{\min} = -100^\circ\text{C}$, $T_{\max} = 100^\circ\text{C}$) storage modulus, loss modulus and loss factor of the rubber was measured at frequencies of 1, 10, and 100 Hz. Fig. 4.55 shows the temperature dependent material properties of the wiper blade at $f=10$ Hz. The results indicate that the glass transition temperature is about -50°C while the highest value of loss factor is 0.6. The hardness of the wiper blade was 45 Shore A which had been measured by Mitutoyo Hardmatic HH-300.

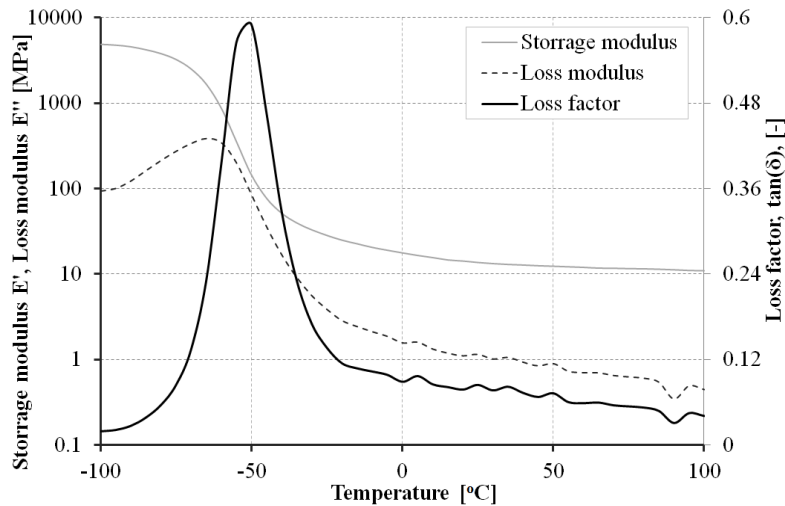


Fig. 4.55. Temperature dependent storage modulus, loss modulus and loss factor of the rubber wiper blade studied by Bódai and Goda ($f=10$ Hz) [10]

In the present simulations, the real inhomogeneous (SWF Duotec is made of two different rubbers) wiper blade was modeled as a homogeneous one because the material properties of the different components were not available. Elastic modulus of the homogeneous wiper blade was determined from a fit to the measured force-displacement curve of the wiper blade. As reported by Bódai and Goda [10], at a modulus of $E=4.5$ MPa the simulated force-displacement curve agrees well with the measured one. The agreement, however, degrades as the wiped lip becomes strongly deformed. It must also be mentioned that the numerical simulations of the author do not take into consideration the effect of surface treatments/coatings. The only reason why this effect was not involved in the simulations is that no data were available for the modulus and the thickness of the surface layer on the wiper lip influenced by surface treatment. At the same time this effect could be considered easily in the elaborated numerical models if the data mentioned above were available.

In the simulations of Bódai and Goda [10, 75], Salant et al.'s [41] approach is adopted where the deformation of rubber component is computed through a separate FE model. With this approach one can take into consideration the real geometry of wiper blade and it is not needed to replace it, for example, with a half cylinder as it is done by Persson and Scaraggi [63]. In the mixed lubrication regime, one part of the normal load is carried by the water film, while the rest is carried by asperity contacts. Since the length of the wiper blade is much larger than the width of the nominal contact area, the fluid pressure is computed from the one-dimensional, steady-state Reynolds equation (water being assumed to be Newtonian, isothermal and incompressible) with pressure independent viscosity. In other words, the numerical value of pressure-viscosity coefficient is close to zero thus the water is considered to be an iso-viscous liquid. In each step of the iterative computational procedure the contact pressure and the fluid pressure were computed for a given film thickness distribution. The fluid mechanics problem (Reynolds equation) was solved numerically by the finite difference method. Using this technique the nominal contact area was discretized and the differential (Reynolds) equation was substituted by a system of algebraic equations. In Bódai and Goda [10], a one-dimensional mesh with 71 nodes was used. The sum of the contact and fluid pressure was assumed to be known and equal to the static contact pressure computed by FE technique because the hydrodynamic pressure is negligible in comparison to the static pressure. At the end of each iteration step the deformation of the wiper blade induced by the difference between the sum of fluid and contact pressure and the FE static contact pressure was computed. As a last step the film thickness distribution was updated. This was done iteratively until the film

thickness converged i.e. the difference between the sum of fluid and contact pressure and the FE contact pressure disappeared. As measurement results of Bódai and Goda [10] show, if the sliding speed is close to 100 mm/s, then the apparent coefficient of friction is essentially constant at a normal load per unit length of 37.5 N/m. This indicates that a thin water film separates the wiper lip from the glass. Here the FE contact pressure distribution computed at a normal load per unit length of 37.5 N/m and an apparent coefficient of friction of $\mu=0.16$ (measured at sliding velocity of 150 mm/s by Bódai and Goda [10]) is used for simulation purposes. The effect of surface roughness on the fluid flow was taken into consideration through flow factors. Additionally, the rubber surface was considered to be rough (isotropic Gaussian roughness) while the glass surface was treated as ideally smooth, rigid one. As input data the following parameters were used: elastic modulus and Poisson ratio of rubber (E, ν), sliding velocity (v), dynamic viscosity of the water (η), asperity radius (R), RMS roughness of rubber (σ), and asperity density (χ). The asperity radius can either be measured or estimated. It is important to mention that the pressure was measured relative to the atmospheric pressure.

Fig. 4.56a shows the numerical results of Bódai and Goda [10] for the contact and fluid pressure distributions. The nominal film thickness distribution computed is depicted in Fig. 4.56b. The gap between the mean surfaces of the contacting bodies first converges (this is where the water enters into the gap) then diverges. According to this, cavitation occurs at x coordinates above ~ 0.05 mm where the gap is diverging. In the current simulations, the cavitated region of contact area is characterized by zero fluid pressure. The fluid pressure reaches its maximum value at $x=0.017$ mm which is in the middle of converging gap region. However, the contact pressure is higher with orders of magnitude than the fluid pressure (the peak value of the asperity-type contact pressure is 0.8 MPa while that of the fluid pressure is lower with three orders of magnitude) which proves that the sliding velocity is not high enough to cause full film lubrication. Therefore it can be concluded that the gap is controlled by the solid-solid contact.

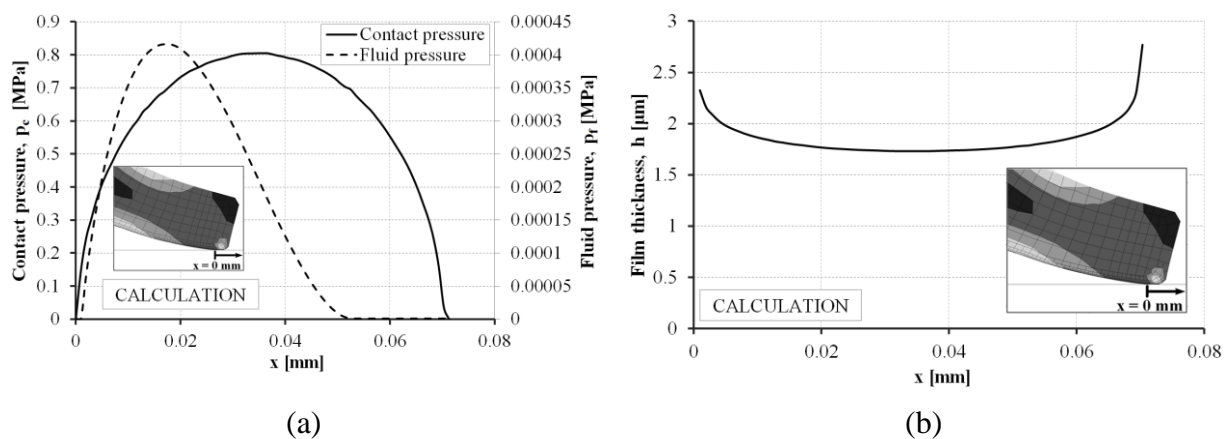


Fig. 4.56. (a) Contact and fluid pressure distribution, and (b) average film thickness ($E=4.5$ MPa, $\nu=0.49$, $v=150$ mm/s, $\eta=0.001$ Pas, $R=1$ μm , $\sigma=1$ μm , $\chi=10^{13}$ m^{-2}) reported by Bódai and Goda [10]

The simulation results make it probable that a thin water film is responsible for the relatively low friction force (thin film lubrication). For the sake of clarity it must be mentioned that the film thickness computed (see Fig. 4.56b) represents the gap between the mean surfaces of the contacting bodies but not the real, local gap. The thickness of the water film reported by Deleau et al. [73] is at least one order of magnitude lower than the film thickness computed here. Independently of the fact that the film thickness computed and the actual (local) thickness of the thin lubricating film are different, the predictive capability of frequently

used contact laws must be studied in depth in the near future because, as reported by Bódaí and Goda [64], they provide drastically different results for the separation. Based on this it seems the present simulation overestimates the mean gap between the contacting surfaces (mean film thickness or mean water gap between surfaces). Nevertheless it is believed that the mixed friction model presented here will motivate further studies in the simulation of lubrication state of wiper lips. Further simulation results on mixed friction of windscreen wiper lips are not presented here but are available in Bódaí and Goda [75].

As it is well known, the magnitude of adhesive force that can arise in lubricated contacts is not significant. However, the capillarity introduces additional friction effect (deformation and shearing of capillary bridges) into the sliding friction of windscreen wipers if capillary bridges appear between the contacting solid surfaces. Capillary forces are of great importance because water has very high surface tension. The magnitude of surface tension depends, among others, on the temperature and the properties of the solid surfaces. In Bódaí and Goda [10], both the wiper lip and the glass surface were cleaned before each test. However, in reality, neither the windscreen nor the wiper lip is clear which may modify surface tension significantly. In wet friction, a thin film of adsorbed water is always present on the solid surfaces. At low sliding velocities i.e. in the boundary lubrication regime the adsorbed water film is very thin (few molecules thick). The density and viscosity of this adsorbed layer are different from those of the bulk water at the same temperature and pressure. On the basis of all this, it can be concluded that water adsorption plays critical role in the tribological behavior of wiper lip.

Due to the complexity of the elastohydrodynamic lubrication problem of wiper lip a number of simplifying assumptions have been introduced in the model presented. The most important characteristics of the model are as follows: (a) adhesion and capillary effects are neglected, (b) the drastically varying asperity (local) contact pressure is replaced with a locally averaged contact pressure which is related to the local mean gap, (c) the effect of solid-solid or fluid-solid interaction induced deformation of asperities on the average fluid flow is neglected (Patir and Cheng model), (d) the contact of rough surfaces is treated by the Greenwood-Williamson contact model.

4.5.8. Sealing application: O-ring

The work presented in this chapter focuses on the primary sealing interface (nominal contact area between the rod and the seal) of reciprocating O-rings and has been reported in Goda [12] and Goda and Bódaí [78]. By using Goda's [69] mixed friction code both the pressure distribution within the lubricating film, and the amount of fluid flow transport during outstroke and instroke (their difference defines the amount of leakage) have been predicted.

As it is well known seals can be divided into two categories: (a) seals with a preset, fixed clearance, and (b) seals where the face separation is dynamically controlled. In the first case, the clearance is bounded by the rigid surfaces and a preset sealing gap is formed. In the second case, the seal is designed to reduce the film thickness automatically as sealed pressure increases. As explained by Müller and Nau [76] O-rings belong to the category of seals where the film thickness is dynamically controlled. In dynamically controlled seals (contact seals) the leakage path is completely closed by solid contact between the mating surfaces, at least so long as the sealing faces are stationary. When they begin to slide, relative to each other, various factors cause the sealing surfaces to separate slightly and an interfacial fluid film to form. Such dynamic fluid films usually have thicknesses in the range 0.1 to 1 μm , which is comparable to the roughness and waviness of the sealing surfaces. The film dimension in the sliding direction (direction of leakage flow) is much greater than its thickness; it is in mm order of magnitude. Since oil and water molecules are no more than about one nanometer across, fluid molecules are still very small compared to the thinnest dynamic films. Hence even in such

very thin films the laws of fluid continua (conventional hydrodynamic laws) are still valid as concluded by Müller and Nau [76]. When the mating surfaces are separated by only a few molecule thick layer, boundary interaction has to be taken into account. In the boundary lubrication regime, surface chemistry effects dominate. If the contacting surfaces slide on each other, the viscous fluid is drawn along by the moving surface, just as in a hydrodynamic bearing. The results of this is that the fluid pressure increases in regions where the film converges, lifting the faces apart. In reciprocating rubber seals, the mating seal faces can be separated by a hydrodynamic fluid film maintained in this way. Although the seal faces may be in contact when at rest, they can be separated when in motion, due to the hydrodynamic effect. In reciprocating applications, the leakage rate is predictable and is governed by the pressure difference and the relative motion. The leakage flow rate during outstroke (the rod moves from the sealed pressure region to the ambient pressure one) does not equal to the real leakage because rod seals have an inherent ability for inward pumping (pumped return flow) during instroke. Under optimal conditions, such inward pumping can prevent leakage. Net leakage is defined as the difference between fluid transports during outstroke and instroke.

In order to predict the film thickness distribution, the leakage rate and the friction force of reciprocating rubber seals, in most cases, the EHL (elastohydrodynamic lubrication) theory is used in which full film lubrication and smooth sealing surfaces are assumed. However experiments did not proved its adequacy. The measured leakage rate and friction force did not agree with simulation results and the measurements showed that instead of full film lubrication mixed lubrication is present through part of the sealing interface and the seal roughness has an effect on the seal behavior. One of the most promising models which try to overcome these problems by considering both the mixed lubrication and the effect of surface roughness is that of Salant et al. [41]. While simulations made by Salant et al. resulted in leakage if the roughness of the seal was above a critical one, the conventional EHL theory predicted zero leakage for the same seal. In Salant et al.'s model [41], the surface roughness of the rod is neglected, while that of the seal lip is taken into consideration. The authors emphasize that this assumption is reasonable because during the run-in period, the rod is polished to a very smooth finish; consequently the rod surface roughness is typically one-tenth of that of the seal surface. The frictional shear stress arising at the contacting asperities was computed by using an empirical friction coefficient of $\mu=0.25$. In a recent paper of Wohlers et al. [45], a similar mixed friction model is presented for reciprocating O-rings. In order to prove the simulation results experimental results were also reported by Wohlers et al. for the case where the oil is not pressurized (zero sealed pressure). The resulting friction forces from experiment and computation were compared for the same conditions. In the computation a constant friction coefficient of $\mu = 0.5$ was used for the solid-solid contact related friction component which is computed using the hysteresis friction theory of Persson [3]. In order to treat the solid/solid contact in the mixed lubrication regime Persson's contact theory [65] was adopted by Wohlers et al. [45]. The experiments presented for hydraulic reciprocating seal (U-cup seal made of polyurethane) by Bullock et al. [77] also showed that the measured friction levels to be at least an order of magnitude greater than predicted by elastohydrodynamic theory. This indicates that theoretical models on full film lubrication are inadequate. Bullock et al. [77], however, found a reasonable experimental agreement for the outstroke friction predicted by the adopted Greenwood-Williamson-average Reynolds simulation whose physical concept is the same as used by Salant et al. [41] for lip seals. At the same time the high friction levels simulated during instroke did not appear in the measurements. Finally, they concluded that inclusion of the Greenwood-Williamson (GW) contact model allows friction levels in the correct order of magnitude to be predicted.

Goda's [69] mixed friction code (see Section 4.5.3) makes it possible to study the steady state behavior of different hydraulic seals. It is valid for applications in which the

stroke length is significantly larger than the primary sealing interface (nominal contact area between the seal and the rod). Typical output are the pressure distribution within the lubricating film (fluid pressure), the pressure distribution due to asperity contacts (contact pressure), the amount of fluid flow transport during outstroke and instroke and the magnitude of the friction force. Here Goda's computer code was used to study the hydraulic O-ring of 8 x 1.5 mm. As a first step the static contact pressure distribution of the mounted in, pressurized O-ring was computed by FE technique. For this purpose an axisymmetric FE model has been developed in MSC.Marc. Surface roughness of the seal and the thin lubricant film between contacting surfaces are not being considered here but are included in a later phase of the simulation process. The sealed pressure is applied to non-contacting elements of the seal while the effect of friction force on the contact pressure distribution is neglected. In other words, the contact between the seal and the rod is assumed to be frictionless in this FE model. Fig. 4.57 shows the O-ring before mounting in and after it under the sealed pressure ($p_{\text{sealed}}=6$ bar and it acts on the left side of the O-ring) as reported by Goda and Bódaí [78]. On the right side of the O-ring atmospheric pressure ($p_a=1$ bar) is present. The static contact pressure distribution and the static film thickness distribution provided by Greenwood-Williamson's contact law were reported by Goda and Bódaí [78] and can be seen in Fig. 4.58. The length of the contact area was 0.798 mm. All the simulations were performed with the following parameters: RMS roughness of the seal is $\sigma=0.4 \mu\text{m}$, asperity radius is $R=1 \mu\text{m}$, asperity density is $\chi=10^{13} 1/\text{m}^2$, elastic modulus of the O-ring is $E=10 \text{ MPa}$, Poisson ratio of the seal is $\nu=0.48$. For the sake of simplicity here it is assumed that the seal obeys Hooke's law.

In order to compute the radial deformation of the O-ring under a given pressure distribution the influence coefficient method was used. The influence coefficient method takes into consideration the effects of the forces at all nodes of the contact area on the deformation at a given node. In the present case, the number of nodes located within the contact area was 41, which implies that the distance between two neighboring nodes was $19.966 \mu\text{m}$. The elements of the influence coefficient matrix (I_{ik}) have been computed by FE technique as described in Goda and Bódaí [78]. I_{ik} represents the deformation at node i produced by a unit pressure at node k .

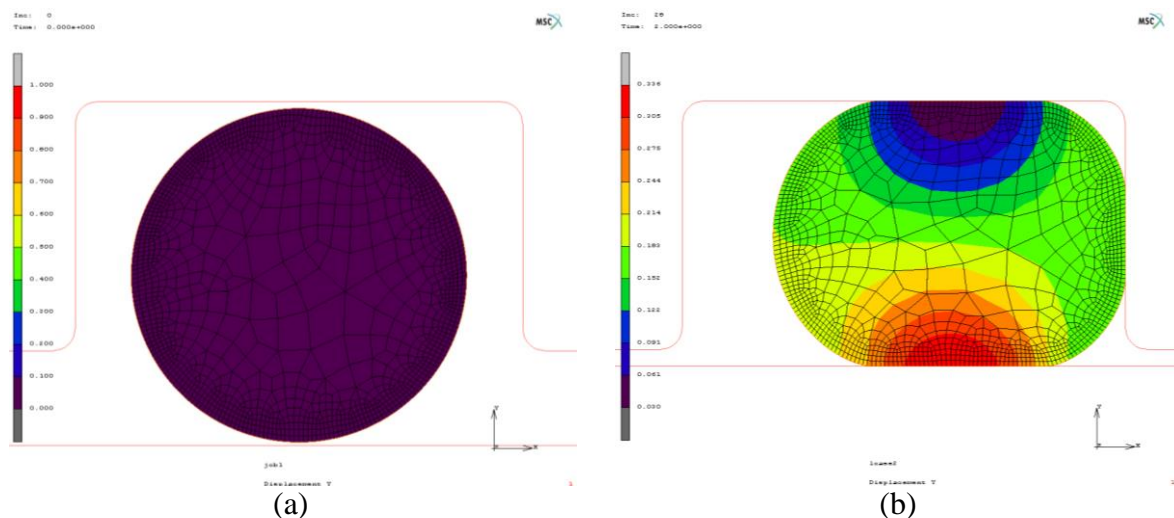


Fig. 4.57. FE model of the O-ring: (a) initial state, (b) after mounting in and under sealed pressure [78]

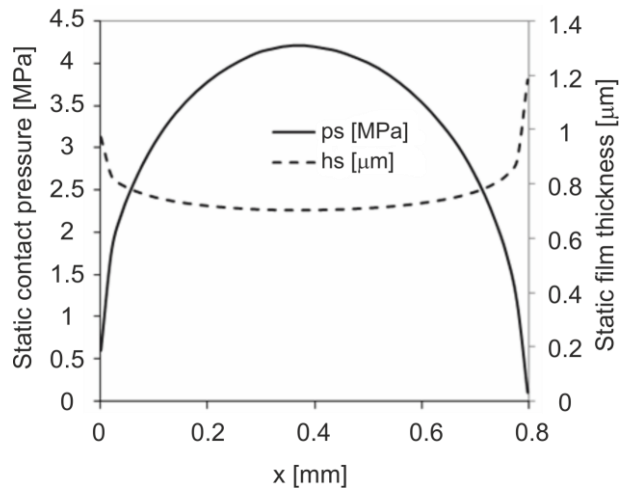


Fig. 4.58. Static contact pressure and static film thickness distribution computed by Goda and Bódai [78]

The leakage simulation was performed under the following conditions: (a) sliding speed during in- and outstroke is $U = 50$ mm/s, (b) dynamic viscosity of the fluid at atmospheric pressure is $\eta_0 = 0.02$ Pas, (c) pressure-viscosity coefficient is $\alpha = 20 \cdot 10^{-9}$ 1/Pa, (d) both the inlet and the outlet of the solution domain are flooded i.e. the cavitation index is $F=1$ at these locations, (e) the cavitation pressure is assumed to be 0.1 MPa that is equal to ambient or atmospheric pressure. The comparison of the static film thickness and the film thickness for in- and outstroke was reported in Goda [12] and is shown in Fig. 4.59. As it can be seen the nominal lubricant film thickness during outstroke is larger than during instroke. The computed contact and fluid pressure distribution during in- and outstroke were firstly presented by Goda [12] and are depicted here in Fig. 4.60. During outstroke there is a cavitated region within the nominal contact area where the fluid pressure equals to the atmospheric pressure. At $x=0.12$ mm, the fluid pressure reaches its maximum value of 0.76 MPa. The computed fluid flow transport (volumetric flow rate per unit circumferential length) during outstroke was 0.0124 mm²/s. As the diameter of the rod is 8 mm this fluid flow value corresponds to a flow rate of 0.312 mm³/s. In case of instroke (see Fig. 4.60), there is no cavitation within the nominal contact area and the maximum fluid pressure is equal to the sealed pressure (0.6 MPa). Furthermore the fluid pressure is lower than or equal to the sealed pressure at every point of the nominal contact area. The computed fluid flow transport (volumetric flow rate per unit circumferential length) during instroke was 0.0107 mm²/s which corresponds to a flow rate of 0.269 mm³/s. As the leakage is interpreted as the difference between the fluid flow transport during out- and instroke the leakage rate has a value of 0.043 mm³/s (see Table 4.4). All the results show that the O-ring studied here operates in the mixed lubrication regime during in- and outstroke.

As an illustration, Fig. 4.61 shows the film thickness, fluid and contact pressure distributions computed during outstroke for a sliding speed of 100 mm/s. As anticipated, due to the hydrodynamic effect the fluid pressure values are higher than at sliding speed of 50 mm/s. At this higher sliding speed the fluid flow transport has a value of 0.618 mm³/s. Similar to the lower speed the cavitation is present, but here the cavitated region is wider. In order to study the effect of sliding velocity its magnitude was varied (10, 50, 100, 200 mm/s) during the simulations. Dependence of film thickness, contact and fluid pressure on sliding velocity can be seen in Fig. 4.62. As expected the film thickness increases as the velocity increases (increased hydrodynamic effect). Contrary the film thickness is practically insensitive to the change in sliding velocity at the ambient pressure side of the sealing interface which indicates

(in accordance with the fluid pressure distribution) cavitation in this region. In the cavitated region, the fluid pressure equals with the ambient pressure. However extension of the cavitated region decreases with the decreasing sliding velocity. It can also be concluded that the increasing sliding velocity increases the highest value of fluid pressure and shifts it toward the ambient pressure side. Furthermore, in the cavitated region, the contact pressure is equal to the static contact pressure but as the cavitation disappears the fluid film significantly decreases the dominance of asperity contact (see Fig. 4.62b). Fig. 4.63 proves that the effect of viscosity is similar to that of sliding velocity. The increased viscosity induces increased fluid pressure (hydrodynamic effect) and contributes to the extension of the cavitated region. Naturally, any increase in fluid pressure involves decreasing of the contact pressure.

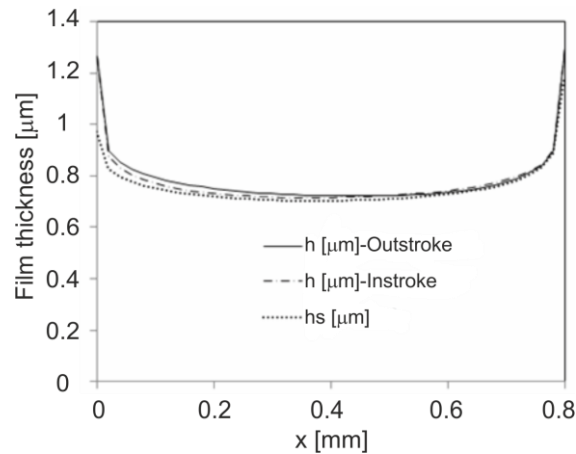


Fig. 4.59. Comparison of the static film thickness and the film thickness for instroke and outstroke as reported by Goda [12]

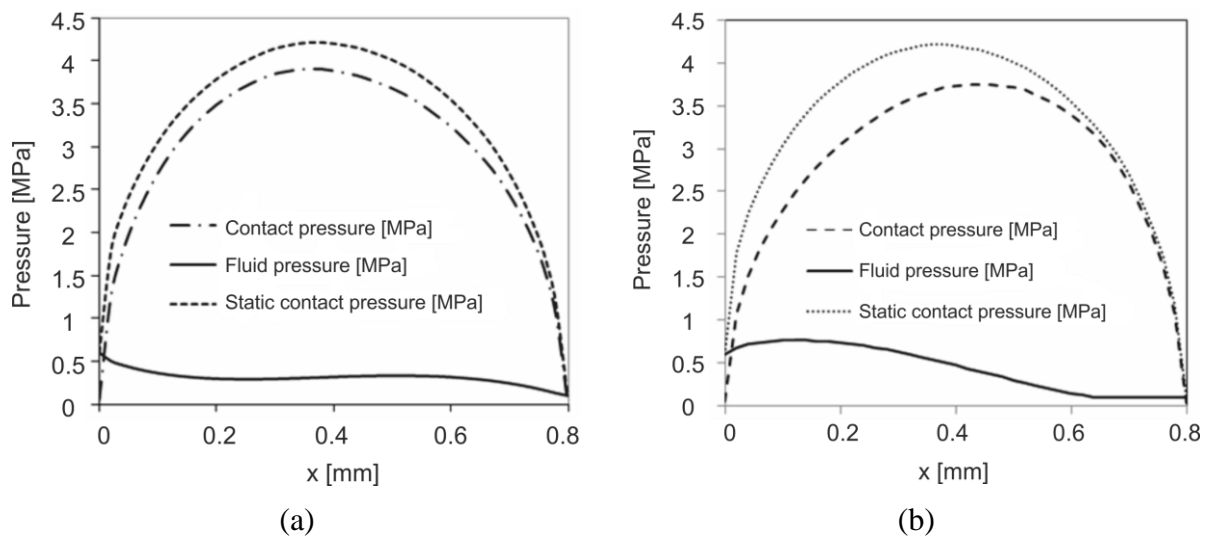


Fig. 4.60. Film thickness, fluid pressure, contact pressure and static contact pressure distribution during (a) in- and (b) outstroke [12]

Fluid flow transport [mm ³ /s]		Leakage [mm ³ /s]
Outstroke	Instroke	
0.312	0.269	0.043

Table 4.4. Fluid flow transport (volumetric flow rate) values for outstroke and instroke as reported by Goda [12]

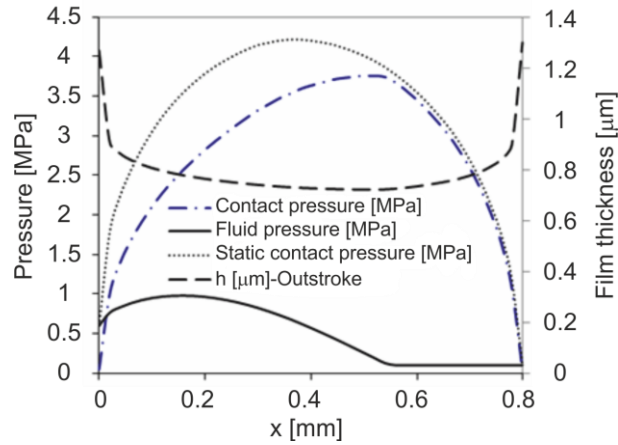


Fig. 4.61. Film thickness, contact and fluid pressure distributions during outstroke (sliding velocity is 100 mm/s) [78]

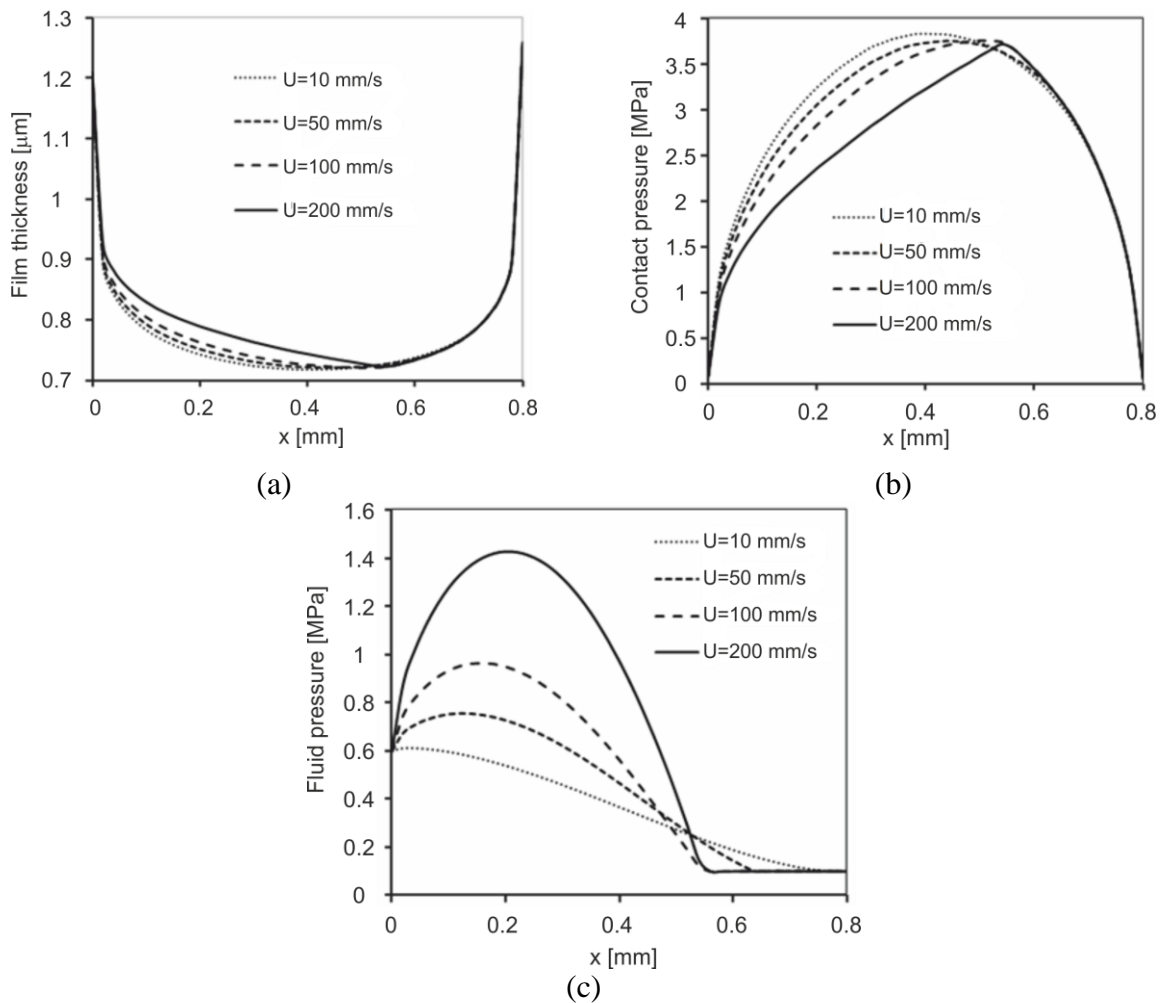


Fig. 4.62. Effect of sliding velocity on the (a) film thickness, (b) contact pressure and (c) fluid pressure during outstroke (dynamic viscosity is 0.02 Pas) [78]

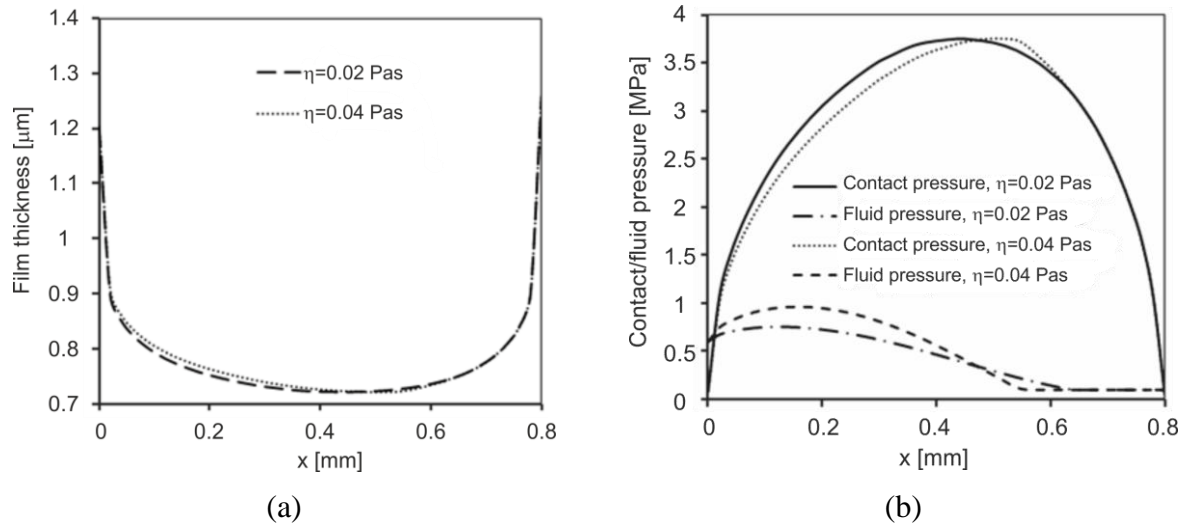


Fig. 4.63. Effect of dynamic viscosity on the (a) film thickness, and (b) contact/fluid pressure during outstroke ($U=50$ mm/s) [78]

5. Numerical modeling of wall (macro-scale) friction in hoppers/silos using simple law of friction at the particle-(micro-) scale: Discrete modeling approach

The discrete modeling approach means the application of the Discrete Element Method (DEM). Unless otherwise specified, here the term Discrete Element Method refers to the three-dimensional Distinct Element Method, where the computational domain consists of rigid spheres (ball-type model) with compliant contacts. Consequently the interpenetration (overlapping) of rigid spheres is allowed („soft” particle model) which can be interpreted as local deformation of the contacting spheres. The distinct element method was originally developed by Cundall in 1971 for the analysis of rock mechanics problems and then applied to soils by Cundall and Strack [79] in 1979. However, it must be mentioned that, in the literature, the term discrete element method includes various techniques where not only the geometry (spheres, polyhedral, etc.) and the behavior (rigid or deformable) of the elements but also the computation of the contact forces may be different. The common characteristics of these methods are as follows: the computational domain consists of rigid or deformable elements (particles), the contacts between particles are detected continuously, and the forces between interacting particles are computed by simple contact laws.

5.1. Fundamentals of DEM

In contrast to continuum mechanical models, the discrete element method models the material as an assembly of rigid overlapping particles being in interaction with one another. Discrete element modeling intends to follow the motion of all the particles and detection their collisions with other particles and with the environment (rigid, moving and non-moving walls). In order to calculate the motion of each particle, all the forces acting on a particle are summed and the resulting equations of motion are numerically integrated. As reported by Candall and Strack [79] if the time step is chosen sufficiently small, it can be assumed that during each time step the instantaneous motion of a particle is determined only by its immediate neighbors it is in contact with. This assumption greatly reduces the computer memory requirement.

Each particle has two types of motion: translational and rotational. These motions can be described by Newton’s second law given by

$$m\dot{\underline{v}} = \sum (\underline{F}_n + \underline{F}_t) + m\underline{g}, \quad (5.1)$$

$$\underline{\theta}\dot{\underline{\omega}} = \sum \underline{M}, \quad (5.2)$$

where m , $\underline{\theta}$, \underline{v} and $\underline{\omega}$ are the mass, tensor of mass moment of inertia, velocity vector and angular velocity vector of the particle, respectively. The forces considered in Eq. (5.1) are the gravitational force vector $m\underline{g}$, and the contact force vectors in normal (\underline{F}_n) and in tangential direction (\underline{F}_t). Naturally, additional forces can also be added to them if it is needed. The moment vector \underline{M} , is generated by tangential contact forces and causes the rotation of the particle, because the contact forces act at the contact point and not at the particle center. Generally, each particle is in contact with several other particles or wall elements, therefore all the contact forces acting on a particle must be summed. This operation is indicated by index i and the summation symbol. The dot in equations (5.1-5.2) denotes the derivative with respect to time. The suffixes n and t mean the components corresponding to the normal and the tangential direction, respectively.

The particles are permitted to overlap with one another while normal and tangential contact forces are developed due to the normal and tangential contact laws (force-overlap or force-displacement contact laws). The derivation of a proper law for the tangential contact is usually very challenging because the tangential contact force may be normal contact force and history dependent. At the same time, the normal contact forces may depend on both amount and time rate of change of the overlap (deformation). In order to obtain DE models being representative of the reality the parameters of the contact laws used must be determined from a fit to calibration tests.

5.2. Application of the discrete modeling approach in numerical tribology

Continuum mechanics-based numerical methods are widely used in engineering to model contact mechanics problems, analyze flow of lubricant, simulate frictional heat generation, etc. At the same time, whilst several studies prove that the discrete modelling approach is very powerful for studying static and dynamic behavior of granular materials its application for contact mechanics is less known. The aim of this subchapter is to give a short overview on the application of discrete modelling approach in contact mechanics.

The contact problem of nano-asperities, in several cases, is studied by Molecular Dynamics (MD) simulation which is an extensively used technique of theoretical physics [87]. However, in MD simulations, instead of inter-particle forces inter-atomic forces are computed and summed up before solving Newton's second law of motion. In [80], Anciaux and Molinari treat the 3D contact at nano-scale by using molecular dynamics simulation for interactions of nano-asperities (atomic domain) and finite element technique for long range elastic interactions (continuum mechanics domain). The multi-scale coupling method developed for contact problems was validated on Hertzian and rough surface contacts. In [81], Jerier and Molinari apply the discrete element method for studying the normal contact between a rigid rough (fractal) surface and an elastic body modeled by spheres. The authors of [81] came to the conclusion that the DEM holds some promise to study contact mechanics. Kargulewicz et al. [82] found that the DEM is a promising method to study magnetorheological (MR) fluids at the microscopic and macroscopic scales as an aid to tribological design. MR fluid is defined in [82] as a suspension composing of microscopic iron particles suspended in a carrier fluid and having increasing viscosity due to an external magnetic field. Molecular dynamics simulations of Yang and Persson [67] show that numerical results (contact pressure distribution, real contact area, interfacial separation) for the contact between a rigid solid with a ran-

domly rough surface and an elastic block with a flat surface are in good agreement with the predictions based on continuum contact mechanics. In order to avoid the computationally very expensive simulations (very high number of atoms) a multi-scale modeling approach is proposed. Due to limitations of continuum mechanics models, in [83], Fillot et al. developed a two-dimensional discrete element model to study the flows of third body (detached) particles inside a contact. As the numerical model developed does not allow for particles to leave the contact a stable layer of detached particles forms after a certain degradation time. In order to add the possibility for the particles to leave the contact Fillot et al. [84] propose a three-dimensional discrete element model. It is able to model wear through the simulation of detachment of particles, their flow in the contact and their ejection. The authors came to the conclusion that the classical wear laws (such as Archard's law), assuming that no particle stays in the contact can be considered as a limit case of their model. Mollon [85] applies the concept of Discrete Element Modeling for simulation of friction and wear of rough surfaces. In order to illustrate the capability of the numerical framework using Voronoi polyhedrons for the prediction of friction force and third-body flow pattern a three-dimensional simulation has been performed. Besides emphasizing the importance of proper model calibration the author mentions that researchers dealing with numerical tribology make considerable effort to perform multi-scale modeling through the coupling of DEM and FEM and to incorporate the effect of heat in the discrete models. As it is mentioned by Renouf et al. [130] many variants of the discrete element method are used in tribology. They are frequently applied to simulate the flow of the interface (third body) separating the bodies in contact. Contrary to continuous approaches where conservation principles are used to model the flow of third body, in the discrete approach equations of motion and laws for computation of inter-particle forces are adopted. In [130], Renouf et al. noted that the numerical particle, in many cases, represents elementary volume but not real particle.

5.3. Implementation of the discrete element method in 3D

The study of wall friction with the aid of the discrete element (DE) technique cannot be imagined without efficient and reliable computer code. The three-dimensional discrete element simulations presented in this thesis have been conducted with the aid of a computer code implemented by Goda [93] in C++. The computational algorithm implemented is based on Cundall and Strack's [79] time stepping explicit scheme where the modeling of the motion and interaction of arbitrarily-sized spherical particles involves the execution of many thousands of time steps. At each step, Newton's second law is integrated to obtain updated velocities and new positions from the forces acting on the particles. The contact forces governing both the translational and rotational motion of particles are computed from normal and tangential contact laws. In order to develop a simulation tool which is competitive with commercial discrete element software the author of this thesis made his computer code suitable for input data processing, numerical model specification, graphical visualization, output data processing and graphical/text file creation. The main aim of this chapter is to give insight into the implementation process of this general purpose simulation tool.

Basic assumptions of the computational algorithm implemented are as follows. (a) Particles are rigid bodies and are permitted to overlap with one another (soft contact approach). (b) Contacts occur over a vanishing small area (point contact). (c) The amount of the overlap is related to the contact force via the force-overlap (force-deformation) contact law. (d) The time step chosen is so small that the forces acting on any particle are determined exclusively by its interaction with the particles and walls it is in contact with. (e) The wall elements do not interact with one other, they only interact with particles. The most important characteristics of walls (wall elements) are as follows. (a) Planar walls with three or four edges are used (see Fig. 5.1). (b) Only one side of the wall is considered to be active. (The unit

normal vector \underline{n} of the planar wall identifies the active side of the wall which can handle the ball/wall interaction.) (c) Walls may be activated and deactivated at any time instant of simulation. (d) The position of the walls is fixed. (Dynamic walls and walls constructed from particles are not realized yet.) (e) The active side of the wall is defined by the numbering (labeling) of vertices (right hand rule).

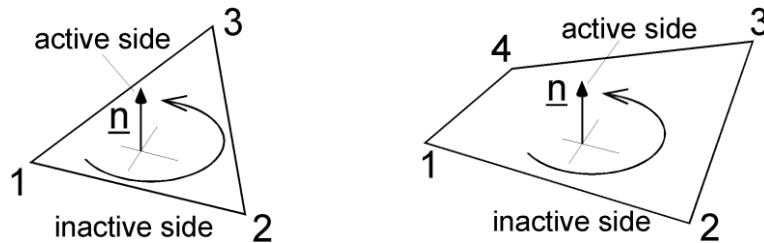


Fig. 5.1. Planar walls with three and four edges

The particles and walls interact with one another via the forces arisen at the contacts. However the position of the walls is specified by the user i.e. forces acting on a wall do not influence its position. The contact force arisen between two particles or a particle and a wall is decomposed into normal component acting in the direction of the unit normal vector and shear (tangential) component acting in the common contact plane. The contact laws relate these two components of contact force to the corresponding components of the relative displacement via the normal and shear stiffness of the contact.

The current version of the program operates in menu-driven mode on any IBM-compatible computers running Microsoft Windows operating system. Graphics facilities implemented in the code allow wireframe and solid-rendered plots to be generated at any time instant (see Figs. 5.2 and 5.3). The graphical user interface allows the user to view the simulation space or its certain part at any stage of the simulation. The model can be magnified on the screen for optimum viewing and all the plotted output can be saved in bitmap files. Additionally, simulation results may be saved in output files for later visualization or processing. The smallest possible model that may be analyzed with the program consists of a single particle. Most problems, however, are defined by assemblies of hundreds or thousands of particles. If two particles are collided, then a point contact forms. Each particle can touch several other particles while the number of contacts can change dynamically as the particles move. The user can specify the numerical model via a data (input) file. This file is created by the user and contains commands, geometrical sizes, parameter values, etc. needed for the definition of discrete element model. The mapping of 3D simulation space onto 2D is realized using both parallel and perspective projection. From particles color or grayscale-rendered while from walls solid-rendered, wireframe or combined plots can be generated at any stage of the simulation (see Fig. 5.3). Techniques and methods of computer graphics used here can be found in Szirmay-Kalos's book [86]. Main advantage of this approach is that it yields a standalone computer code where it is not needed to use external software for graphical visualization. Normal components of the contact forces are displayed graphically through force lines (see Figs. 5.4 and 5.5). The widths of the lines are proportional to the magnitudes of the forces. In case of particle-particle contact, the color of force line is blue and their length is equal to the sum of the radii of the contacting particles. For particle-wall contact the force lines have red color and their length is equal to the distance between the particle center and the contact point.

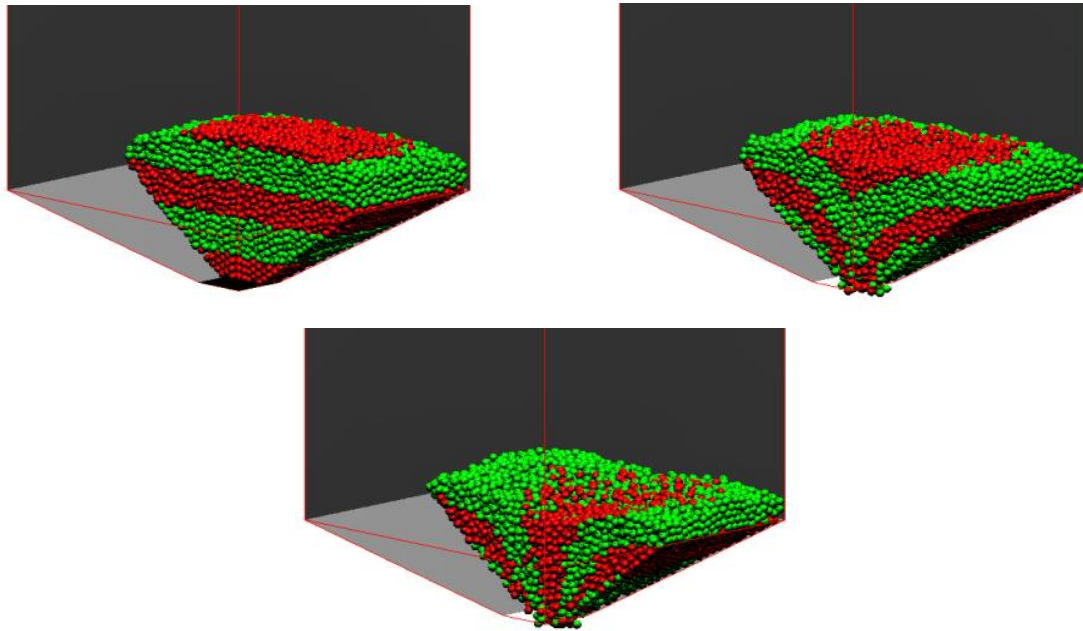


Fig. 5.2. Color-rendered plot of particles and walls. Snapshots from the discrete element software developed.

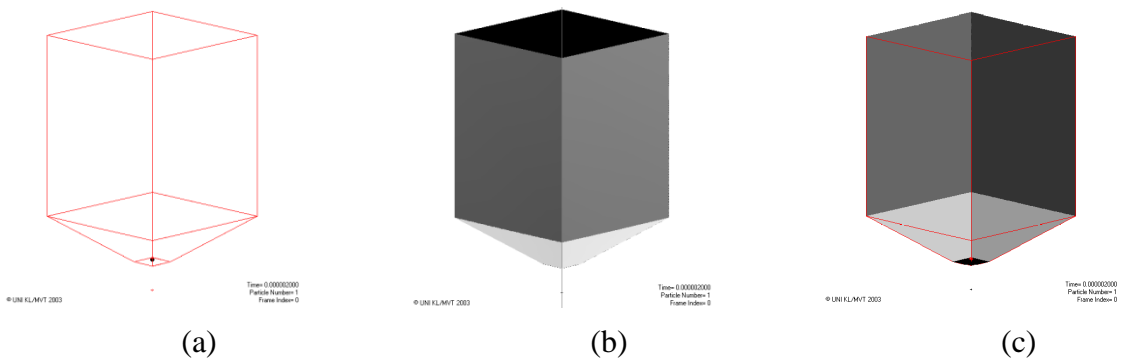


Fig. 5.3. (a) Wireframe, (b) solid-rendered and (c) combined plot of walls. Snapshots from the discrete element software developed.

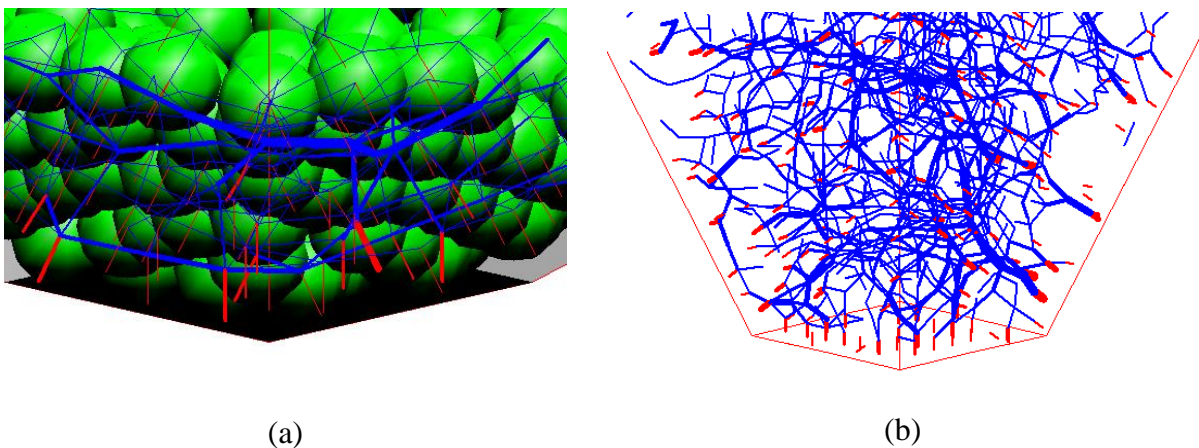


Fig. 5.4. Plots of contact forces (a) with and (b) without particles. Snapshots from the discrete element software developed.

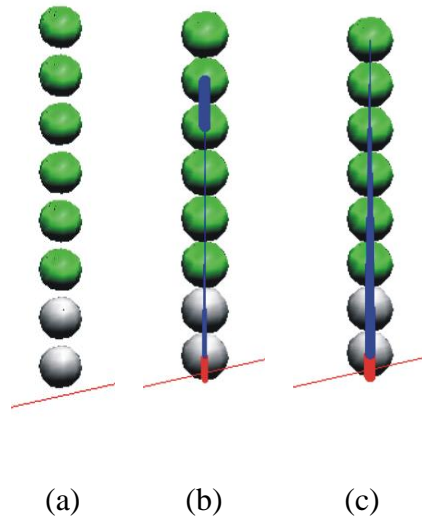


Fig. 5.5. (a) Free falling spherical balls approaching a wall element, (b) contact forces arisen at time instant t_1 , (c) steady-state contact forces. Snapshots from the discrete element software developed.

In order to detect the contacts the simulation space is divided into 3D (cubic) cells (see Fig. 5.6). This method is known in the literature as link-cell or grid method. The size of the grid cells is equal to or slightly larger than the diameter of the largest particle. If the center point of a particle is within a given cell then the particle is assigned to the cell. This approach allows us to identify the interacting particles through the investigation of particles assigned to the neighboring cells only.

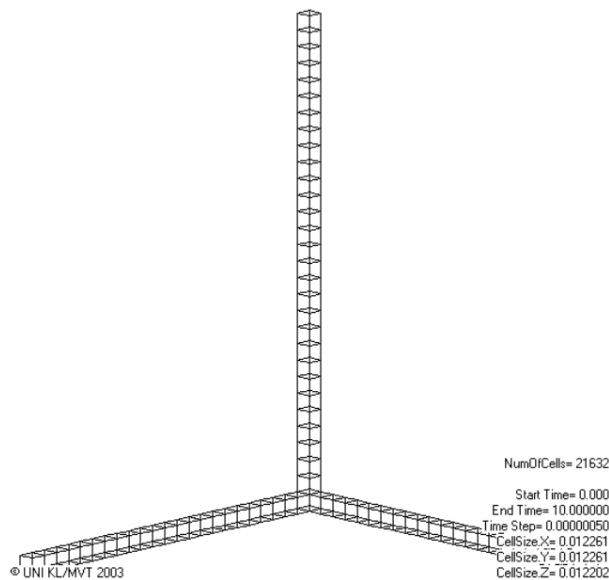


Fig. 5.6. Division of the simulation space into cubic cells. Snapshot from the discrete element software developed. One part of cells is visualized only.

To set up a model and run a simulation it is required to specify the particles (In the current version of the program, creation of new particles and/or removing of already existing particles may be realized at any time instant of the simulation.), the normal and tangential contact law, the material properties and the boundary conditions (wall elements). The re-

sponse of the assembly is studied by adjusting the parameters at particle and contact level. The constitutive behavior is then derived automatically from the contact model and the material properties. When the particle interacts with another particle (particle-particle contact) or with wall element (particle-wall contact) contact force arises. The contact occurs at a single point through which the contact force acts. The role of the contact model is to describe the physical behavior occurring at a contact. Although a particle assembly may exhibit complex nonlinear constitutive behavior, it is achieved through the use of relatively simple contact laws incorporating stiffness properties (normal and shear stiffness). When the shear component of the contact force reaches the maximum allowable shear contact force (defined as the coefficient of friction of the contacting objects multiplied by the magnitude of the clamping force) the objects in contact slide relative to one another (sliding phase).

In order to integrate the equations of motion governing the translational and the rotational motion of particles the method of central differences (Feynman-Newton method) with a fixed time step Δt is used. Most important advantage of this method is the fastness and the great accuracy. The method can be summarized as follows: the position of a particle is computed at the end of a time step by using the velocity in the middle of a Δt interval.

$$x(t + \Delta t) = x(t) + v(t + \frac{1}{2} \Delta t) \Delta t, \quad (5.3)$$

where $x(t)$ is the particle position at time t . In order to find the velocity halfway through the Δt interval, the following equation is used:

$$v(t + \frac{1}{2} \Delta t) = v(t - \frac{1}{2} \Delta t) + a(t) \Delta t, \quad (5.4)$$

where a is the acceleration of the particle. To start the calculation, the following equation can be used:

$$v(\frac{1}{2} \Delta t) = v(0) + a(0) \frac{\Delta t}{2}. \quad (5.5)$$

In order to compute the contact forces simple contact laws are implemented. When two particles or a particle and a wall are in contact, the normal component of the contact force is given by the Hertz-Kuwabara-Kono equation [87] derived for viscoelastic materials (nonlinear spring resulting in repulsive (Hertz) force connected parallel with viscous dissipation resulting in velocity-dependent damping):

$$F_n = -k_n \xi_n^{3/2} - \gamma_n \xi_n^{1/2} v_n, \quad (5.6)$$

where k_n is a stiffness parameter connecting to the material properties, ξ_n is the overlap between the contacting entities, γ_n is a damping parameter characterizing the inelastic behavior and v_n is the normal component of the relative velocity defined at the contact point. As reported by Schäfer et al. [87] this normal contact law gives velocity dependent collision time and decreasing coefficient of normal restitution (ratio of the relative normal post-collisional and pre-collisional (initial) velocity) with increasing initial relative normal velocity in agreement with experimental results. Since the cohesion is not taken into consideration in the current version of the computer code, the normal contact force computed is always repulsive. As the reduced mass (m_{eff}) is not involved in the damping term of Eq. 5.6 the contact model is unable to take into consideration the mass dependence of the coefficient of normal restitution as it is concluded by Schäfer et al. [87]. The tangential contact law implemented takes into consideration both the tangential elasticity and the Coulomb friction law. The former allows coefficient of tangential restitution (ratio of the relative tangential post-collisional and pre-

collisional velocity) to be not only positive but also negative while the latter limits the magnitude of the tangential (friction) force. The negative coefficient of tangential restitution indicates that the direction of the tangential velocity is changed during the collision. The tangential contact law implemented may be written as ([87])

$$F_t^* = -k_t \xi_t - \gamma_t v_t, \quad (5.7)$$

where k_t and ξ_t are the stiffness and elongation of a “virtual” spring, γ_t is a damping constant and v_t is the tangential component of the relative velocity defined at the contact point. At this point, however, it must be mentioned that the damping constant γ_t has no clear physical interpretation [87]. In order to obtain a non-zero friction force at rest (when $v_t=0$), a “virtual” tangential spring (“Cundall spring” [79]) is located between the contacting entities when two particles or a particle and a wall start to touch one another. The total elongation of this spring is set to zero at the initiation of the contact and then it is integrated over the entire collision time:

$$\xi_t(t_i) = \xi_t(t_{i-1}) + \int_{t_{i-1}}^{t_i} v_t dt. \quad (5.8)$$

When contacting entities are no longer in contact with one other the “virtual” spring is removed. According to the Coulomb criterion, the maximum possible value of the frictional force, however, is proportional to the normal (clamping) force multiplied by the dynamic coefficient of friction μ . Consequently, the tangential contact law may be written as

$$F_t = \min(F_t^*, -\text{sgn}(v_t)\mu|F_n|). \quad (5.9)$$

In the case of sliding, the elongation of the tangential spring is frozen at a value of $\mu F_n/k_t$ that is in accordance with the Coulomb criterion. As it is pointed out by Schäfer et al. [87] the normal and tangential contact laws used here give results being in agreement with the experimental results as long as the model parameters are selected with care. [87], among others, is concerned in depth with the calibration of model parameters too. The experiments of Foerster et al. ([91]) on cellulose acetate spheres with diameter of 6 mm are used for this purpose. According to Schäfer et al. [87] the non-linear normal stiffness connected to the elastic properties and to the radii of the spheres through

$$k_n = \frac{4}{3} \sqrt{R_{\text{eff}}} E_{\text{eff}}, \quad (5.10)$$

where $R_{\text{eff}} = (R_1 R_2)/(R_1 + R_2)$ is the effective radius and E_{eff} is related to Young’s modulus E and Poisson’s ratio ν of contacting spheres through $1/E_{\text{eff}} = (1 - \nu_1^2)/E_1 + (1 - \nu_2^2)/E_2$. For Foerster et al.’s cellulose acetate spheres $k_n = 9 \cdot 10^7 \text{ N/m}^{3/2}$. The damping constant γ_n is connected to the radii of the spheres and the two coefficients of bulk viscosity [87]. For Foerster et al.’s cellulose acetate spheres the measured coefficient of normal restitution for initial relative normal velocities varying between 0.29 and 1.2 m/s is $e_n \approx 0.87$ which results in damping constant of $\gamma_n = 190 \text{ kg/m}^{1/2}\text{s}$. As it is mentioned by Schäfer et al. [87], the ratio k_t/k_n determines the results of an oblique collision where the numerical value of k_t is nearly 1000 times smaller than that of k_n . Additionally, it is also concluded that k_t has to be set such that for one particular impact velocity, the ratio of the duration of the tangential as well as the normal collision to be about one ($t_t/t_n \approx 1$). In case of non-linear repulsive (Hertz) force the velocity-dependent duration of the normal collision is [87]

$$t_n = 3.21 \left(\frac{m_{\text{eff}}}{k_n} \right)^{2/5} v_n^{-1/5}, \quad (5.11)$$

where $m_{\text{eff}} = (m_1 m_2) / (m_1 + m_2)$ is the effective mass and v_n is the initial relative normal velocity. Using the ‘‘Cundall spring’’ the duration of the tangential collision is [87]

$$t_t = \pi \left(\frac{k_t}{m_{\text{eff}}} \left(1 + mR^2 / I \right) \right)^{-1/2}, \quad (5.12)$$

where $I = \frac{2}{5} mR^2$ is the mass moment of inertia. For Foerster et al.’s cellulose acetate spheres $k_t = 9.45 \cdot 10^4 \text{ N/m}$ if $t_t / t_n = 1$ at $v_n = 1 \text{ m/s}$. With these parameters and a time step of $\Delta t = t_n / 100$, the numerical predictions of Schäfer et al. [87] were in good agreement with Foerster et al.’s experimental data.

5.4. Application of the computer code developed by the author of the thesis for wall friction prediction

In this chapter, the three-dimensional simulation tool of the author of this thesis is applied for the simulation of wall friction in three-dimensional hoppers/silos. The results presented here were reported in Goda and Ebert [93].

In order to design silos/hoppers properly and to avoid silo collapse the designer has to predict accurately, among others, the friction force and the pressure acting on the walls and the bottom of the hopper/silo for both filling and discharge. Although the hopper flow is intensively studied in the literature, the former three-dimensional DE simulations had been concentrated on cylindrical/conical (axisymmetric) hoppers only. In contrast, Goda and Ebert [93] focused on rectangular hoppers and silos and not only the hopper flow and the spatial distribution of wall forces/pressures but also the effect of hopper/silo geometry on static and dynamic behavior were investigated quantitatively in 3D. Additionally, before 2005, the majority of DE simulations studied hopper/silo flow in 2D and only a few three-dimensional simulations were available in this field. It must also be mentioned that the number of particles involved in the preceding analyses was, practically without exception, much smaller than used in the work of Goda and Ebert [93].

5.4.1. Literature results

Containers with a variety of shapes are widely used in industry for storage of granular materials. The wall stresses arisen at the end of the initial fill and during the subsequent discharge can be predicted on the basis of both analytical and numerical computations. Recently, two numerical methods are widely used to study the mechanical behavior of granular materials in containers: the continuum mechanics-based finite element method (FEM) and the discrete element method (DEM). The applicability of continuum mechanics for hopper flow, however, is strongly limited because it is unable to take into consideration the discrete nature of granular materials. On the other hand, the DEM is a powerful numerical method, in which the motion of each individual particle is determined on the basis of all the forces acting upon it (see the study of Cundall and Strack [79]). Contrary to the continuum techniques it simulates effects at particle level.

Many reports exist on hopper flow, but most of them are concerned with two-dimensional simulation and use cylindrical particles, as in the studies of Ristow and Herrmann [88], Masson and Martinez [89] and Sanad et al. [90], to simplify the mathematical

treatment and reduce the computer memory requirements. Additionally, in most cases, the numerical investigations are performed by using commercial computer codes. The two-dimensional DE analyses provide satisfactory results for several problems but there are many phenomena and effects (e.g. effect of the real three-dimensional geometry on hopper flow and wall forces/pressures) that require three-dimensional approach. In Langston et al.'s paper [92], two and three dimensional discrete element simulations have been carried out for filling and discharge under gravity from model hoppers as well as studying the granular flow and the wall stresses. The granular material was modeled as an assembly of non-cohesive discs (2D) and spheres (3D). In 3D, the number of particles was 8000 and only axisymmetric (cylindrical, conical) hoppers were studied. The normal contact laws applied (linear spring-dashpot model, Hertz law with linear damping), however, were less realistic. As it has been presented by Schäfer et al. [87], the linear spring-dashpot model gives a coefficient of normal restitution being independent of the relative initial or pre-collisional normal velocity while the Hertz law combined with linear damping results in increasing coefficient of normal restitution with increasing relative pre-collisional normal velocity. At the same time, the measurements cited by Schäfer et al. [87], shows clearly that the coefficient of normal restitution usually decreases slightly as the relative pre-collisional normal velocity increases. In [92], Langston et al. concluded that the results for discharge rate and wall stress are in good agreement with that of corresponding continuum theories and empirical predictions.

The granular flow in three-dimensional cylindrical hoppers with flat bottom was investigated in depth by Zhu and Yu [136-138]. In [136], the spatial and statistical distributions of interaction forces and their dependence on the geometric and physical properties of hopper and particles were analyzed. However, the spatial distribution of wall forces/pressures obtained by DEM was not reported. The relationship between the normal force and the normal deformation was described by the Hertz law with linear viscous damping which, contrary to the experimental observations, gives a coefficient of normal restitution increasing with the relative normal pre-collisional velocity [87]. As in the normal contact law, a linear viscous damping appeared also in the tangential contact law. It must be mentioned, however, that the parameters of the contact models were not calibrated experimentally. The granular material filled in the cylindrical silo was modelled as an assembly of 24000 multi-sized spherical particles of uniform size distribution in a range of $0.8-1.0d$, where d denotes the maximum particle diameter. The flow investigated is steady-state because the particles discharged were filled back to the hopper. It was observed that large forces are experienced by particles at the walls around the bottom corner and the distribution of the total force is affected by the geometry and physical parameters of the hopper and particles. In [137], the macroscopic properties (velocity, mass density, and stress components) of steady-state hopper flow (discharging particles to be filled back) were determined by averaging microscopic data (velocities of particles, interaction forces between particles and particles and walls) obtained from three-dimensional discrete element simulation. The hopper (cylindrical hopper with flat bottom), the size and number of particles, the contact laws and their parameters were the same as in [136]. It was shown that the interaction forces between particles and between particles and walls contribute directly to the magnitude of normal and shear stress components. Large vertical and radial normal stresses were observed in the region close to the bottom corner while large shear stresses appeared in the region adjacent to the vertical wall. It was also pointed out that the magnitude of stress components depends on the geometric and physical parameters of the hopper and the particles. In [138], the unsteady-state hopper flow (discharging particles not to be filled back) was studied by three-dimensional discrete element simulation. The hopper, the number and the size of the particles, the normal and tangential contact laws were the same as in [136]. Additionally it was assumed that the wall and particle properties, excepting the coefficient of sliding friction, are the same. The numerical results showed that the trends of the

stress distribution in unsteady-state hopper flow are similar to those of steady-state hopper flow. However, the magnitude of the stress components in different regions had different rates of variation. The magnitudes of the vertical and the radial normal stress components (obtained by averaging microscopic quantities) varied little with time in the orifice region, but decreased in other regions. The magnitude of the shear stresses far from the bottom wall and central axis of the hopper decreased also with time. A detailed review on the three-dimensional DE modelling of hopper flow can be found in the review paper of Zhu et al. [139].

5.4.2. Discrete element simulations for nonaxisymmetric hoppers/silos filled with viscoelastic granular material

The main aim of this work is (a) to determine how many percentage of the weight of the initial material head (static case) is carried by the friction forces arising on the walls, and (b) to investigate the behavior of granular material and the wall pressure after the initial fill (static state) and during the discharge (dynamic state) of different containers. Here, a system of 40,000 mono-sized cellulose acetate spheres of diameter $d=6\text{mm}$ is considered (total weight of the spheres is $G=58.546\text{ N}$) although the program developed allows to investigate also the effect of particles with different diameters on the flow behavior. As the diameter of the cellulose acetate spheres is the same as that of Foerster et al.'s acetate spheres it was not needed to take into consideration the mass dependence of the coefficient of normal restitution (e_n). For numerical investigations, the following container types have been chosen: a pyramidal (wedge-shaped) hopper (Fig. 5.7a), a silo with a hopper bottom (Fig. 5.7b), and a vertical-sided silo with a flat bottom (Fig. 5.7c). The hopper has an opening angle $\theta=20^\circ$ and a square cross section. The silo with a hopper bottom is $72d$ in height, has a square cross section with a size of $30d \times 30d$ and a converging section with a hopper half angle of $\theta=35^\circ$. The flat-bottomed silo is $85d$ in height and has a square cross section with a size of $27d \times 27d$. In all the cases studied, the size of the outlet on the bottom plate is $8d \times 8d$ and it has a square cross section. With these sizes, the height of the densely packed configuration of particles at rest is approximately the same in each case. The only external force acting on the system is the gravitational force ($g=9.81\text{ m/s}^2$). At the beginning of the simulations, the containers were filled by regularly located, non-overlapping particles. While particles had no initial velocity in the case of the hopper, a small random initial velocity is assigned to each particle in the other two cases. Subsequently, the systems are allowed to settle in order to obtain densely packed configurations before the container opening. At the end of settling, the static packing height of the particles is about 0.3m in all the cases studied. The outlets are kept closed during the settling process. Based on preliminary computations, a settling time of 1.5s has been specified for each simulation. At $t=1.5\text{s}$, the outlets are opened and at the same time the discharge of containers is started. During the simulation the equations of motion belonging to the translational as well as the rotational motions are integrated by using the Feynman-Newton method with a fixed time step of $\Delta t = 5 \cdot 10^{-7}\text{ s}$.

The material properties of the acetate sphere used in the present study and the parameters of the contact models are listed in Table 5.1. Here it is assumed that the maximum impact velocity during the simulations is about $v_{max}=1\text{m/s}$. On the basis of test calculations, a value of $190\text{ kg/m}^{1/2}\text{s}$ was selected for the normal damping parameter in order to achieve $e_n \approx 0.87$ [87]. e_n is the coefficient of normal restitution. Since the parameter γ_t has no clear physical interpretation (see the study of Schäfer et al. [87]), its value is chosen to be equal to zero in the present analysis. As a first assumption, the same stiffness and damping parameters are used for both the particle/particle and the particle/wall collisions in the simulations. Finally, it must be mentioned that proper calibration of a discrete element model can be performed

based on experimental observations and measurements only. In this regard, the model parameters used here can be considered to be calibrated because the experimentally calibrated parameters of Schäfer et al. [87] were applied in the simulations.

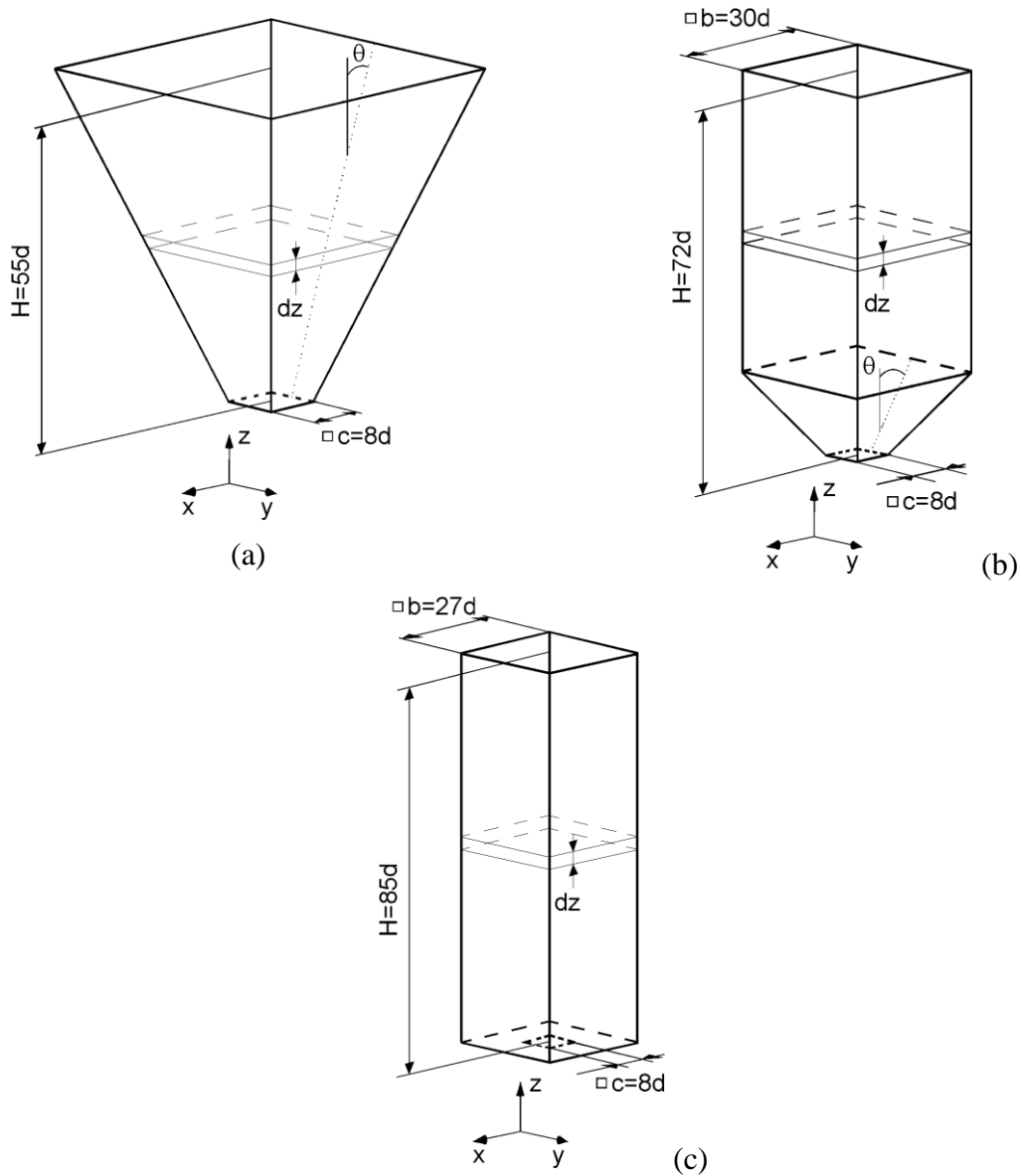


Fig. 5.7. Geometry details of the containers studied: (a) pyramidal hopper, (b) silo with a hopper bottom, and (c) silo with a flat bottom (d is the particle diameter) [93]

Acetate particle		Parameters of the contact models	
Young's modulus [N/m^2]	$3.2 \cdot 10^9$	k_n [$\text{N/m}^{3/2}$]	$9 \cdot 10^7$
Poisson's ratio	0.28	γ_n [$\text{kg/m}^{1/2}\text{s}$]	190
Density [kg/m^3]	1319	k_t [N/m]	$9.45 \cdot 10^4$
		γ_t [kg/s]	0
		μ	0.3

Table 5.1. Material properties and contact parameters [93]

5.4.3. Results for hopper

Fig. 5.8 shows snapshots of the settling process. Only the half of the particle assembly is visualized in order to obtain an insight into the interior of the granular material. The same way of presentation is followed for all the cases studied. At the beginning of simulation, the particles (balls with the same diameter) with zero initial velocity are located regularly within the hopper. Due to the friction and damping forces the motion of particles (caused by the gravitational force) decays as the time increases. The total kinetic energy of the system as a function of time (Fig. 5.9) represents clearly this process. Although the system has a small kinetic energy at the end of the settling process (settling time= 1.5 s) practically the system of spheres (balls) can be considered to be at rest at $t=1.5$ s.

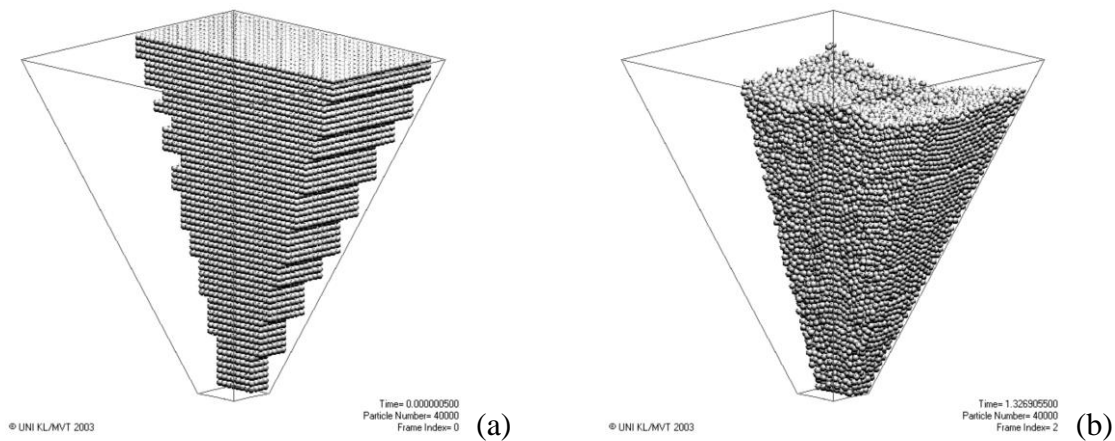


Fig. 5.8. Position of particles during settling in the case of hopper: (a) at $t=0s$ (initial configuration), and (b) at $t=1.327 s$ [93]

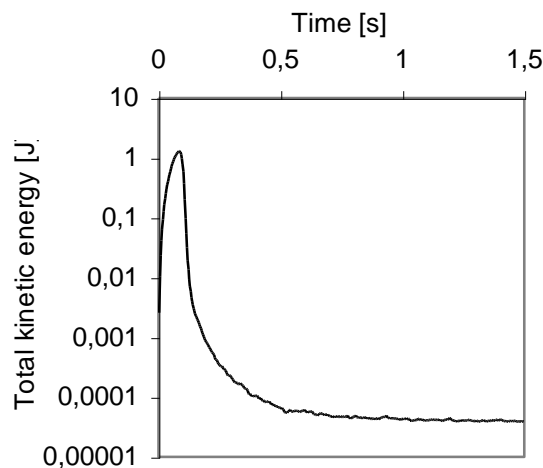


Fig. 5.9. Total kinetic energy (translational and rotational) of the system as a function of time in the case of hopper [93]

At $t= 1.5$ s, the outlet is opened and the hopper discharge is started. To indicate the characteristic motion of the granular material one portion of the particles is shaded by dark gray which yields a pattern of bands. Fig. 5.10 shows snapshots of the granular material flowing out of the hopper. The motion of the particles can be followed easily through the movement of the interfaces between the bands. The interfaces deform across the whole cross section of the hopper and have a characteristic “V” shape within a section located parallel to the

y - z plane. Distributions of the absolute velocity and the absolute angular velocity at $t=2.45$ s are shown in Figs. 5.11-5.12. The gray code of the individual particles indicates the magnitude of the depicted quantity. Since all the particles have the same diameter and mass, the tendencies of the translational and rotational kinetic energy distributions were similar to Figs. 5.11-5.12. As anticipated, the most intensive flow appears near and above the outlet. Near the walls, the particles move slower than in the center region of the granular material.

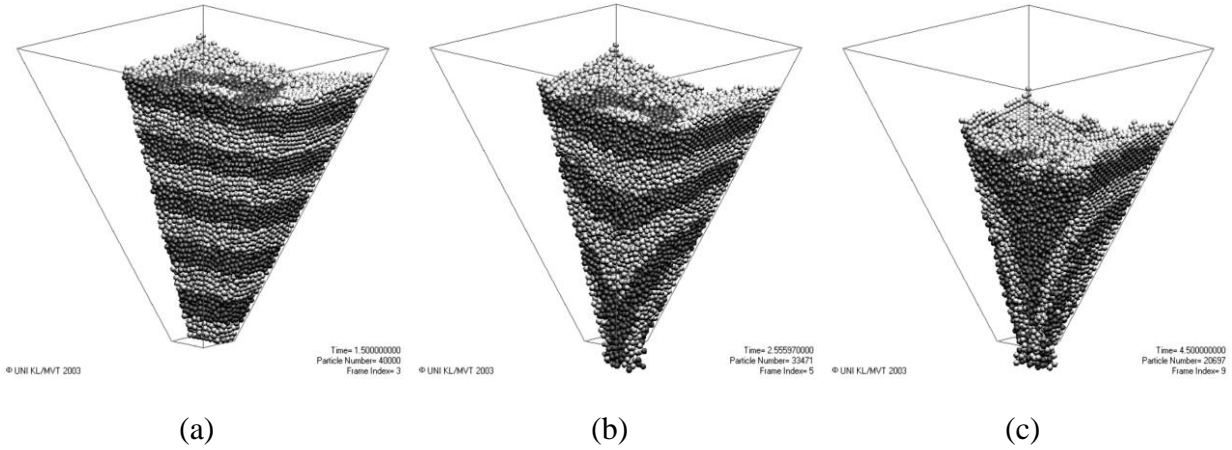


Fig. 5.10. Flow patterns at different simulation times in the case of hopper: (a) at $t=1.5$ s (static state at the end of the filling process), (b) at $t=2.55$ s, and (c) at $t=4.5$ s [93]

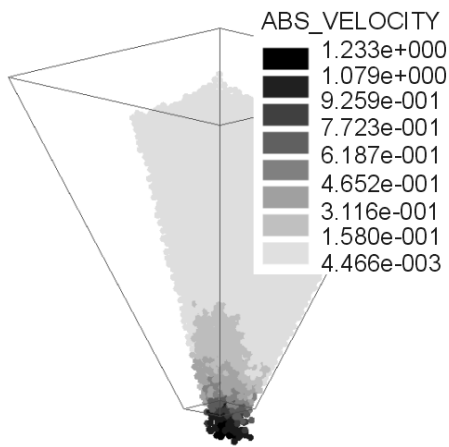


Fig. 5.11. Absolute velocity distribution at $t=2.45$ s in the case of hopper (in m/s);

$$\left(v_{\text{abs}} = \sqrt{v_x^2 + v_y^2 + v_z^2} \right) [93]$$

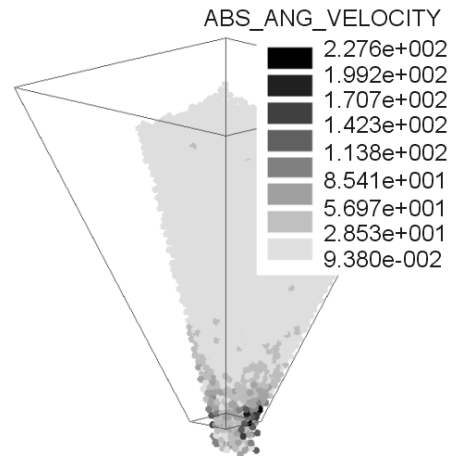


Fig. 5.12. Absolute angular velocity distribution at $t=2.45$ s in the case of hopper (in 1/s) (the depicted quantity is derived in the same manner as in Fig. 5.11) [93]

In the case of static state ($t=1.5$ s), the distributions of normal wall forces and mean wall pressures along the walls as a function of height from the bottom of the hopper are shown in Fig. 5.13. The distributions of the normal wall forces are represented on the basis of the normal component of particle/wall contact forces. In this study, the expression normal wall force is used as a synonym for the normal component of particle/wall contact force. The sum of the normal forces (resultant normal force) acting on the horizontal wall of Fig. 5.13 is $\Sigma F_{\text{bottom}}=5.17$ N. For the right and the left wall of Fig. 5.13, these values are as follows: $\Sigma F_{\text{right}}=34.17$ N, $\Sigma F_{\text{left}}=33.65$ N. In case of granular materials, one part of the weight of the initial material head obtained at the end of the filling process is carried by the friction forces

arising on the walls. The contribution of friction forces can be determined from the equilibrium of forces as

$$\Sigma F_{bottom} + 4\bar{F}_{N,z}^{wall} + 4\bar{F}_{fric,z}^{wall} = G, \quad (5.13)$$

where $\bar{F}_{N,z}^{wall}$ and $\bar{F}_{fric,z}^{wall}$ denote the z component of the total normal force and the total friction force arising on a single inclined wall ($\bar{F}_{N,z}^{wall} = \bar{F}_N^{wall} \sin \Theta = \frac{\Sigma F_{right} + \Sigma F_{left}}{2} \sin \Theta$). The simulation shows that about 12% of the weight of the initial material head is carried by the friction forces arising on the walls. Additionally, it can also be concluded that mostly the inclined walls carry the weight of the granular material.

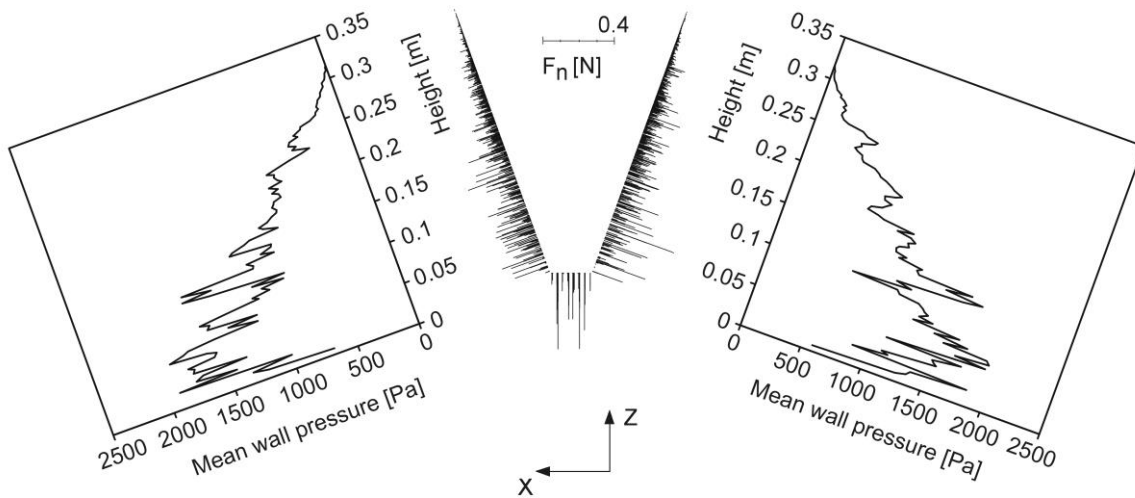


Fig. 5.13. Distributions of normal wall forces and mean wall pressures acting on the walls of the hopper at the end of the filling process (at $t=1.5$ s). The expression normal wall force is a synonym for the normal component of particle/wall contact force. [93] Contrary to Figs. 5.4 and 5.5 here not the width but the length of the lines representing contact forces is proportional to the magnitude of the force.

The wall pressures are averaged on a wall segment of height dz (see Fig. 5.7a). In the present study, dz is taken to $2d$. For each evaluation the segment boundary is moved by half particle diameter in vertical direction (z -direction). In the case of a given wall, the height dz belongs to a trapezoid-shaped wall segment. In order to compute the mean wall pressure, as a first step, the normal forces acting on the actual wall segment are summed. The mean wall pressure (moving average) is defined as the total force acting perpendicular to a wall segment divided by the area of the wall segment. Since the mean wall pressure distribution is computed from the normal component of the particle/wall contact forces, it shows a fluctuation along the wall. It must be noted that the fluctuation is strongly affected by the averaging method applied to the pressure computation. It can be seen clearly that there is no significant deviation from linear pressure dependence in Fig. 5.13. As it is well known, the wall pressure acting on the walls of a container filled with any fluid decrease linearly with increasing height because no shear forces are exerted between the fluid and the solid boundary if the fluid is at rest. Contrary to fluids, in the case of real granular material, the static wall pressures reach a constant, height-independent value at a sufficiently large depth below the free surface (pressure saturation) because the shear forces transfer one portion of the weight of the granular material to the walls. This tendency can hardly be identified in Fig. 5.13. The reason for this is that the system modeled is not sufficiently high to show unambiguously this tendency; so,

only the linear approximation of the wall pressure distribution valid in the neighborhood of the free surface is described. In order to determine the wall pressure distribution during the outflow, the pressures are averaged both on a wall segment of height dz and over 1000 time steps. In the case of hopper, the mean wall pressure distribution during discharge is shown in Fig. 5.14. The results reported here are in accordance with both the two-dimensional ones of Ristow and Herrmann [88] and the analytical calculation of Walters [94].

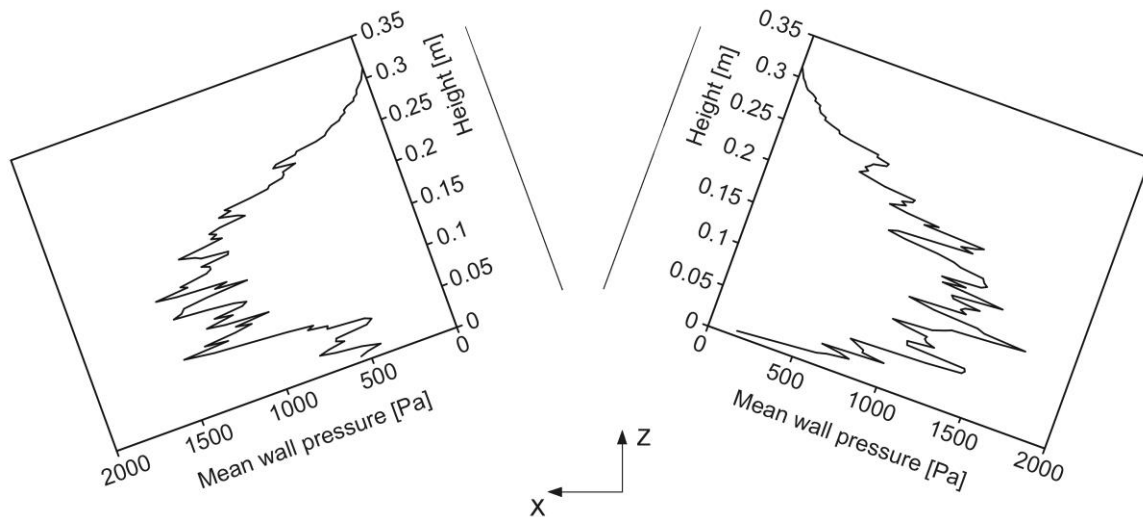


Fig. 5.14. Mean wall pressure distribution along the walls in the case of hopper outflow (at $t=1.8\text{ s}$) [93]

5.4.4. Results for silo with a hopper bottom

In this case, a small, randomly distributed velocity is assigned to the particles in order to obtain an irregular densely packed configuration before the silo opening. During settling, the total kinetic energy vs. time function has a similar tendency as shown in Fig. 5.9. The snapshots of the settling process, shown in Fig. 5.15, illustrate clearly the motion of the particles. Figs. 5.15b and 5.15c show an enlarged segment of the silo. The static, densely packed configuration of particles together with the banded pattern can be seen in Fig. 5.16a.

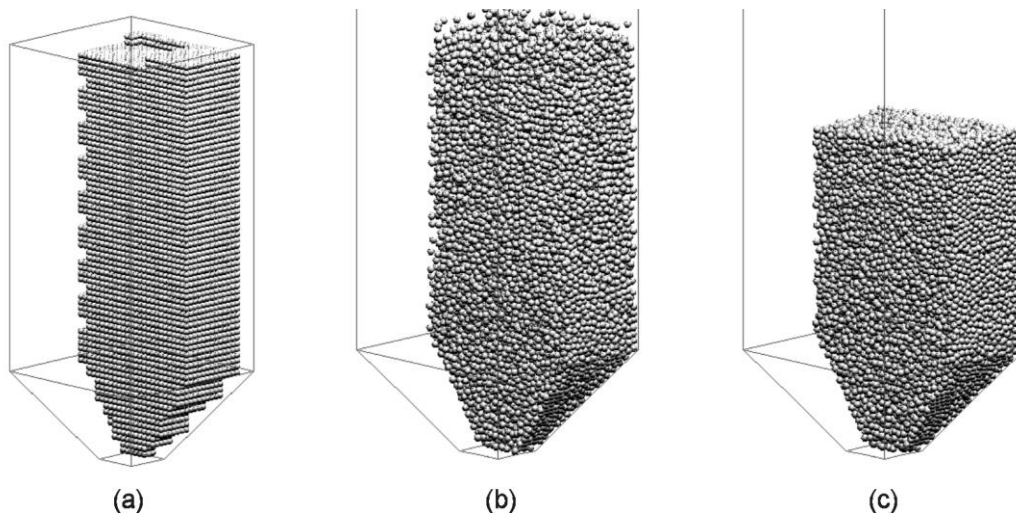


Fig. 5.15. Position of particles during settling in the case of silo: (a) at $t=0\text{ s}$ (initial configuration), (b) at $t=0.1\text{ s}$, and (c) at $t=1\text{ s}$ [93]

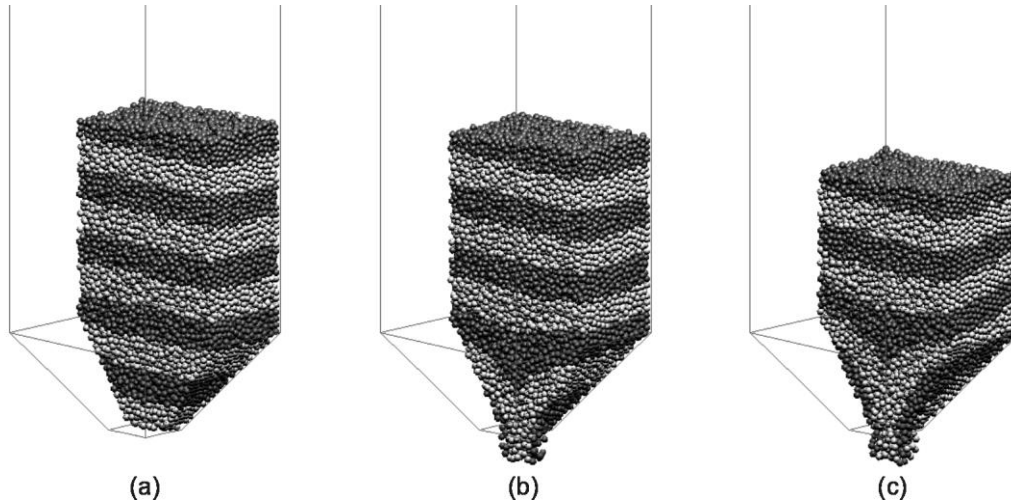


Fig. 5.16. Flow patterns at different time instants in the case of a silo: (a) at $t=1.5$ s (static state at the end of the filling process), (b) at $t=2$ s, and (c) at $t=3.25$ s [93]

At $t=1.5$ s, the silo is opened to initiate the silo discharge. The motion of particles and the deformation of the interfaces between the bands during discharge are shown in Fig. 5.16. Similar to the previous case, the interfaces deform across the whole cross section of the silo and have a characteristic “V” shape within a section located parallel to the y - z plane. Since the absolute velocity distribution has a similar tendency as shown in Fig. 5.11 for the hopper flow, the v_y velocity component at $t=2.48$ s is presented here (see Fig. 5.17). The absolute angular velocity is represented in Fig. 5.18. The figures make clear that the flow is the most intensive near and above the outlet.

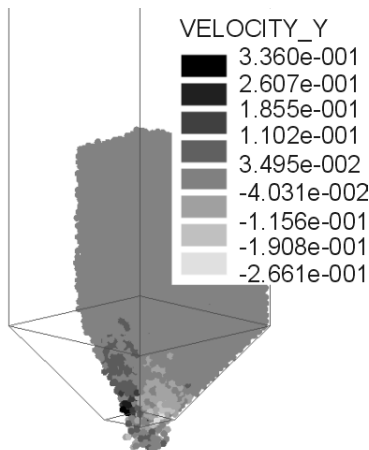


Fig. 5.17. The v_y velocity component at $t=2.48$ s in the case of silo (in m/s) [93]

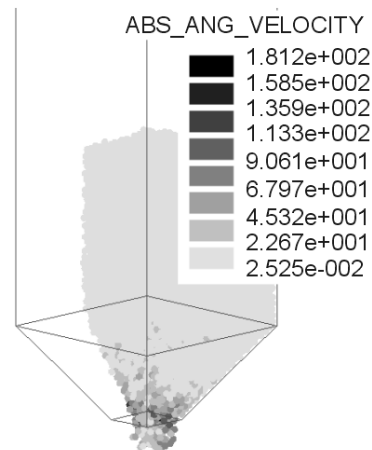


Fig. 5.18. Absolute angular velocity distribution at $t=2.48$ s in the case of silo (in 1/s) [93]

In case of the silo, the mean wall pressures are plotted horizontally for both the vertical-sided and the hopper sections. As Fig. 5.19 shows, at the end of the filling process, the wall pressures in the hopper section are slightly above those predicted from the extension of the near linear dependence, which was obtained for the vertical-sided section of the silo. The sum of the normal forces acting on the horizontal wall of Fig. 5.19 is $\Sigma F_{bottom}=5.19$ N. For the walls of vertical and hopper sections of the silo located on the right side, the sums of normal forces are as follows: $\Sigma F_{right\ vertical}=19.49$ N, $\Sigma F_{right\ hopper}=19.42$ N. For the left side of Fig. 5.19 these forces are $\Sigma F_{left\ vertical}=19.61$ N, $\Sigma F_{left\ hopper}=19.95$ N. As it has already been mentioned one

part of the weight of the initial material head is carried by the friction forces arising on the walls. In this case, the contribution of friction forces can be determined from the equilibrium of forces as

$$\Sigma F_{bottom} + 4\overline{F}_{N,z}^{inclined\ wall} + 4\overline{F}_{fric,z}^{vertical\ wall} + 4\overline{F}_{fric,z}^{inclined\ wall} = G, \quad (5.14)$$

where $\overline{F}_{N,z}^{inclined\ wall}$ and $\overline{F}_{fric,z}^{inclined\ wall}$ denote the z component of the total normal force and the total friction force arising on a single inclined wall while $\overline{F}_{fric,z}^{vertical\ wall}$ is the z component of the total friction force arising on a single vertical wall

($\overline{F}_{N,z}^{inclined\ wall} = \overline{F}_N^{inclined\ wall} \sin \Theta = \frac{\Sigma F_{righthopper} + \Sigma F_{lefthopper}}{2} \sin \Theta$). The simulation shows that

about 14% of the weight of the initial material head is carried by the friction forces arising on the walls. Additionally, it can also be concluded that mostly the inclined walls carry the weight of the granular material.

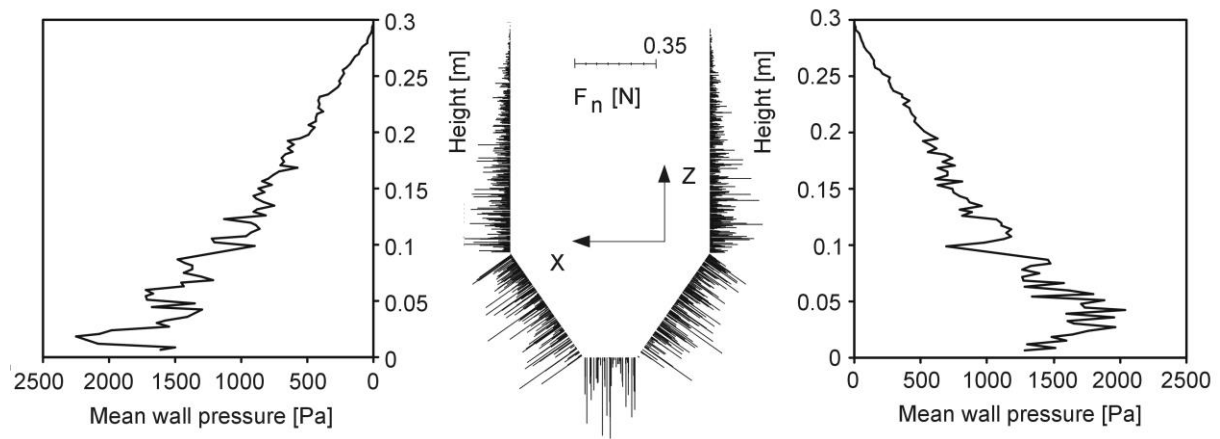


Fig. 5.19. Distributions of normal wall forces and mean wall pressures acting on the walls of the silo at the end of the filling process (at $t=1.5\ s$) [93] Contrary to Figs. 5.4 and 5.5 here not the width but the length of the lines representing contact forces is proportional to the magnitude of the force.

As it can be seen from Fig. 5.20, the hopper bottom has a strong effect on the wall pressures that develop during discharge. The mean wall pressure increases with increasing depth measured from the free surface of the granular material. At the transition from the vertical-sided section to the hopper bottom, a pressure peak occurs, which is a consequence of the sudden change in wall slope. For similar reason, the pressures are greater below the transition than above it. The peak value in the hopper section is about two times greater than the one in the vertical-sided section. The pressure distributions obtained here are in accordance qualitatively with both Walters's analytical [94] and Yang and Hsiau's two-dimensional numerical [95] results.

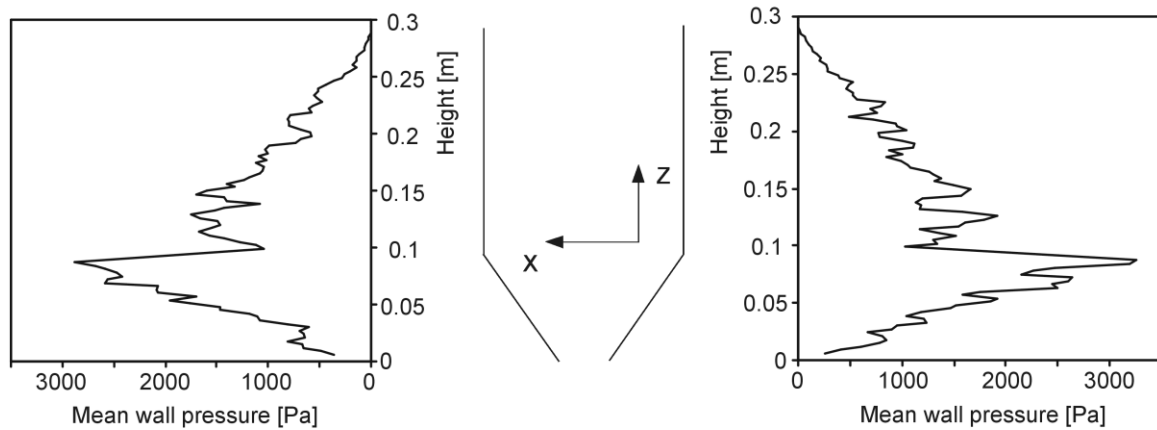


Fig. 5.20. Mean wall pressure distribution along the walls in the case of silo outflow (at $t=1.8$ s) [93]

5.4.5. Results for flat-bottomed silo

Similar to the previous case, the regularly generated particles (Fig. 5.21a) have a small, random initial velocity at the beginning of simulation. The transition from a regularly, loosely packed configuration to an irregular, densely packed one is illustrated in Fig. 5.21. The snapshots of the settling process show the position of particles at different time steps. In Figs. 5.21b-d, the lower part of the flat-bottomed silo is enlarged. The static, densely packed configuration has a height of 0.3 m.

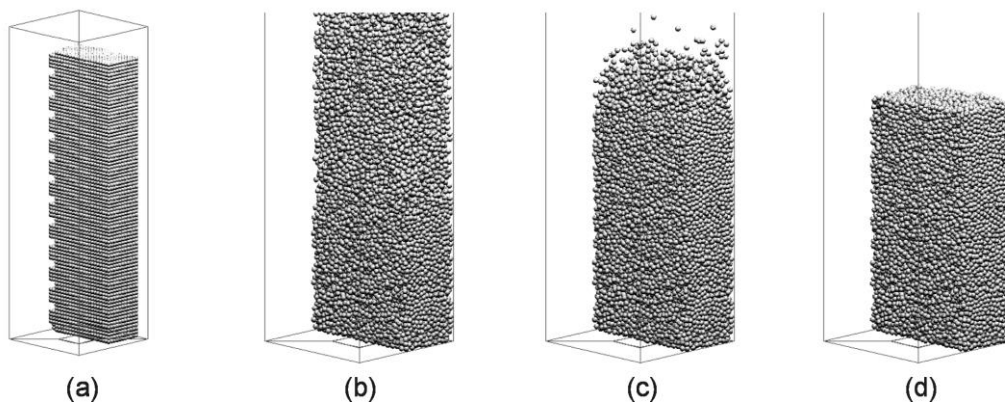


Fig. 5.21. Position of particles during settling in the case of flat-bottomed silo: (a) at $t=0$ s (initial configuration), (b) at $t=0.15$ s, (c) at $t=0.2$ s, and (d) at $t=1$ s [93]

Comparison of Fig. 5.22 with Figs. 5.10 and 5.16 shows that the flow pattern is more concentrated than in the other two cases. The flow is most intensive near and above the outlet and the deformation of interfaces between the bands is strongly localized. From the velocity distributions, shown in Figs. 5.23 and 5.24, similar conclusions can be drawn.

In the case of static state, the mean wall pressure distribution as a function of height is represented in Fig. 5.25. There is no significant deviation from linear pressure dependence due to the small size of the model measured in vertical direction (z -direction). The sum of the normal forces acting on the horizontal wall of Fig. 5.25 is $\Sigma F_{bottom}=48.88$ N. For the right and the left wall of Fig. 5.25, these values are as follows: $\Sigma F_{right}=37.82$ N, $\Sigma F_{left}=37.55$ N. The part of the weight of the initial material head that is carried by the friction forces arising on the walls can be determined from the equilibrium of forces as

$$\Sigma F_{bottom} + 4\bar{F}_{fric,z}^{wall} = G, \quad (5.15)$$

where $\bar{F}_{fric,z}^{wall}$ denotes the z component of the total friction force arising on a single vertical wall. The simulation shows that about 16.5% of the weight of the initial material head is carried by the friction forces arising on the vertical walls.

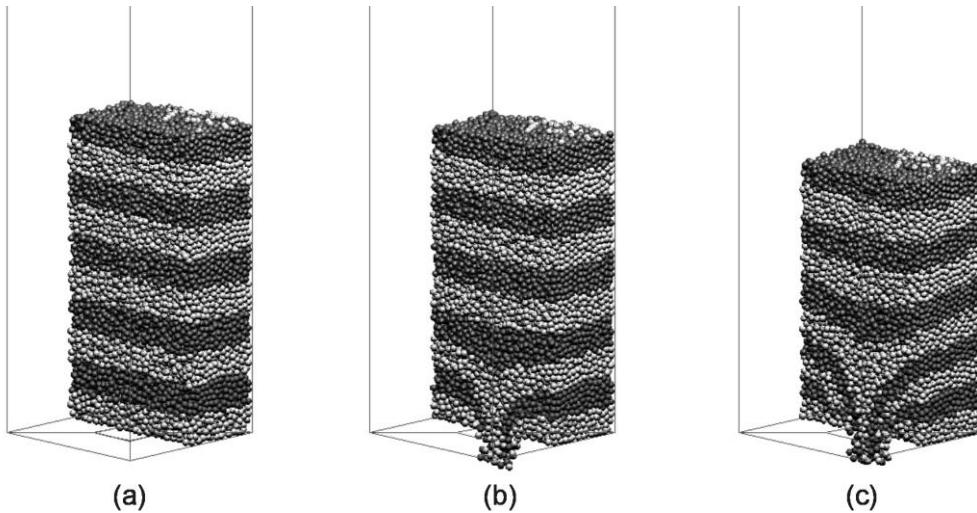


Fig. 5.22. Flow patterns at different simulation times in the case of flat-bottomed silo: (a) at $t=1.5$ s (static state at the end of the filling process), (b) at $t=2$ s, and (c) at $t=3.25$ s [93]

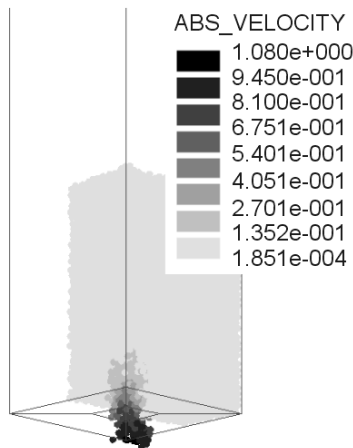


Fig. 5.23. Absolute velocity distribution at $t=4.47$ s in the case of flat-bottomed silo (in m/s) [93]

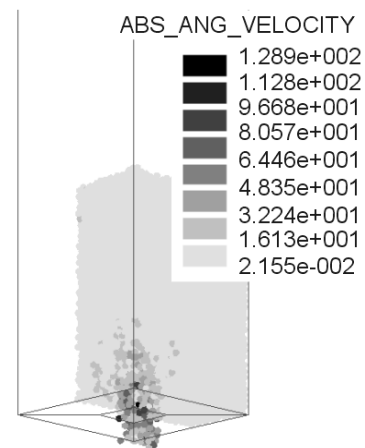


Fig. 5.24. Absolute angular velocity distribution at $t=4.47$ s in the case of flat-bottomed silo (in 1/s) [93]

As it was anticipated, in the case of flat-bottomed silo, mostly the horizontal wall carries the weight of the granular material if the system is at rest. Fig. 5.26 shows the wall pressures developed during discharge as a function of height. The greatest pressures appear in the region located near the bottom of the silo. The averaging method is the same as in the former two cases. The results agree qualitatively with the wall pressure distributions of Sanad et al. [90] obtained by two-dimensional DE analysis. In order to make the pressure saturation visible the simulation was repeated with a silo being half as large in width as the former one. The number of the particles was 20.000, which leads to an about two times higher closed packed configuration at rest than obtained previously. The contact parameters are naturally the same. Figs. 5.27 and 5.28 show the wall pressure distributions obtained at rest. In Fig. 5.27, the

height of the wall segment, on which the wall pressures are averaged is $2d$ similar to Fig. 5.25. For Fig. 5.28, this height is $4d$.

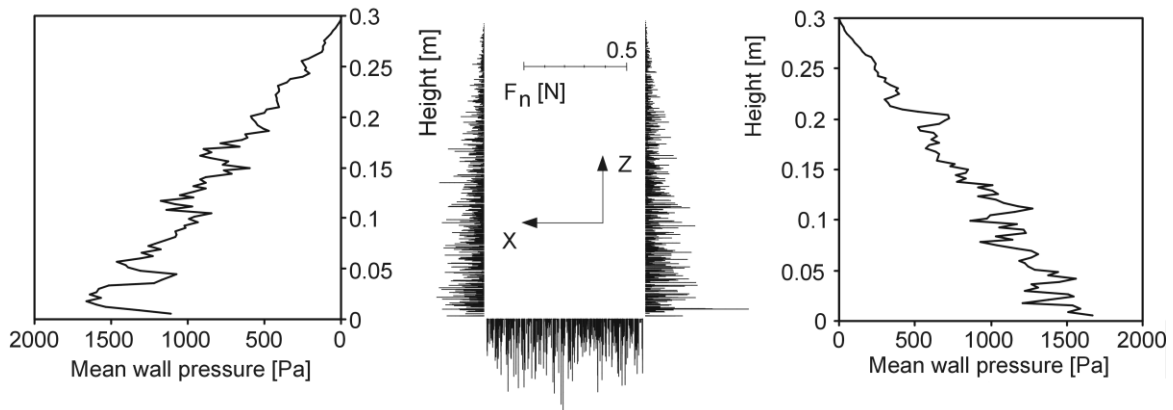


Fig. 5.25. Distributions of normal wall forces and mean wall pressures acting on the walls of the flat-bottomed silo at the end of the filling process (at $t=1.5$ s) [93] Contrary to Figs. 5.4 and 5.5 here not the width but the length of the lines representing contact forces is proportional to the magnitude of the force.

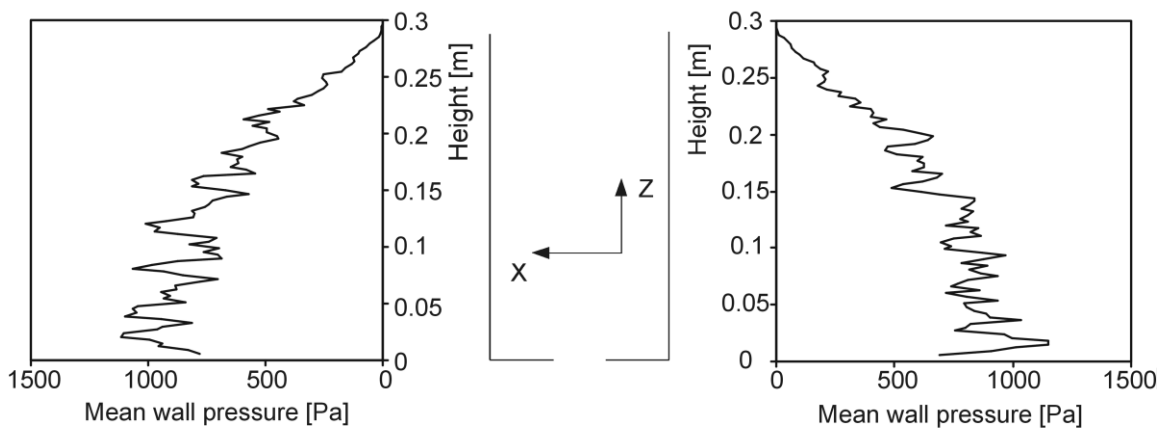


Fig. 5.26. Mean wall pressure distribution along the walls in the case of outflow from the flat-bottomed silo (at $t=1.8$ s) [93]

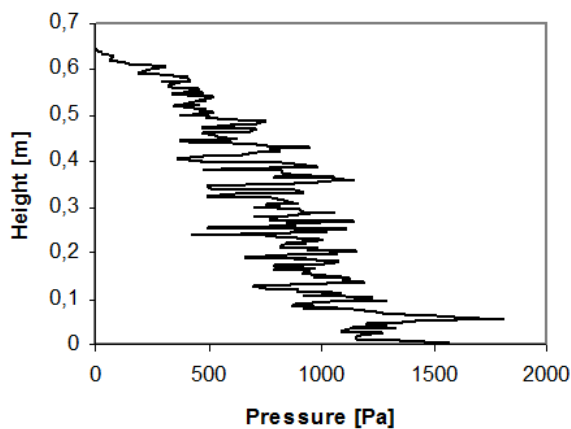


Fig. 5.27. Wall pressure distribution for a flat-bottomed silo (wall pressures were averaged on a wall segment of height of $2d$, $\mu=0.3$) [93]

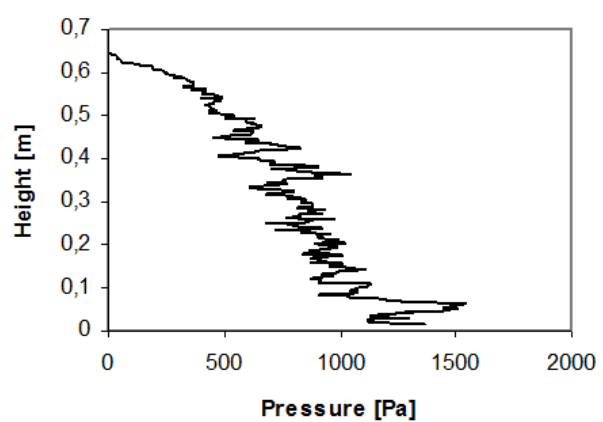


Fig. 5.28. Wall pressure distribution for a flat-bottomed silo (wall pressures were averaged on a wall segment of height of $4d$, $\mu=0.3$) [93]

5.4.6. Discussion of the flow behavior

Comparing the motion of particles in the hoppers and silos studied, the following conclusions may be drawn on the basis of simulation results. In the cases of hopper and silo with a hopper bottom, all the materials are in flowing condition during the discharging process. According to this, the flow type for these cases is mass flow. The vertical velocity of particles in the central part of the material is larger than at the sidewalls. Immediately above the outlet, the particles are in free fall. In the case of silo, the uppermost layer of dark particles at $t=3.25$ s is not deformed, which means that the particles located within this region move with the same vertical velocity.

In the case of flat-bottomed silo, the funnel flow phenomenon can be recognized on the basis of the flow patterns. At the beginning of the discharging process, similar to the previous cases, five layers of dark colored particles can be distinguished (see Fig. 5.22a). As it can be seen in Fig. 5.22c, at $t=3.25$ s, all of these layers are recognizable near the sidewalls. It follows from this that in the bottom part of the silo, near the silo walls; the particles flow very slowly or are stagnant during the discharging process. The regions where the velocities of the particles are nearly equal to zero are the so-called stagnation or dead zones. In spite of the fact that the friction coefficient used in the present study is rather low, the stagnation zones have been appeared unambiguously during discharging. Appearance of stagnant zones reduces the flow performance and makes it difficult to unload the silo. In contrast to funnel flow, the mass flow is an ideal flowing type for the unloading of a silo. In the upper section of the silo, the magnitudes of vertical velocities are small and almost constant across its whole cross section at $t=3.25$ s. The uppermost layer of dark particles is not deformed, which confirms the statement for the constant velocity profile. In the middle part of the silo, the magnitudes of velocities near the sidewalls are smaller than those in the central region.

The static wall pressure distributions obtained for the silos show no significant deviation from linear pressure dependence. The reason for this is that the systems modeled are not sufficiently high to show the asymptotic behavior of wall pressures. It must be noted that an additional simulation for a slender flat-bottomed silo, which is double as large in height and half as large in width than the one used here, has showed already the asymptotic behavior as expected, for example, by the Janssen formula.

As it has been proved here, the DEM is able to capture the container flow dynamics to a large extent. At the same time, it must be noted that the flow behavior of real granular materials is strongly affected, for example, by the interparticle cohesion and the particle shape. In order to take into account these factors, the simulation program of the author of this thesis should be extended.

6. Summary

The first part of the thesis deals with the finite element modeling of the surface roughness generated (micro-scale) viscoelastic component of the friction force. The 2D and 3D finite element models developed employ different modeling approaches to take into consideration the surface roughness (asperity-scale approach using smooth/rough asperity, multi-scale approach using sine wave as well as superposition of sine waves, direct modeling approach using the measured surface micro-topography). The second part of the thesis, as the end of the research activity dealing with the apparently smooth surface generated viscoelastic friction, focuses on the experimental investigation of the phenomenon. In order to close the research activities related to the apparently smooth surface generated viscoelastic friction the second part of the thesis focuses on the experimental investigation of the viscoelastic component of the friction force using measurement results taken from the literature. *When studying the surface roughness generated viscoelastic component of friction numerically and experimentally in EPDM and NBR rubber it has been pointed out that the micro-hysteresis friction component exists even for apparently smooth lubricated surfaces but its value cannot be as high as stated by Mofidi et al. in [44] because neither the FE simulations, nor the measurement results discussed in this thesis prove quantitatively the results of [44].*

Hydraulic rod seals applied in the mechanical engineering practice in great numbers operate frequently in the mixed lubrication regime. In case of mixed lubrication, the lubricating film induced by the hydrodynamic effect is not able to separate completely the contacting surfaces hence solid contacts are formed among the asperities. Because of the importance of Greenwood and Williamson's as well as Persson's contact theory for the definition how the distance between the mean planes of apparently smooth surfaces is related to the nominal contact pressure, the thesis analyzes the two theories in depth then compares their predictions quantitatively. *Using Greenwood and Williamson's [27] as well as Persson's [3, 63, 65] contact theory for an elastomer plate in contact with a rigid flat it has been shown that the difference in the predicted values of the distance between the mean plane of the rough surface and the ideally smooth surface varies between one and four orders of magnitude for RMS roughness of $1\ \mu\text{m}$ and nominal contact pressure between 0.1 and 1 MPa but becomes smaller and smaller as the nominal contact pressure decreases.* As a next step, a computational algorithm employing Salant and his coworkers' [Salant R., Maser N., Yang B. *Numerical model of a reciprocating hydraulic rod seal. Journal of Tribology, Vol. 129, pp. 91-97 (2007)*] numerical scheme and developed for the simulation of mixed friction of reciprocating rod seals/sliding components is presented in depth. The steady-state model is able to take into consideration the effect of the surface roughness, the cavitation, the elastic deformation and the pressure dependent viscosity simultaneously. Among the results of the computational algorithm not only the nominal film thickness, the fluid pressure and the contact pressure but the leak rate and the friction force expected can also be found. The part of the thesis that is related to the modeling of mixed friction is closed with the numerical modeling of the lubrication performance for an O-ring and the wiper lip of a commercial windscreen wiper. *Applying Salant et al.'s [41] steady-state, one-dimensional mixed friction model to an O-ring it has been pointed out that the nominal lubricant film thickness during outstroke is larger than during instroke, during outstroke a cavitated region appears within the nominal contact area while the peak value of the fluid pressure within the non-cavitated region does not exceed 0.76 MPa and during instroke there is no cavitated region and the fluid pressure does not exceed the sealed pressure.* Furthermore, *applying Salant et al.'s [41] mixed friction model to the wiper lip of a commercial windscreen wiper it has been pointed out that the gap between the mean surfaces of the contacting bodies first converges then diverges as moving away from the point where the wa-*

ter enters into the gap, a cavitated region appears within the nominal contact area where the gap diverges, the asperity-type contact pressure reaches a peak value of 0.8 MPa and, finally, the peak value of the fluid pressure is lower with three orders of magnitude than that of the asperity-type contact pressure.

The last part of the thesis deals with the prediction of the structural level forces (normal force and friction force) acting on the walls of silos/hoppers used to store viscoelastic granular material by modeling the interactions among the grains. After discussing the theoretical background and the applicability of the discrete element method as a representative of the discrete modeling approach the computer program of the author of this thesis is presented in depth. The program is able to follow the motion of each particle separately while the contacts of particles with other particles or walls are also detected continuously. In contrast to continuum mechanics-based methods this technique gains the behavior of the material modeled from the interactions of the particles. The discrete element models developed for the simulation of the friction force arising on the walls of non-axisymmetric hoppers and silos as well as for the filling and the unsteady-state outflow process have been constructed and solved using the computer program of the author of this thesis. The objective of the simulations is to determine quantitatively the forces acting on the walls at the end of the filling process (static case) and at the beginning of the discharge (dynamic case) as well as the pressure distributions induced. In order to achieve the objective normal contact law considering the viscoelastic material behavior and tangential contact law with capability to model the static friction as well as model parameters calibrated experimentally are incorporated in the numerical models. *Using the computer program of the author of this thesis developed on the basis of Cundall and Strack's [79] three-dimensional discrete element method it has been shown that the total friction force arising on the inclined and vertical walls of hoppers and silos with different bottom and square cross section at the end of the filling process is equal to 12...16% of the weight of the stored material in case of local particle-particle and particle-wall coefficient of friction of $\mu=0.3$ and experimentally calibrated contact law.*

7. New scientific results

Thesis 1.

When studying the surface roughness generated viscoelastic component of friction (micro hysteresis caused friction) numerically and experimentally in EPDM and NBR rubber it has been pointed out that the micro-hysteresis friction component exists even for apparently smooth lubricated surfaces but its value cannot be as high as stated by Mofidi et al. in [44] (In [44], apparent coefficients of friction of $\mu = 0.48 \dots 0.66$ are reported for highly polished steel surface having RMS roughness of about $0.1 \mu m$ and sliding on oil lubricated NBR rubber and it is stated that they can be explained by the dominance of micro hysteresis.) because neither the FE simulations, nor the measurement results discussed in this thesis prove quantitatively the results of [44].

Closely related papers: [131, 60, 35, 32]. Additional papers in this topic: [38, 113, 11, 28, 29].

Thesis 2.

Using Greenwood and Williamson's [27] as well as Persson's [3, 63, 65] contact theory for an elastomer plate in contact with a rigid flat it has been shown that the difference in the predicted values of the distance between the mean plane of the rough surface and the ideally smooth surface varies between one and four orders of magnitude for RMS roughness of $1 \mu m$ and nominal contact pressure between 0.1 and 1 MPa but becomes smaller and smaller as the nominal contact pressure decreases.

Closely related papers: [64].

Thesis 3.

Applying Salant et al.'s [41] steady-state, one-dimensional mixed friction model (originally developed for reciprocating hydraulic rod seals and with capability to take into consideration the effect of cavitation, elastic deformation, surface roughness and pressure dependent viscosity simultaneously) to an O-ring (8 x 1.5 mm (rod diameter x ring thickness), RMS roughness = $0.4 \mu m$, elastic modulus = 10 MPa, sealed pressure = 0.6 MPa, sliding speed during in- and outstroke = 50 mm/s) it has been pointed out that the nominal lubricant film thickness during outstroke is larger than during instroke, during outstroke a cavitating region appears within the nominal contact area while the peak value of the fluid pressure within the non-cavitating region does not exceed 0.76 MPa and during instroke there is no cavitating region and the fluid pressure does not exceed the sealed pressure.

Closely related papers: [12, 78]. Additional papers in this topic: [69].

Thesis 4.

Applying Salant et al.'s [41] mixed friction model to the wiper lip of a commercial wind-screen wiper (elastic modulus = 4.5 MPa, RMS roughness = $1\ \mu\text{m}$, sliding speed = 150 mm/s) it has been pointed out that the gap between the mean surfaces of the contacting bodies first converges then diverges as moving away from the point where the water enters into the gap, a cavitated region appears within the nominal contact area where the gap diverges, the asperity-type contact pressure reaches a peak value of 0.8 MPa and, finally, the peak value of the fluid pressure is lower with three orders of magnitude than that of the asperity-type contact pressure.

Closely related papers: [10]. Additional papers in this topic: [75].

Thesis 5.

Using the computer program of the author of this thesis developed on the basis of Cundall and Strack's [79] three-dimensional discrete element method employing ideally rigid spheres where their interpenetration (overlapping) in the vicinity of the contact point is allowed it has been shown that the total friction force arising on the inclined and vertical walls of hoppers and silos with different bottom and square cross section (filled with granular material being composed of 40000 mono-sized viscoelastic spherical cellulose acetate particles up to about the same height) at the end of the filling process is equal to 12...16% of the weight of the stored material in case of local particle-particle and particle-wall coefficient of friction of $\mu = 0.3$ and experimentally calibrated contact law.

Closely related papers: [93]. Additional papers in this topic: [132].

References

- [1] Grosch, K. The relation between the friction and visco-elastic properties of rubber. Proceedings of the Royal Society of London. Series A, Mathematical and Physical Sciences, Vol. 274 (1356), pp. 21-39 (1963)
- [2] Lorenz B., Persson B.N.J., Dieluwit S., Tada T. Rubber friction: Comparison of theory with experiment. European Physical Journal E, Vol. 34, pp. 129-140 (2011)
- [3] Persson B.N.J. Theory of rubber friction and contact mechanics. Journal of Chemical Physics, Vol. 115 (8), pp. 3840-3861 (2001)
- [4] Hegmon, R.R. The contribution of deformation losses to rubber friction. Auto, Safety Research Program, Report No. 29. The Penn. State University (1968)
- [5] Moore D.F. The friction and lubrication of elastomers. Pergamon Press in Oxford, New York (1972)
- [6] Kummer H.W. Unified theory of rubber and tire friction. Eng. Res. Bulletin B-94, The Pennsylvania State University, Vol. 6-7 (1966)
- [7] Heinrich, G., Klüppel M., Vilgis T.A. Evaluation of self-affine surfaces and their implication for frictional dynamics as illustrated with a Rouse material. Computational and Theoretical Polymer Science, Vol. 10, pp. 53-61 (2000)
- [8] Smith R.H. Analyzing friction in the design of rubber products and their paired surfaces. CRC Press, Taylor & Francis Group (2008)
- [9] Klüppel M., Heinrich G. Rubber friction on self-affine road tracks. Rubber Chemistry and Technology, Vol. 73, pp. 578-606 (2000)
- [10] Bódai G., **Goda T.J.** Sliding friction of wiper blade: Measurement, FE modeling and mixed friction simulation. Tribology International, Vol. 70, pp. 63-74 (2014)
- [11] Felhős D., Xu D., Schlarb A.K., Váradi K., **Goda T.** Viscoelastic characterization of an EPDM rubber and finite element simulation of its dry rolling friction. Express Polymer Letters, Vol. 2 (3), pp. 157-164 (2008)
- [12] **Goda T.J.** Numerical prediction of friction, wear, heat generation and lubrication in case of sliding rubber components. In: Rudas I J, Fodor J, Kacprzyk J (Editors) Towards Intelligent Engineering and Information Technology. 736 p. Berlin ; Heidelberg: Springer, pp. 519-530. (Studies in Computational Intelligence; Vol. 243) ISBN: 3642037364; 978-3642037368 (2009)
- [13] Koenen A., Sanon A. Tribological and vibroacoustic behaviour of a contact between rubber and glass (application to wiper blade). Tribology International, Vol. 40, pp. 1484-1491 (2007)
- [14] Le Gal A., Klüppel M. Investigation and modelling of rubber stationary friction on rough surfaces. J. Phys. Condens. Matter., Vol. 20, 015007 (2008)
- [15] Schallamach A. A Theory of Dynamic Rubber Friction. Wear, Vol. 6, pp. 375-382 (1963)
- [16] Pálfi L.: A súrlódás hiszterézis komponensének vége-selemes modellezése gumi-éres felület csúszó pár esetén. PhD Thesis, Budapest University of Technology and Economics (2010)
- [17] Bódai G. Material and frictional behavior of rubber sliding on glass surface, PhD Thesis, Budapest University of Technology and Economics (2012)
- [18] Grosch K. Relation between the friction and viscoelastic properties of rubber. Nature, Vol. 197, pp. 858-859 (1963)
- [19] Lindner M., Sextro W., Popp K. Hysteretic friction of a sliding rubber element. PAMM Proc. Appl. Math. Mech., Vol. 4, pp. 101-102 (2004)
- [20] Bui Q.V., Ponthot J.P. Estimation of rubber sliding friction from asperity interaction modeling. Wear, Vol. 252, pp. 150-160 (2002)

- [21] Nettingsmeier J., Wriggers P. Frictional contact of elastomer materials on rough rigid surfaces. *PAMM Proc. Appl. Math. Mech.* Vol. 4, pp. 360–361 (2004)
- [22] Achenbach M., Frank E. Reibung von Elastomeren. *Tribologie und Schmierungstechnik*, Vol. 48 (4), pp. 43-47 (2001)
- [23] Palasantzas G., De Hosson J. Th. M. Effects of self-affine surface roughness on the friction coefficient of rubbers in the presence of a liquid interlayer. *Journal of Applied Physics*, Vol. 95 (1), pp. 389-392 (2004)
- [24] Westermann S., Petry F., Boes R., Thielen G. Experimental investigations into the predictive capabilities of current physical rubber friction theories. *KGK-Kaut Gummi Kunst*, Vol. 57, pp. 645-650 (2004)
- [25] Scaraggi M., Persson B.N.J. Rolling friction: comparison of analytical theory with exact numerical results. *Tribology Letters* Vol. 55, pp. 15–21 (2014)
- [26] Nguyen D.T., Ramakrishna S., Fretigny C., Spencer N.D., Le Chenadec Y., Chateau-minois A. Friction of rubber with surfaces patterned with rigid spherical asperities. *Tribology Letters*, Vol. 49, pp. 135–144 (2013)
- [27] Greenwood J. A., Williamson J. B. P. Contact of nominally flat surfaces. *Proceedings of the Royal Society A: Mathematical, Physical and Engineering Sciences*, Vol. 295, pp. 300-319 (1966)
- [28] Soós E., **Goda T.** Numerical analysis of sliding friction behavior of rubber. *Materials Science Forum*, Vol. 537-538, pp. 615-621 (2007)
- [29] Békési N., **Goda T.** A hiszterézis vége-selemes vizsgálata gumi és merev érdes ellenfelület csúszó súrlódása során. *Gép*, LVII (8-9), pp. 22-25 (2006)
- [30] Békési N. *Elastomer anyagok és csúszótömítések súrlódása és kopása*. PhD thesis, Budapest University of Technology and Economics (2011)
- [31] Archard J.F. Elastic deformation and the laws of friction. *Proc. R. Soc. Lond. A*, Vol. 243, pp. 190-205 (1957)
- [32] Pálfi L., Békési N., **Goda T.**, Váradi K., Czifra Á. FE simulation of the hysteresis friction considering the surface topography. *Periodica Polytechnica Mechanical Engineering*, Vol. 52 (2), pp. 83-91 (2008)
- [33] Herdy M. *Introductory theory manual ViscoData and ViscoShift*. IBH-Ingenierbüro (<http://www.viscodata.de/>) (2003)
- [34] Wriggers, P., Reinelt J. Multi-scale approach for frictional contact of elastomers on rough rigid surfaces. *Computer Methods in Applied Mechanics and Engineering*, Vol. 198, pp. 1996-2008 (2009)
- [35] Pálfi L., **Goda T.**, Váradi K., Garbayo E., Bielsa J.M., Jiménez M.Á. FE prediction of hysteretic component of rubber friction. *Advances in Tribology*, pp. 1-12 (2012)
- [36] MSC.Marc User Manual, Version 2007R1, MSC.Software corporation (2007)
- [37] Pálfi L., **Goda T.**, Czifra Á. Súrlódási tényező hiszterézis komponensének vége-selemes vizsgálata gumi/fém csúszópárok esetén. *Műszaki Szemle*, pp. 305-309 (2008)
- [38] Pálfi L., **Goda T.**, Váradi K. Theoretical prediction of hysteretic rubber friction in ball on plate configuration by finite element method. *Express Polymer Letters*, Vol. 3 (11), pp. 713-723 (2009)
- [39] Greenwood J. A., Tabor D. The friction of hard sliders on lubricated rubber: The importance of deformation losses. *Proceedings of the Physical Society*, Vol. 71, pp. 989-1001 (1958)
- [40] Persson B.N.J. Rolling friction for hard cylinder and sphere on viscoelastic solid. *The European Physical Journal E*, Vol. 33, pp. 327-333 (2010)
- [41] Salant R., Maser N., Yang B. Numerical model of a reciprocating hydraulic rod seal. *Journal of Tribology*, Vol. 129, pp. 91-97 (2007)

- [42] Campbell W.E. Boundary lubrication. in F.F. Ling, E.E. Klaus, R.S. Fein (editors), Boundary lubrication: an appraisal of world literature, American Society of Mechanical Engineers (ASME), New York, pp. 87-117 (1969)
- [43] Persson B.N.J., Albohr O., Mancosuc F., Peveric V., Samoilov V.N., Sivebaek I.M. On the nature of the static friction, kinetic friction and creep. *Wear*, Vol. 254, pp. 835-851 (2003)
- [44] Mofidi M., Prakash B., Persson B.N.J., Albohr O. Rubber friction on (apparently) smooth lubricated surfaces. *Journal of Physics: Condensed Matter*, Vol. 20, pp. 1-8 (2008)
- [45] Wohlers A., Heipl O., Persson B.N.J., Scaraggi M., Murrenhoff H. Numerical and experimental investigation on O-ring seals in dynamic applications. *International Journal of Fluid Power*, Vol. 10, pp. 51-59 (2009)
- [46] Fina E., Gruber P., Sharp R.S. Hysteretic rubber friction: application of Persson's theories to Grosch's experimental results. *Journal of Applied Mechanics*, Vol. 81, pp. 1-6 (2014)
- [47] Wang Y.X., Wu Y.P., Li W.J., Zhang L.Q. Influence of filler type on wet skid resistance of SSBR/BR composites: Effects from roughness and micro-hardness of rubber surface. *Applied Surface Science*, Vol. 257, pp. 2058-2065 (2011)
- [48] Mokhtari M., Schipper D.J., Tolpekina T.V. On the friction of carbon black- and silica-reinforced BR and S-SBR elastomers. *Tribology Letters*, Vol. 54, pp. 297-308 (2014)
- [49] Mofidi M.R., Prakash B. Influence of counterface topography on sliding friction and wear of some elastomers under dry sliding condition. *Proceedings of the Institution of Mechanical Engineers, Part J, Journal of Engineering Tribology*, Vol. 222 (5), pp. 667-673 (2008)
- [50] Carbone G., Lorenz B., Persson B.N.J., Wohlers A. Contact mechanics and rubber friction for randomly rough surfaces with anisotropic statistical properties. *The European Physical Journal E*, Vol. 29, pp. 275-284 (2009)
- [51] Denny D.F. The influence of load and surface roughness on the friction of rubber-like materials. *Proc. Phys. Soc. B*, Vol. 66, pp. 721-727 (1953)
- [52] Mofidi M., Prakash B. Frictional behavior of some sealing elastomers in lubricated sliding conditions. 15th Nordic Symposium on Tribology- NordTrib 2012, 12-15 June 2012, Trondheim, Norway, pp. 1-6, Paper# 00154
- [53] Mofidi M., Simmons G. F., Prakash B. Friction and wear characteristics of elastomers in lubricated contact with various EALs. 13th Nordic Symposium on Tribology – NordTrib 2008, 10-13 June 2008, Tampere, Finland, pp. 1-11
- [54] Fernandez-Diaz B., Bayón R., Igartua A. Alternative Cr+6-free coatings sliding against NBR elastomer. *Tribology – Lubricants and lubrication*, Chang-Hung Kuo (Ed.), ISBN: 978-953-307-371-2, pp. 287-304 (2011)
- [55] Mofidi M., Kassfeldt E., Prakash B. Tribological behavior of an elastomer aged in different oils. *Tribology International*, Vol. 41, pp. 860-866 (2008)
- [56] Rana A., Sayles R., Nikas G., Jalisi I. An experimental technique for investigating the sealing principles of reciprocating elastomeric seals for use in linear hydraulic actuator assemblies. *Proceedings of the 2nd World Tribology Congress*, 3-7 September 2001, Vienna, Austria (on CD) (2001)
- [57] Arnold S.P., Roberts A.D., Taylor A.D. Rubber friction dependence on roughness and surface energy. *J. Nat. Rubb. Res.*, Vol. 2, pp. 1-14 (1987)
- [58] Patir N., Cheng H.S. An average flow model for determining effects of three-dimensional roughness on partial hydrodynamic lubrication. *Journal of Lubrication Technology*, Vol. 100, pp. 12-17 (1978)
- [59] Patir N., Cheng H.S. Application of average flow model to lubrication between rough sliding surfaces. *Journal of Lubrication Technology*, Vol. 101, pp. 220-229 (1979)

- [60] Czifra Á., **Goda T.**, Garbayo E. Surface characterisation by parameter-based technique, slicing method and PSD analysis. *Measurement*, Vol. 44 (5), pp. 906-916 (2011)
- [61] Ren N., Zhu D., Chen W.W., Liu Y., Wang Q.J. A three-dimensional deterministic model for rough surface line-contact EHL problems. *Journal of Tribology*, Vol. 131, pp. 1-9 (2009)
- [62] Minet C., Brunetière N., Tournier B. A deterministic mixed lubrication model for mechanical seals. *Journal of Tribology*, Vol. 133, p. 1-11 (2011)
- [63] Persson B.N.J., Scaraggi M. On the transition from boundary lubrication to hydrodynamic lubrication in soft contacts. *J. Phys. Condens. Matter.*, Vol. 21, pp. 1-22 (2009)
- [64] Bódai G., **Goda T.J.** Friction force measurement at windscreen wiper/glass contact. *Tribology Letters*, Vol. 45, pp. 515-523 (2012)
- [65] Persson B.N.J. Relation between interfacial separation and load: a general theory of contact mechanics. *Physical Review Letters*, Vol. 99, pp. 1-4 (2007)
- [66] Johnson K.L. *Contact mechanics*. Cambridge University Press, England (1985)
- [67] Yang C., Persson B.N.J. Contact mechanics: contact area and interfacial separation from small contact to full contact. *Journal of Physics: Condensed Matter*, Vol. 20, pp. 1-13 (2008)
- [68] Jackson R.L., Streater J.L. A multi-scale model for contact between rough surfaces. *Wear*, Vol. 261, pp. 1337-1347 (2006)
- [69] **Goda T.J.** Numerical modeling of lubrication in reciprocating hydraulic rod seals. *Gépészet 2008: Proceedings of Sixth Conference on Mechanical Engineering*. Budapest, 2008.05.29-2008.05.30., pp. 1-11. ISBN: 978-963-420-947-8 (2008)
- [70] Sahlin F., Almqvist A., Larsson R., Glavatskih S. A cavitation algorithm for arbitrary lubricant compressibility. *Tribology International*, Vol. 40, pp. 1294-1300 (2007)
- [71] Kozma M. Fluid film lubrication between elastomer/rigid pairs. *Future Trends of Tribological Components in Drive Engineering OTG Symposium*, 23rd November 2006 Steyr (on CD)
- [72] Kozma M. Hydrodynamic and boundary lubrication of elastomer seals. *19th International Conference on Fluid Sealing*, Poitiers, France, 25-26 September 2007, BHR Group Limited 19-28.
- [73] Deleau F., Mazuyer D., Koenen A. Sliding friction at elastomer/glass contact: Influence of the wetting conditions and instability analysis. *Tribology International*, Vol. 42, pp. 149-159 (2009)
- [74] Allen JS. An analytical solution for determination of small contact angles from sessile drops of arbitrary size. *J. Coll. and Int. Sci.*, Vol. 261, pp. 481-489 (2003)
- [75] Bódai G., **Goda T.** Mixed friction of windscreen wiper: numerical analysis. *Gépészet 2012: Proceedings of the eighth international conference on mechanical engineering*. Budapest, 2012. pp. 22-28. ISBN: 978-963-313-055-1 (on CD)
- [76] Müller H. K., Nau B. S. *Fluid Sealing Technology*. Marcel Dekker, New York (1998)
- [77] Bullock A. K., Tilley D. G., Johnston D. N., Bowen C. R., Keogh P. S. Non-linear friction in reciprocating hydraulic rod seals: simulation and measurement. *Journal of Physics: Conference Series*, Vol. 181 (2009)
- [78] **Goda T.**, Bódai G. O-gyűrű szivárgás számítása korszerű numerikus módszerrel. *Gép, LX (10-11)*, pp. 43-46 (2009)
- [79] Cundall P. A., Strack O. D. L. A discrete numerical model for granular assemblies. *Geotechnique*, Vol. 29 (1), pp. 47-65 (1979)
- [80] Anciaux G., Molinari J.F. Contact mechanics at the nanoscale, a 3D multiscale approach. *International Journal for Numerical Methods in Engineering*, Vol. 79, pp. 1041-1067 (2009)

- [81] Jerier J.F., Molinari J.F. Normal contact between rough surfaces by the Discrete Element Method. *Tribology International*, Vol. 47, pp. 1-8 (2012)
- [82] Kargulewicz M., Iordanoff I., Marrero V., Tichy J. Modeling of magnetorheological fluids by the Discrete Element Method. *Journal of Tribology*, Vol. 134, pp. 1-9 (2012)
- [83] Fillot N., Iordanoff I., Berthier Y. A granular dynamic model for the degradation of material. *Journal of Tribology*, Vol. 126, pp. 606-614 (2004)
- [84] Fillot N., Iordanoff I., Berthier Y. Simulation of wear through mass balance in a dry contact. *Journal of Tribology*, Vol. 127, pp. 230-237 (2005)
- [85] Mollon G. A numerical framework for discrete modelling of friction and wear using Voronoi polyhedrons. *Tribology International*, Vol. 90, pp. 343-355 (2015)
- [86] Szirmay-Kalos L. Számítógépes grafika. ComputerBooks, Budapest (2001)
- [87] Schäfer J., Dippel S., Wolf D. E. Force schemes in simulations of granular materials. *Journal de Physique I*, Vol. 6 (1), pp. 5-20 (1996)
- [88] Ristow G. H., Herrmann H. J. Forces on the walls and stagnation zones in a hopper filled with granular material. *Physica A: Statistical Mechanics and its Applications*, Vol. 213 (4), pp. 474-481 (1995)
- [89] Masson S., Martinez J. Effect of particle mechanical properties on silo flow and stresses from distinct element simulations. *Powder Technology*, Vol. 109, pp. 164-178 (2000)
- [90] Sanad A. M., Ooi J. Y., Holst J. M., Rotter J. M. Computations of Granular Flow and Pressures in a Flat-Bottomed Silo. *Journal of Engineering Mechanics*, Vol. 127 (10), pp. 1033-1043 (2001)
- [91] Foerster S. F., Louge M. Y., Chang H., Allia K. Measurements of the collision properties of small spheres. *Physics of Fluids*, Vol. 6 (3), pp. 1108- (1994)
- [92] Langston P. A., Tüzün U., Heyes D. M. Discrete element simulation of granular flow in 2D and 3D hoppers: dependence of discharge rate and wall stress on particle interactions. *Chemical Engineering Science*, Vol. 50 (6), pp. 967-987 (1995)
- [93] Goda T.J., Ebert F.** Three-dimensional discrete element simulations in hoppers and silos. *Powder Technology*, Vol. 158 (1-3), pp. 58-68 (2005)
- [94] Walters J. K. Theoretical analysis of stresses in axially-symmetric hoppers and bunkers *Chemical Engineering Science*, Vol. 28, pp. 779-789 (1973)
- [95] Yang S. C., Hsiau S. S. The simulation and experimental study of granular materials discharged from a silo with the placement of inserts. *Powder Technology*, Vol. 120, pp. 244-255 (2001)
- [96] Dorfmann A. L. Modeling of rubber materials. in Janusz R. Klepaczko, Tomasz Lodygowski (editors) *Advances in Constitutive Relations Applied in Computer Codes, CISM Courses and Lectures*, Vol. 515 (2010) ISBN 978-3-7091-1095-9
- [97] Treloar L.R.G. *The physics of rubber elasticity*. Third edition, Oxford University Press (1975)
- [98] Achenbach M., Streit G. *Thermodynamische Beschreibung der Gummielastizität. Kautschuk, Gummi, Kunststoff (GAK)*, Vol. 54 (3), pp. 164-178 (2001)
- [99] Ferry J.D. *Viscoelastic Properties of Polymers*. JohnWiley & Sons Inc., New York. (1980)
- [100] Christensen R. M. *Theory of Viscoelasticity*. 2nd Edition, Academic Press, New York, (1982)
- [101] Findley W. N., Lai J. S., Onaran K. *Creep and relaxation of nonlinear viscoelastic materials*. Amsterdam: North-Holland (1976)
- [102] Aklonis J. J., MacKnight W. J. *Introduction to polymer viscoelasticity*. Second Edition. New York: John Wiley (1983)
- [103] Tschoegl N. W., Knauss W. G., Emri I. Poisson's ratio in linear viscoelasticity – A critical review. *Mechanics of Time-Dependent Materials*, Vol. 6, pp. 3–51 (2002)

- [104] Pandini S., Pegoretti A. Time and temperature effects on Poisson's ratio of poly(butylene terephthalate), *eXPRESS Polymer Letters* Vol.5 (8), pp. 685–697 (2011)
- [105] Bardenhagen S.G., Stout M.G., Gray G.T. Three-dimensional, finite deformation, viscoplastic constitutive models for polymeric materials. *Mechanics of Materials*, Vol. 25, pp. 235-253 (1997)
- [106]** Soós E., **Goda T.** Mechanical behavior of glass fiber-reinforced bosses: experiments and FE simulations. *Periodica Polytechnica-Mechanical Engineering*, Vol. 55 (1), pp. 3-14 (2011)
- [107] Bodor G., Vas L. M. *Polimerek anyagszerkezetana*. Műegyetemi Kiadó, Budapest, (2001)
- [108] Roylance D. *Mechanics of materials*. John Wiley and Sons, New York (1996)
- [109] Pahl M., Gleißle W., Laun H.M. *Praktische Rheologie der Kunststoffe und Elastomere*. VDI-Gesellschaft Kunststofftechnik, VDI-Verlag, Düsseldorf (1991)
- [110] Wiechert E. Gesetze der elastischen Nachwirkung für konstante Temperaturen I. *Wiedemann's Ann Phys Chem*, Vol. 50, pp: 336-348 (1893)
- [111] Kaliske M., Rothert H. Formulation and implementation of three-dimensional viscoelasticity at small and finite strains. *Computational Mechanics*, Vol. 19, pp. 228 – 239 (1997)
- [112] Sharma S. Critical Comparison of Popular Hyperelastic Material Models in Design of Anti-Vibration Mounts for Automotive Industry through FEA. *Constitutive Models for Rubber III* (2003) ISBN 9058095665
- [113]** Bódai G., **Goda T.** A new, tensile test-based parameter identification method for large-strain generalized Maxwell-model. *Acta Polytechnica Hungarica*, Vol. 8 (5), pp. 89-108 (2011)
- [114] Holzzapfel G. A. *Nonlinear solid mechanics: A continuum approach for engineering*. John Wiley & Sons, Chichester (2000)
- [115] Urzsumcev J.Sz., Makszimov R.D. *A műanyagok alakváltozása*. Műszaki Könyvkiadó, Budapest (1982)
- [116]** Bódai G., **Goda T.** Parameter identification methods for generalized Maxwell models: Engineering approach for small strain viscoelasticity. *Materials Science Forum*, Vol. 659, pp. 379-384 (2010)
- [117] Persson B.N.J. Rubber friction: role of the flash temperature. *Journal of Physics: Condensed Matter*, Vol. 18, pp. 7789-7823 (2006)
- [118] Williams M. L., Landel R. F., Ferry J. D. The temperature dependence of relaxation mechanisms in amorphous polymers and other glass-forming liquids. *Journal of the American Chemistry Society*, Vol.77, pp.3701–3707 (1955)
- [119] Stan F., Munteanu A.V., Fetecau C. Analysis of visco-elastic-plastic behavior of short glass fiber-reinforced polyamide 66 composite (PA66 GF30). *Materiale Plastice*, Vol. 48 (1), pp. 1-6 (2011)
- [120]** Pálfi L., **Goda T.**, Felhős D. Parameter identification for the generalized Maxwell-model on the basis of DMTA and stress relaxation measurements. VI. Országos Anyagtudományi Konferencia, 14-16th October, 2007, Siófok (2007) oral presentation
- [121]** Bódai G., **Goda T.** On the relation between stress relaxation and constant strain rate tensile behavior for linear viscoelastic materials; an engineering approach. *Materials Science Forum*, Vol. 729, pp. 314-319 (2013)
- [122] Gent A. N. *Engineering with Rubber: how to design rubber components*. 2nd Edition (2001)
- [123] Yeoh O.H. Phenomenological Theory of Rubber Elasticity. In: *Comprehensive Polymer Science*, Ed. S.L. Aggarwal, 2nd Supplement, Pergamon Press (1995)

- [124] Stout K. J., Sullivan P. J., Dong W. P., Mainsah E., Luo N., Mathia T., Zahouni H. The development of methods for characterisation of roughness in three dimensions. Printing Section, University of Birmingham, Edgbaston (1993)
- [125] Schargott M., Popov V. Diffusion as a model of formation and development of surface topography. *Tribology International*, Vol. 39, pp. 431-436 (2006)
- [126] Persson B. N. J., Albohr O., Tratagliano U., Volokitin A. I., Tosatti E. On the nature of surface roughness with application to contact mechanics, sealing, rubber friction and adhesion. *J Phys Cond Matter*, Vol. 17, pp. 1-62 (2005)
- [127] Carbone G., Putignano C. Rough viscoelastic sliding contact: theory and experiments. *Physical Review E*, Vol. 89, pp. 1-9 (2014)
- [128] Lorenz B., Pyckhout-Hintzen W., Persson B.N.J. Master curve of viscoelastic solid: using causality to determine the optimal shifting procedure, and to test the accuracy of measured data. *Polymer*, Vol. 55, pp. 565-571 (2014)
- [129] De Lorenzis L., Wriggers P. Computational homogenization of rubber friction on rough rigid surfaces. *Computational Materials Science*, Vol. 77, pp. 264-280 (2013)
- [130] Renouf M., Massi F., Fillot N., Saulot A. Numerical tribology of a dry contact. *Tribology International*, Vol. 44, pp. 834-844 (2011)
- [131] Goda T.J.** Effect of track roughness generated micro-hysteresis on rubber friction in case of (apparently) smooth surfaces. *Tribology International*, Vol. 93, pp. 142-150 (2016)
- [132] Goda T.J., Horváth S.** Szemcsés anyagok sajátos tulajdonságainak modellezési lehetőségei. *Gép*, LVI (9-10), pp. 60-62 (2005)
- [133] Mokhtari M., Schipper D.J. Existence of a tribo-modified surface layer of BR/S-SBR elastomers reinforced with silica or carbon black. *Tribology International*, (2014) doi: 10.1016/j.triboint.2014.09.021
- [134] Mokhtari M., Schipper D.J., Vleugels N., Noordermeer J.W.M. Existence of a tribo-modified surface layer on SBR elastomers: balance between formation and wear of the modified layer. *Tribology Letters*, Vol. 58, No. 22, pp. 1-13 (2015)
- [135] Wagner P., Wriggers P., Klapproth C., Prange C., Wies B. Multiscale FEM approach for hysteresis friction of rubber on rough surfaces. *Computer Methods in Applied Mechanics and Engineering*, Vol. 296, pp. 150-168 (2015)
- [136] Zhu H.P., Yu A.B. Steady-state granular flow in a three-dimensional cylindrical hopper with flat bottom: microscopic analysis. *Journal of Physics D: Applied Physics*, Vol. 37, pp. 1497-1508 (2004)
- [137] Zhu H.P., Yu A.B. Steady-state granular flow in a 3D cylindrical hopper with flat bottom: macroscopic analysis. *Granular Matter*, Vol. 7, pp. 97-107 (2005)
- [138] Zhu H.P., Yu A.B. Micromechanic modeling and analysis of unsteady-state granular flow in a cylindrical hopper. *Journal of Engineering Mathematics*, Vol. 52, pp. 307-320 (2005)
- [139] Zhu H.P., Zhou Z.Y., Yang R.Y., Yu A.B. Discrete particle simulation of particulate systems: A review of major applications and findings. *Chemical Engineering Science*, Vol. 63, pp. 5728-5770 (2008)
- [140] Fan Jin, Qiang Wan, Xu Guo. Plane Contact and Partial Slip Behaviors of Elastic Layers With Randomly Rough Surfaces. *Journal of Applied Mechanics*, Vol. 82(9), pp. 1-7. (2015)
- [141] Meng F., Wang Q.J., Hua D., Liu S. A simple method to calculate contact factor used in average flow model. *Journal of Tribology*, Vol. 132, pp. 1-4 (2010)
- [142] Harp S.R., Salant R.F. An average flow model of rough surface lubrication with interasperity cavitation. *Journal of Tribology*, Vol. 123, pp. 134-143 (2001)
- [143] Patankar S.V. Numerical heat transfer and fluid flow (Series in computational methods in mechanics and thermal sciences), McGraw-Hill, New York (1980)

Összefoglalás

Az értekezés első része a súrlódási erő felületi érdesség által generált (mikroszintű) viszkoelasztikus összetevőjének végeselemes modellezésével foglalkozik. A kidolgozott 2D-s és 3D-s végeselemes modellek a felületi érdesség figyelembevételére különböző modellezési megközelítéseket alkalmaznak (érdességcsúcshoz, sima/érdes érdességcsúcsra épülő megközelítés; szinuszhullámra, illetve szinuszhullámok összegére épülő többszintű megközelítés; mért felületi mikrotopográfia közvetlen felhasználására épülő megközelítés). A látszólag sima felületek által generált viszkoelasztikus súrlódással kapcsolatos kutatások lezárásaként, az értekezés második része a súrlódási erő viszkoelasztikus összetevőjének szakirodalomból vett mérési eredményekre épülő kísérleti vizsgálatára koncentrál. *A súrlódási erő felületi érdesség által EPDM és NBR gumiban generált viszkoelasztikus összetevőjének numerikus és kísérleti vizsgálata során kimutattam, hogy mikro-hiszterézis eredetű súrlódási erő látszólag sima, kent felületek esetén is fellép, de ennek nagysága nem lehet olyan nagy, mint ahogy Mofidi és szerzőtársai [44] állítják, mert sem a végeselemes szimulációk, sem az értekezésben bemutatott mérési eredmények nem igazolják mennyiségileg [44] eredményeit.*

A gépészmérnöki gyakorlatban igen nagy számban előforduló hidraulikus dugattyúrúd tömítések gyakran vegyes súrlódási állapotban üzemelnek. Vegyes súrlódási állapot esetén a hidrodinamikusan hatékony felépülő kenőfilm nem képes teljesen elválasztani a felületeket egymástól, így az érdességcsúcsok között szilárdtest érintkezés alakul ki. A Greenwood-Williamson- és a Persson-féle, egymással érintkező, érdes sík felületek középsíkjai közötti távolság és a névleges érintkezési nyomás kapcsolatát megadó érintkezési elméletek jelentősége miatt, az értekezés részletesen elemzi a két modellt, majd mennyiségi szempontból összehasonlítja a modellek által szolgáltatott eredményeket. *A Greenwood-Williamson- [27] és a Persson-féle [3, 63, 65] érintkezési elméletet merev síkkal érintkező elasztomerre alkalmazva kimutattam, hogy az érdes felület középsíkjának a tökéletesen sima felülethez mért távolságának elméleti értékei közötti különbség, 1 μm -es RMS érdesség, valamint 0,1 és 1 MPa közötti névleges érintkezési nyomás esetén, egy és négy nagyságrend között változik, de a különbség a névleges érintkezési nyomás csökkenésével folyamatosan csökken.* Ezt követően, részletesen bemutatásra kerül egy hidraulikus dugattyúrúd tömítések vegyes súrlódási állapotának modellezésére kidolgozott számítási algoritmus, amely Salant és szerzőtársai [Salant R., Maser N., Yang B. Numerical model of a reciprocating hydraulic rod seal. *Journal of Tribology*, Vol. 129, pp. 91-97 (2007)] numerikus modelljét alkalmazza. Az állandósult állapotbeli modell képes a felületi érdesség, a kavitáció, a rugalmas alakváltozás és a nyomásfüggő viszkozitás hatásának egyidejű figyelembe vételére. A számítási algoritmus által szolgáltatott eredmények között a névleges kenőfilm vastagság, a kenőfilmben kialakuló nyomás, a szilárd test-szerű érintkezés következtében kialakuló érintkezési nyomás mellett a szivárgás és a súrlódási erő várható nagysága is megtalálható. Az értekezés vegyes súrlódási állapot modellezéséhez kapcsolódó része egy O-gyűrű és egy kereskedelmi forgalomban kapható ablaktörlő lapát törlőél kenési állapotának numerikus modellezésével zárul. *Salant és szerzőtársai [41] állandósult állapotbeli, 1D-s, vegyes súrlódási állapotot leíró modelljének O-gyűrűre történő alkalmazásán keresztül kimutattam, hogy kitolás esetén a névleges kenőfilm vastagság nagyobb, mint behúzás esetén; a névleges érintkezési tartományon belül a kitolás során kavitáció alakul ki, miközben a kenőfilmben kialakuló nyomás csúcserő a kavitáció mentes tartományon belül nem haladja meg a 0,76 MPa-t; és a behúzás során nem lép fel kavitáció és a kenőfilmben kialakuló nyomás nem haladja meg a tömített nyomás értékét.* Továbbá, *Salant és szerzőtársai [41] vegyes súrlódási állapotot leíró modelljének kereskedelmi forgalomban kapható ablaktörlő lapát törlőéleire történő alkalmazásán keresztül kimutattam, hogy az érintkező testek középfelületei közötti rés a víz belépési pontjától távolodva*

először szűkül, majd tágul; a névleges érintkezési tartomány táguló részhez tartozó részén kavitáció alakul ki; az érdességcsúcs-típusú érintkezés következtében fellépő érintkezési nyomás legnagyobb értéke eléri a 0,8 MPa-t; és a kenőfilmben kialakuló nyomás csúcserőke három nagyságrenddel kisebb, mint az érdességcsúcs érintkezés következtében fellépő legnagyobb érintkezési nyomás.

Az értekezés utolsó fejezete viszkoelasztikus szemcsékből álló anyag tárolására használt silók/tölcsérek falaira ható szerkezetszintű erők (normális erő és súrlódási erő) szemcse-szintű kölcsönhatások modellezésére épülő becslésével foglalkozik. A diszkrét modellezési megközelítést képviselő diszkrét elem módszer elméleti háttérének és alkalmazhatóságának áttekintését követően részletesen bemutatásra kerül a dolgozat szerzője által kifejlesztett szimulációs program. A program minden egyes szemcse mozgását külön-külön vizsgálja, miközben a szemcsék más szemcsékkel és környezeti elemekkel való érintkezéseit is folyamatosan nyomon követi. A kontinuum mechanikán alapuló módszerekkel szemben, ez a technika a modellezett közeg viselkedését a szemcsék közötti kölcsönhatásokból származtatja. Az értekezésben bemutatott nem tengelyszimmetrikus tölcsérek, illetve silók falain fellépő súrlódási erő becslésével, valamint a töltési és a nem állandósult állapotbeli ürítési folyamat szimulációjával foglalkozó diszkrét elemes modellek mindegyike a szerző saját fejlesztésű számítógépes programjával készült, illetve annak segítségével került megoldásra. A számítások célja a töltési folyamat végén (statikus eset) és az ürítési folyamat kezdetén (dinamikus eset) fellépő falakra ható erők, és az abból származó nyomáseloszlások mennyiségi meghatározása. A kitűzött cél elérése érdekében a numerikus modellek viszkoelasztikus anyagi viselkedést figyelembe vevő normális és statikus súrlódás modellezésére is alkalmas tangenciális érintkezési modelleket, valamint kísérletek alapján meghatározott modell paramétereket használnak. *Cundall és Strack [79] háromdimenziós diszkrét elem módszere alapján általam kidolgozott számítógépes program alkalmazásával kimutattam, hogy négyzet keresztmetszetű tölcsér, illetve alsó kialakításban eltérő silók esetén a ferde és függőleges falakon a töltési folyamat végén fellépő súrlódási erő nagysága $\mu=0,3$ lokális, szemcse-szemcse és szemcse-fal súrlódási tényező és kísérletileg kalibrált érintkezési modell alkalmazása mellett a töltet súlyának 12...16%-a.*

Acknowledgements

I thank **Prof. Károly Váradi** (Budapest University of Technology and Economics) for turning my attention to numerical tribology when I was his PhD student and for inviting me, as young researcher, in his research group involved in the integrated project “Knowledge-based Radical Innovation Surfacing for Tribology and Advanced Lubrication (KRISTAL)” and supported by the 6th Framework Program of the European Commission, under contract NMP3-CT-2005-515837. FE prediction of viscoelastic friction and development of the computational algorithm for mixed friction was supported partly by the European Commission. Furthermore I am grateful to Prof. Váradi for the helpful discussions on FE modeling of friction related contact problems.

I thank **Prof. Fritz Ebert** (University Kaiserslautern) for drawing my attention to the discrete element method and its wide-ranging applicability as well as for supporting my work during an almost 2 years stay at University Kaiserslautern where I developed and implemented the discrete element-based computational algorithm. My research work was supported by the project “Numerische Simulation technischer Partikelsysteme auf Hochleistungsrechnern” of German Research Fund (DFG).

I would like to express my thanks to all the *coauthors* including *my former PhD students* (Gábor Bódai, Enikő Soós) for their work with which they contributed to the successful completion of research activities presented and summarized here and indirectly to the birth of this thesis.

I would like to express my special thanks to **Prof. Mihály Kozma** (Budapest University of Technology and Economics) for helpful discussions on interpretation and evaluation of friction tests and modeling of lubrication.

I thank **Dr. Sándor Horváth** (Óbuda University) for his interest and for supplying me with high-performance mobile computers without which this thesis would not have come into being.

Finally, I gratefully acknowledge the support of the János Bolyai Scholarship of the Hungarian Academy of Sciences and the “Development of quality-oriented and harmonized R+D+I strategy and functional model at BME” project supported by the New Hungary Development Plan (Project ID: TÁMOP-4.2.1/B-09/1/KMR-2010-0002). FE prediction of viscoelastic friction and numerical modelling of mixed friction was supported partly by the János Bolyai Scholarship.

Appendix A

A.1. Modeling of time independent, nonlinear (perfectly) elastic response of rubbers and rubberlike materials

The modeling of rubberlike materials is described, among others, by Dorfmann [96]. According to Dorfmann [96] the stress response of a hyperelastic material is given by the derivative of the scalar-valued strain energy function, being defined per unit volume (strain energy density function) in the reference configuration and representing the work done on the unit volume at a typical material particle (identified by a position vector) in changing the deformation gradient tensor from I (the identity tensor) to F . A brief overview of different strain energy functions for both incompressible and compressible hyperelastic materials (such as incompressible and compressible Mooney-Rivlin energy formulation, neo-Hookean, Blatz-Ko, Ogden, Gent, Arruda-Boyce or eight chain model) can also be found in the study of Dorfmann [96]. For additional details on rubber elasticity one can consult with works of Treloar [97], Achenbach and Streit [98] and Bóday [17].

A.2. Finite element modeling of small strain linear viscoelastic behavior of rubbers and rubberlike materials

The viscoelastic material behavior is modelled here by a spring-dashpot model. Such a phenomenological modeling approach does not take into consideration the real molecular structure of the material but it may be able to model accurately the macroscopic material response.

Considering the material behavior of rubber and rubber-like materials the generalized Maxwell-model (several Maxwell-models connected in parallel) connected parallel to a spring can be a reasonable choice as a material model because it is a widely accepted constitutive law and available in the most, commercial FE software packages. At the same time, it must be mentioned that its applicability depends strongly on the number of Maxwell elements. Even in case of 15-term Maxwell-model, there is a strong fluctuation in the loss factor-frequency curve that may cause inaccurate modeling results, especially when the excitation frequency varies in a broad frequency range. According to the experience of the author of this thesis a 40-term Maxwell model is able to describe with high accuracy the time dependent material behavior of viscoelastic materials in a wide frequency range.

Description of linear viscoelasticity can be found, among others, in the books of Ferry [99], Christensen [100], Findley et al. [101], and Aklonis and MacKnight [102]. Linear viscoelastic deformation is commonly described using the Boltzmann integral representation (convolution integral) in its relaxation form (stress relaxation) as [99]:

$$\sigma = \int_0^t E(t-t') \frac{d\varepsilon(t')}{dt'} dt', \quad (\text{A.1})$$

where σ and ε denote the stress and the strain, respectively. The information concerning time-dependent material behavior is involved in the tensile relaxation modulus ($E(t)$). In other words, $E(t)$ is the relaxation modulus at time t . This equation can be rewritten as

$$\sigma(t) = E_0 \int_0^t e(t-t') \frac{d\varepsilon(t')}{dt'} dt', \quad (\text{A.2})$$

where $e(t)$ is the normalized relaxation modulus, defined as $e(t) = E(t)/E_0$. Here $E_0 = E(t=0)$ is the instantaneous (or glassy) modulus. The normalized relaxation modulus is defined (approximated with desirable accuracy) as a Prony series (sum of exponentials) and can be formulated as

$$e(t) = 1 - \sum_{i=1}^N e_i \left(1 - e^{-\frac{t}{\tau_i}} \right). \quad (\text{A.3})$$

Similarly, the relaxation modulus is defined as

$$E(t) = E_0 - E_0 \sum_{i=1}^N e_i \left(1 - e^{-\frac{t}{\tau_i}} \right) = E_0 \left[1 - \sum_{i=1}^N e_i \left(1 - e^{-\frac{t}{\tau_i}} \right) \right] = E_0 - \sum_{i=1}^N E_i + \sum_{i=1}^N E_i e^{-\frac{t}{\tau_i}}, \quad (\text{A.4})$$

where $E_i = e_i \cdot E_0$ is the i -th modulus and τ_i is the i -th relaxation time. Here the Poisson's ratio is assumed to remain unchanged over time. Consequently, it does not appear in the stress relaxation formulation. The physical interpretation of time independent Poisson's ratio is that relaxation processes in mutually orthogonal directions proceed in the same manner. Although, in many cases, this assumption is a good approximation it must be mentioned that, in real polymers, the Poisson's ratio usually exhibits time- and temperature dependent behavior as reported by Tschoegl et al. [103] and Pandini and Pegoretti [104].

This representation of the relaxation modulus emphasizes that the relaxation occurs not at a single time, but at many, different time instants (spectrum of relaxation times). The specification of the linear viscoelastic model by a Prony series is extremely useful for the FE prediction of hysteresis friction because, in most finite element software packages, this specification is used. The above equation of stress relaxation (reduction of stress under constant strain) can be represented graphically by using a generalized Maxwell-model connected parallel to a spring. Such a model is depicted in Fig. A1.

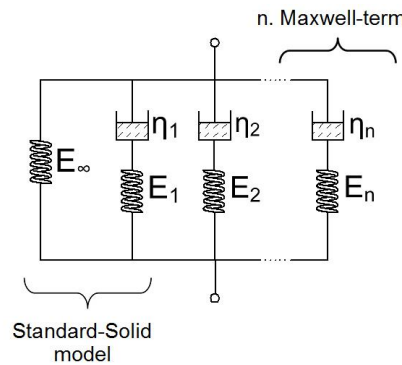


Fig. A1. Schematic representation of a generalized Maxwell-model connected parallel to a spring [106]

It is worth noting that there is no consensus in the literature regarding the precise name of the viscoelastic model. In FE software packages, research papers dealing with FE modeling and many papers investigating the viscoelastic response of polymers or elastomers (for example in the paper of Bardenhagen et al. [105]) the material model seen in Fig. A1 is termed generalized Maxwell-model. In this thesis, the term generalized Maxwell-model indicates several Maxwell-models (a linear spring and dashpot in series) connected parallel. One of the possibilities available in MSC.Marc to model linear viscoelasticity is to use the generalized Maxwell-model connected parallel to a spring. As dictated by its graphical representation

the stress in such a viscoelastic model is the sum of stresses in the Maxwell-elements and in the spring E_∞ . The model consists of linear springs and dashpots. In case of linear spring, the modulus is constant while the stress-strain relationship is linear. Contrary to this, in case of linear dashpot, the stress-strain rate relationship is linear while their ratio, the viscosity, is constant (stress or strain rate independent viscosity).

Denoting the modulus of the separate spring by E_∞ (relaxed modulus) the interrelation among the normalized moduli can be written as

$$e_\infty + \sum_{i=1}^N e_i = 1, \quad (\text{A.5})$$

where $e_\infty = E_\infty / E_0$ and N is the number of the Maxwell branches. Consequently, the relation between the moduli is formulated as

$$E_0 = E_\infty + \sum_{i=1}^N E_i. \quad (\text{A.6})$$

The i -th relaxation time of the generalized Maxwell model (τ_i) is defined as $\tau_i = \frac{\eta_i}{E_i}$, where η_i is the dynamic viscosity of the i -th dashpot.

As the viscoelastic model connected parallel to a spring is used for hysteresis friction prediction (prediction of friction force due to the hysteresis) in this thesis the dynamic modulus of rubber has primary importance. If a linear viscoelastic material is subjected to a sinusoidally varying strain having an amplitude ε_0 and angular frequency ω then the steady-state response (stress) will also be sinusoidal with the same frequency (ω) but some time delay. This time delay or phase shift is represented by the so-called phase angle δ . In case of elastic material $\delta = 0$, while in case of totally viscous material $\delta = 90^\circ$. For rubbers the phase angle is greater than 0° but smaller than 90° ($0^\circ < \delta < 90^\circ$) as reported by Bodor and Vas [107]. The stress response can be written as

$$\sigma(t) = \sigma_0 \sin(\omega t + \delta) = \sigma_0 \cos(\delta) \sin(\omega t) + \sigma_0 \sin(\delta) \cos(\omega t), \quad (\text{A.7})$$

where σ_0 is the stress amplitude. According to the latter expression the stress response can be divided into two parts. One part of the stress ($\sigma_0 \cos(\delta) \sin(\omega t) = \sigma_0' \sin(\omega t)$) is in phase with the strain (elastic stress) while its other part ($\sigma_0 \sin(\delta) \cos(\omega t) = \sigma_0'' \cos(\omega t)$) is out of phase with a phase angle of 90° (viscous stress). Considering the stress as a complex quantity (σ^*) having a norm of σ_0 it can be written that

$$|\sigma^*| = \sigma_0 = \sqrt{(\sigma_0')^2 + (\sigma_0'')^2}, \quad (\text{A.8})$$

where σ_0' denotes the real part of stress (being in phase with the strain) and σ_0'' denotes the imaginary part of stress (being out of phase with a phase angle of 90° compared with the strain). The strain energy associated with the in-phase stress and strain is the energy stored in the material (reversible strain energy). Contrary the strain energy associated with the out of phase stress and strain is the energy converted into heat (irreversible strain energy) [107]. The complex dynamic modulus E^* is defined as the stress amplitude divided by the strain amplitude i.e.

$$|E^*| = \frac{\sigma_0}{\varepsilon_0} = \sqrt{\left(\frac{\sigma_0'}{\varepsilon_0}\right)^2 + \left(\frac{\sigma_0''}{\varepsilon_0}\right)^2} = \sqrt{\left(\frac{\sigma_0 \cos \delta}{\varepsilon_0}\right)^2 + \left(\frac{\sigma_0 \sin \delta}{\varepsilon_0}\right)^2} = \sqrt{(E')^2 + (E'')^2}, \quad (\text{A.9})$$

where E' is the storage (elastic) modulus (real part of the complex dynamic modulus) and E'' is the loss (viscous) modulus (imaginary part of the complex dynamic modulus). As reported by Roylance [108] the storage modulus represents the energy stored (elastic portion) and the loss modulus represents the energy dissipated as heat (viscous portion).

As it was mentioned the N-term generalized Maxwell-model consists of N Maxwell models in parallel. With regard to the serial connection of the linear spring and the linear dashpot of a Maxwell-model the resultant deformation of the model is given as the sum of deformations of the spring and the dashpot. This can be written in mathematical form as

$$\dot{\varepsilon} = \frac{\dot{\sigma}}{E} + \frac{\sigma}{\eta}, \quad (\text{A.10})$$

where $\dot{\varepsilon}$ denotes the resultant strain rate, E denotes the modulus of the linear spring, and η denotes the dynamic viscosity of the dashpot. Based on this equation both the frequency dependent storage and loss moduli of the Maxwell-model can be derived as presented by Pahl et al. [109].

$$E'(\omega) = E \frac{\tau^2 \omega^2}{1 + \tau^2 \omega^2}, \quad (\text{A.11})$$

$$E''(\omega) = E \frac{\tau \omega}{1 + \tau^2 \omega^2}, \quad (\text{A.12})$$

where $\tau = \eta/E$ is the relaxation time and ω denotes the angular frequency of the excitation. The loss factor ($\tan(\delta)$) is defined as the ratio of the loss and storage modulus thus it can be formulated as

$$\tan(\delta) = \frac{E''(\omega)}{E'(\omega)} = \frac{1}{\tau \omega}. \quad (\text{A.13})$$

Now, consider a generalized Maxwell element in which finite number of Maxwell-models are connected in parallel as done by Wiechert [110]. In the case of generalized Maxwell element, the relationship for storage and loss modulus can be written as the sum of separate Maxwell models (elements) i.e.

$$E'(\omega) = E_0 \sum_{i=1}^N e_i \frac{\tau_i^2 \omega^2}{1 + \tau_i^2 \omega^2}, \quad (\text{A.14})$$

$$E''(\omega) = E_0 \sum_{i=1}^N e_i \frac{\tau_i \omega}{1 + \tau_i^2 \omega^2}, \quad (\text{A.15})$$

where N denotes the number of Maxwell elements and τ_i denotes the relaxation time of the i-th Maxwell element.

Finally, consider the viscoelastic model where a finite number of Maxwell elements and a separate linear spring (E_∞) are connected in parallel (see Fig. A1). The linear spring E_∞ is responsible for the time-independent elastic part of the deformation while the finite number of Maxwell elements represents the time-dependent elastic (viscoelastic) part of the deformation. Derivation of the frequency dependent complex dynamic modulus of the viscoelastic model can be found, among others, in studies of Kaliske and Rothert [111], Achenbach

and Frank [22], and Achenbach and Streit [98]. Using these results the storage and loss modulus can be written as

$$E'(\omega) = E_0 \left[1 - \sum_{i=1}^N e_i \right] + E_0 \sum_{i=1}^N e_i \frac{\tau_i^2 \omega^2}{1 + \tau_i^2 \omega^2} = E_0 - E_0 \sum_{i=1}^N e_i \frac{1}{1 + \tau_i^2 \omega^2}, \quad (\text{A.16})$$

$$E''(\omega) = E_0 \sum_{i=1}^N e_i \frac{\tau_i \omega}{1 + \tau_i^2 \omega^2}. \quad (\text{A.17})$$

In other words, the relationships between storage ($E'(\omega)$) and loss modulus ($E''(\omega)$) and a continuous relaxation spectrum can be approximated with any desirable accuracy as the above expressions show. Contribution of the different Maxwell elements to the cumulative (resultant) frequency-dependent material behavior of the viscoelastic model is shown in Fig. A2. In many cases, components of the dynamic modulus are expressed in function of the cyclic frequency f . As $\omega = 2\pi f$ the cyclic frequency dependence of the storage modulus can be written as

$$E'(f) = E_0 \left[1 - \sum_{i=1}^N e_i \right] + E_0 \sum_{i=1}^N \frac{e_i \cdot \tau_i^2 \cdot (2 \cdot \pi \cdot f)^2}{1 + \tau_i^2 \cdot (2 \cdot \pi \cdot f)^2}. \quad (\text{A.18})$$

The above shows that the time dependence of relaxation modulus and frequency dependence of storage and loss modulus can be captured by a spring-dashpot model with a sufficient number of elastic and viscous elements [99].

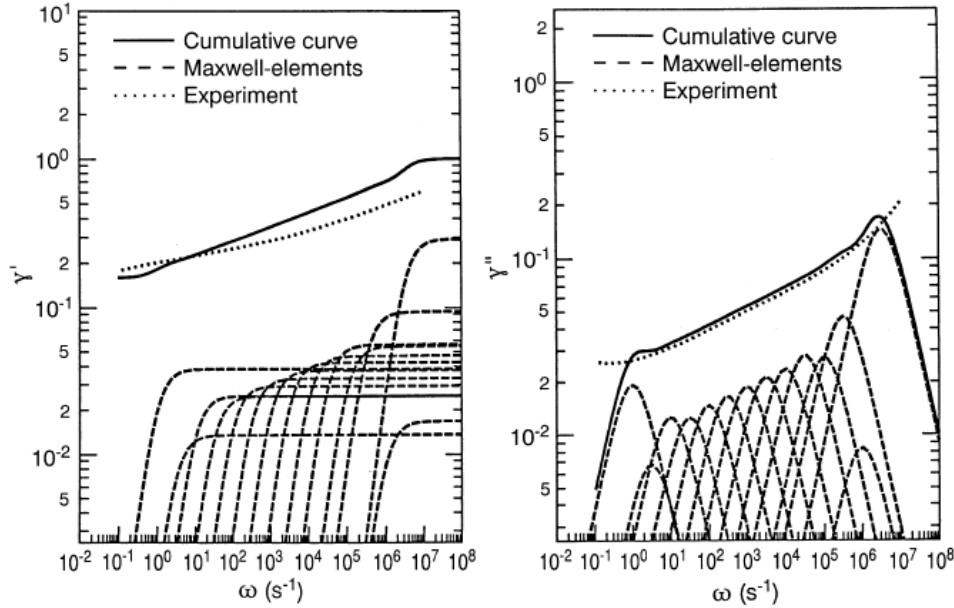


Fig. A2. Contribution of Maxwell elements to the cumulative (resultant) normalized storage

$$\left(\gamma' = 1 + \sum_{i=1}^N \gamma_i \frac{\tau_i^2 \omega^2}{1 + \tau_i^2 \omega^2} = \frac{E_\infty}{E_0} + \sum_{i=1}^N \frac{E_i}{E_\infty} \frac{\tau_i^2 \omega^2}{1 + \tau_i^2 \omega^2} \right) \text{ and loss modulus}$$

$$\left(\gamma'' = \sum_{i=1}^N \gamma_i \frac{\tau_i \omega}{1 + \tau_i^2 \omega^2} = \sum_{i=1}^N \frac{E_i}{E_\infty} \frac{\tau_i \omega}{1 + \tau_i^2 \omega^2} \right) \text{ of a 14-term generalized Maxwell model connected parallel to a separate spring [111]}$$

Experimental data from either creep or relaxation tests can be used to identify the model parameters with the software's built-in algorithm. In other words, more sophisticated

commercial FE software packages are able to compute the model parameters (e_i, τ_i) automatically from experimental data. However, most of the software packages have limited capability for “calibrating” n-term Maxwell model. In most cases, the number of terms is limited anywhere between ten and fifteen. As an example MSC.Marc is able to identify automatically the model parameters from a fit to creep or stress relaxation tests but cannot to do this if DMTA data are available only. Additionally, the number of terms in the fitted viscoelastic model is limited to ten. Finally, it is worth to mention that in case when model parameters are specified using the graphical user interface of the software the number of Maxwell-terms is limited to fifteen. As it is pointed out in Appendix C the models calibrated by without over passing the capability of the applied, commercial FE software have strongly limited accuracy when they are used for hysteresis friction prediction.

A.3. Finite element modeling of large strain (finite) linear viscoelastic behavior of rubbers and rubber-like materials

In this subchapter, the large strain viscoelastic model available in MSC.Marc and used in the prediction of the viscoelastic friction component is presented briefly. As it is well known, the mechanical behavior of rubber-like materials is principally characterized by a nonlinear stress-strain curve and time and temperature dependency [97, 99, 100]. The short-time (instantaneous or glassy) behavior of the generalized Maxwell-model connected parallel to a nonlinear spring can be specified, among others, by a strain energy density function (W^0). In the hysteresis friction computations reported in this thesis the isotropic, incompressible two-term Mooney-Rivlin strain energy formulation is used. According to Dorfmann [96] a strain energy function may be formulated in terms of the invariants I_1 , I_2 and I_3 by expanding the energy function in the Taylor series. It must be mentioned that for an incompressible material $I_3 = 1$. The Mooney-Rivlin energy formulation is the linear expansion of the strain energy function thus it has the form

$$W = C_{10}(I_1 - 3) + C_{01}(I_2 - 3), \quad (\text{A.19})$$

where I_1 and I_2 are the first and second invariants of the right or left Cauchy-Green deformation tensor, while C_{10} and C_{01} are material constants to be determined experimentally.

Combination of hyperelastic model and generalized Maxwell-model results in a large-strain viscoelastic model showing both the time dependency and the nonlinear behavior of rubber. The instantaneous strain energy density is distributed among the branches of the spring-dashpot model by assuming that the instantaneous strain energy in the i-th Maxwell element can be computed as

$$W_i = e_i W^0, \quad (\text{A.20})$$

where W^0 is the instantaneous strain energy defined by the Mooney-Rivlin model. It must be mentioned that the two parameter Mooney-Rivlin material law cannot describe stress-strain curves having inflexion point at very large strain (stiffening of rubber at large tensile strains). Consequently, if the strain exceeds the value belonging to the inflexion point then the Mooney-Rivlin formulation should be replaced with a multi-parameter (see for example the Signorini hyperelastic material model). In the Signorini hyperelastic material model [36, 112] the strain energy density function is formulated as

$$W = C_{10} \cdot (I_1 - 3) + C_{01} \cdot (I_2 - 3) + C_{20} \cdot (I_1 - 3)^2, \quad (\text{A.21})$$

where C_{10} , C_{01} , and C_{20} are material constants to be determined experimentally.

As it is known from continuum mechanics stresses can be computed by differentiation of the strain energy density function with respect to the Green-Lagrange strains. For instance, the second Piola-Kirchhoff stress response of the model for instantaneous deformations is obtained by differentiation. A detailed review of the large strain viscoelastic model used can be found in the study of Bódai and Goda [113]. For more detail on the model see the works of Holzapfel [114] and Kaliske and Rothert [111]. As it was concluded by Kaliske and Rothert [111] combination of such a material model with the finite element method provides an efficient numerical tool for large scale computations of time- and frequency-dependent materials.

Finally, it must be mentioned that whilst at small strains the linear viscoelastic theory describes accurately the behavior of elastomers however at large strains - especially in presence of filler particles such as carbon black or silica particles - they exhibit strongly nonlinear viscoelastic behavior. In the latter case, the accuracy of numerical models using Prony series fitting for the description of viscoelasticity can suffer to some extent from the nonlinearity of rubber rheology [25]. In case of nonlinear viscoelasticity, the time dependent response of the material depends on the magnitude of stress or strain.

A.4. Parameter identification based on the time (frequency)-temperature correspondence principle

In general, the spectrum of relaxation times of polymers includes both the very fast (dynamic load) and the quite slow (static load) relaxation processes [115]. The dynamic spectrum ranging from 10^{-6} to 10 s can be determined from dynamic data while the static spectrum ranging from 1 to 10^8 s can be determined from long lasting tests (e.g. creep or relaxation tests). The transition from the dynamic to the static spectrum has already been proved experimentally [115]. In order to study the viscoelastic response at low strains, among others, the dynamic mechanical (thermal) analysis (DM(T)A) is used, where the specimen undergoes repeated small-amplitude strains at different temperatures and excitation frequencies. The DMTA test provides frequency dependent dynamic properties (storage modulus ($E'(\omega)$), loss modulus ($E''(\omega)$), and loss factor or loss tangent ($\tan \delta(\omega)$)) at different temperatures. If DMA data are available the parameters of the viscoelastic material model may be determined from a fit to the so called master curve. The construction of master curve or generalized curve is described in depth, among others, Ferry [99], Felhős et al. [11], Herdy [33], Bódai and Goda [116] and Urzsumcev and Makszimov [115]. Due to this, here a brief description is presented only.

If the material behaves thermorheologically simple, then its deformation is governed by a single relaxation mechanism. This relaxation mechanism manifests itself as a spectrum of relaxation times and is accelerated by the temperature through specific shift function as

$$\tau_i(T) = \tau_i(T_r) \cdot a_T(T), \quad (\text{A.22})$$

where $a_T(T)$ denotes the shift factor along the time axis at temperature T, $\tau_i(T_r)$ is the i-th relaxation time at the reference temperature, while $\tau_i(T)$ is the corresponding relaxation time at temperature T. In other words, in order to determine the material behavior at a temperature other than the reference one we need to specify the relaxation times ($\tau_i(T)$) according to the above expression. This principle, known in the literature as time-temperature correspondence principle or time-temperature superposition principle, emphasizes the equivalence of time and temperature. In general, the time-temperature correspondence principle may be written as

$$t(T) = t = t(T_r) \cdot a_T(T), \quad (\text{A.23})$$

where $t(T) = t$ is the time at temperature T , and $t(T_r)$ is the time at the reference temperature or as

$$E(t, T) = E(t(T_r), T_r) = E\left(\frac{t}{a_T(T)}, T_r\right), \quad (\text{A.24})$$

where $E(t, T)$ denotes the modulus at time t and temperature T . The latter may be written in an alternative form as

$$E(t(T_r), T_r) = E(t(T_r) a_T(T), T). \quad (\text{A.25})$$

By introducing the excitation (cyclic) frequency f which is a reciprocal time quantity the time-temperature correspondence principle may be written, in general, as [115]

$$E^*(f, T) = E^*(f a_T(T), T_r), \quad (\text{A.26})$$

or as

$$E^*(f(T_r), T_r) = E^*\left(\frac{f(T_r)}{a_T(T)}, T\right), \quad (\text{A.27})$$

where f is the cyclic frequency at temperature T , $f(T_r)$ is the cyclic frequency at the reference temperature, $a_T(T)$ is the shift factor along the frequency axis and E^* is the complex dynamic modulus. The shift along the abscissa (horizontal shift) is typical at amorphous thermoplastic polymers however, at resins, partially crystalline polymers and elastomers a shift along the ordinate (vertical shift) may also be necessary during the master curve construction [115]. In the latter case, the time-temperature correspondence principle has the following form

$$E^*(f, T) = b_T(T) E^*(f a_T(T), T_r), \quad (\text{A.28})$$

where $b_T(T)$ denotes the vertical shift factor. At the reference temperature, naturally, there is no need for shifting thus $a_T(T_r) = b_T(T_r) = 1$. In case of unfilled rubber, $b_T \approx 1$ (no vertical shift is needed) and the temperature dependency of a_T is (approximately) given (as in most cases) by the Williams-Landel-Ferry (WLF) equation [117]. The WLF equation can be formulated (see [118]) as

$$\log a_T = \frac{-C_1(T - T_r)}{C_2 + (T - T_r)}, \quad (\text{A.29})$$

where a_T is the shift factor, T_r is the reference temperature (usually the glass transition temperature), while C_1 and C_2 are the WLF parameters at the reference temperature T_r . For many amorphous thermoplastic polymers $C_1 = 17.4$, $C_2 = 51.6^\circ\text{C}$ (universal WLF parameters). Strictly speaking, however, the WLF equation is valid in the range of $T_g < T < T_g + 100$, where T_g denotes the glass transition temperature of the polymer and the temperature is measured in $^\circ\text{C}$. In [119], Stan et al. found that the agreement with the measurement can be improved if two different sets of WLF parameters are used above and below the glass transition temperature. If the reference temperature differs from the glass transition temperature (T_g) of the material then the WLF parameters at any reference temperature T_r (C_1 and C_2) may be easily related with those at T_g (C_{1g} and C_{2g}) [99] by

$$C_1 = \frac{C_{1g} \cdot C_{2g}}{C_{2g} + (T_r - T_g)}, \quad (\text{A.30})$$

and

$$C_2 = C_{2g} + (T_r - T_g) \quad (\text{A.31})$$

At the same time it must be mentioned that below T_g the temperature dependency (shift of the relaxation times along the time or frequency axis) can be described more accurately by the so called Arrhenius equation [115]. According to this the application of WLF equation in this temperature range is usually an approximation (see Fig. A3).

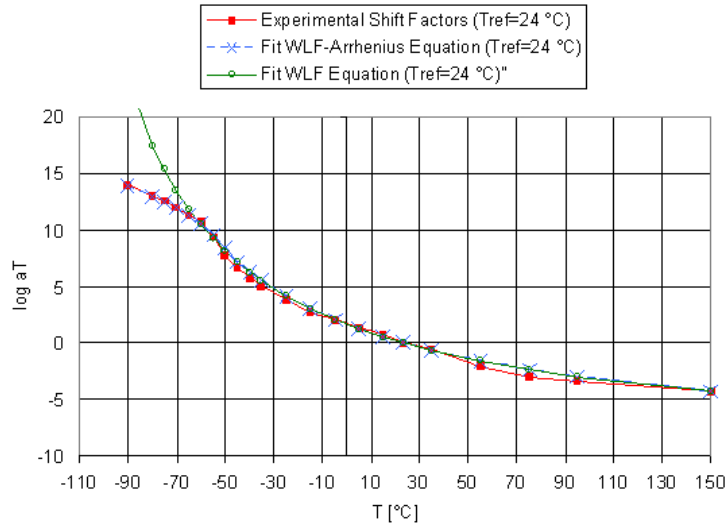


Fig. A3. Temperature dependency of shift factor (EPDM 75° IRH rubber, DMTA test, $f=1 \dots 100$ Hz, $T=-90 \dots 150^\circ\text{C}$, $\Delta T=10^\circ\text{C}$) [120]

According to the time-temperature correspondence principle one can transform the storage modulus isotherms measured to a continuous storage modulus master curve belonging to a reference temperature. As Fig. A4 shows the DMA isotherms are shifted horizontally along the frequency axis with respect to the reference isotherm. Naturally, the isotherm belonging to the reference temperature is not shifted i.e. remains its original position. In Fig. A4, no vertical shifting is performed. The master curve predicts the behavior over a very wide frequency range from isotherms measured in a narrow frequency domain. In order to obtain material model parameters (e_i , τ_i , E_0 , N) the model chosen has to be fitted, for example, to the storage modulus master curve. In case of n-term generalized Maxwell model, this means that the storage modulus function (see Eq. (A.16)) has to be fitted to the experimentally determined storage modulus master curve. However if the fitting is performed in respect of a single function only, then it cannot be guaranteed that the material model will describe the real (E') and imaginary (E'') part of the complex modulus with the same accuracy.

In general, if DMTA data are available the viscoelastic model parameters (e_i , τ_i , E_0 , N) may be determined by fitting the storage modulus function ($E'(\omega)$) to measured storage modulus master curve (see the works of Achenbach and Frank [22], Herdy [33], and Nguyen et al. [26]), the loss modulus function ($E''(\omega)$) to measured loss modulus master curve (see the work of Kaliske and Rotherth [111]) or the (norm of the) complex modulus function ($E^*(\omega)$) to (norm of the) measured complex modulus master curve (see Scaraggi and

Persson's study [25]) based on an optimization method. The latter is used to minimize the residual (or the error) between the modulus function fitted and the measured master curve with respect to the model's parameters. As an example, in the method of least squares, sum of square error is minimized. For the sake of simplicity, in [111], the model parameters have been chosen on the basis of the measured loss modulus. As it can be seen in Fig. A2, in such a case, discrepancies between experiment and model curve may be found for the storage modulus. As an alternative the deviation of measured data and mathematical approximation could be distributed to both the real (storage modulus) and the imaginary (loss modulus) part when model parameters are identified from a fit to the complex modulus using a refined identification algorithm. Additionally, the viscoelastic model parameters may also be identified e.g. from standard tensile tests performed at wide temperature range as reported by Bódai and Goda [121].

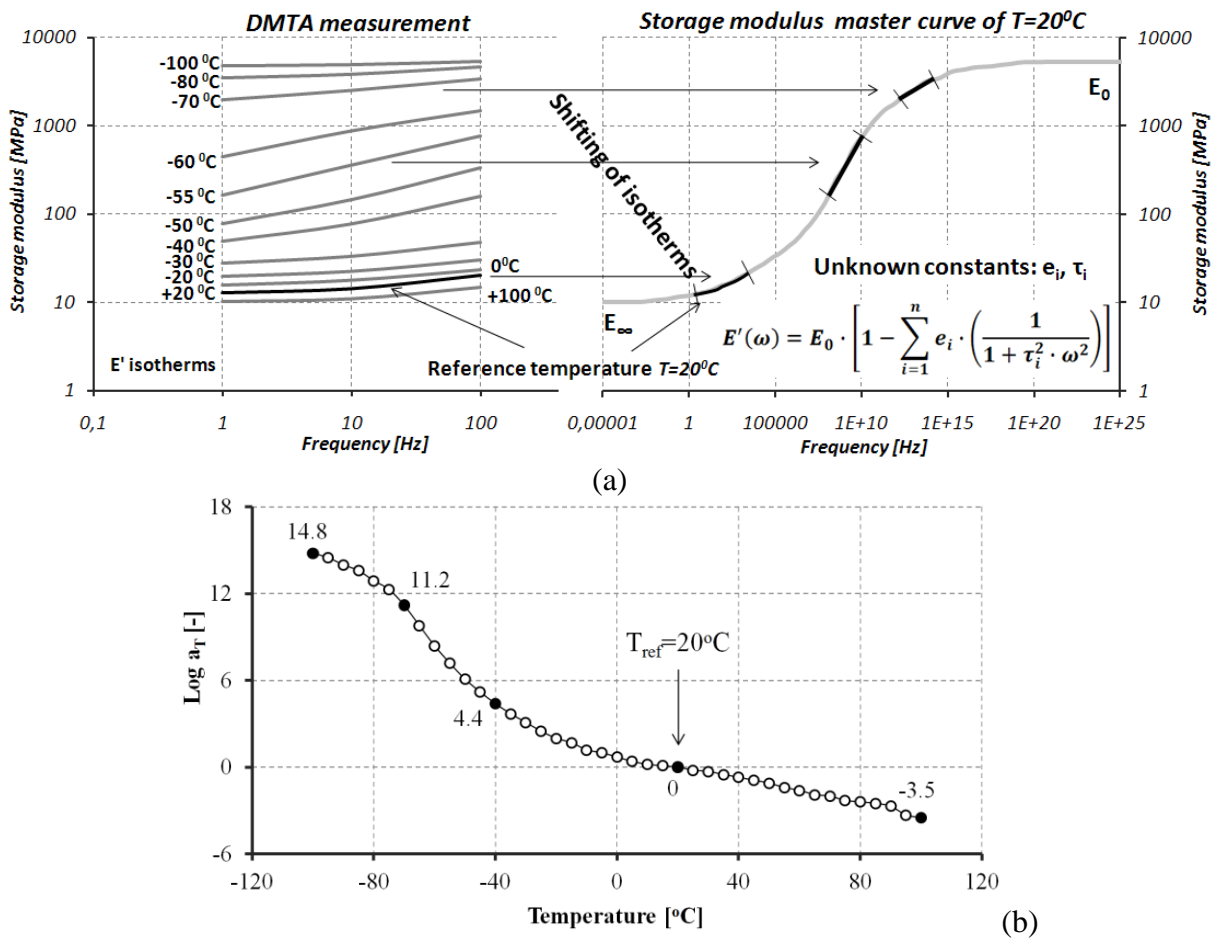


Fig. A4. (a) Construction of storage modulus master curve (prismatic specimen having a length of 21.7 mm, width of 3.75 mm, thickness of 1.32 mm and cutting from a SWF Duotec+ commercial windscreen wiper blade; static preload=0.1 N; sinusoidally varying strain excitation with 1% amplitude; temperature step= 5°C). For the sake of simplicity only one part of measured isotherms are depicted. [116] (b) Values of $\text{Log } a_T$ at a reference temperature of 20°C [121]

The time independent hyperelastic behavior being defined by C_{10} and C_{01} can be investigated experimentally by using quasistatic stress-strain tests in tensile, simple shear, etc. mode. (However when identifying model parameters by curve fitting we have to work carefully because, as mentioned by Yeoh [123] the Mooney-Rivlin model obtained by fitting ten-

sile data is quite inadequate in other modes of deformation, especially compression.) As none of them was available the Mooney-Rivlin parameters (C_{10}, C_{01}) were identified as follows. Among others, Gent [122] pointed out that, in case of simple shear, the Mooney-Rivlin model obeys Hooke's law i.e.

$$\tau = G\gamma = 2(C_{10} + C_{01})\gamma, \quad (\text{A.32})$$

where τ denotes the shear stress, γ is the shear strain, and G is the shear modulus. Using the relationship between the shear modulus and Young's modulus (E) valid for homogeneous and isotropic materials and a Poisson ratio (ν) of 0.5 the Mooney-Rivlin hyperelastic model results in a Young's modulus of

$$E = 3G = 6(C_{10} + C_{01}). \quad (\text{A.33})$$

The glassy Mooney-Rivlin parameters used in the prediction of the viscoelastic friction component are computed from the compressive glassy modulus (E_0) provided by DMTA test as

$$E_0 = 6(C_{10} + C_{01}), \quad (\text{A.34})$$

and

$$\frac{C_{01}}{C_{10}} = \frac{1}{4}. \quad (\text{A.35})$$

The latter is a reasonable assumption if only the Young's modulus is available and not the full uniaxial stress-strain curve [36].

The large strain linear viscoelastic model used in this thesis requires the following parameters to be known from fits to experiments: $C_{10}, C_{01}, E_0, e_i, \tau_i$ ($i = 1 \dots N$), and N . In order to obtain a good fit, the smallest number of Prony series terms should equal the number of time decades spanned in the test/master curve as concluded by Urzsumcev and Makszimov [115].

A.5. Extension of the material model over the viscoplastic material behavior

As the hysteresis may be explained by both viscous and plastic deformation it is worth to extend the material model to viscoplasticity. Soós and Goda [106] extended the spring-dashpot model introduced above over the viscoplastic material behavior by replacing the linear spring with an „elastic-plastic” spring as proposed by Bardenhagen et al. [105] (see Fig. A5). The key characteristic of this approach is the addition of stresses corresponding to viscoelastic and elastic-plastic constitutive model components. Similar to the former parts of the Appendix the phenomenological modeling approach used does not take into consideration the real molecular structure of the material but it may be able to model accurately the macroscopic material response. For the sake of simplicity the “elastic-plastic spring” consists of only two linear elastic springs and a “slider element”. The “elastic-plastic spring” behaves linearly (with a modulus of E_S) until the element stress does not reach the yield strength (σ_y) because the “slider element” behaves as an ideally rigid element in this range. When the element stress becomes greater than or equal to the yield strength the “slider element” slides and the spring with modulus E_T starts to work. In other words, the plastic deformation is only active when a yield criterion is met. At and above the yield strength the “elastic-plastic spring” behaves as a linear spring with modulus

$$E = (E_S \cdot E_T) / (E_S + E_T), \quad (\text{A.36})$$

because the two springs (E_S and E_T) are connected in series. As the modulus E_T does not depend on the plastic strain the instantaneous modulus E of the “elastic-plastic spring” is plastic strain independent. If one needs a plastic strain dependent “elastic-plastic spring” then the linear spring with modulus E_T has to be replaced by a non-linear spring. In our case, the “elastic-plastic spring” has three parameter (E_S , E_T , σ_y) but, in fact, only two parameters must be determined from additional experiments, because E_S is known from the storage modulus master curve ($E_S=E_\infty$). Strictly speaking the original viscoelastic model is modified by taking into consideration the rate independent plasticity.

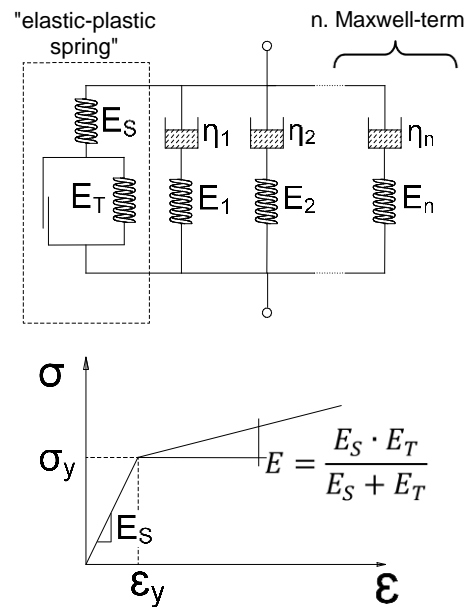


Fig. A5. Schematic representation of the viscoplastic material model (E_∞ -relaxed modulus, E_i -modulus of the i th spring, η_i -viscosity of the i th dashpot, n - number of Maxwell terms, E_S , E_T -moduli of “elastic-plastic spring”, σ_y -yield strength, ϵ_y -yield strain). The mechanical behavior of the “elastic-plastic spring” is shown in the stress-strain diagram. (From [106].)

The viscoplastic material model, which is not used directly in this thesis, has been incorporated into axisymmetric FE models of short glass fiber reinforced polyamide tubes by Soós and Goda [106]. The material model was built in the FE models through the overlay method. The basic concept of the overlay model is that the material behavior can be divided into a number of parallel fractions with simple constitutive models and adequate material parameters. The translation of the overlay model in a FE scheme is based on generating a model with several identical overlaid meshes sharing the same nodes. As each FE mesh may have different material behavior it is possible to model even the very complex material responses. In the viscoplastic FE simulations reported by Soós and Goda [106] the Von Mises yield criterion and the isotropic work hardening rule were used. According to the Von Mises yield criterion if the Mises-type equivalent stress reaches the yield strength (σ_y) of “elastic-plastic” spring then plastic strain appears.

Appendix B

B.1. Surface roughness spectral density

Surface roughness spectral density function or spectrum depicts the components of surface height profile of rough surfaces as a function of inverse of wavelength (spatial frequency). Surface height profile of a rough surface can be considered as a signal which describes the variation of a random process in the space. As it is well known the spectral analysis is a frequently used method of signal processing.

Conventionally, statistical parameters are used for characterizing surface roughness. However it is well known that these parameters depend on the resolution (sampling interval) and scan length (sampling length) of the surface roughness measurement. Using surface roughness spectral analysis of rough surfaces these problems can be avoided. Although many experts urge the application of 3D surface topography characterization instead of 2D traditionally and in accordance with international standards, the micro-geometry of operating surfaces, in the most cases, is characterized in two dimensions. Beside the application of statistical parameters obtained from 2D and 3D parameter-based technique, nowadays, two dominant research trends can be observed. Either of them puts the focus on the local features of topographies through the identification of asperities and scratches. The other concentrates on the “global” surface characterization and uses complex mathematical methods. For instance, in the theory of Persson [3] developed for the prediction of fractal surface generated viscoelastic friction the surface roughness spectrum is used to characterize multi-scale nature of rough surfaces (asperities at multiple scales). Proper characterization of surface roughness is of primary importance because output of the friction models depends strongly on the reliability of the surface roughness model applied as input data. In [60], Czifra et al. compares the capability and results of three different surface characterization techniques (parameter based technique, slicing method for identification of asperities/scratches and surface roughness spectral analysis) through the analysis of brake plungers manufactured by three different surface finishing techniques (cork-wheel, sand paper, rolling). Rough surfaces obtained by using line-scan instrument can be seen in Fig.B1.

One of the main objectives of this section is to describe briefly the way of surface roughness spectral analysis in 3D. Surface roughness spectral density can be obtained from the measured 3D topography (height profile) using Fourier transformation. Fourier transformation of 3D engineering topography (see [124]) can be written as

$$F(p, q) = \iint z(x, y) e^{-i2\pi(px+qy)} dx dy. \quad (\text{B.1})$$

Its discrete form, i.e. the discrete Fourier transformation (DFT) is given as

$$F(p_k, q_l) = \Delta y \cdot \Delta x \sum_{d=1}^N \sum_{c=1}^M z(x_c, y_d) e^{-i2\pi(x_c p_k + y_d q_l)}, \quad (\text{B.2})$$

where p_k is the k^{th} spatial frequency in direction x , q_l is the l^{th} spatial frequency in direction y , $z(x_c, y_d)$ is the height coordinate located at x_c, y_d , M is the number of points in profile, N is the number of profiles, $\Delta x, \Delta y$ are sampling distances, e is the basis of the natural logarithm, whilst i is the imaginary unit. As it can be seen DFT gives complex result.

$$F(p_k, q_l) = \text{Re}(F(p_k, q_l)) + i \cdot \text{Im}(F(p_k, q_l)). \quad (\text{B.3})$$

The surface roughness spectral density (surface roughness spectrum) is defined as

$$A(p_k, q_l) = \frac{F(p_k, q_l)F^*(p_k, q_l)}{MN\Delta x\Delta y} = \frac{\text{Re}^2 F + \text{Im}^2 F}{MN\Delta x\Delta y}. \quad (\text{B.4})$$

The surface roughness spectrum is usually represented in log-log scale. For rough surfaces with isotropic statistical properties (isotropic surface roughness) the surface roughness spectrum appears as a truncated conical surface. In this case, the surface roughness spectral density may be given by the $A(q)=C(q)$ function (spectral density curve) where

$$q = \sqrt{p_k^2 + q_l^2}. \quad (\text{B.5})$$

The dimension of surface roughness spectral density $A(q)$ is also $[\mu\text{m}^4]$, relating that results come from 3D surface roughness spectral analysis. The slope of the straight line fitted to the spectral density curve has correlation with fractal dimension of surface topography defined as

$$D_f = 3 - H, \quad (\text{B.6})$$

where H i.e. the Hurst exponent. With this the slope of the spectral density curve is

$$\text{Slope} = -2(H + 1). \quad (\text{B.7})$$

In order to accelerate the computation of surface roughness spectrum a computer code has been developed and implemented in C++ by the author of this thesis. Spectrum analysis reported by Czifra et al. [60] has been performed using this code. Fig. B2 shows clearly that, in case of three-dimensional surface topography, the surface roughness spectrum will appear as a surface (PSD surface). In many cases, the input data for surface roughness spectrum, however, is not a complete three-dimensional topography but a single profile as in the study of Schargott and Popov [125]. In this case, the spectrum appears as a curve rather than a surface. Many studies deal with the computation of micro hysteresis friction but the full surface roughness spectrum (PSD surface) of the rough surface is presented in none of these. Only averaged or non-averaged surface roughness spectral density curves can be found in these works. For surfaces with anisotropic surface roughness the surface roughness spectrum is dependent on both the location and direction of line scans. Consequently, the curve-based representation of the spectrum, strictly speaking, may be used for surface roughness with translational and rotational invariant (i.e. isotropic) statistical properties where the spectrum is independent of the location and direction of line scans.

Visualization of surface roughness spectrum needs adequate frequency distribution. Partitions of frequencies in the interesting frequency range are automatically generated using a logarithmic division. The lowest frequency is the inverse of sampling length: $q_{min}=1/(M*\Delta x)$, while the highest is the inverse of double of the sampling distance (resolution): $q_{max}=1/(2*\Delta x)$. Discrete values of frequencies are computed according to the following equations, where n is the number of frequencies and $i=1 \dots n$.

$$q_q = \frac{q_{max}}{q_{min}}^{1/(n-1)}, \quad (\text{B.8})$$

$$q_i = q_{(i-1)}q_q. \quad (\text{B.9})$$

If the frequency sampling is uniform in range of $q_{min} \dots q_{max}$, as it is the case in Persson et al.'s study [126], then the spectral density curve becomes dense at higher frequencies, so the features having small wavelength are enhanced, that greatly influence the slope of the fitted line. As these values carry the majority of measuring errors, inaccuracy of measurements may greatly influence the results. If uniform wavelength sampling is used, the low-frequency range becomes dense, and low-spacing topographic elements are not taken into consideration properly.

Although surface roughness spectrum-based representation of rough surfaces is able to capture the multi-scale (asperities are covered by smaller and smaller asperities) nature of real engineering surfaces it does not represent the real asperity geometry properly. As it is mentioned by Nguyen et al. [26] the real asperity geometry is likely not described accurately with the surface roughness spectrum in current rubber friction theories. In [26], an order-of-magnitude agreement is obtained between experimental and theoretical results for a very simple micro-topography (smooth silica lenses having RMS roughness of 0.3 nm covered with nano-spheres having average diameter of 77 nm) which shows that the viscoelastic dissipation computed is very sensitive to the details of the micro-topography (asperity slope and height distribution). Furthermore, as it is known, Persson's theory has been developed for fractal surfaces, however, real engineering surfaces are not true fractal surfaces. In [68], arbitrary machined metal sample is studied and it is concluded that fractal parameters are sensitive to the range of length-scales considered because the surface is not true fractal. In most cases, the fractal characterization can be considered as an approximation of the real surface topography.

Majority of surface roughness spectra available in the literature is for road surfaces because Persson's rubber friction theory is extensively used for tires. However the theory may also be used for apparently smooth engineering surfaces (sealing applications). At the same time, only few surface roughness spectrums are available in the literature for apparently smooth engineering surfaces. The work of Czifra et al. [60] can be considered as an exception because it focuses on surface roughness spectral analysis of real apparently smooth surfaces.

Finally, as the slope of asperities has great effect on the viscoelastic friction it is worth to investigate one of the most important parameters of fractal surfaces, namely the fractal dimension, in depth. In [44], viscoelastic component of rubber friction is studied for highly polished steel surface with RMS roughness of about $0.1 \mu m$ using Persson's theory developed for fractal surfaces. The fractal dimension extracted from the spectrum of the surface roughness was, however, quite large ($D_f \approx 2.66$). As it is mentioned by Mofidi et al. [44] the large fractal dimension implies that the ratio between the amplitude and the wavelength of a given component of surface roughness strongly increases as the wavelength decreases (the larger the fractal dimension, the faster the ratio of amplitude and wavelength will increase as the wavelength decreases), and it is why the contribution of short-wavelength roughness to viscoelastic friction is more important than the one of long-wavelength roughness. Analyzing surface roughness spectrum of apparently smooth metal surfaces (plungers of real brake cylinder) finished by different techniques (cork wheel, sand paper, rolling) Czifra et al. [60] pointed out that the fractal dimension obtained from micro-scale roughness (measured by diamond stylus profilometer) ranges from $D_f \approx 2.2$ to 2.5. Larger fractal dimension values are characteristic of surfaces finished by cork wheel. In case of sand paper and rolling, the fractal dimension obtained from micro-scale roughness is much smaller and is very far from $D_f \approx 2.66$ reported by Mofidi et al. [44]. Furthermore, it is worth to mention that, in case of rolling, the fractal dimension extracted from nano-scale roughness (measured by Atomic Force Microscope) is close to 2.5 which is significantly larger than that from micro-scale roughness but still smaller than 2.66.

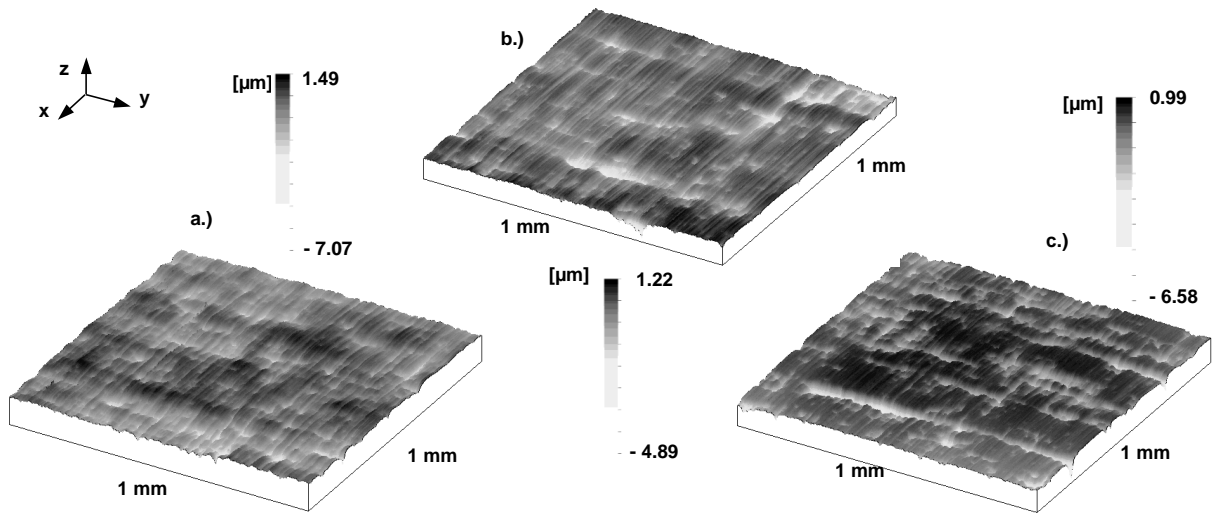


Fig. B1. Rough surfaces measured (a. A1 topography: cork wheel; b. B1 topography: cork wheel; c. C2 topography: sand paper) [60]

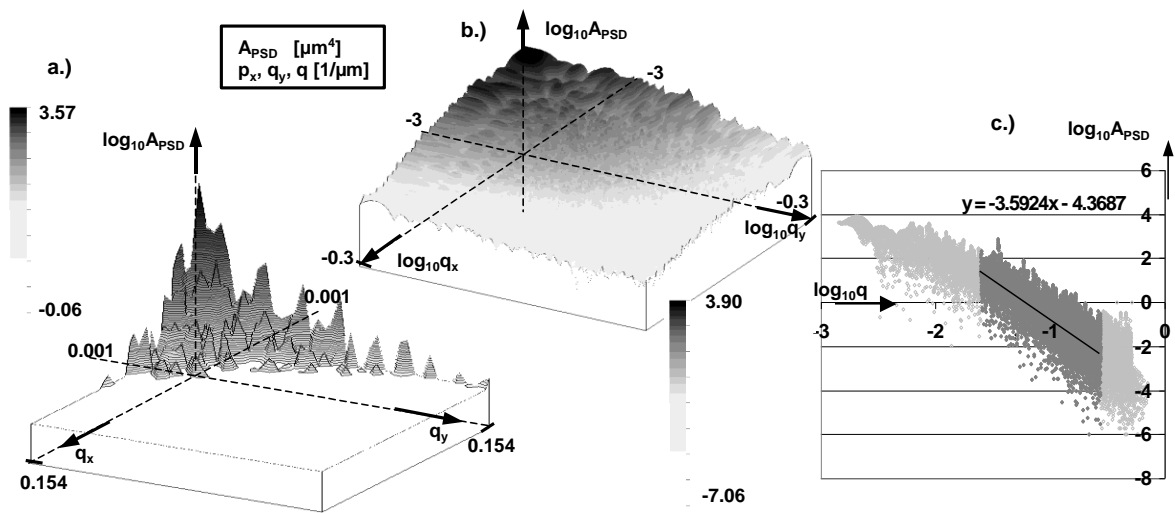


Fig. B2. (a-b) Spectral density surfaces and (c) spectral density curve of C2 topography [60]

Appendix C

C.1. Modeling of viscoelastic material behavior of EPDM 75 IRHD

Majority of numerical friction predictions presented in this thesis has been performed using carbon black filled ethylene-propylene-diene-monomer (EPDM) rubber plates denoted as EPDM 75 IRHD (International Rubber Hardness Degree). It is the material of reciprocating seals built, among others, in hydraulic brake cylinders of TRW Automotive (Pamplona, Spain). In order to characterize its material behavior DMA tests with compressive static load of 100 N, sinusoidally varying dynamic load of 50 N and excitation frequency of 1, 10 and 100 Hz have been performed on rubber samples (10.8 x 11 x 6.33 mm, length x width x height) at the Institute for Composite Materials of University Kaiserslautern. Their results are storage (E') and loss (E'') modulus vs. frequency isotherms (in our case from $T = -90$ °C to $T = +150$ °C with a temperature increment of 10 °C) which make the construction of master curves possible. The master curve describes the material behavior in a broad frequency range and at a given reference temperature. According to the time-temperature correspondence or superposition principle (expressing equivalence of time and temperature) master curves have been constructed by shifting horizontally the measured isotherms. Naturally, the isotherm belonging to the reference temperature remains unchanged and only the rest of the isotherms are shifted horizontally. As a next step 15- and 40-term generalized Maxwell-models (viscoelastic solids characterized by 15 and 40 relaxation times) have been constructed by the author of this thesis for modeling purposes. Parameters of the generalized Maxwell-models have been identified by fitting the material model to the storage modulus master curve. Here the software ViscoData [33] has been used for this purpose. At this point, it must be noted that most of the commercial FE software packages have limited capability for “calibrating” n-term generalized Maxwell-model. In most cases, the number of terms is limited anywhere between ten and fifteen and calibration algorithms for creep and stress relaxation tests are available only. In respect of MSC.Marc [36], the 40-term model is far beyond the calibration capability of the software. Furthermore MSC.Marc is able to handle high-order generalized Maxwell-models in the computations but its graphical user interface for model parameter specification is limited to 15-term model. However this limitation can be bypassed by specifying model parameters directly in the data file of MSC. Marc. In order to analyze the effect of temperature on the material behavior master curves have been constructed at three different temperatures ($T = -50, 25$ and 150 °C) by the author of this thesis. The calibration of viscoelastic material model is performed at each temperature separately.

Fig. C1 and C2 show the measured and fitted storage modulus vs. frequency curves, while Fig. C3 and C4 show the loss factor vs. frequency curves in case of the 15- and 40-term viscoelastic models (generalized Maxwell-model connected parallel to a spring) fitted to the storage modulus master curve, at three different temperatures. In case of 15-term model, it can be observed that there is a good agreement between the measurement and the fitted models with regard to storage modulus, but the loss factor exhibits large oscillations. By increasing the number of Maxwell elements up to 40, the fluctuation becomes smaller; however, even in this case, the model strongly underestimates the value of the loss factor within a broad frequency range. This implies that the 15-term model cannot describe, with adequate accuracy, either the nature of the loss factor or its numerical value. The 40-term model fitted to the storage modulus master curve already properly represents the loss factor vs. frequency curve determined from the measurement in terms of quality – and also in terms of quantity at most frequencies – but it still cannot provide acceptable accuracy in case of certain frequencies. However no reliable energy dissipation can be computed numerically unless the material model can properly represent both the storage modulus and loss factor master curve. As it can be seen material models fitted to the storage modulus master curves cannot describe the stor-

age modulus and the loss factor master curves with the same accuracy within the entire frequency range, therefore care must be taken when they are used. This is particularly important because engineering surfaces have multi-scale nature thus the material model must be able to describe material behavior in a sufficiently wide frequency range (interesting frequency range). Additionally, any variation in temperature shifts the frequency dependent material behavior towards higher or lower frequencies that results in situations where different parts of the material model curves fall into the interesting frequency range.

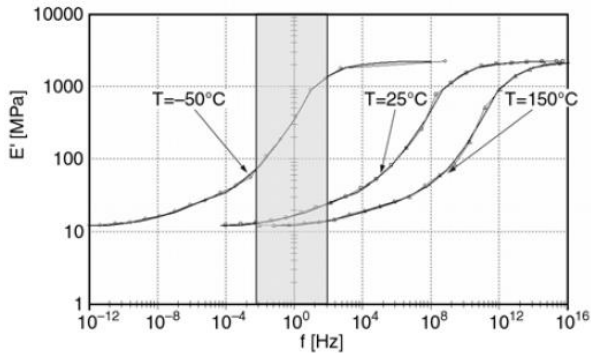


Fig. C1. Comparison of the measured (solid line) and fitted (line with markers) storage modulus vs. frequency curves in case of 15-term generalized Maxwell-model connected parallel to a spring and fitted to the storage modulus master curve (strain amplitude = 0.01%) [38]

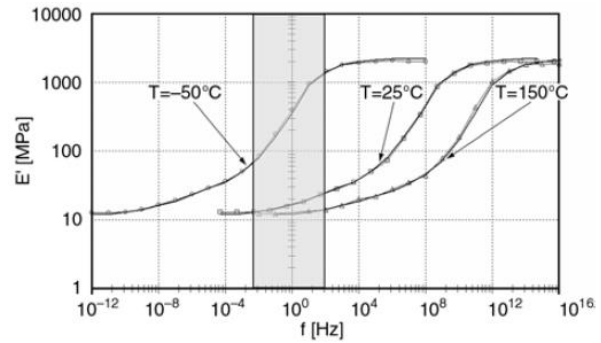


Fig. C2. Comparison of the measured (solid line) and fitted (line with markers) storage modulus vs. frequency curves in case of 40-term generalized Maxwell-model connected parallel to a spring and fitted to the storage modulus master curve (strain amplitude = 0.01%) [38]

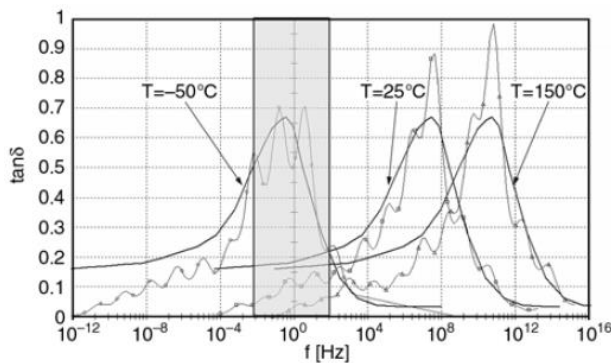


Fig. C3. Comparison of the measured (solid line) and fitted (line with markers) loss factor vs. frequency curves in case of 15-term generalized Maxwell-model connected parallel to a spring and fitted to the storage modulus master curve [38]

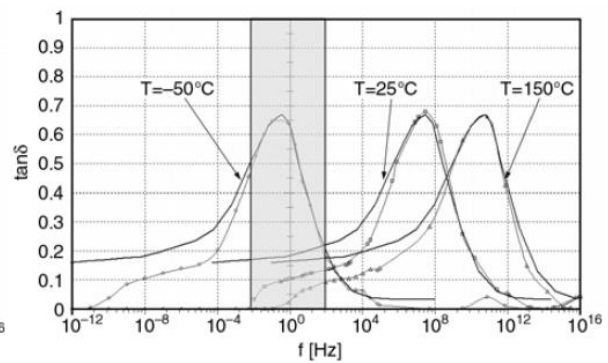


Fig. C4. Comparison of the measured (solid line) and fitted (line with markers) loss factor vs. frequency curves in case of 40-term generalized Maxwell-model connected parallel to a spring and fitted to the storage modulus master curve [38]

The figures show clearly that the application of more terms reduces the oscillation of the fitted loss factor curve but practically has no effect on the agreement between measurement and fitting. Consequently, even the 40-term model provides much smaller loss factor ($\tan(\delta)$) values than the measurement for a broad frequency range. This implies that FE predictions using this material model will underestimate the hysteresis friction force within this frequency range. Modification of model parameters provided by ViscoData offers a natural way to decrease the discrepancy between measured and fitted loss factor curve or to fit the model to the

measured storage and loss modulus curve simultaneously. Since ViscoData is able to fit to the measured storage modulus master curve only the modification has been realized manually by the author of this thesis using a trial-and-error technique. The aim of this modification is to obtain parameters with which the loss factor master curves can be described more accurately in the interesting frequency range i.e. close to the characteristic excitation frequencies. Naturally, such a manual modification of model parameters has an effect not only on the $\tan(\delta)$ but also the E' curve of the material model. In viscoelastic material models used for friction prediction, the multi-term generalized Maxwell-model is combined with two-parameter Mooney-Rivlin model as described in Appendix A. Its parameters belonging to the glassy state are as follows: $C_{10} = 289.33 \text{ MPa}$, $C_{01} = 72.33 \text{ MPa}$ when fitting to the storage modulus master curve, and $C_{10} = 406.66 \text{ MPa}$, $C_{01} = 101.66 \text{ MPa}$ when fitting to the loss factor master curve. As it can be seen the Mooney-Rivlin parameters change due to the manual modification of parameters obtained by ViscoData. The normalized moduli (e_i) and relaxation times (τ_i) of the modified generalized Maxwell-model are obtained by manual modification from those of the Maxwell-model fitted to the storage modulus master curve. If one used the same glassy Mooney parameters in both cases, an accurate relaxed modulus for the Maxwell-model fitted to E' would be obtained while, for the Maxwell-model fitted to $\tan(\delta)$, the relaxed modulus would be considerably underestimated in the interesting frequency range. To minimize this underestimation i.e. to approach E' to the measured values, the glassy Mooney parameters have been changed. Thus one obtains higher glassy modulus than the measured one but the agreement, within the interesting frequency range, between the modeled and measured E' values will be better than in the case of same Mooney parameters.

For the sake of simplicity rubber is often considered to be linear viscoelastic. In many cases, this gives fair agreement with real rubber behavior but there are cases when this assumption causes significant errors. For small strains, the viscoelastic behavior, in most cases, is linear. For larger strains, however, the nonlinear viscoelastic theory usually yields more accurate results. While, in this thesis, constant coefficients are used for the springs and dashpots of the material model, in case of nonlinear viscoelasticity, variable coefficients (material model parameters) would be required. As mentioned by Urzsumcev and Makszimov [115], in several cases, the difference between rheological parameters of loading and unloading increases with increasing load. In order to model this behavior, different coefficients would be required in the loading and unloading phase. In the viscoelastic models used here a generalized Maxwell-model (parallel connection of several Maxwell-models or Maxwell elements) is connected parallel to a nonlinear spring and the coefficients for the springs and dashpots are constant. As it has already been mentioned dashpots with Newtonian viscosity are used in the viscoelastic model. In this case, the viscosity is independent of strain or shear rate. However when the viscosity is dependent on the shear rate the material exhibits shear thinning or shear thickening. In case of shear thinning, the material can be deformed relatively easier (with lower force than in case of shear rate independent viscosity) at higher shear rates. Consequently, in case of shear thickening, higher force is needed to deform the material at higher shear rates than in case of shear rate independent viscosity. Figs. C5 and C6 show frequency-dependent E' and $\tan(\delta)$ curves of 40-term viscoelastic models fitted to the loss factor master curve in comparison with measured curves at three different temperatures. In case of fitting to the loss factor at 25 and 150°C, the storage modulus is underestimated below a certain frequency while it is overestimated above that. At -50°C, the interesting frequency range falls right from the maximum of the $\tan(\delta)$ curve therefore the Maxwell-parameters differ from the ones applied at 25 and 150°C in case of fitting to the measured loss factor curve. Due to this, at -50°C, the storage modulus curves of the two types of fitting run together up to 10000 Hz, while it becomes overestimated above this frequency. As regards the loss factor curves of Fig. C6, it can be

concluded that there is a good agreement between the simulated and the measured loss factor curves at $T=25^{\circ}\text{C}$ and 150°C .

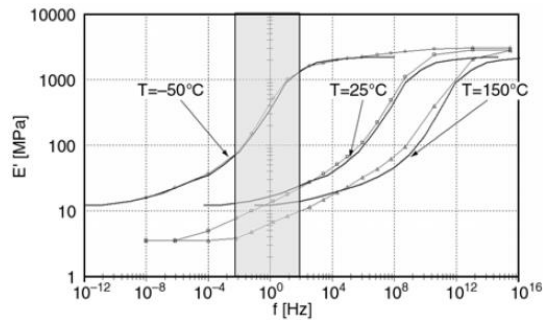


Fig. C5. Comparison of the measured and simulated storage modulus vs. frequency curves in case of 40-term generalized Maxwell-model connected parallel to a spring and fitted to the loss factor master curve (strain amplitude = 0.01%)

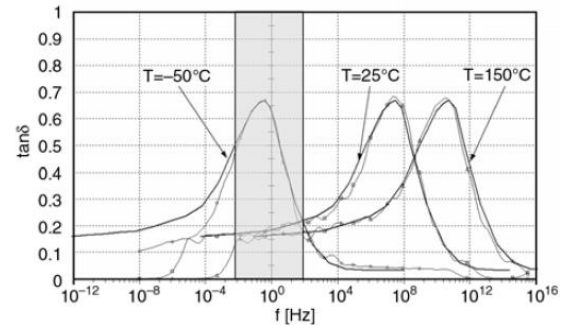


Fig. C6. Comparison of the measured and simulated loss factor vs. frequency curves in case of 40-term generalized Maxwell-model connected parallel to a spring and fitted to the loss factor master curve (strain amplitude = 0.01%)

At small frequencies where relaxation processes with long relaxation times dominate the time dependent behavior the loss tangent (loss factor) of EPDM rubber filled with carbon black is close to 0.2. (In [40], Persson came to similar conclusion for styrene-butadiene rubber filled with carbon black.) In this frequency range, the viscoelastic friction (frictional resistance caused by energy dissipation in rubber) cannot be predicted accurately if the 40-term viscoelastic model fitted to storage modulus master curve (conventional approach for curve fitting) is used. At this point it must be mentioned that only few FEM-based viscoelastic friction predictions were available in the literature before our first studies ([11, 29, 32, 37, 38]). Their common characteristic was that the rubber behavior is described by few relaxation times only (unrealistic rubber behavior). As real rubber behavior cannot be characterized by few relaxation times they were suitable for qualitative analysis only. Nowadays the importance of using proper number of relaxation times in numerical viscoelastic friction predictions is widely accepted. For instance, Scaraggi and Persson in their very recent numerical study on rolling friction [25] use viscoelastic material models characterized by 34 relaxation times. The viscoelastic model parameters are determined from a fit to measured master curve where number of frequency decades was between 20 and 25. In the paper of Carbone and Putignano [127], 34-term viscoelastic model having relaxation times in geometric progression ($\tau_{i+1}/\tau_i = e$ where e denotes the Euler's number) is fitted to master curve spanning 12 decades of frequencies. In a very recent study of Lorenz et al. [128], Persson has revised his former opinion on the requested number of relaxation times (he stated in [40] that it is usually enough to include $n \approx 15$ relaxation times if $\tau_{i+1} \approx 10\tau_i$) and concluded that it is usually enough to use 100 (or less) relaxation times and $\tau_{i+1} \approx 3\tau_i$. Furthermore the viscoelastic model was fitted to the viscoelastic (complex) modulus master curve in order to increase the accuracy. Besides quantitative analyses qualitative analyses can also be found in the literature of numerical viscoelastic friction prediction. For instance, in studies of Wriggers and Reinelt [34] and De Lorenzis and Wriggers [129], viscoelastic friction predictions for road surfaces are performed using viscoelastic solid characterized by 6 relaxation times only. However, it must be mentioned that, in the improved version of the multi-scale modelling approach (see the work of Wagner et al. [135]) originally proposed for FE prediction of viscoelastic friction by De Lorenzis and Wriggers [129] no less than 24 relaxation times are used for characterizing viscoelastic solids.